THE UNIVERSITY OF CHICAGO

SKIPPING TO THE FINISH LINE: SUB-ELECTRON RESOLUTION MEASUREMENTS WITH DAMIC-M CCDS FOR DARK MATTER DETECTION

A DISSERTATION SUBMITTED TO
THE FACULTY OF THE DIVISION OF THE PHYSICAL SCIENCES
IN CANDIDACY FOR THE DEGREE OF
DOCTOR OF PHILOSOPHY

DEPARTMENT OF PHYSICS

BY
JULIAN JOAQUIN CUEVAS-ZEPEDA

CHICAGO, ILLINOIS
DECEMBER 2024

Copyright © 2024 by Julian Joaquin Cuevas-Zepeda

All Rights Reserved

To my parents, my family: sus sacrificios no fueron en vano.

"Caminante, son tus huellas

el camino y nada más;

Caminante, no hay camino,

se hace camino al andar."

— Antonio Machado, *Caminante, No Hay Camino*

TABLE OF CONTENTS

LIST OF FIGURES viii

LIST OF TABLES xi

ACKNOWLEDGMENTS xii

ABSTRACT xiv

1 INTRODUCTION TO DARK MATTER 1
1.1 What is Dark Matter? 1
1.2 A Brief History With Dark Matter 2
1.3 Dark Matter Candidates 5
1.3.1 Weakly Interacting Massive Particles 5
1.3.2 Sub-Gev Dark Matter 6
1.4 Detecting Dark Matter 7
1.4.1 Direct Detection of Dark Matter: Experiments 8
1.5 Final Remarks 10

2 DAMIC-M 11
2.1 Overview 11
2.2 Charge-Coupled Devices 12
2.2.1 Conventional CCDs 12
2.2.2 Skipper CCDs 18
2.3 The DAMIC-M Experiment 21
2.3.1 CCDs as Particle Detectors 21
2.3.2 Dark Matter Interactions 23
2.3.3 Future Projections 25

3 DEVELOPMENT AND COMMISSIONING OF TEST CHAMBERS 27
3.1 Overview 27
3.2 What Is A Test Chamber? 27
3.3 The University of Chicago Test Chambers 29
3.3.1 Test Chamber 1 29
3.3.2 Test Chamber 2 31
3.3.3 The Calibration Chamber 32
3.3.4 Development of the Slow-Control System 35
3.4 The Low-Background Chamber 35
3.5 Final Remarks 37

4 COMPTON SCATTERING MEASUREMENT . . . 39
4.1 Overview . . . 39
4.2 Compton Scattering . . . 39
4.2.1 Other Physics Processes . . . 42
4.2.2 The So-Called Compton Steps . . . 42
4.2.3 Silicon Binding Energies . . . 44
4.3 Experimental Setup . . . 44
4.3.1 Source Selection . . . 45
4.3.2 Hardware . . . 46
4.3.3 Data Runs Configuration . . . 48
4.3.3.1 Serial Register Data . . . 51
4.4 Image Processing and Event Reconstruction . . . 51
4.4.1 WADERs . . . 52
4.4.2 Key Image Parameters . . . 52
4.4.2.1 Dark Current . . . 53
4.4.2.2 Detector Resolution . . . 54
4.4.2.3 Calibration Constant . . . 56
4.4.3 Clustering . . . 56
4.4.4 Data Quality Monitoring . . . 57
4.5 Data Quality Monitoring and Cleaning . . . 57
4.5.1 Baseline Shifts . . . 58
4.5.2 Quality Cuts . . . 60
4.6 Spectral Analysis . . . 61
4.6.1 Compton Continuum . . . 62
4.6.1.1 Background Subtraction . . . 63
4.6.1.2 Area Method . . . 64
4.6.2 L-Shell and Energy Threshold . . . 66
4.7 Final Remarks . . . 68

5 IONIZATION YIELD FROM NUCLEAR SCATTERS . . . 70
5.1 Overview . . . 70
5.2 Ionization From Nuclear Scatters . . . 71
5.2.1 Recent Measurements . . . 73
5.3 Experimental Setup . . . 75
5.3.1 Source Selection . . . 75
5.3.2 Hardware . . . 79
5.3.3 Data Runs Configuration . . . 81
5.4 Data Processing . . . 86
5.4.1 Overview . . . 86
5.4.2 Calibration Constant . . . 89
5.4.3 Clustering Parameters . . . 89
5.4.4 Data Cleaning . . . 94
5.4.4.1 Skyline Shifts . . . 96

5.4.4.2 Skyline Shift Detection Algorithm . . . 97
5.4.4.3 Skyline Shift Cluster Masking . . . 99
5.4.4.4 Row Selection Cuts . . . 106
5.4.4.5 Summary . . . 107
5.5 Spectral Analysis . . . 108
5.5.1 Overview . . . 108
5.5.2 Average Cluster Rate and Gamma Intensity . . . 108
5.5.3 Standard bin-by-bin Subtraction . . . 112
5.6 Spectral Fit . . . 115
5.6.1 Overview . . . 115
5.6.2 Cumulative Gaussian Fit . . . 117
5.6.3 400-Skip and 1600-Skip Comparison . . . 121
5.7 Ionization Efficiency . . . 122
5.7.1 Overview . . . 122
5.7.2 Nuclear Recoil Spectrum . . . 123
5.7.2.1 ENDF-VII vs. Oak Ridge National Lab Cross-Section . . . 127
5.7.2.2 Neutron Distribution In Detector . . . 129
5.7.3 Calculation of Neutron Flux Throughout Data Taking . . . 130
5.7.4 Data Preparation . . . 137
5.7.4.1 Cluster Reconstruction and Characterization Efficiency . . . 137
5.7.4.2 High-Energy Neutron Contribution . . . 140
5.7.5 Ionization Yield . . . 142
5.8 The Nuclear Fano Factor . . . 145
5.8.1 Overview . . . 145
5.8.2 The Nuclear Fano Factor in Silicon . . . 146
5.8.3 A Charge Ionization Model . . . 148
5.8.4 The Iteration Method . . . 151
5.9 Systematic Checks . . . 155
5.9.1 Baseline Configuration . . . 155
5.9.2 Systematic Checks . . . 157
5.10 Results . . . 162
5.11 Final Remarks . . . 166

6 CONCLUSION . . . 167

REFERENCES . . . 169

LIST OF FIGURES

1.1 Matter-Energy Composition in the Universe 1
1.2 Planck Temperature Power Spectrum 3
1.3 The Bullet Cluster 4
1.4 Dark Matter Masses 4

2.1 6K × 4K Skipper CCD 13
2.2 Serial Register Photograph and Pixel Anatomy 14
2.3 WIMP Scattering In Pixel 15
2.4 CCD Anatomy + Charge Readout 16
2.5 Skipper Readout Stage 18
2.6 Skipper CCD Sub-Electron RMS 19
2.7 Particle Tracks in a CCD 21
2.8 Dark Matter Interaction In Silicon 23
2.9 DAMIC-M Detector Design Cross-section 24
2.10 The DAMIC-M Experiment Projections 25

3.1 Test Chambers 1 and 2 30
3.2 Multi-CCD Test Chamber Configuration 30
3.3 The Calibration Chamber 33
3.4 The Low-Background Chamber Commissioning 36

4.1 Compton Scattering 40
4.2 Compton Continuum 41
4.3 Compton Steps and Binding Energies 44
4.4 silicon Scattering Cross-Sections 45
4.5 Compton Experimental Setup 47
4.6 Am-241 Source Holster 48
4.7 Example 64-skip Data Image 50
4.8 Dark Current Fit 53
4.9 Skipper Resolution Comparison 54
4.10 Non-Linearity of Calibration Constant 55
4.11 Example Image with Noise 58
4.12 Example Data with Baseline Shifts 59
4.13 Low-Energy Cluster Injections 60
4.14 Low-Energy Spectral Features After Quality Cuts 61
4.15 Compton Continuum 62
4.16 Low-Energy Data Components 63
4.17 Area Method 65
4.18 Final Spectrum 67

5.1 SuperCDMS Ionization Yield Results 74
5.2 ^{9}Be(γ, n)^{8}Be Cross Section 76
5.3 ^{9}Be(γ, n)^{8}Be MCNPx Neutron Yield 78

5.4 Experimental Setup . . . 79
5.5 Material targets and Antimony source pellets . . . 80
5.6 Source Cell . . . 81
5.7 Neutron and Gamma Flux On CCD . . . 82
5.8 ENDF-VIII and ORNL Neutron Cross-Section . . . 83
5.9 400-Skip Data Example . . . 84
5.10 1600-Skip Data Example . . . 85
5.11 Distribution of CCD Resolution and Gain . . . 88
5.12 Comparison of Clustering Parameters . . . 90
5.13 Comparison of Clustering Parameters at Low Energy . . . 91
5.14 Comparison of Clustering Parameters for 1600-Skip Data . . . 92
5.15 Zero-Peak Sigma Throughout Data Campaign . . . 93
5.16 Selected Run With Skyline Shifts . . . 95
5.17 Al Target Data with Skyline Shift Clusters . . . 96
5.18 Skyline Shift Flagging Algorithm . . . 98
5.19 Skyline Shift Pixel Energy Properties . . . 100
5.20 Skyline Shift Pixel Tagging Algorithm Example . . . 101
5.21 Skyline Shift Cluster Position Mapping, $N_{SS} = 0$ . . . 103
5.22 Skyline Shift Cluster Position Mapping, $N_{SS} = 1$ . . . 104
5.23 Skyline Shift Cluster Energy Contribution . . . 105
5.24 Skyline Shift Column Cuts . . . 106
5.25 Selection Cuts: 1600-Skip Data . . . 107
5.26 Average Cluster Rate vs Time . . . 109
5.27 Gamma-Only Data vs. Ambient Background . . . 111
5.28 Neutron Spectral Data: 400-Skip . . . 112
5.29 1600-Skip Spectral Data . . . 114
5.30 1600-Skip Spectral Subtraction . . . 116
5.31 Cumulative Gaussian Fit on 1600-Skip Data . . . 117
5.32 Spectral Subtraction From Gaussian Fit . . . 120
5.33 400-Skip and 1600-Skip Data Comparison . . . 121
5.34 Source Simulation MCNPX Geometry . . . 123
5.35 MCNPX Full Experimental Geometry . . . 125
5.36 Nuclear Recoil Energy Spectrum . . . 126
5.37 Scaled ENDF-VII Library . . . 128
5.38 Simulated Neutron Distribution . . . 129
5.39 Neutron Activity Characterization . . . 131
5.40 1600-Skip Image Mask . . . 136
5.41 Reconstruction Efficiency . . . 138
5.42 Cluster Characterization Efficiency . . . 140
5.43 Neutron Offset . . . 141
5.44 Integral Method Histograms . . . 143
5.45 Ionization Yield with F=0 . . . 144
5.46 Fano Factor Cartoon . . . 145

5.47 SuperCDMS Fano Factor Measurement 147
5.48 Gaussian Ionization Model At Different Fano Factor Values 148
5.49 Poisson Charge Ionization Model 150
5.50 Toy Monte Carlo for the Iteration Method 152
5.51 Iteration Method on Toy MC 153
5.52 Iteration Method Applied On The Measurement Data 154
5.53 Systematic Uncertainty 158
5.54 Systematic Checks 159
5.55 Systematic Checks 160
5.56 Final Integral Method 162
5.57 Final Result 165

6.1 A Questionable Particle Track 168

LIST OF TABLES

4.1 Am-241 Emission Lines 46
4.2 Compton Data Summary 50

5.1 Sb-124 Emission Lines 78
5.2 Sb-124 Activity Measurements 85
5.3 Neutron Data Summary 86
5.4 Neutron Flux Measurements 161
5.5 Results Summary 164

ACKNOWLEDGMENTS

Without a doubt, the work in this thesis would not have been possible without the support of the many mentors, colleagues, family, and friends who supported me throughout this journey. First and foremost, I would like to extend my deepest gratitude to my advisor Paolo Privitera. Throughout my Ph.D. tenure, Paolo provided me with unwavering kindness, mentorship, and guidance that strengthened my resolve to continuously push myself to be the best physicist I could be. I could not have asked for a better advisor. Second, I thank Juan I. Collar for his unwavering kindness and friendship throughout my Ph.D. I am grateful for all the great conversations and guidance he provided, and for allowing me the pleasure of occasionally working alongside him and his group. I would also like to thank the rest of my committee, Young-Kee Kim and Carlos Wagner, for their support and guidance throughout the years.

Next, I would like to thank my colleagues in DAMIC-M. First, a big thank you to Danielle Norcini for being the best post-doc, mentor, and friend a grad student could have. Second, a big thank you to Radomir Smida for the endless conversations, guidance, and support he provided me throughout my tenure in DAMIC-M. Third, I would like to thank my current and former fellow students from DAMIC-M at UChicago Rachana Yajur, Sugata Paul, Sravan Munagavalasa, Karthik Ramanathan, Ryan Thomas, Ariel Matalon, Carly Kleinstern, and Nick Corso for their support, friendship, and just great times. I would also like to thank Alvaro Chavarria for his mentorship and support during my REU and Ph.D. Being a member of DAMIC-M was an absolute pleasure, and I am grateful for all the people I was fortunate to work alongside during my Ph.D.

I am eternally grateful to my undergraduate advisor Dustin Kleckner for taking me in as his student, for his mentorship throughout the years, and for believing in me. I am indebted to Carrie Menke for being the first person to encourage me to pursue physics. Without her unwavering support, I would surely not be here today. A huge huge thank you to Putri Kusumo for her support, for her friendship, and for helping me navigate through the Ph.D.

bureaucracy.

I am grateful to all the friends that made this journey bearable. To my friends from Chicago: Edgar M., Mark L., Alec H., Joel F., Jonty P., Sravan M., Rachana Y., Lukas P., Duncan R., Joey G., Dan S., Tracy C., Lucas B., Kaeli H., Arjun V., Rosemary C., Sara C., Nina C., Claire B., and Umang M. thank you for the great memories, laughs, and for putting up with my particularities. I could not have done this without you all. To my friends from Merced: Alec M., Steven M., Mark C., Dennis C., Enrique C., Kayla S., Annie A., Kristy B., Tania M., Isabel R., Monica V., Omar P., Noel N., Jesse J., Jessica D., and Kevin C. you guys kept me together throughout the years. Thank you for all the moments we shared, the late nights, and the endless support and encouragement. Thank you to Paola Avila for entering my life and being the biggest source of support and encouragement I could ask for. Thank you for everything.

I can never thank my family enough. It is because of their sacrifices, their patience, their love, and their courage that I am able to present this thesis. First, thank you to my parents, Patricia and Joaquin. Without their endless support, consistent encouragement, and decisive sacrifices I would not be the person that I am today. It is for them that I pushed to get this work done. Thank you to my younger sister, Estefania, for always being so supportive and caring. I am constantly in awe of what you are accomplishing. I am thankful for having the privilege to call you a fellow scientist. Mil gracias a mi abuelo Juan. Nunca podré repagarle sus sacrificios, pero el apoyo que me ofreció siempre lo llevaré en mi corazón. Thank you to all my family; this thesis is dedicated to you.

ABSTRACT

Dark matter constitutes ∼27% of the matter-energy distribution in the Universe. Over the past several decades, low-background experiments have been built at underground facilities to search for direct interactions with the elusive particle(s). In order to detect rare signals from dark matter interactions, great efforts must be taken to reduce, characterize, or model the natural radiation backgrounds in the laboratory environment. Detectors that are sensitive to electron and neutron scatters are subject to interactions from gamma rays and neutrons that originate from radioactive decays in nearby materials. Interactions in the detector from these particles can mimic dark matter interactions, so their signal needs to be precisely characterized.

In this thesis, I present my contributions towards the research and development efforts for the DAMIC-M experiment. Two dedicated measurements were conducted at the University of Chicago campus with silicon skipper CCDs; whose floating gate amplifier allows for multiple Non-Destructive Charge Measurements (NDCMs) to reduce a pixel's readout noise to a sub-electron level. The first measurement exposed the detector to gamma rays from an Am-241 source. The resultant Compton spectrum demonstrated clear features of silicon's atomic shells and measured for the first time a clear signature of the L_1 - $L_{2,3}$ atomic shells and scattering off of valence-shell electrons. This measurement successfully demonstrated the efficacy of skipper technology (in contrast to conventional CCDs) by pushing the measurement threshold to 23 eV with only 64 NDCMs. The second measurement exposed the detector to an antimony-beryllium photo-neutron source to measure the ionization efficiency of silicon from nuclear scatters. This measurement demonstrates the full power of skipper technology's ability to resolve single electrons and measures the ionization yield down to an $\mathcal{O}$(eV) of charge-ionization.

These two measurements demonstrate the sensitivity of DAMIC-M detectors to dark matter interactions with silicon electrons or nuclei.

CHAPTER 1

INTRODUCTION TO DARK MATTER

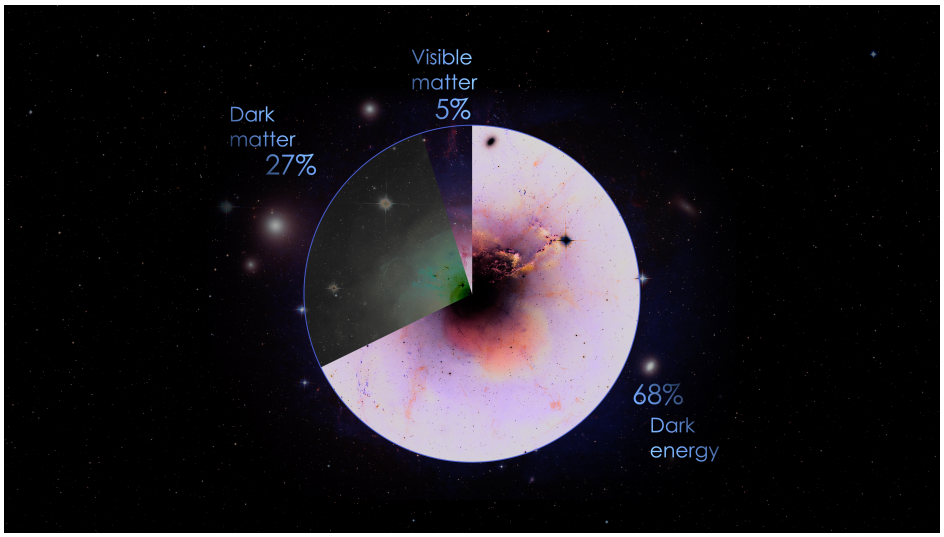

Figure 1.1: An illustration from NASA Goddard Space Flight Center partitioning the matter-energy composition of the Universe based on results from the Planck mission [58]

1.1 What is Dark Matter?

For centuries, human breakthroughs in science and technology were limited to phenomena that could be *seen*. Achievements that ranged from discovering humanity's place amongst the stars, to deploying large-scale telescopes that led to the discovery that the Universe is expanding [28, 36]. These scientific breakthroughs have shaped our understanding of the Universe and its history; motivating generations of scientists to continuously push the boundary of what is known and *observable*. Today, one of the greatest mysteries is understanding the matter-energy composition of the Universe. Measurements of the Cosmic Microwave Background (CMB) have determined that the Universe consists of approximately 5% baryonic matter, 27% dark matter, and 68% dark energy [58]. Baryonic matter refers to ordinary matter – comprised of protons and neutrons – and represents the matter that we have studied and interacted with for centuries. Dark matter is a form of non-luminous matter, devoid

of any interaction with the electromagnetic force, and predicted to be weakly coupled to ordinary matter. Dark energy is a form of vacuum energy theorized to contribute toward the accelerating expansion of the Universe. Since their discovery, these dark constituents have motivated physicists to build numerous experiments dedicated to their study, with hope that these measurements will provide insights into the structure and history of the Universe.

In this thesis, we will focus on the study of dark matter, its detection mechanisms, and considerations that must be taken into account when searching for its ever-elusive signal.

1.2 A Brief History With Dark Matter

The first evidence for the existence of dark matter happened in 1970 when Vera Rubin and Kent Ford published their rotation curves for M31, otherwise known as the Andromeda galaxy. In their work, they found that the rotational velocities of stars in M31 did not have a steep drop-off as you increased in distance from the galactic center, as is expected from Newtonian mechanics, but rather the velocities seemed to plateau. This strange result was later confirmed en-masse with their 1980 paper that studied the rotation curves of 21 spiral galaxies and reported the same result: 'non-luminous matter exists beyond the optical galaxy'[65, 66]. From these measurements spawned a plethora of research that matured our understanding of the role dark matter plays in the structure of the Universe. For instance, today it is believed that all galaxies reside within a dark matter halo; the luminous, baryonic matter is gravitationally bound in the core of the dark matter halo and contributes a small fraction of the encased matter [12, 29, 35, 56, 57, 76]. Ultimately, it is the Milky Way's dark matter halo that sources the flux of dark matter particles that experiments have been hoping to detect over the past several decades.

At large, cosmological scales astronomical observations and measurements have only strengthened the case for the existence of dark matter. With ΛCDM acting as the modern cosmological model, precision measurements of the CMB provide the most definitive

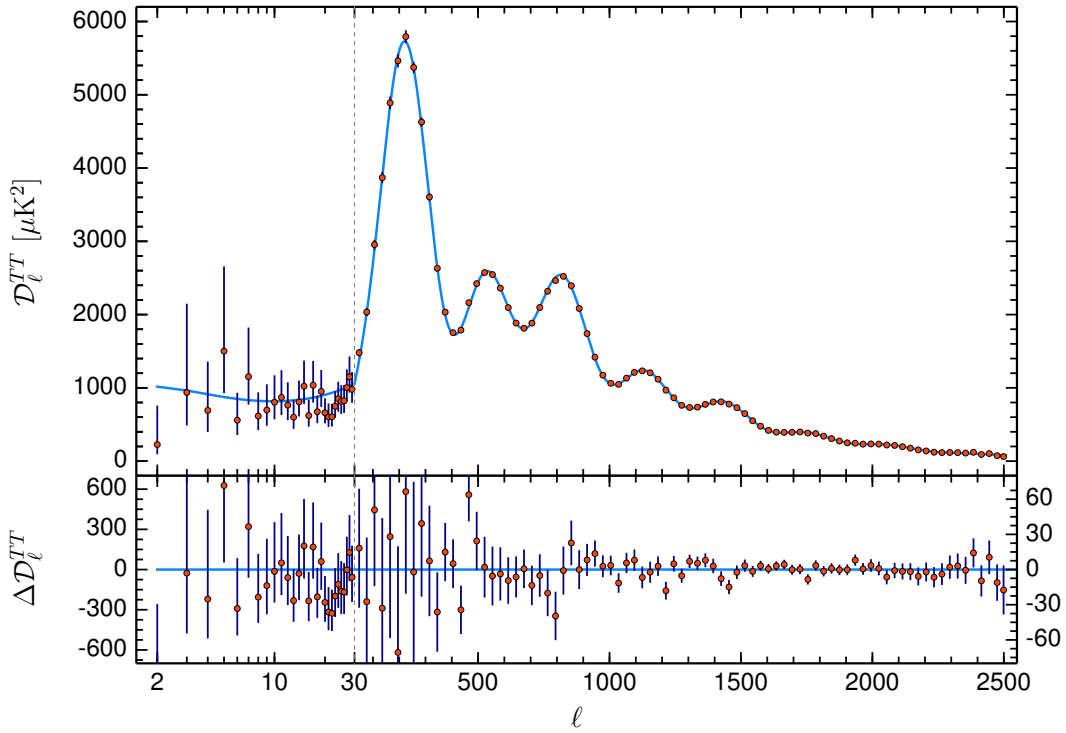

Figure 1.2: Planck 2018 measurement of the Cosmic Microwave Background. Best fit results show an excellent agreement with ΛCDM cosmology model [58].

validation of the existence of dark matter to date. The power spectrum shown in Figure 1.2 shows the remarkable agreement between the Planck 2018 measurement of the CMB and ΛCDM — that assumes the existence of dark energy and cold dark matter in the Universe[1] [35, 58]. In addition to the CMB measurements briefly presented here, gravitational lensing in regions of space that seemingly lack the matter necessary to produce such drastic lensing effects unless there is a form of non-luminous matter present [35, 49, 50]. The most famous example of such phenomena is the Bullet cluster that is shown in Figure 1.3.

Ultimately, the scientific community is convinced that dark matter plays a dominant role in the structure of the Universe. The following sections will briefly describe some particle candidates and detection techniques employed by the community.

1. Cold dark matter refers to dark matter candidates that have cooled enough to not be relativistic and are hence capable of forming large-scale structures in the Universe.

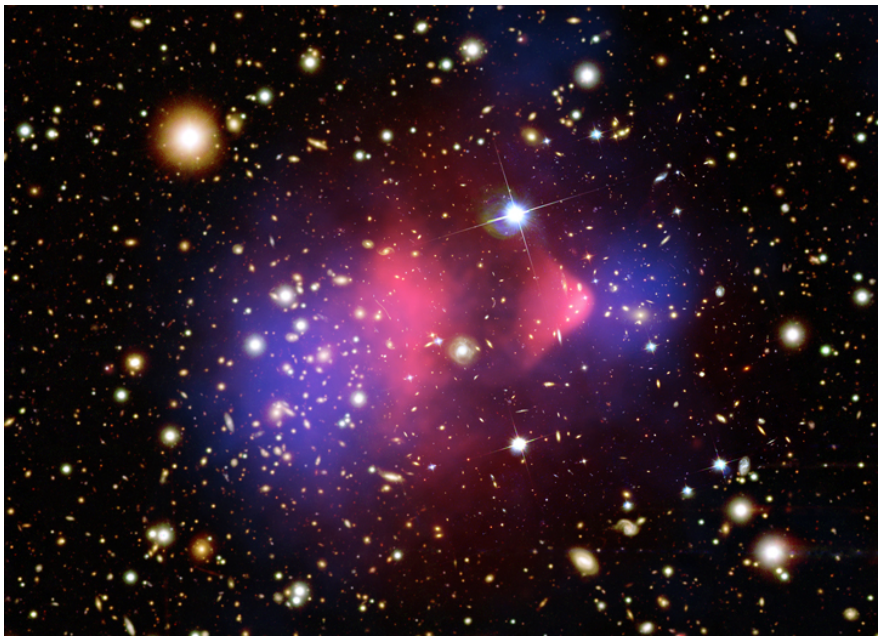

Figure 1.3: Composite image of the Bullet cluster from the Chandra X-Ray Observatory. The regions in pink are regions of hot gas and are indicative of normal matter. The regions in blue are the regions that were found to contain the most mass after applying gravitational lensing techniques [49].

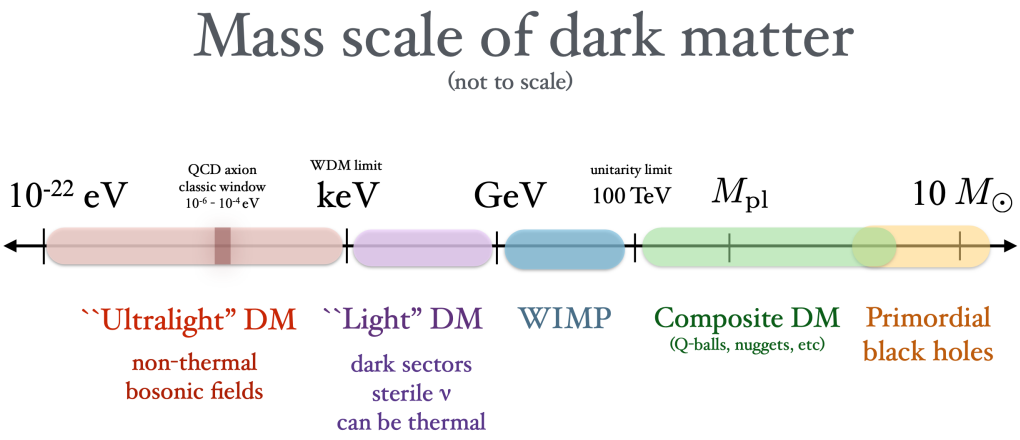

Figure 1.4: Cartoon mass scale for allowed dark matter candidates. Colored ranges are not to scale. The figure is from T. Lin's 2019 TASI lecture [47].

1.3 Dark Matter Candidates

When considering the particle nature of dark matter, there are a few constraints that must be discussed. First, dark matter must be, well *dark*. All evidence of the existence of dark matter demonstrates its non-luminous nature, and its decoupling from the electromagnetic force and the strong nuclear force. Moreover, the dark matter candidate should be feebly interacting with standard model particles — it is often assumed that dark matter can only interact with the standard model particles through the weak nuclear force or gravity. Second, dark matter must be cold (non-relativistic) to allow for its gravitational collapse into halo structures and to remain consistent with observational evidence. Third, the dark matter candidate must be stable, and long-lived in respect to cosmological time scales [35, 47]. These constraints are the basis on which many dark matter candidates arise. Ultimately, the goal for any hypothesized dark matter candidate is to provide insight into the structure of the Universe, whilst remaining consistent with astronomical observations and the current matter-energy distribution of the Universe.

1.3.1 Weakly Interacting Massive Particles

The most popular and naturally motivated dark matter candidate class are Weakly Interacting Massive Particles, or WIMPs. These particle species are believed to have been at thermal equilibrium with standard model particles in the early Universe and then 'frozen out' to their current abundance in the Universe today [12, 15, 35, 47]. They are well-motivated by theories that posit particles beyond the standard model and have been the main candidate experiments have been in search of. With a mass range approximately between 10 GeV/c^2 to 10 TeV/c^2 and an annihilation cross-section of roughly $\sigma v \sim 10^{-26}$ cm^3/s that is strikingly similar to an annihilation cross-section predicted by the weak nuclear force, physicists are optimistic that a WIMP signal can be detected [12, 47].

It is expected that the WIMP is coupled to the weak nuclear force, and thus is capable of

scattering off of nuclei in detectors. From the scattering process, a WIMP will deposit energy into the detector that will be subsequently converted into an electrical signal. However, the rate of interaction between WIMPs and atomic matter is expected to be low, thus many experiments are built to be quite large in order to maximize the likelihood of DM-nucleon scattering. Some examples of detector types and detection mechanisms will be discussed in the next section.

1.3.2 Sub-Gev Dark Matter

Another dark matter class is conventionally referred to as 'light dark matter' and exists in the approximate mass range of 1 keV/c^2 to 10 GeV/c^2 [47]. This class of dark matter was also in thermal equilibrium with standard model particles in the early Universe, however, its signal is much more difficult to detect in modern experiments. Given the lower mass dark matter, any recoils between sub-GeV DM and atomic nuclei would produce lower ionization signals that can be reasonably detected. However, the solution is to instead search for DM-electron interactions within target materials. For semi-conductor targets, such as silicon or Germanium, the crystal's band gap is in the order of a few single eV and ionization from a broad range of sub-GeV DM candidates is accessible. Thus, experiments are gearing towards improving their resolution thresholds through extensive research and development [27].

Ultimately, the aforementioned dark matter classes present the modern top-candidates for detection. While dark matter as a whole can exist with masses outside of these ranges, the discussion in this thesis will be limited to WIMPs and sub-GeV dark matter. Figure 1.4 shows a mass-scale of dark matter. For more a more rigorous discussion on dark matter and its history see the following reference [12, 15, 27, 35, 47].

1.4 Detecting Dark Matter

Dark matter searches are usually split into three categories: generation of dark matter at particle accelerators, indirect searches (eg. annihilation signals), or direct detection. In this thesis we will focus on the latter type of search — direct dark matter detection. Previously, I mentioned that our galaxy is enveloped in a dark matter halo, meaning there is a constant flux of dark matter particles as the Earth travels through space. Physicists have built experiments that rely on this fact to design, large underground detectors to search for dark matter.

The flux of dark matter can be thought of as sourcing from a dark matter wind, with a relative velocity distribution that is calculated from astronomical data. The DM velocity distribution, $f(\mathbf{v}, t)$, can be modeled using Maxwell-Boltzmann statistics, and constrains the relative velocities incident on a terrestrial detector. The expected event rate in the detector should exhibit an annual modulation signature due to the Earth's relative position around the Sun; the presence of this signature solidifies the claim for a dark matter signal [29, 45, 68]. The expected dark matter rate in the detector is dependent on the mass of the detector, the interaction cross-section between the atomic nuclei of the detector and the dark matter candidate, and the flux of dark matter particles passing through the detector at a given time. For WIMP-like dark matter, the relation is expressed as,

$$\frac{dR}{dE_{nr}} = \frac{\rho_\chi}{2m_\chi \mu^2}\sigma(q)\int_{v_{min}}^{\infty}\frac{f(\mathbf{v},t)}{v}d^3v \tag{1.1}$$

where dR/dE_{nr} is the differential rate for dark matter scatters with atomic nuclei (usually expressed in terms of events/kg/day/keV, or dru), ρ_χ is the local WIMP-like dark matter density, m_χ is the WIMP mass, μ is the reduced mass of the DM-nucleus system (expressed as $\mu = (m_\chi M)/(m_\chi + M)$), $\sigma(q)$ is the effective cross-section of the system, and the integral expression is the mean inverse speed of the dark matter flux; where v_{min} would describe

the minimum WIMP speed needed to produce a nuclear recoil [13, 29, 45, 46, 68]. The equation shown in Equation 1.1 is used to model the detector rate resulting from WIMP-like interactions in a detector. An analogous relation for sub-GeV dark matter scatters with electrons takes into consideration semiconductor devices with sensitivities capable of detecting such interactions, and develops a relation dependent on the semiconductor crystal properties and their bound-state electrons — further information on the differential rate for DM-electron scatters in detectors can be found in Reference [27]. From Equation 1.1 it is apparent that the key parameter needed to detect a dark matter interaction is a proper selection of target medium — a target that maximizes the scattering cross-section between dark matter and the target's atomic nucleus, and a detector that can be scaled to increase the scattering rate in the detector's active media.

1.4.1 Direct Detection of Dark Matter: Experiments

For a physicist, designing an experiment to detect dark matter usually involves selecting a detector sensitive to a set of dark matter candidates and selecting a location to conduct a measurement. Focusing on the latter decision, given the expected low rate of dark matter scatters in a detector, a dark matter experiment's data collection period normally spans multiple years. The experiment is built with as much target mass as reasonably achievable by the technology available at the time, and any collected data is reported in a grams-day exposure convention. Given the length of time these experiments run for, a common challenge amongst the community is reducing the event rate in the detector from any natural radiation. Natural radiation can source from either cosmic sources – think cosmic rays and their by-products after interaction in the Earth's atmosphere – or through decays in the materials that surround the dark matter detector. To shield from the cosmic sources, experiments are built in large underground facilities where they employ the natural rocky terrain to shield the detector from cosmic radiation. However, the shielding of radiation from material decays

is more involved. Often, the experimental teams develop extensive research and development efforts to fully categorize and assay any radiogenic source that can induce unwanted events in the detector during operation. These efforts coupled with changes to fabrication and packaging techniques in the detectors, better material selection, and a 'smarter' detector design (ie. choosing ancient lead as shielding material for the detector core) have allowed experiments to achieve remarkably low background rates. With the increased sensitivity to dark matter interactions, many experiments have placed world-leading constraints on dark matter candidates. A few detectors techniques and experimental collaborations will now be listed.

Scintillating Detectors. A material that produces photons as a by-product of energy deposition from external radiation is referred to as a scintillator. When an incident particle deposits energy into this class of detector, the material will scintillate (produce light), and that light will be collected by a light-sensitive detector (eg. photo-multiplier tube) and amplified to a recognizable signal to be analyzed. Many experimental collaborations employ this class of detectors, most notably DAMA/LIBRA and the XENON collaboration [11, 20]. The former experiment employs NaI[Tl] crystals and has been in scrutiny by the scientific community due to their controversial claim to dark matter detection with an irreproducible result from similar detector experiments [1]. The latter experiment employs liquid Xenon coupled with a time projection chamber to search for dark matter scatters. The experiment relies on a signal generated from scintillation and a slower-moving signal from charge-ionization (from the same scattering event) to produce a 3D reconstruction of the energy deposition event. This technique allows for better rejection of background events in the detector [20].

Bubble Chambers. Experiments such as PICO-500 will employ a superheated flourinated compound as its target for a dark matter search. This detector class is uniquely sensitive to WIMP-proton interactions and is capable of probing a spin-dependent set of

WIMP candidates. Moreover, these type of detectors have the ability to naturally reject gamma and beta backgrounds, thus making them well suited for dark matter searches [6, 31].

Semiconductors. As particle detectors, semiconductors are uniquely positioned to probe low energy thresholds of interaction. With band gaps in the order of single electron-volts, silicon and Germanium based detectors have been positioned as ideal targets for dark matter searches. These detectors are sensitive to ionization from several mechanisms: photo-absorption, electronic recoils, and nuclear recoils. However, their detection mechanism are not limited to ionization, phonon-sensitive devices – such as those employed by CDMS/SuperCDMS – are capable of determining how much energy was deposited in a detector through a complimentary access of phonon and ionization channels. This makes these types of detectors capable of discriminating between nuclear recoil events (phonon + charge ionization) and electronic recoil events (charge ionization). However, other silicon based detectors, namely charge coupled-devices (CCDs), have been widely studied and matured. Recent advances in CCD technology have positioned collaborations like DAMIC, SENSEI, and DAMIC-M to leverage the so-called Skipper CCDs to achieve sub-electron resolution in their detectors. With a band gap of $\sim$ 1.1 eV and an electron-hole pair creation energy of $\sim$ 3.7 eV, these detectors are sensitive to an $\mathcal{O}$(10 eV) of ionization signal, and are capable of probing DM-nucleus and DM-electron interactions.

1.5 Final Remarks

With extensive astronomic evidence pointing towards the existence of dark matter, many experiments have been commissioned to search for its signal. This thesis will focus on the DAMIC-M experiment, and my contributions towards the development of the detector technology. In order to increase the sensitivity of our detectors, extensive R&D efforts and calibration measurements need to be carried out.

CHAPTER 2

DAMIC-M

2.1 Overview

In the previous chapter, we discussed the history of dark matter, its evidence and implications, and the detector technologies employed to explore the vast parameter space that describes the elusive particle and its potential interactions. This chapter, and the subsequent chapters, will be dedicated to the DAMIC-M experiment and its choice of detectors, my contributions towards the hardware and instrumentation developments, and scientific measurements intended for calibrating and characterizing the detector in search of dark matter interactions.

The DAMIC-M experiment – which stands for the [Da]rk [M]atter [I]n [C]CDs at [M]odane – specializes in the development and use of scientific charge-coupled devices (CCDs) as ionizing radiation detectors. The DAMIC-M experiment will be constructed at the Laboratoire Souterrain de Modane (LSM) in Modane, France. This facility lies 1,700 meters beneath the Frejus Peak and was selected due to the mountainous region's ability to shield the experiment from inbound cosmic rays. At the facility, the detectors will be subject to ambient background radiation consisting of neutrons, γ-rays, x-rays, muons, beta-particles, and alpha-particles — all emitted as decay products of the surrounding materials of the facility or the experimental system. Interactions between these particles and the detector generate unique signatures in the detector, and their contributions towards the ionization signal can be either reduced through the implementation of radiation shielding and/or careful selection of material processing, or they can be modeled as a background signal and subtracted from the resultant ionization signal. Of course, this is a simplification of the myriad of methodologies and techniques that are employed to achieve the desired background rate upon the commissioning of the detector, but it serves as an illustration of some of the challenges that

the collaboration must overcome and why these experiments are conducted at underground facilities. In the final sections of this chapter, I will discuss DAMIC-M goals, status, and projections through 2025 [2, 7, 10, 17].

DAMIC-M is the successor to the DAMIC at SNOLAB experiment that employed 16 Mpixel silicon CCDs in search of dark matter. The DAMIC experiment was based at the SNOLAB underground laboratory in Sudbury, Ontario, Canada. The experiment successfully demonstrated the efficacy of scientific CCDs as a target material; throughout the experiment's tenure, the collaboration has developed a comprehensive background model and material assays for the immediate detector components, has reported competitive dark matter constraints, and has reported a confirmed spectral excess at $\sim$80 eV_{ee} of unknown origins [2, 3, 19, 24, 25]. The majority of these results were conducted with *conventional* scientific CCDs – which is a statement of the readout stage of the electronics – and were limited to a $\sim$2 electron readout noise (RMS). For DAMIC-M, the intended detector will employ the novel Skipper readout process that is capable of conducting multiple non-destructive charge measurements. These CCDs are capable of producing sub-electron resolution and will be instrumental in pushing towards measurement thresholds in the order of 2-3 electrons (e-)[1] [7, 10, 74].

2.2 Charge-Coupled Devices

2.2.1 Conventional CCDs

The CCD was first developed in 1969 at Bell Labs in an attempt to develop a new memory device [37]. Since its inception, the CCD has evolved from a small collection of 'closely spaced MOS capacitors' to the massive $\sim$9 gram, 6144 $\times$ 4128 (6K $\times$ 4K) pixel-arrays employed by DAMIC-M for the prototype detector experiment — see Figure 2.1 [5, 7, 8].

1. In this thesis, results will be presented in units of electrons (e-). This unit is meant to be equivalent with an average electron-hole pair creation energy of 3.74 eV.

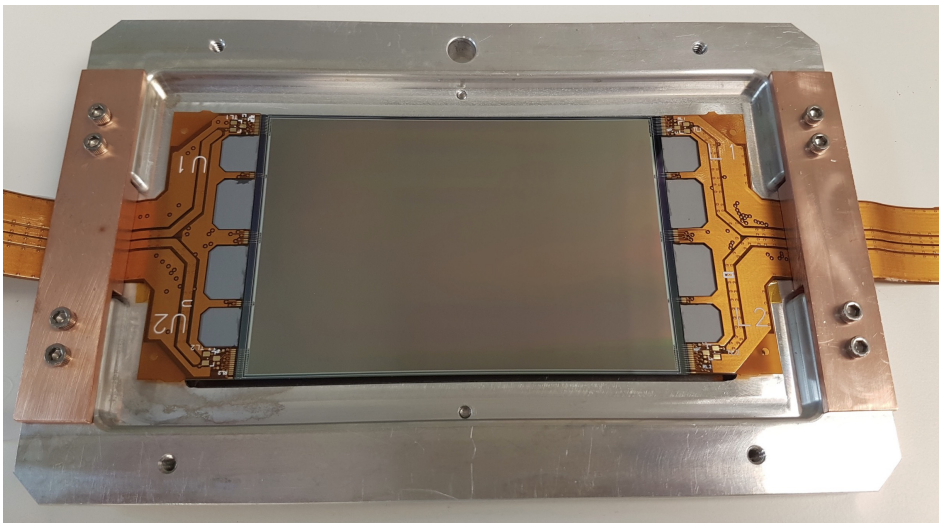

Figure 2.1: A photograph of a 6K × 4K Skipper CCD in its testing packaging at the University of Chicago. A Kapton flex cable is connected to either side of the CCD to provide the operating voltages. Labeled in each corner is a corresponding amplifier: U1, U2, L1, L2. Photographs presented in this thesis were taken by myself, or are allowed for general use by DAMIC-M members.

To start, a charge-coupled device, or CCD, is a pixelated image sensor that converts electronic excitations into localized voltage signals to form an image. DAMIC-M CCDs are composed of a backside metal contact, a thick n-type silicon substrate (∼670 μm), a buried p-channel, a SiO_2 insulating layer, and metal gate contacts on the front side of the device — effectively making a CCD an arrangement of metal-oxide-semiconductor (MOS) capacitors [37]. Each of the pixels that make up the CCD image sensor consists of three of these MOS capacitors connected together to form a respective phase of the pixel readout during operation. In Figure 2.2 we can see a side-by-side photograph of a DAMIC-M CCD serial register at 50x magnification and a cartoon diagram of the general anatomy of a pixel. In the photograph, the in-focus region known as the serial register is the region of the CCD tasked with transferring the collected charge in the CCD to the readout stage — this will be discussed in the following paragraphs. This region is also comprised of pixels, and a repeating, brown-tinted vertical stripe delimits them; the region within each stripe contains the aforementioned metal gate contacts that comprise a pixel. For DAMIC-M CCDs, a pixel

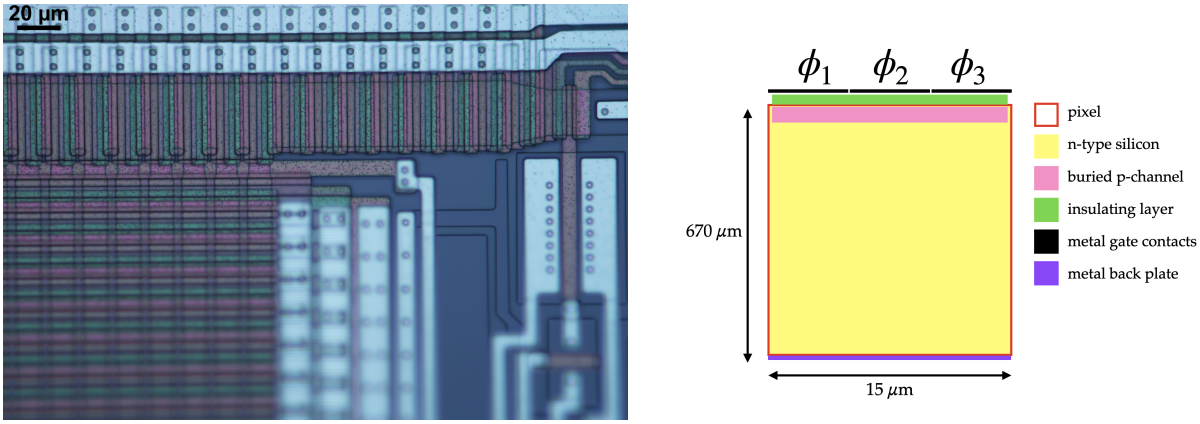

Figure 2.2: *Left*: A photograph of a DAMIC-M prototype CCD at 50x magnification. A scale is shown on the top left corner to be 20 μm. The in-focus region is a portion of the CCD's serial register in the corner of the U2 amplifier. Each pixel can be seen delimited by a vertical, brown-tinted stripe and the corresponding pixel phase-gates are contained within. *Right*: A cartoon diagram of the anatomy of a pixel. Each component is described in the provided legend. ϕ_i is a general description for the respective phase in a pixel.

is operated in a three-phase system, meaning that within each pixel boundary, you will find three metal contacts that control the potential wells that *clock* the collection and motion of charge.

In order to operate a CCD, the first step is to apply a bias voltage across the entire device. This bias voltage, or substrate voltage (V_{sub}), is required to generate a depletion region within the silicon that depletes intrinsic free charge carriers and prevents recombination of any generated charge – in that region – during CCD operation. DAMIC-M CCDs are fabricated out of high-resistivity silicon ($>$ 10 kΩ cm) that allows for full depletion of the bulk silicon volume[2] during operation at $V_{sub} \geq 40$ V [7, 19]. The full depletion of the CCD prevents any recombination of charge when an ionization event occurs and increases the certainty of charge reconstruction during the analysis of an image. After the full depletion of the CCD, whenever an ionizing particle deposits energy – greater than the electron-hole pair creation energy $\epsilon_{e-h} \sim 3.7$ eV (1 e-) – into the silicon bulk of the detector, any generated

2. The bulk silicon volume of the CCD is generally the 670 μm thick region composed of n-type silicon. This is the primary region of interest when discussing charge generation from incident particles.

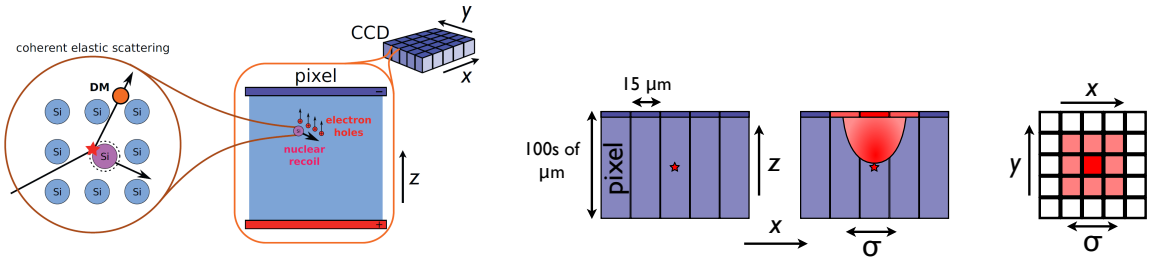

Figure 2.3: *Left*: An incident dark matter particle coherently scatters off a silicon atom and ionizes charge in the CCD. *Right*: After charge ionization, the charge drifts toward the corresponding pixels. Throughout the drift, the charge will diffuse. The width (σ) of diffusion is dependent on the silicon CCD's fabrication procedure, the operating conditions, and is directly proportional to the depth (z) of the scattering event. The diagrams presented in this thesis were created by myself, or are allowed for general use by DAMIC-M members.

charge carriers will drift towards their respective poles of the bias voltage. For our CCDs, electrons will drift toward the back plate of the detector, and positively charged holes will drift toward the front of the detectors and accumulate in the potential well of a pixel's buried p-channel until charge-readout. A diagram of this process can be seen in Figure 2.3. Once the charge arrives at the respective pixels, it will either remain in stasis, and accumulate until charge readout begins, or it will become aggregate to its respective pixel's present charge and be clocked towards the readout electronics. The former is colloquially known as the *exposure* stage and the latter is the *readout* stage.

Before proceeding to a discussion of how collected charge is converted into an image, it is important to discuss the general structure of a CCD's anatomy. In the top image of Figure 2.4 we see a magnified image of a DAMIC-M prototype CCD. In the image, there are seven labeled regions. The first, the pixel array, is commonly denoted as the *active* region. The pixel array represents the primary area of interest, and any charge generated in the silicon bulk corresponding to this region will accumulate in the corresponding pixels until charge readout. A user of the CCD can designate a specific portion of the CCD to be read out; this of course, is dependent on the specific use case, but the portion of the CCD that is read out determines the size of an image. The second region of interest is the vertical clocks region.

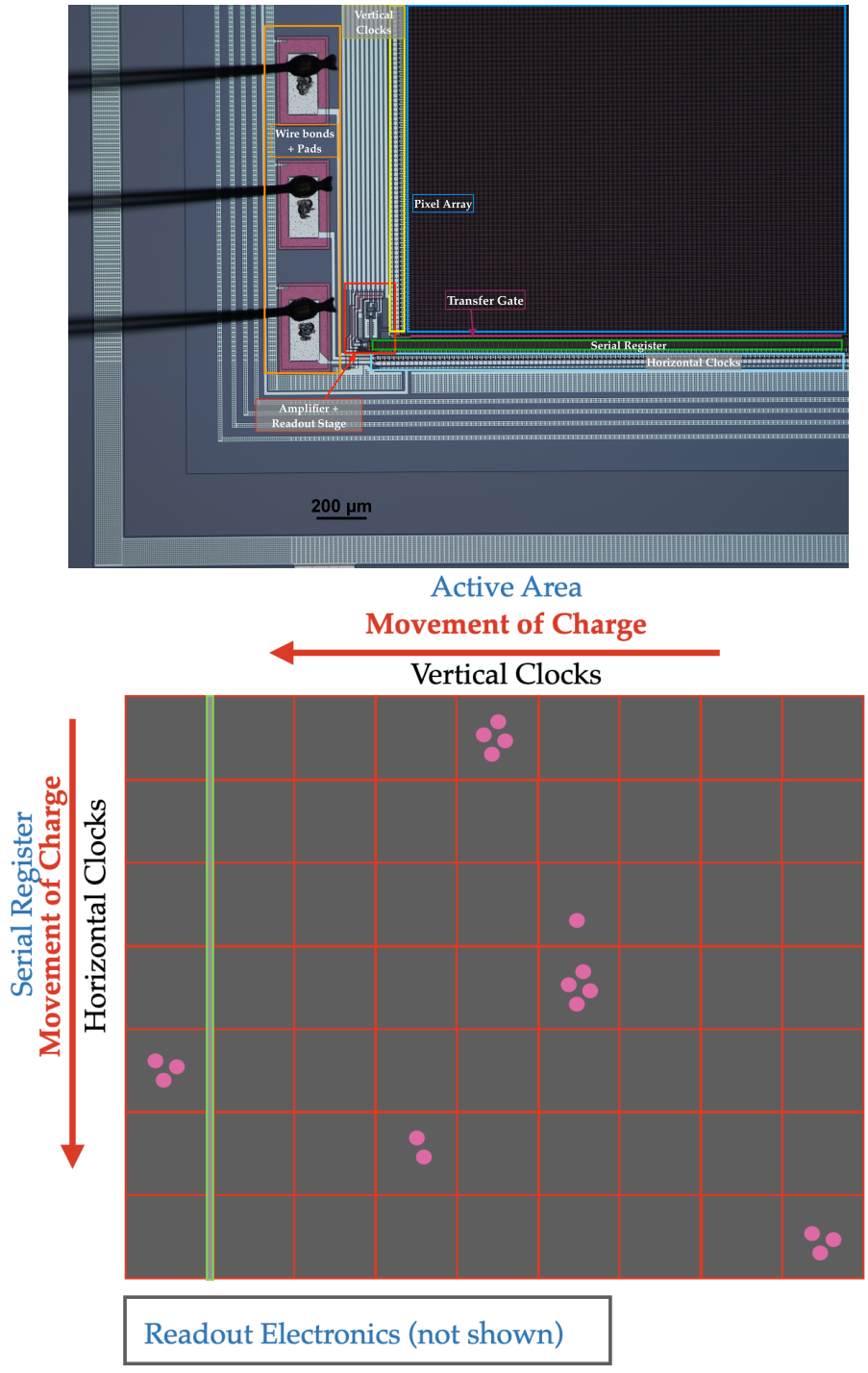

Figure 2.4: *Top*: A photograph (at 5x magnification) of a DAMIC-M Skipper CCD. In the image, the general anatomy of a CCD is labeled. *Bottom*: A diagram detailing the general motion of charge after the exposure stage of the CCD.

As previously mentioned, a DAMIC-M CCD functions as a three-phase system, therefore, the vertical clock region is split into three: V_1, V_2, and V_3. Each pixel is connected to the vertical phase clocks, and during the operation of the CCD, these clocks provide a voltage for each pixel – in a High/Low configuration – to either accumulate or move charge across the pixel array toward the serial register. Pixel charge is moved in unison with other pixels of the same row. The idea, which is diagrammed in the bottom cartoon of Figure 2.4, is that all charge of the ith row will be simultaneously transferred row-by-row until it reaches the serial register. After a row is deposited into the serial register, the pixel readout can commence, and charge is individually transferred toward the readout stage of the CCD. While the charge is being transferred, the vertical clock region is stalled, awaiting the final pixel of the row to be read out. To prevent any leakage of charge onto the serial register from the pixel array, a potential barrier exists between the two sections. This potential barrier is referred to as the *transfer gate* and is only lowered to allow the transfer of charge between the pixel array and the serial register. The serial register and transfer gate represent the third and fourth regions of interest. The fifth region of interest is the horizontal clocks region. This region, similar to the vertical clocks region, is split into three phases: H_1, H_2, and H_3. The horizontal clocks control the motion of charge in the serial register and transfer the charge toward the readout stage. The sixth region of interest is the amplifier and readout stage. Once a pixel exits the the serial register, it enters an area known as the *prescan* region, this region is a collection of 8 pixels that are members of the readout stage of the electronics. At this point, charge travels toward the sense node where the total charge of a pixel is read, and then converted into a voltage signal by the amplifier; the voltage is later digitized by the readout electronics. The final step is to drain the charge from the system, away from the amplifier, and continue reading charge until the desired number of pixels are read out. The final labeled region in the image is the wire bonds that connect to the CCD and supply the necessary voltages for operation.

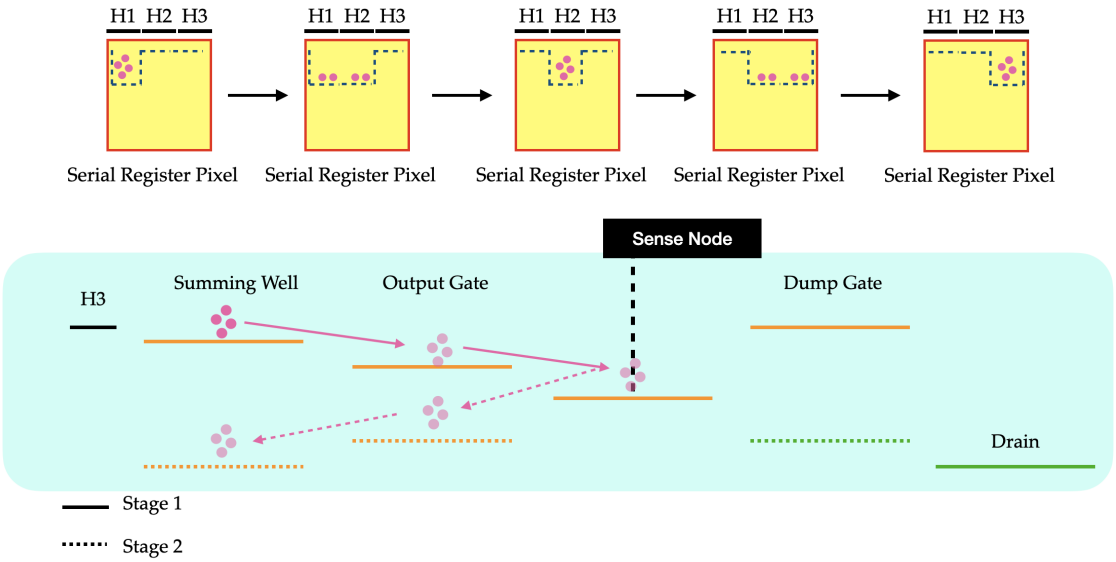

Figure 2.5: Stacked diagrams detailing the motion of charge from the final pixel in the prescan region towards the sense node that measures the total charge. On the top figure, H-gates are being lowered/raised until charge reaches the H_3 gate. At this point, we transition towards the bottom figure where the 2 stages of charge motion is labeled. The dump gate is only lowered to the 'green' stage when the charge has been read out the desired number of times.

Ultimately, this procedure describes how *conventional* CCDs work. For several decades, the development of these CCDs led them to be the primary image sensors in commercial cameras and electronics, the choice detector in many telescope systems or other laboratory settings due to their remarkably low levels of noise, and the choice detectors for DAMIC at SNOLAB [19, 24, 70]. However, the remainder of this chapter will describe the transition towards the new Skipper CCD and DAMIC-M.

2.2.2 Skipper CCDs

The conventional CCDs employed by DAMIC were limited by their readout (RMS) noise of $\sim$2 e- per pixel. This limitation places a constraint on the sensitivity to low-mass dark matter candidates that the detector can confidently measure. Following a letter by Janesick et al in 1990, the development of a CCD capable of producing multiple pixel-charge measurements

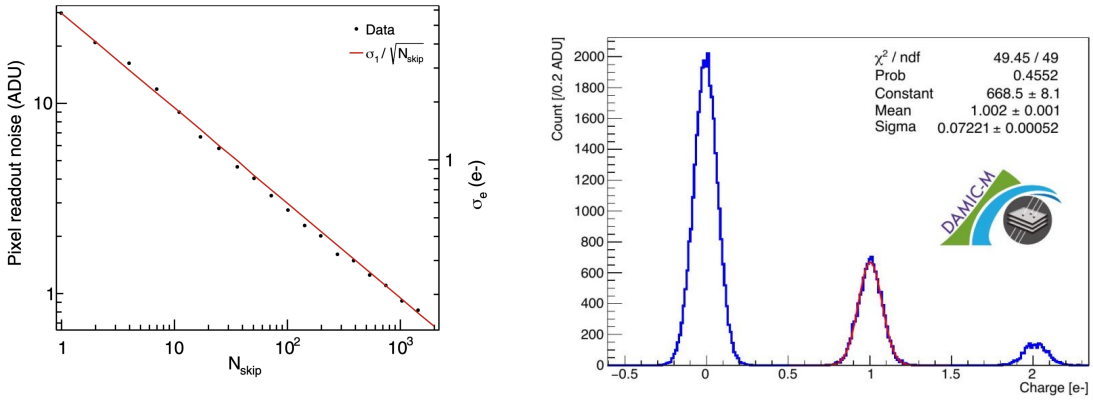

Figure 2.6: *Left*: The RMS, σ_{pix}, as a function of number of skips for an image. *Right*: A demonstration of the sub-electron resolution that is capable for NDCMs >2000. In the figure we see the 0, 1, and 2 electron peaks clearly defined.

had begun. In 2017, a team of scientists at Fermilab demonstrated the first CCD capable of generating multiple non-destructive charge measurements (NDCMs) and producing a sub-electron RMS of ~ 0.18 e- per pixel [38, 74]. This CCD became known within the community as a *Skipper* CCD. The key difference between the conventional CCD and the Skipper CCD is the modification of the output stage. In Figure 2.5 we see charge move from the final pixel of the prescan region towards the output stage. Once the charge is on the H_3 gate, it is transferred onto the summing-well gate and H_3 is raised to prevent charge from moving back onto the pixel. The first stage of the Skipper readout system involves transferring the charge from the summing-well gate, to the output gate, and finally to the floating gate sense node. At this point, the charge is measured; and if multiple samples are required, then the charge is transferred back onto the output gate, then the summing-well gate. Once the charge is on the summing-well gate, the sense node has transferred the measured charge value to the readout electronics and the reference voltage on the sense node is reset. Thus, this process continues until the desired number of samples has been achieved. After the last charge measurement is complete, the dump gate is lowered, and the charge can be drained away from the output stage — allowing the next pixel's charge to be read out [74].

With the Skipper readout system, for every NDCM, or *skip*, of a pixel's charge the RMS

of that pixel has been demonstrated to reduce by $\sigma_1/\sqrt{N_{skip}}$. Here, σ_1 is the RMS of a pixel for a single charge measurement and N_{skip} represents the number of NDCMs, or skips, sampled in a pixel. In Figure 2.6 the left figure demonstrates the reduction of RMS as the number of skips is increased, while the right figure depicts the remarkable ability of a Skipper CCD to resolve single electron peaks with enough skips ($N_{skip} \geq 500$ with the current readout electronics). The clear, well-spaced distance between the 0 e- and 1 e- peaks functions as the calibration value between energy (eV) and digital units (ADU). Prior to the development of the Skipper CCD, calibrating a conventional CCD required the placement of known radiation sources to derive a calibration value between ADU to eV. At low energies, the calibration source was an infrared (IR) photon source – to leverage the high quantum efficiency[3] of the CCD – while at higher energy values, other fluorescence peaks of well-known energies were used to calibrate [19, 24, 62]. This type of calibration was rather inconvenient since it implied adding an extra source of radiation near the detector. However, now Skipper CCDs have been demonstrated to have a strong linearity – constant peak separation – and are capable of being self-calibrated to convert between digital units to units of energy [54, 74]. Moreover, through the single-electron resolution these detectors' dark current rate can be directly measured; this is accomplished by performing a fit involving the convolution of a Poisson distribution with a Gaussian distribution. The rate parameter, λ, in the Poisson distribution is a measure of dark current in the CCD (the dark current will be discussed in later chapters), and the Gaussian parameters, μ_i and σ_i, detail the position and width (RMS) of the peaks respectively.

Ultimately, with the advent of Skipper CCDs, DAMIC-M has a powerful detector capable of probing deeper into the dark matter parameter space. With the ability of Skipper CCDs to self-calibrate, coupled with their sub-electron RMS, DAMIC-M will be able to reliably probe

3. The quantum efficiency is the measure of a CCD to convert incident photons to photo-electrons (via the photoelectric effect); such that the efficiency is given by the ratio N_{e-h}/N_λ where N_{e-h} is the number of electron-hole pairs generated by a photon of a specific wavelength (λ) and N_λ represents the number of photons incident in the CCD.

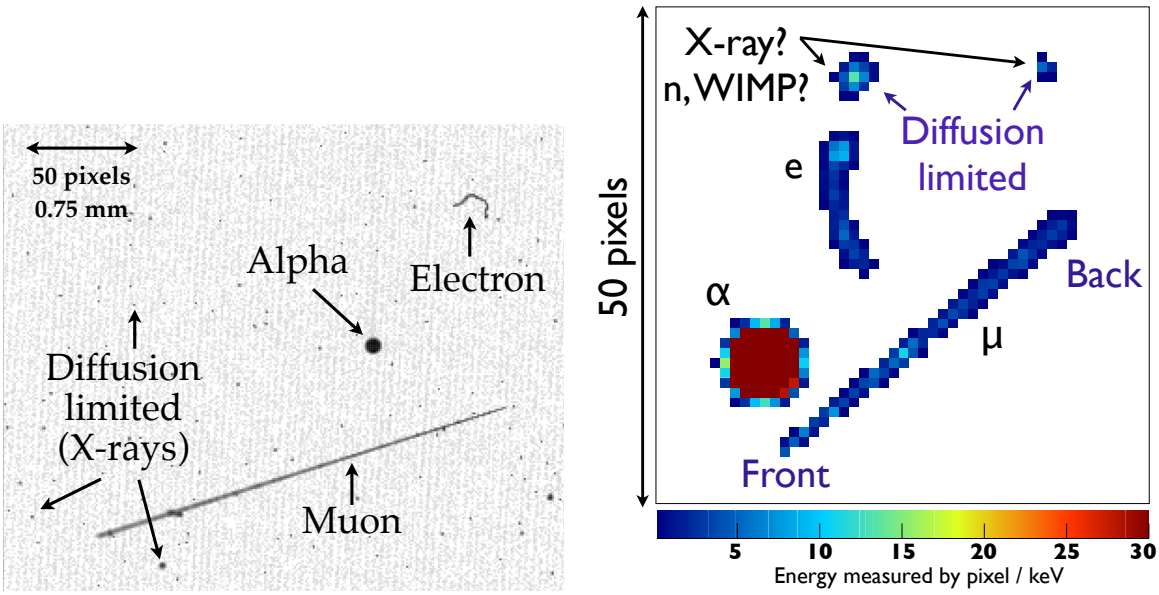

Figure 2.7: *Left*: Example image indicated common particle tracks of varying particle species. *Right*: Example image showing the energy density of varying particle species.

down to the projected 2-3 e- threshold. The final section of this chapter will demonstrate the efficacy of CCDs as particle detectors and present the expected science projections for DAMIC-M.

2.3 The DAMIC-M Experiment

2.3.1 CCDs as Particle Detectors

Now, having discussed the history of CCDs, their evolution, and the general performance and operation of Skipper CCDs, we are ready to discuss their efficacy as general particle detectors. Originally, CCDs were intended as traditional image sensors (ie. converting photons into photo-electrons), however, due to their inability to discriminate between sources of radiation, any particle capable of depositing energy surpassing the electron-hole pair creation energy in silicon ($\epsilon_{e-h} \sim 3.7$ eV) is capable of generating charge in the silicon bulk. Highly energetic particles are capable of continuously generating charge throughout the CCD, and when charge is collected, the particle's projected track will be visible in the

image. A particle's track is treated as a unique signature to specific particle species – based on the species' physical properties and interaction behavior in matter – that allows us to quickly identify the most common deposition event by eye. Figure 2.7 shows two selected images that detail the most common particle tracks in a CCD. The most easily identifiable tracks in a CCD image are those of the muon, the alpha particle, and the beta particle. In general, the more energetic a particle is, the more charge the particle can ionize and the more prominent its track is. Of course, this is assuming no other physical process takes place in the silicon. Usually, the muon is the most energetic and common track found in a CCD image. It is characterized by its long, straight, and sharp particle tracks. The beta particle is characterized by its 'wiggle'-like path; whose shifts in momentum is due to interactions it encounters within the silicon. The alpha particle is characterized by its large 'blob' like deposition. Most of the charge encapsulated in the center (as seen in the right figure) and it does not travel very far in the CCD before being stopped. Other particle interactions such as low-energy neutron scatters, x-rays, γ-rays, or potential dark matter scatters are indistinguishable by eye through their particle tracks; rather, in order to study their signature and properties, we need to perform analysis on the image and study the resultant energy spectrum of the CCD.

A key feature of the CCDs, and a powerful tool during analysis, is a CCD's ability to reconstruct a particle track in 3 dimensions. Given the x-y coordinates of a particle's track, one can calculate the depth (z) where the particle's energy depositions took place. The way to do this is to use the charge-diffusion properties of a fully depleted CCD given by,

$$\sigma_{xy}^2(z, E) = -A \ln(1 - bz) \cdot (\alpha + \beta E)^2 \tag{2.1}$$

where σ_{xy} is the lateral spread of charge as it drifts from the silicon bulk towards its respective pixels, z is the depth where the deposition occurred, E is the energy that was deposited, and the rest of the parameters, A, b, α, and β, are determined as fit values from the CCD during

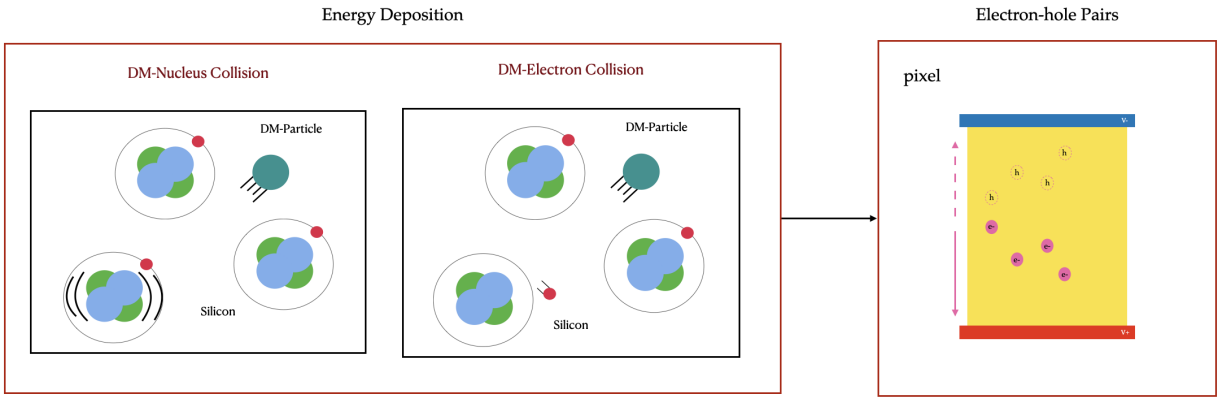

Figure 2.8: Cartoon diagram depicting the possible interaction processes between dark matter and silicon. The right figure is another representation of charge generation after a DM-silicon scattering event.

operation [2, 3, 25]. The ability to apply a 3D reconstruction to a particle track allows us to place fiducial cuts in the silicon bulk, and reject any deposition that is not likely to have resulted from a dark matter interaction in the silicon [2, 3, 24, 25]. Ultimately, making the CCD a powerful detector capable of selectively discriminating against various particle species based on their respective signatures.

2.3.2 Dark Matter Interactions

To detect dark matter in our silicon detector, there are a few things to remember. One, dark matter is largely believed to be a neutral particle, meaning that its interaction in semiconductor devices will not be directly with an electron, rather it will be through scatters with the silicon nuclei or other mediating interactions. Two, the interaction rate in the active silicon will be low; therefore, a dark matter search requires long data-taking campaigns to acquire sufficient statistics to either see a notable excess in the energy spectrum, or to place constraints on dark matter masses. And three, given the detector's sensitivity to *any* particle species, extensive efforts to reduce the flux of environmental radiation in the detector needs to be undertaken or the sensitivity to dark matter interactions will be lessened [2, 3, 8, 9, 13, 19, 27, 29].

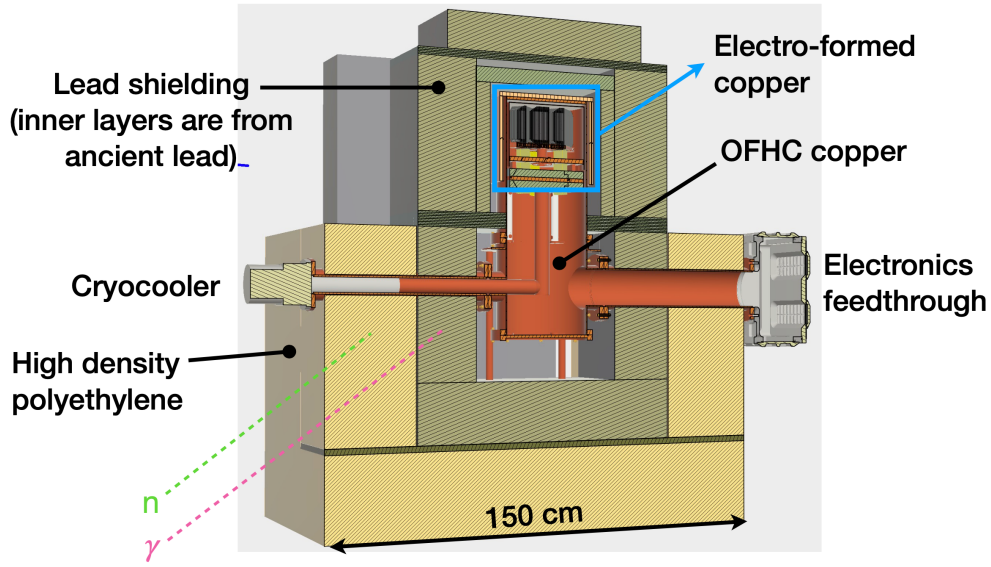

Figure 2.9: Cross-section diagram of the DAMIC-M experiment design.

For a dark matter interaction in the silicon bulk of the CCD – depending on the dark matter model – the charge it generates in the detector is dependent on whether the interaction was between the DM particle and the silicon nucleus, or whether the interaction was with an electron. If the interaction was between a DM-particle and the nucleus, then the deposited energy will not directly translate to ionized charge, rather the recoiling atom will undergo a relaxation process that will subsequently ionize charge dependent on the recoil energy — further details on this process will be discussed in Chapter 5. However, if the interaction is between dark matter and an electron, or a mediator (ie. dark photon) and an electron, then the deposited energy will almost entirely translate towards charge ionization. For either interaction mechanism the ability to generate any ionized charge is limited to either the electron-hole pair creation energy ($\epsilon_{e-h} \sim 3.7$ eV), or the silicon band gap energy (~ 1.1 eV) [18, 27, 42, 47, 54, 60, 62]. Figure 2.8 is a cartoon representation of this process.

Given the low interaction rate between dark matter and silicon, the DAMIC-M experiment needs to be designed to accommodate extensive data collection periods. During data collection, the CCDs will be operating and continuously recording any charge ionization

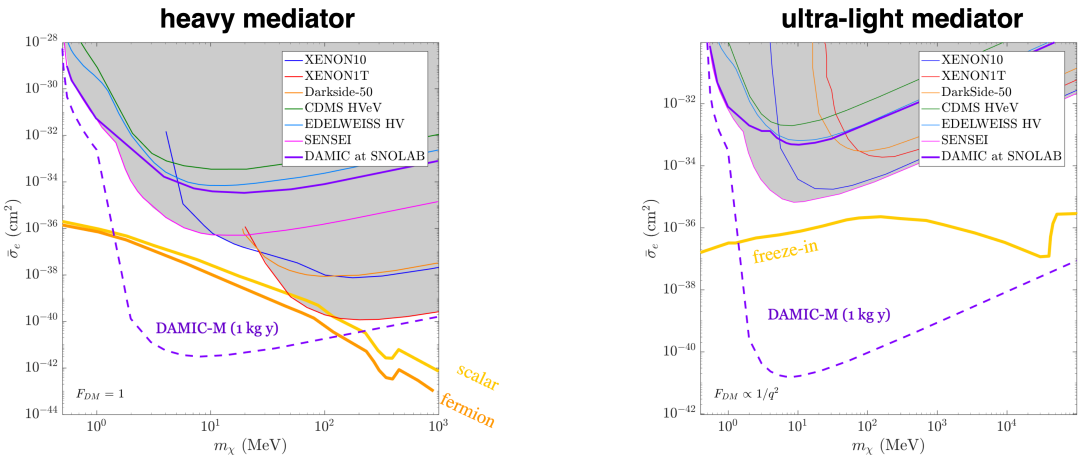

Figure 2.10: DAMIC-M expected projections for dark matter constraints.

without discrimination to its source. At the LSM, there will be a prevalent radiogenic background originating from decays in the surrounding material of the experiment, as well as near the detector itself [2, 10]. These particles have a potential to mimic dark matter interactions in the detector, so their signatures need to be studied and modeled into a background model that will be subtracted from any acquired signal, or their intensity needs to be severely attenuated. DAMIC-M will employ a combination of techniques in the final detector construction to mitigate any radiogenic background effects. Including, the addition of radio-pure materials such as ancient lead or electro-formed copper; the modification of the CCD fabrication, packaging, and handling to reduce exposure to material activation; and the inclusion of external shielding materials such as lead (gammas) and high density polyethylene (neutrons) [10]. The combination of these mitigating procedures, as well as extensive R&D efforts amongst the collaboration, will ensure the experiment achieves a $\sim$ 0.1 dru (1 event/kg/day/keV) background rate.

2.3.3 Future Projections

The DAMIC-M experiment will employ 9Mpixel Skipper CCDs for the construction of the experiment. In the detector there will be an array of CCD modules – each containing 4

Skipper CCDs – as the functional target silicon mass of $\sim$ 728 grams. DAMIC-M aims to achieve an exposure rate of 1 kg-year, a sub-electron resolution, a background rate in the order of 0.1 dru, and a dark current rate less than 0.5 e-/mm^2/day. The detector is estimated to begin construction in early 2025 at the LSM in Modane, France. Given the success of the prototype detector (the Low-Background Chamber), we are confident in the projected reach of this experiment. In Figure 2.9 and 2.10 a cross-section view of the detector design is shown on the former figure, while the projected sensitives is shown on the latter figure.

Overall, DAMIC-M is expected to probe a significant portion of the dark matter parameter space; sensitive to both nuclear and electronic interactions. The following chapter will be dedicated to the R&D efforts that I contributed to while completing my doctoral degree, and the later two chapters will focus on two key measurements: the Compton scattering measurement and the ionization efficiency measurement in silicon.

CHAPTER 3
DEVELOPMENT AND COMMISSIONING OF TEST CHAMBERS

3.1 Overview

To achieve the proposed background rate in the DAMIC-M experiment, all collaborating institutions must undertake extensive research and development. The background rate depends on varying factors; all contributing factors must be explored from the readout electronics that read the CCD to the impurities in materials that contribute to the radiogenic background.

At the University of Chicago, several test chambers have been commissioned and purposed for the testing of CCD performance under varying operating conditions. In this chapter, I will detail my contributions to these test chambers and their intended use cases.

3.2 What Is A Test Chamber?

To start, what I refer to as a test chamber is an experimental system that houses a Skipper CCD. The test chamber size may vary, but the operating specifications cannot. All chambers must: be able to achieve and maintain a stable, nominal vacuum of 1E-5 mbar; have available ports for electronic feed-throughs and temperature control; have an operating cryostat system to cool CCDs to a nominal operating temperature between 120-140 Kelvin; and be electrically isolated from the environment. Other configurations can exist based on the intended use, but these factors represent the core functions of all test chambers.

In general, to achieve a high signal-to-noise ratio the CCD needs to be cooled to an operating temperature that minimizes the rate of any spontaneous charge generation through electronic or thermal processes such as dark current or shot noise. Since, the CCDs will be operated for long periods of exposure when conducting a science measurement, any sponta-

neous charge generation will accumulate in a pixel and limit the measurement threshold of a science run. In practice, the collaboration has found that CCDs operating at temperatures between 120 K to 140 K have been sufficiently cooled to minimize the charge generation and achieve a desirable signal-to-noise ratio. At these temperatures, the dominant noise region will be at the $\sim 3-4$ electron-hole pair energies (in electron units), or $\sim 10-15$ eV. However, to effectively cool the CCD to these temperatures, the CCD must be in vacuum, otherwise any moisture from the surrounding air that is present on the detector will condensate and risk damaging the detector. This presents the key necessity in operating the detector under a stable vacuum and cooling system. Additionally, care needs to be taken when cooling the system, since a cooling rate that is too high will risk damaging the CCD through mechanical stressors that arise from the different thermal expansion coefficients present in the different materials of the system, or the expansion rate of the silicon itself. Any mechanical stress provided to the CCD directly, or indirectly, can generate defects that are indistinguishable to the naked eye, but will flood the detector with charge during standard operations. This effect can render a detector unsuitable for any scientific use, and could potentially delay the advancement of a test or measurement in the order of days, or even months. Therefore, the hardware installation of any CCD into a test chamber must be done with care and consideration of any mechanical, thermal, or electrical effects that the detector is susceptible to.

Another systematic source of investigation for the commissioning of the CCD into a test chamber, is the readout electronics and electrical isolation of the CCD. The combination of the amplifier boards, power supplies, and readout electronics provide all the necessary voltages required to fully deplete a CCD, clock charges toward the amplifier systems, and record an image. If the corresponding wiring is not properly fixed, the user risks shorting the CCD and inflicting permanent damage; or if the CCD and its electronic system are not electrically isolated from the environment, the signal-to-noise ratio will be greatly affected

and care will be needed to isolate the noise injection. The electrical isolation of a CCD test system presents the most difficult, and unique challenge to any user since there can be a range of subtle sources of noise originating from immediate metallic contact of two instruments, to the electrical infrastructure of the laboratory. Therefore, any CCD user must exhibit great care, attention to detail, and ultimately patience when attempting to diagnose sources of electrical noise.

3.3 The University of Chicago Test Chambers

At the University of Chicago, there are three active test chambers: test chamber 1, test chamber 2, and the calibration chamber. Each test chamber serves a niche purpose, and my work throughout my tenure in the collaboration has been to either fully commission, or assist in the internal design and commissioning of each chamber.

3.3.1 Test Chamber 1

First, test chamber 1 (TC1) has been the designated chamber for the testing of any newly developed readout electronics and their configuration files. This chamber can be seen in Figure 3.1. In the figure we see a thick copper box attached to the cold finger of the cryostat. The box is encasing a 1K $\times$ 6K Skipper CCD that has been extensively tested, and verified to be of scientific quality; and with the copper box acting as shielding, the ambient background rate was reduced by an order of magnitude. Additionally, the test system was electrically isolated and the noise of the CCD was thoroughly characterized. The quality of the CCD, the thick copper box, and the extensive characterization of the electrical noise ensure a benchmark to compare any newly developed electrical components or readout boards. My contribution to this system was the machining and constructing the support structure for the copper box and CCD ensemble, the chemical etch cleaning for the copper, and the commissioning of the chamber.

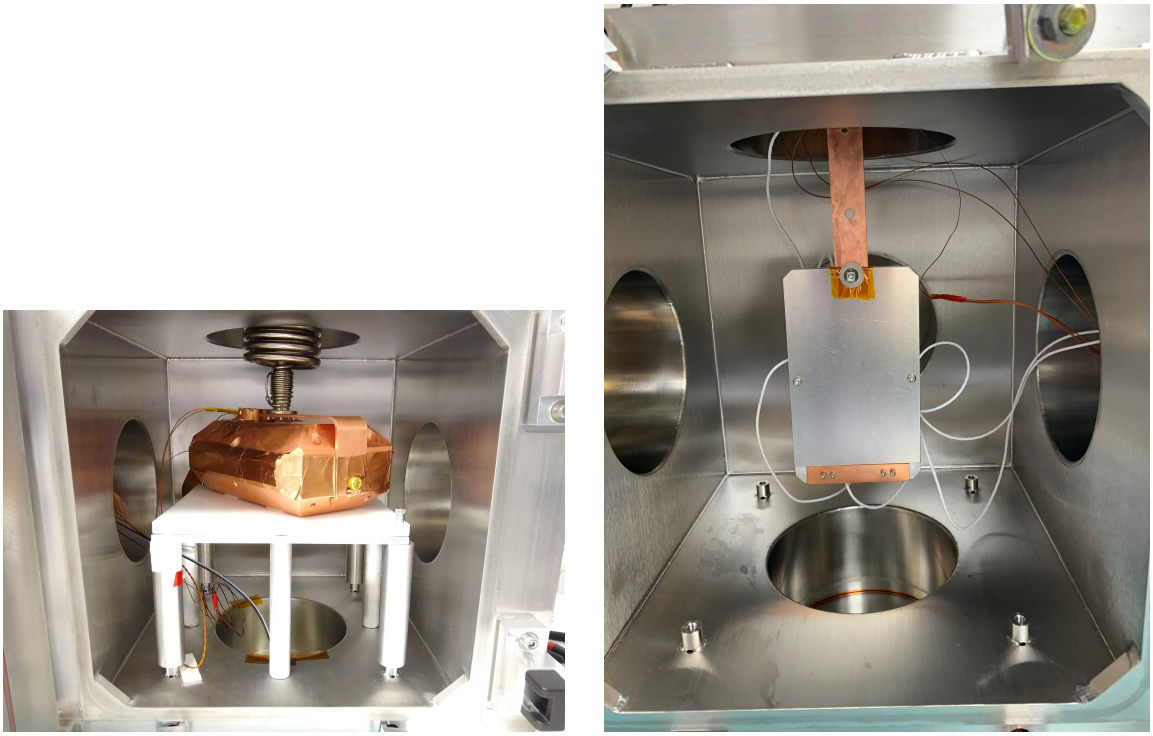

(a) Test Chamber 1 Interior.

(b) Test Chamber 2 Interior.

Figure 3.1: Interior configuration of TC1 and TC2. *Left*: TC1 shows a thick, pure, copper box encasing a 1K × 6K Skipper CCD. The copper box reducing the environmental background by an order of magnitude. *Right*: TC2 shows a packaged Skipper CCD attached to the cold finger through a fixed copper bar.

Figure 3.2: *Left*: An image of the CAD design for the multi-CCD configuration for TC2. *Center*: The realization of the CAD design. The commissioned system in the image employs the mock CCDs used for the thermal testing of the system. *Right*: A selected image of a mock CCD (pure silicon) with an attached temperature probe.

3.3.2 Test Chamber 2

Second, test chamber 2 (TC2) is the designated chamber for the testing and characterization of any prototype CCD. This chamber went through many project life cycles and configurations ranging from detector characterization measurements (ie. noise, quality, performance), to detector defect measurements, to dark current reduction studies, and even en masse prototype testing. Ultimately, this test system has served as the primary system to explore various methodologies and techniques before commissioning the DAMIC-M experiment.

For this system, I was a primary contributor to its first, full-commissioning and the design of several interior configurations. The right image in Figure 3.1 shows the first interior configuration for TC2. Here, we see a packaged CCD suspended in the chamber, and mechanically attached to the cold finger of the cryostat (not shown). At the start, it was important to verify the performance of the test chamber and its ability to maintain vacuum and ensure that CCDs could be successfully operated within the chamber. Therefore, for a first simple pass, I machined a copper bar attachment that directly attached to the cold finger and could accommodate any style CCD. This chamber configuration was temporary and served as a precursor to the multi-CCD test system.

Following the successful commissioning of TC2, there was a pending need to design a chamber interior capable of accommodating multiple CCDs. The DAMIC-M experiment was originally designed to house a total of 1-kilogram mass of active silicon (roughly 50 CCDs); therefore, the selected CCDs would require testing and characterization, and thus, the first step to this endeavor was to measure the detector yield of a fabrication and processing batch of CCDs. To accomplish this, the University of Chicago was designated to handle the prototype testing and detector yield measurement. Up to this point, each test system could only house a single CCD at a time, and swapping CCDs in these chambers took up to 12 hours due to the time required for the system to warm up and return to ambient pressure. Therefore, since the detector yield measurement would require testing of $\sim$50 CCDs, the

chamber needed to be adapted to accommodate more CCDs and optimize testing efficiency.

In Figure 3.2, the left image shows my CAD model for a multi-CCD test configuration. This system incorporates an aluminum support table – similar to TC1 – to elevate and position the horizontally stacked CCDs onto the copper strap that is attached to the cryo finger. Given the direct connection that the table has on the chamber, the system relies on PTFE (Teflon) standoffs to thermally and electrically isolate the CCDs from the environment. The middle image of Figure 3.2 depicts the realization of the design, and its first, successful commissioning. Moreover, the selected image shows the ensemble of temperature probes connected to mock CCDs to conduct a thermal test of the system. This study was conducted to examine whether the cryocooler would be able to effectively cool the increased thermal load. In the study, temperature probes were attached to every layer of the CCD ensemble, at various points, to generate a temperature map across the system. The right image in the figure shows an example of a temperature probe attached to a mock silicon CCD. Ultimately, this test identified that the copper strap that connects the cold finger to the CCD stack had insufficient mass to effectively cool the CCDs. Thus, an addition of three shifted copper straps was incorporated into the design and we were able to cool each CCD to a sustained operating temperature between 120 K - 140 K. The thermal study was my final contribution to the work done with TC2, the remainder of the aforementioned studies and measurements were carried out by colleagues.

3.3.3 The Calibration Chamber

Third and finally, the calibration chamber was designated as the science measurement test chamber at the University of Chicago. This chamber was originally designed to house an 8 Mpixel (2K $\times$ 4K pixels), first-generation DAMIC CCD; where the approximate length of a CCD was $\sim$2.4 inches and the height was $\sim$1.2 inches. Therefore these CCDs' geometry was well suited to be installed in the 6-inch cube, stainless-steel chamber depicted in the

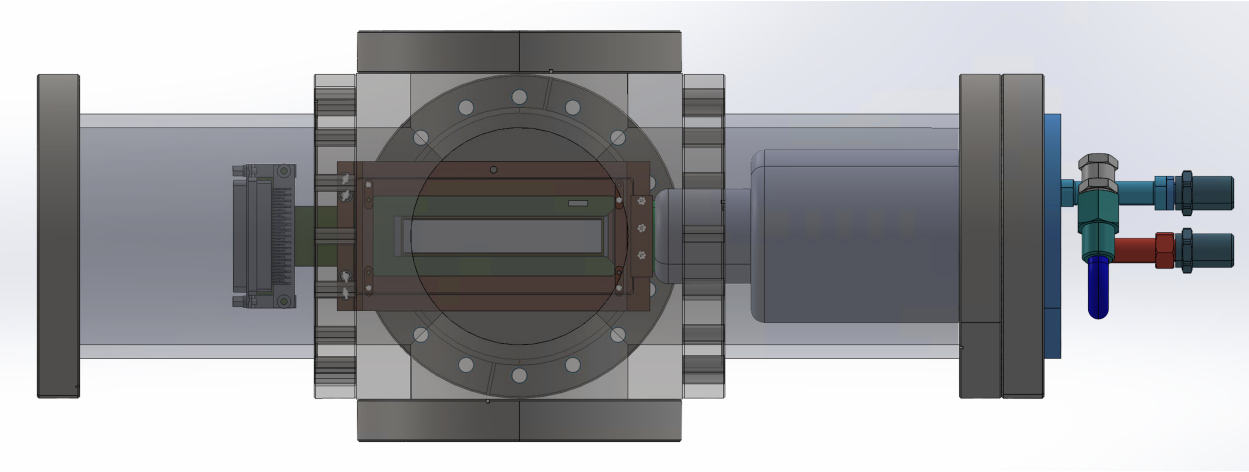

(a) Calibration Chamber CAD Model.

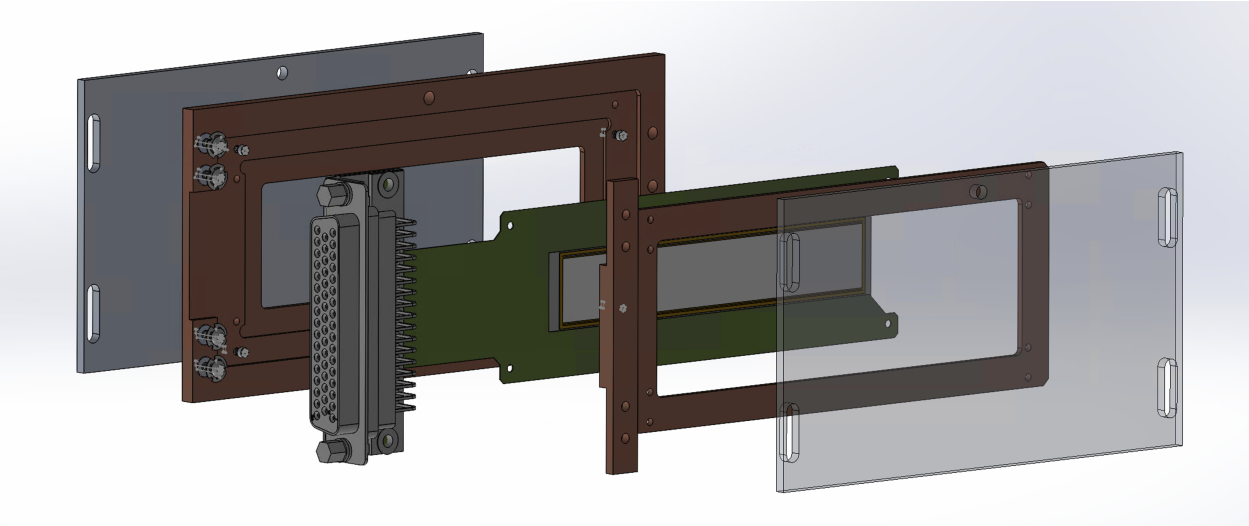

(b) Exploded View For Detector Frame.

Figure 3.3: *Top*: A CAD model of the Calibration Chamber that was used for the design of the detector frame for a 1K × 6K Skipper CCD. *Bottom*: An exploded view of the detector frame and its components. The detector frame is comprised of a copper base frame, a copper face plate, a copper T-bar for thermal contact, and 2 aluminum lids.

top image of Figure 3.3. However, the new 1K $\times$ 6K Skipper CCDs had a different form factor; they measured (3.54 $\times$ 0.59) inches, and thus could not use the previous generation's detector frame for installation.

To accommodate the new DAMIC-M detector prototype I designed, modeled, and commissioned the detector frame depicted in the bottom of Figure 3.3. This frame consisted of five key components: the copper base plate, the copper face plate, a copper T-bar, two aluminum lids, and a copper puck. The base plate was designed with a window to allow the CCD to be back-illuminated and minimize unnecessary scatterings during a measurement. The face plate ensured that the CCD was secured firmly across the base plate – while avoiding contact with any electrical components – to ensure good thermal contact between the CCD and the cold copper. The T-bar served a similar purpose but was additionally equipped with Belleville washers to increase the thermal contact between the Kapton flex cable and the cold-copper base plate. Since the Kapton flex cable was epoxied onto the silicon substrate of the CCD, the Kapton flex cable needed to be at thermal equilibrium with the entire system to ensure the CCD was cooled during operation. The two aluminum lids were used to shield the CCD from infrared photons emitting from the chamber walls. And finally, the copper puck was directly connected to the cold finger of the cryocooler and the copper base plate.

Once all the pieces had been machined, the detector was successfully installed in the calibration chamber. To test the thermal contact and cooling efficiency of the CCD, a temporary temperature sensor was attached near the CCD; this sensor was meant to inform us of any significant temperature gradient between the temperature reported near the cold finger and the temperature of the CCD. From this study, we concluded that there wasn't a significant difference between the two temperatures, and were confident that the CCD was being effectively cooled to an operating temperature between 120 K to 140 K. This chamber was ultimately commissioned and was employed to carry out two calibration measurements:

a measurement on the CCDs response to electronic scatters and a measurement of the nuclear ionization efficiency using a photoneutron source — details on these measurements can be found in Chapter 4 and Chapter 5.

3.3.4 Development of the Slow-Control System

Given the longevity and often remote nature of CCD operation, having a consolidated system to control instruments and monitor key environmental variables is valuable. Through extensive effort between myself and Danielle Norcini, we developed and implemented a slow-control system based on code written by James Nickel [53, 55]. The system functions over TCP/IP and is capable of remotely controlling instruments over a dedicated web server. Each of the aforementioned test systems has a dedicated slow-control system used to remotely control and monitor the power supplies that supply the bias voltages to the readout electronics, the vacuum pump, the pressure gauge, the cryocooler, the temperature controller, and the uninterrupted power supply. Each of these instruments required unique configurations to consolidate the communication within the slow-control system. But, ultimately, the slow-control's successful implementation proved vital in debugging any newly commissioned system and assessing stable operating conditions.

3.4 The Low-Background Chamber

For the DAMIC-M experiment, a prototype test chamber dubbed the Low-Background Chamber (LBC) was designed and commissioned in late 2022 to consolidate all R&D efforts from the collaborating universities and institutions, test the scientific reach of the DAMIC-M CCDs, and conduct preliminary dark matter searches. This chamber was built at the Laboratoire Souterrain de Modane (LSM) in France — it is on the same site where the DAMIC-M experiment will be constructed. Figure 3.4 shows a photograph of the chamber in the early stages of commissioning (top image) and the final configuration with the

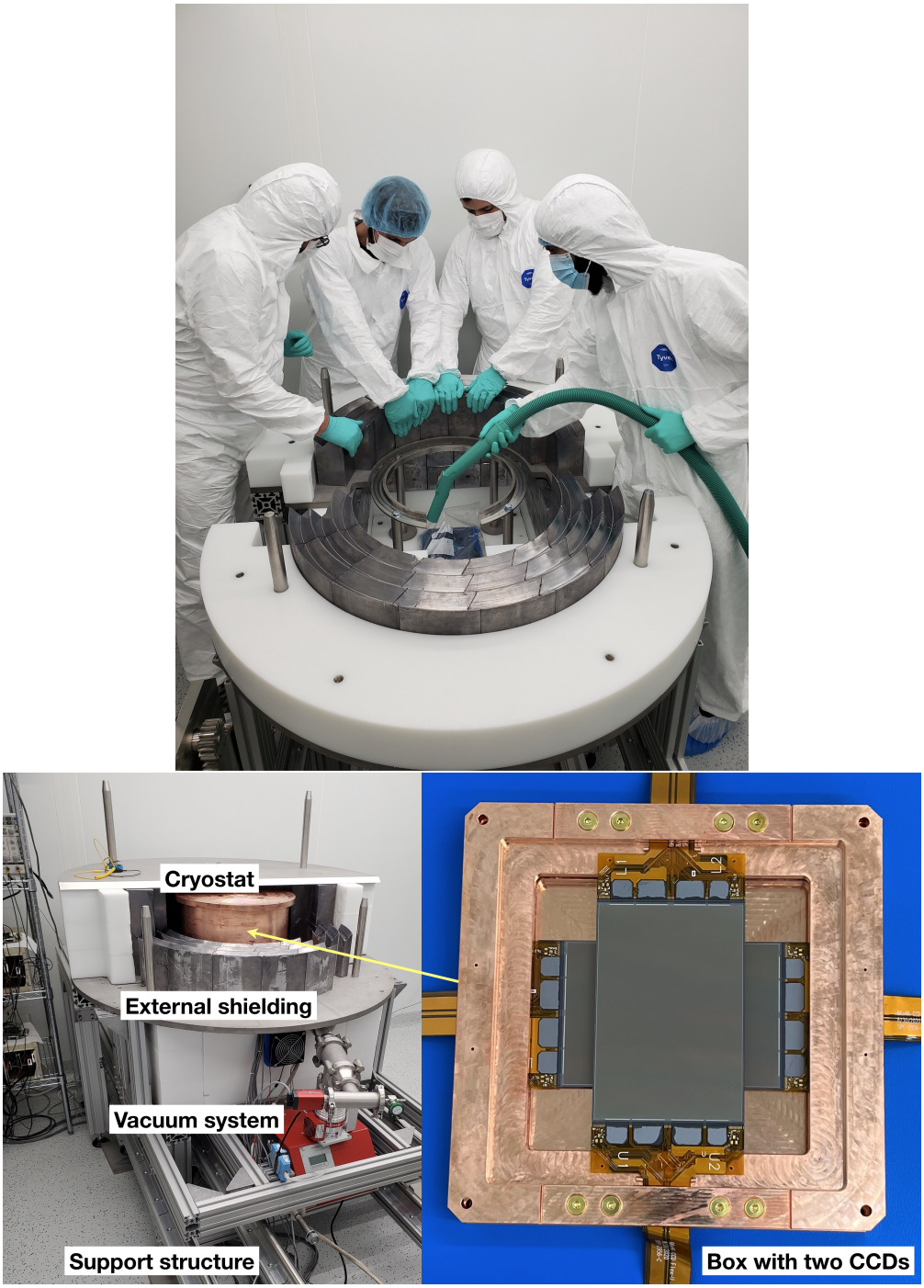

Figure 3.4: *Top*: A photograph taken during the shielding installation of the LBC. In this photograph, Daniel Baxter, Michelangelo Traina, Julian Cuevas-Zepeda, and Ariel Matalon are removing debris from the detector frame while holding lead bricks in place. *Bottom*: Joint photographs of the LBC components and the detector box with two 6K × 4K Skipper CCDs. Notably, the cryostat, external shielding, vacuum system, and support structure (frame) are labeled [8].

chosen detectors (bottom image). The commissioning of the LBC was a holistic effort between all collaboration members. My contributions involved the installation of the external shielding, the cryostat, and all essential instruments for operating the CCDs; as well as the installation of the slow-control system; and the optimization of the copper-etch procedure used to remove any organic residue from copper components before being transferred to the clean-room environment.

The LBC initially employed two 6K $\times$ 4K Skipper CCDs in an altered configuration as is seen in Figure 3.4. These detectors were thoroughly characterized and approved for deployment through joint efforts between the University of Washington and the University of Chicago teams. Furthermore, the cryostat was engineered to house the detectors within the walls of encapsulating radio-pure ancient lead to mitigate any environmental radiation that could originate from the lead. The cryostat was machined out of electroformed copper grown at the Pacific Northwest National Laboratory (PNNL) — further limiting any radiation contaminants from the experiment materials. Additionally, the external shielding encapsulating the cryostat includes layers of lead to attenuate any external environmental gammas and a thick polyethylene shield to moderate any environmental neutrons. The culmination of these measures and a successful detector commissioning has led to several published results within the past several years [8–10, 54].

3.5 Final Remarks

In preparation for the construction of the DAMIC-M experiment, all collaborating institutions have played a pivotal role in maturing the detector technologies that will populate the experiment. At the University of Chicago, several test chambers have been commissioned and studies have been undertaken to ensure that we properly understand the limitations and capabilities of our Skipper CCDs, the readout electronics, and the physical processes (ie. dark current) that govern the detector's performance. In the following chapters of

this thesis, I will explain in detail the aforementioned measurements that transpired at the University of Chicago with the calibration chamber.

CHAPTER 4

COMPTON SCATTERING MEASUREMENT

4.1 Overview

Dark matter interactions in DAMIC-M CCDs can occur via electronic-scattering events within the silicon medium. This mechanism constitutes a dark matter direct-detection event. Where the minimum energy for detection is limited to the semiconductor's temperature-dependent electron-hole pair creation energy, $\epsilon_{e-h}(T)$. Given DAMIC-M's employment of the so-called Skipper CCDs, our detectors are capable of resolving single electrons with an increased number of skips and thus have increased sensitivity to low-energy scatters (as discussed in Section 2.2.2). With the increased sensitivity it is imperative to characterize the detector's behavior to electronic scatters and any environmental process that can mimic a dark matter electronic-scattering event.

While an ideal dark matter experiment would involve a radio-pure environment to discriminately measure a dark matter signal, real experiments must apply sophisticated techniques to either reduce environmental radiation effects on the detector or model the effects as a background model and subtract it from the measured signal. Gamma rays represent a dominant source of background in our experiment – whose deposits in the active silicon medium mimic dark matter interactions and present a significant background in our detector via Compton Scattering [2, 61, 62].

4.2 Compton Scattering

Although DAMIC-M will make an exhaustive effort to reduce the radiogenic background in the experimental apparatus (as detailed in Chapter 2), a dominant gamma background will persist within the environment of the detector. The gammas originate from subsequent radioactive decays of the material impurities within the hardware such as the silicon CCD,

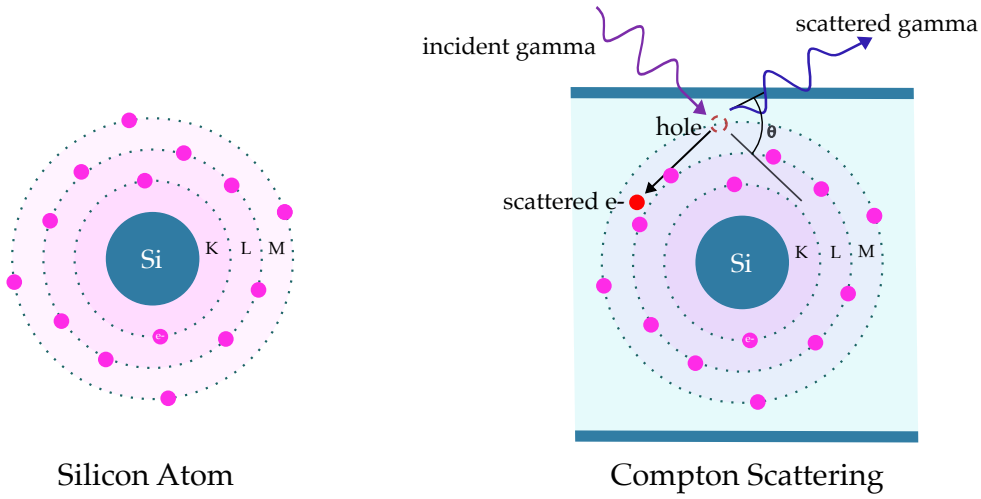

Figure 4.1: (Left) silicon spectroscopic shell-structure. (Right) Diagram of Compton scattering between γ-ray and valence shell electron.

copper components, or external shielding [2, 10, 60]; ^{238}U, ^{226}Ra, and ^{210}Pb are common nuclides which will generate gamma rays in the environment of the detector. Interactions in the active silicon volume from these gamma rays will generate a signal whose spectral features correspond to the electromagnetic process known as Compton scattering.

Compton scattering describes the process of an incident photon imparting some of its energy to a free electron (assumed to be at rest) — see figure 4.1. Upon incidence, the photon is deflected from its original direction at an angle θ. In the absorbing medium, the recoiling electron can be ionized, and thereafter scatter and ionize subsequent electrons in proportion to the imparted photon energy. For a gamma-ray photon of E_γ, the energy after photon scattering, E'_γ, is given by,

$$E'_\gamma = \frac{E_\gamma}{1 + \frac{E_\gamma}{m_0 c^2}\,(1 - \cos\theta)} \tag{4.1}$$

Here $\mathrm{E}_\gamma = h\nu$, $\mathrm{m_0c}^2$ is the rest-mass energy of the electron (0.511 MeV), and θ – as previously mentioned – is the photon's scattering angle. The recoiling electron's energy is given by the difference between the initial and final photon energies, $E_r = E_\gamma - E'_\gamma$, and the maximum

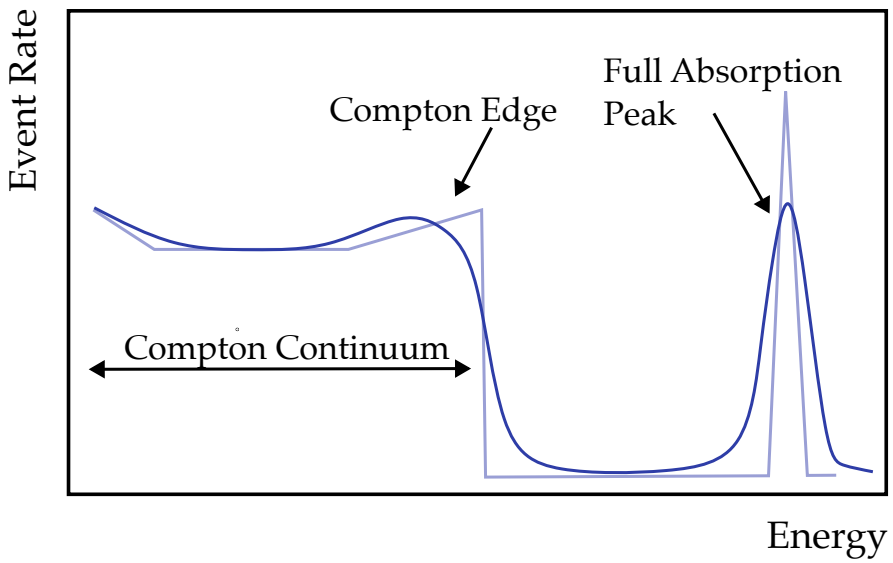

Figure 4.2: Cartoon of spectral features due to Compton scattering. Light blue is an approximate representation of features computed without bound electrons, and darker blue represents a more realistic spectral profile.

energy occurs when the incident photon back-scatters, i.e $\theta = \pi$. Nominally, in a detector gammas are scattered at all angles described by the Klein-Nishina formula,

$$\left[\frac{d\sigma}{d\Omega}\right]_{KN} = Zr_0^2 \left(\frac{1}{1+\alpha\left(1-\cos\theta\right)}\right)^2 \left(\frac{1+\cos^2\theta}{2}\right) \left(1+\frac{\alpha^2\left(1-\cos\theta\right)^2}{\left(1+\cos^2\theta\right)\left(1+\alpha\left(1-\cos\theta\right)\right)}\right) \tag{4.2}$$

where $\alpha = h\nu/m_0c^2$, Z is the atomic number, and r_0 is the classical electron radius [40, 42]. The Klein-Nishina formula gives the angular distribution of scattered gammas and shows that at increasing gamma energies, the tendency towards forward scattering increases. In the energy spectrum recovered from the detector, spectral energies leading up to $\theta = \pi$ form what is known as the *Compton Continuum* and when back-scattering occurs we see an edge form at the location of the maximal energy deposition – this feature is known as the *Compton Edge* and can be seen in the cartoon in figure 4.2.

4.2.1 Other Physics Processes

Compton scattering presents us with a formalism to describe the interaction between highly energetic photons and electrons bound in a target medium. However, this process is limited to distinguishing the high-energy spectral profile from the other micro-physics effects that could occur within the detector. In events where the incident gamma has enough energy to kick out a bound electron within the lattice of the detector, the hole generated by this ionization event would be accompanied by outer-shell electrons filling the vacancy and subsequently emitting a characteristic x-ray. Alternatively, it is also likely for the incident gamma energy to be carried off by an Auger electron.

The photoelectric effect – much like Compton Scattering – is another dominant process that has key signatures in the spectral profile of the detector's energy spectrum. The key feature depicted in the aforementioned cartoon 4.2 as the "photo-peak" represents the complete absorption of the incident gamma minus the energy binding the electron within the target material [33].

4.2.2 The So-Called Compton Steps

For small scattering angles where the electron recoil energy, E_r, is compatible with the binding energy of an inner-shell electron, the Klein-Nishina formalism breaks down and a correction must be made to account for the constrained momentum of the bound electron.

$$\left[\frac{d^2\sigma}{dE \cdot d\Omega}\right]_{nl} = r_0^2 \left(\frac{1+\cos^2\theta}{2}\right) \left(1 - \frac{E}{E_\gamma}\right) S_{nl}\left(q, E\right) \tag{4.3}$$

Equation 4.3 is the double-differential scattering cross-section for an incident photon on an atomic electron [32, 54, 63]. Here, r_0 is the classical electron radius, θ is the scattering angle, E_γ is the initial photon energy, E is the difference between initial and final photon energies,

and $S_{nl}(q, E)$ is the dynamic structure factor.

$$S_{nl}(q, E) = \frac{m}{q}\chi(p_z)J_{nl}(p_z) \tag{4.4}$$

The dynamic structure factor encodes the atomic electron's target material contribution to the scattering cross-section. In the above equation, m is the mass of the electron, q is the module of the photon scattering vector, $\chi(p_z)$ is the relativistic correction factor, and $J_{nl}(p_z)$ is the Compton profile. Here, we can note that the Compton profile is dependent only on p_z — the projection of the electron's initial momentum onto the photon scattering vector. Equation's 4.3 and 4.4 make up what is known as Relativistic Impulse Approximation, or the RIA model.

The RIA model treats the atomic-bound electrons by constraining their momentum distribution. This formalism has proven to be successful in describing features – such as the Doppler broadening of the Compton edge – in the reconstructed energy spectrum from Compton scatters [54, 59, 60]. When considering low-energy scatters, it's important to note that RIA is valid only when $E \geq E_{nl}$, otherwise $d^2\sigma/dEd\Omega = 0$; which is to say that the deposited energy is less than the binding energy of the bound electron. This condition leads to the formation of a discontinuity, or *step*. This discontinuity represents what I will refer to as a *Compton Step*[1] throughout the rest of this chapter. The height of the steps formed is directly proportional to the amount of electrons in a given shell. Figure 4.3 shows the low-energy prediction due to this effect. In the case where $E \approx E_{nl}$, a vacancy will be generated by the scattering gamma, the scattered electron will have negligible kinetic energy, and processes mentioned in the previous section will intercede.

1. It should be noted that while within DAMIC-M and our community, we refer to the discontinuity as a Compton Step, other fields may refer to the features as an absorption edge, K-Edge, etc. The primary difference is that an absorption edge implies the photoelectric effect was the dominant mechanism of generation, whereas in our case Compton scattering generates the edge features.

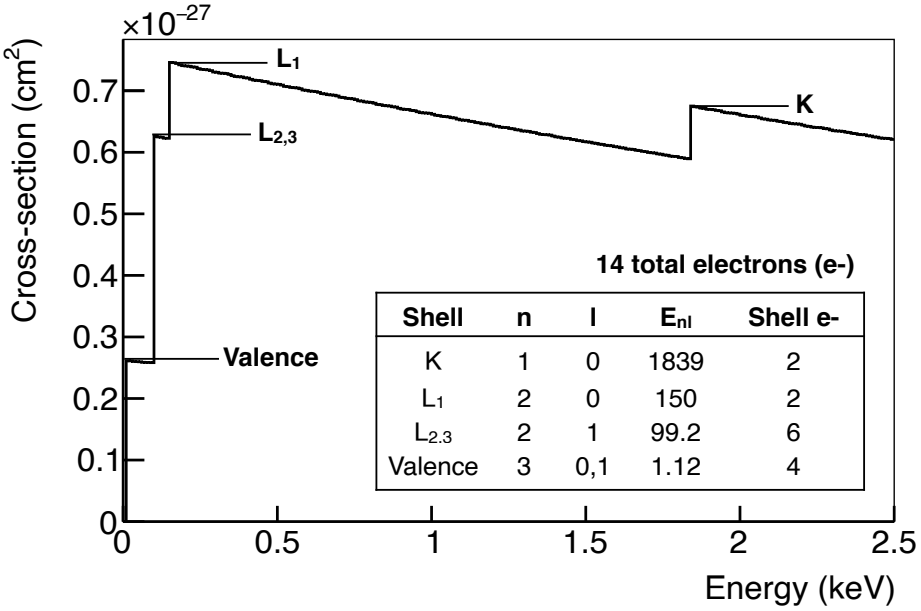

Figure 4.3: Simulated event rate of low-energy scatters via predictions from RIA. The binding energies of each shell are listed in the inset with the corresponding electron number. We note that step heights are proportional to available electrons in each shell[54].

4.2.3 Silicon Binding Energies

For silicon-based detectors, previous measurements have been able to accurately measure the binding energy corresponding to the K-shell of silicon. The inset table in Figure 4.3 shows the binding energy corresponding to the respective electron shells of silicon. Notably, a measurement of the Compton steps was carried out by Ramanathan et. al, with DAMIC generation CCDs to a threshold of 60 eV[62]; where a successful measurement of the K-shell accurately depicted the location of the step at ∼1839 eV. However, due to resolution limitations of the CCDs the L_1 & $L_{2,3}$ steps were not fully resolved.

4.3 Experimental Setup

With DAMIC-M Skipper CCDs, we are now able to overcome the previous generation's limitations with detector resolution and probe down to lower energies with greater detector resolution.

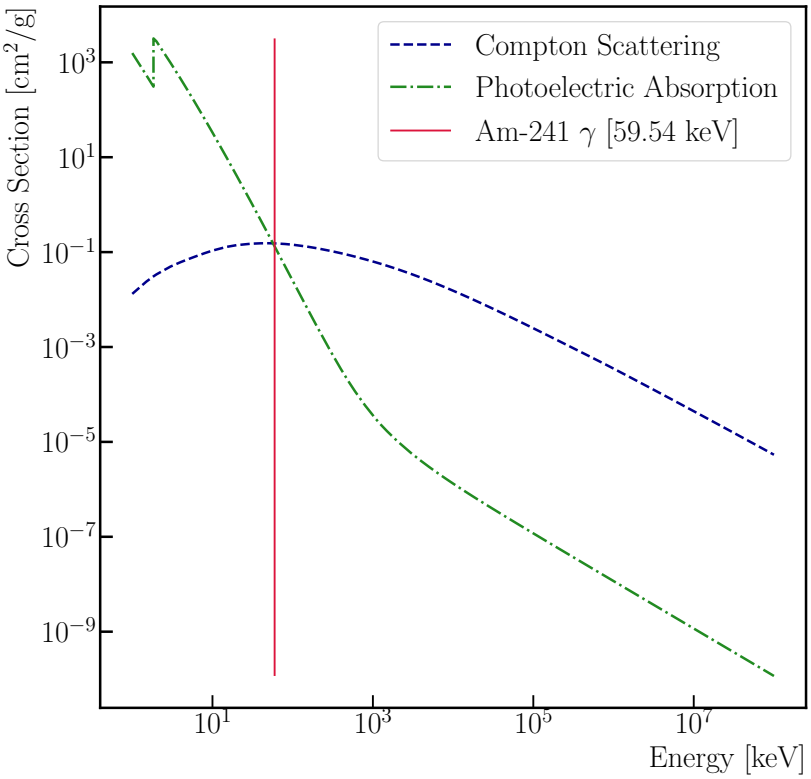

Figure 4.4: Cross-sections for Compton scattering and photoelectric absorption. Am-241 gamma is well positioned at maximum for Compton scattering to dominate. At low energy, we see the K-step in the cross-section from photoelectric absorption. Data taken from NIST XCOM.

When choosing the location of the experiment, the operating hardware components, the primary detector, and the imaging conditions it is important to note that the measurement campaign will be lengthy and thus will require the choice of operating conditions that maximize data quality and stability.

4.3.1 Source Selection

The primary selection criteria for our measurement was the incident gamma energy on our detector. As Equation 4.1 shows, the initial energy is directly proportional to how much charge is generated in the detector. Thus, we require E_γ to be low enough to not saturate a pixel region with charge, and optimized for the Compton scattering process to be the

dominant scattering mechanism. As shown in Figure 4.4 the Americium 241 (Am-241) 59.5 keV gamma is at an ideal energy to meet the specified requirements. With Am-241, Compton scattering will dominate and any low-energy scatters will give rise to edge features in the energy spectrum as discussed in Section 4.2.2.

The Americium-241 isotope is a radioactive alpha-emitter with a half-life of approximately 432.6 years. While the 59.54 keV gamma is the dominant emission, other X-ray and gamma energies are listed in Table 4.1 that occur in the energy region of interest [16].

Source	Half-Life [years]	Emission Type	Energy [keV]	Photons per 100 disintegration
^{241}Am	432.6 (6)	X-ray	11.89 - 22.2	36.7 (21)
		Gamma	26.3446 (2)	2.31 (8)
		Gamma	59.5409 (1)	35.92 (17)

Table 4.1: Emission lines from Am-241 isotope that occur in the energy region of interest. Values taken from reference [16].

4.3.2 Hardware

This experiment was conducted in an on-surface clean room at the University of Chicago. The choice of detector for this measurement was a 1024 x 6176 pixel Skipper CCD. Each pixel is $15 \times 15 \times 675\ \mu m$, with a three-phase polysilicon gate structure. The detector was housed within a stainless steel vacuum chamber and mounted in a copper frame as seen in figure 4.5. Additionally, there are thin aluminum lids placed in both the front and back of the copper frame (not shown) to shield the CCD from IR photons.

During the data-taking campaign, vacuum was held at 10^{-7} mbar, and the CCD was nominally cooled to 126 K. The CCD was fully depleted and lateral diffusion was diminished by applying a substrate voltage of 95 V. The CCD was controlled and data was collected via a commercial CCD electronic system (Astronomical Research Cameras, Inc). All instruments were remotely controlled and monitored via a dedicated slow-control system.

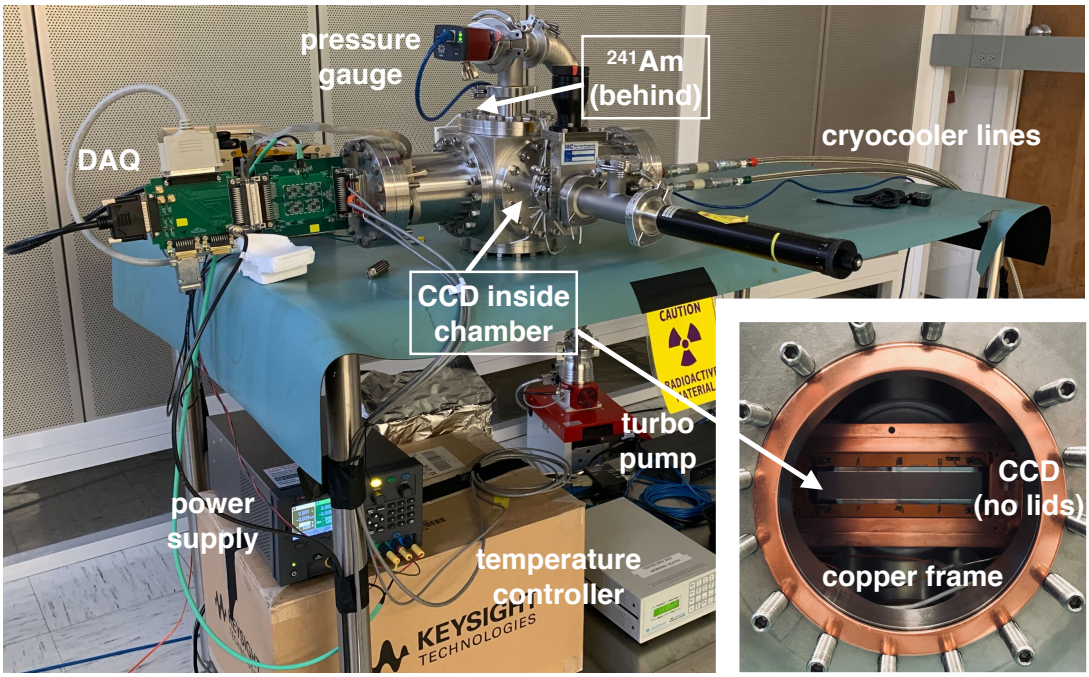

Figure 4.5: The Compton experimental setup is shown. 1K × 6K Skipper CCD is housed within a stainless-steel chamber and mounted onto a copper frame. Hardware components required for CCD operation are labeled[54]. Am-241 source is mounted behind the chamber, see Figure 4.6

.

Since Americium-241 emits X-rays and Gammas that will muddle the reconstructed energy spectrum, we require a way to attenuate lower-energy emission lines listed in Table 4.1. As a solution, we use a 0.5-inch block of aluminum to attenuate the low-energy photons to a negligible level of less than 1 percent of initial intensity. For the source, a 3D-printed holster was designed to house the Am-241 source and the 0.5-inch block of aluminum. The holster was secured behind the vacuum chamber (see Figure 4.6). The holster ensures that the source can be replaced into the same location between the source and ambient background runs.

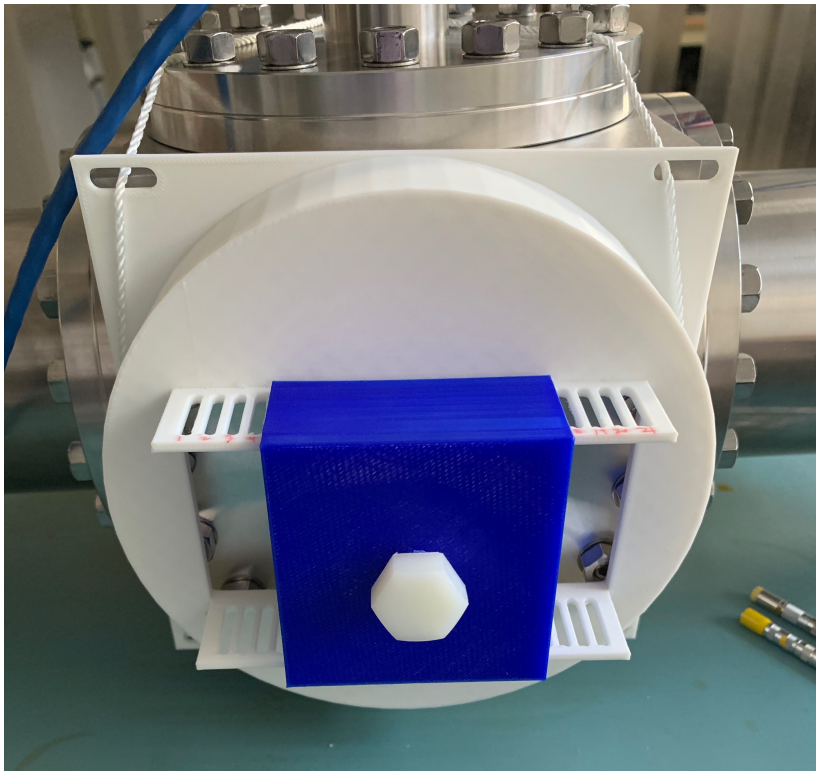

Figure 4.6: Am-241 source is mounted on an aluminum block (not shown) behind a stainless-steel chamber and held in place by 3D printed holster. The source is centered on CCD plane and can be shifted across the plane in equally spaced intervals.

4.3.3 Data Runs Configuration

For any measurement involving ionizing radiation, we need to consider several factors when designing the experimental procedure. First, per operation of the detector, we always expect a functioning baseline of signal to be generated when operating the detector. Silicon CCDs operated at ground level will be subject to the charge generated from thermal effects (such as dark current), cosmic rays, or other decay particles such as alphas and betas. These ionizing backgrounds are constrained to their specific energy ranges and their effects are generally high or low enough in the reconstructed energy spectrum to not interfere with our measurements. As described in Section 2.2.1, when CCD images are read out, data is stored in Analog Digital Units – or ADU – which must be converted to meaningful units via some calibration process. For pixels that are not populated by excess charge, ADU values will

be normally distributed and the mean corresponding to the distribution will be the *baseline* value which should be subtracted from other pixels. This baseline value is extracted from the *overscan* region of the detector; the overscan is generated by reading the serial register a predetermined amount of times and generating a sort of 'dark region' in the image where no charge should be generated. As further described in Section 2.2.2, with Skipper CCDs we can self-calibrate images by increasing the number of skips within the detector. The ability to resolve single-electron peaks in the data gives us a separation distance in ADUs per electron, allowing us to convert between ADU and electron volts.

For this experiment, we introduce the 59.54 keV gamma from an Americium-241 source to measure the Compton steps corresponding to the binding energies of the silicon shells and simultaneously characterize the Skipper CCDs' response to electronic scattering. To properly isolate the effect of the source gammas, we must split our data campaign into two types: source runs and ambient background runs. Since the half-life of Americium is very large in comparison to the intended duration of the measurement, we do not consider any notable depreciation of gamma intensity within the data campaign. With this in mind, the key constraints to data taking must be image size and number of skips.

To maximize diagnostic and data quality assessment, data taking was split into a per-run format. Each data run consisted of 1 single-skip, full-sized image which functioned as a diagnostic tool to assess quality parameters (e.g. visible particle tracks, consistent single-skip readout noise); 400 64-skip, 150 rows $\times$ 260 cols, and 4 $\times$ 4 binned images as primary data sets; and 1 2000-skip, 60 rows $\times$ 260 cols, and 16 $\times$ 4 binned image for calculating the calibration constant per data run. An example data image can be seen in Figure 4.7. As seen in the example image, the 64-skip image is not over-populated and data tracks can be clearly distinguished from one another. Further data set configurations and information can be seen in Table 4.2.

The total data-taking campaign lasted several months, and a substantial amount of data

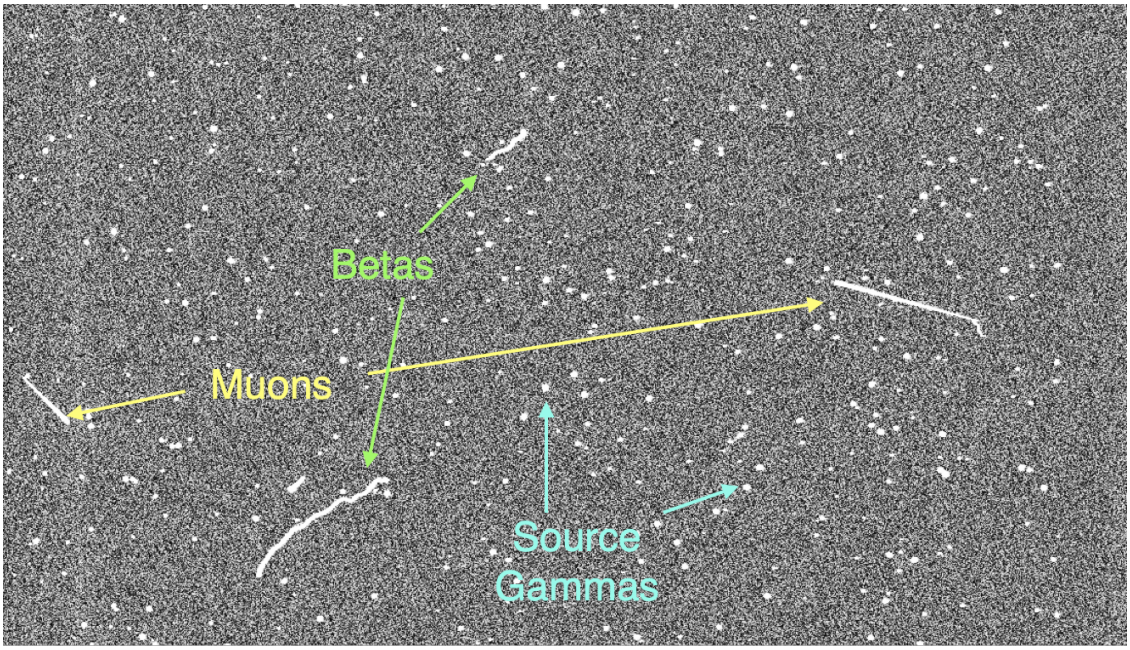

Figure 4.7: Example 64-skip data image from Compton data run. Image labels betas, muon, and source gamma tracks.

was collected for both source and background runs. During the analysis of the data, it became evident that events occurring in the serial register region of the CCD were contributing to lower-energy clusters in the spectrum, so we conducted a dedicated set of runs to study this effect — it is referenced in Table 4.2 as *serial register*.

Source	Binning [row×col]	Image size [row×col]	NDCMs	Images	Exposure [days]	Type
^{241}Am	1×1	6200×1100	1	909	1.3	diagnostic
	16×4	60×275	2000	909	5.9	calibration
	4×4	150×275	64	223 517	105.5	source
	4×4	150×275	64	26 948	11.8	serial register
None	4×4	150×275	64	103 106	48.1	background

Table 4.2: Summary of the data sets used in the analysis. The image size does not include overscan columns. All data were taken with a high Vsub value to limit the lateral diffusion allowing charge from a single interaction to be collected in the 4×4 binned pixel group [54].

4.3.3.1 Serial Register Data

Normally, when data is being read out by the CCD electronics, we move charge from the active region of the CCD to the serial register. While the serial register is not intended to contribute to the active image region, it is effectively an active silicon region in the CCD – spanning 1 full row – which can collect charge from ionizing events that occur during readout. An event of this type is colloquially referred to as a *horizontal cluster* and can be categorized by a horizontal track in the active region of the image.

During ambient background runs, we expect horizontal clusters to be generated by environmental radiation such as cosmic rays, or decays in nearby materials at a rate proportional to the flux of incident radiation. However, in the presence of the Am-241 source, we expose the CCD to an increased rate of ionizing radiation and consequently see an increased rate of horizontal clusters generated when the source is present. These clusters are believed to originate from ionizing events that either occur in the serial register itself or a region close by enough to deposit a fraction of the energy in the serial register pixels.

To study the effects of Am-241 ionizing events occurring near the serial register, the aforementioned serial register data set was carried out by taking images that only read the serial register with the Am-241 present. Additionally, the charge in the active region was clocked towards the second serial register contrary to charge flow during standard data taking. In this configuration, we restrict images to contain only clusters originating in the original serial register.

4.4 Image Processing and Event Reconstruction

As previously mentioned, charge generated in our detector is recorded as analog digital units in our data images. Each pixel carries an ADU value proportional to the amount of charge collected in aggregate per the pixel binning configuration. Ionizing events from particle interactions commonly exhibit particle tracks that span several pixels along the path

traveled by the particle. Each of the affected pixels contributes to the spectral identification and physical characteristics of the incident particle. To extract meaningful information about ionizing events in the detector, respective event clusters need to be identified and analyzed to extract important features such as cluster energy, cluster topology, or other parameters that describe distinguishing properties from neighboring clusters.

4.4.1 WADERs

The DAMIC-M collaboration membership spans several universities and institutions working in unison to develop and mature skipper CCD technology. Consequently, to ensure a standardized approach to relaying key CCD metrics, a python-analysis package dubbed as *softWAre for Dark matter ExpeRiments with Skippers*, or WADERS for short, was developed by Nuria Castello. This analysis package is the standard data-processing tool for DAMIC-M; some key functions performed by WADERS are to process raw data images, undergo event cluster reconstruction, and data quality monitoring.

In this section, the main focus will be to summarize key data parameters and explain how they are processed via WADERs.

4.4.2 Key Image Parameters

To start, when taking data with multiple skips we must first appropriately compress the skipper image. The skipper process – as detailed in Section 2.2.2 – involves reading each pixel N times. Each time a pixel is read out, the readout noise is decreased by a factor of $1/\sqrt{N}$; however, the averaging is not done by the electronics, rather the data is stored as a series of stacked images of shape (rows, columns, number of skips). Thereby making *Skipper image compression* the first necessary processing step.

After image compression, meaningful metrics and analysis can be conducted on collected data. Figure 4.8 shows the pixel charge distribution available with the 2000-skip images

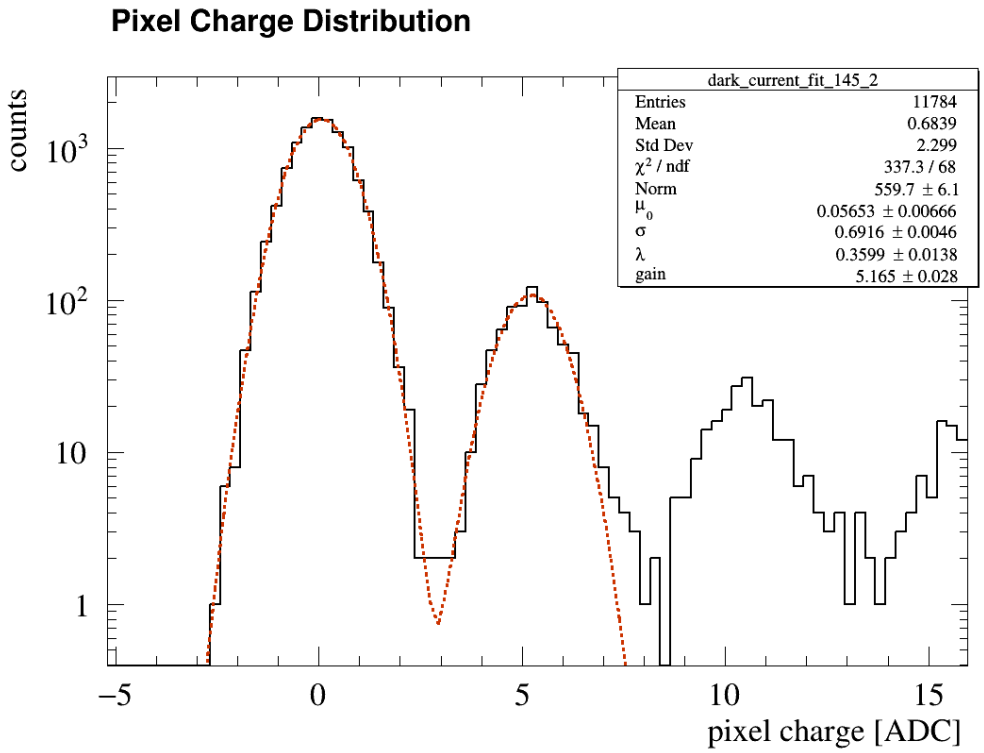

Figure 4.8: Distribution of pixel values across a selected 2000-skip image in ADU. The first three peaks correspond to the 0, 1, and 2 electron peaks. The decay constant, λ, corresponds to the dark current present in CCD. The separation distance between peaks provides calibration constant between electrons and ADU.

taken during data runs. The ability to resolve single-electron peaks is a defining feature of employing multi-skip images with sufficiently large N. The pixel distribution at $N \geq 400$ skips depicts peaks that follow a Poisson distribution. A fit of these peaks with a convolution of a Poisson and Gaussian distribution provides access to the dark current of the detector, the detector resolution, and the calibration constant, or gain, between electrons and ADU values of data images.

4.4.2.1 Dark Current

The dark current described by lambda, λ, is interpreted as the Poisson rate, or the rate of charge generated by intrinsic properties of the detector irrespective of ionizing radiation.

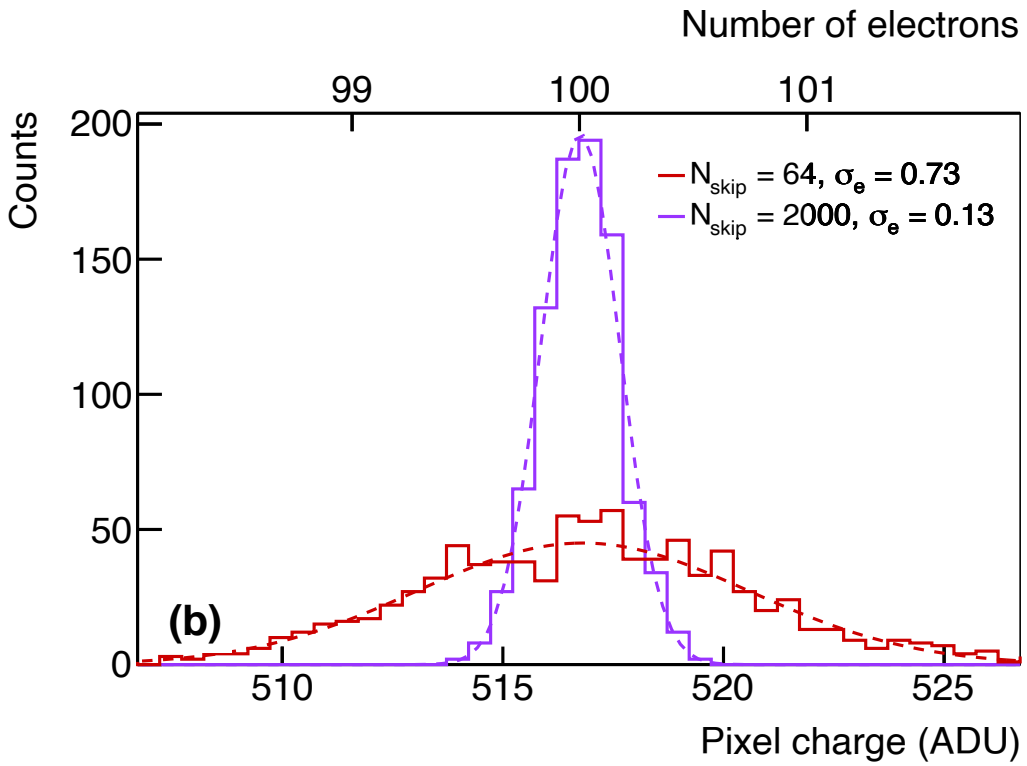

Figure 4.9: Pixel charge distribution with Nskip = 2000 (purple) and Nskip = 64 (red) corresponding to a charge of 100 electrons. The pixels entering the two distributions are the same, with their charge calculated using only the first 64 out of the 2000 NCDMs for Nskip = 64 [54].

Large rates of dark current limit detector resolution, and ultimately our ability to make definitive claims on signal measurements and distinguish meaningful signal from spurious charge. Reducing the dark current rate in a detector involves changes in fabrication and packaging procedures of the detector since material defects or mechanical stress can increase λ; changes in cooling and operation procedures, since large differences in thermal coefficients of surrounding materials can once again result in mechanical stress as a material cools and relaxation process intercede; or more sophisticated techniques such as pocket-pumping [37].

4.4.2.2 Detector Resolution

The hallmark trait of a Skipper CCD is: *as you increase the number of skips, you decrease the readout noise; hence, increase the ability to resolve single electrons*. From Figure 4.8 the

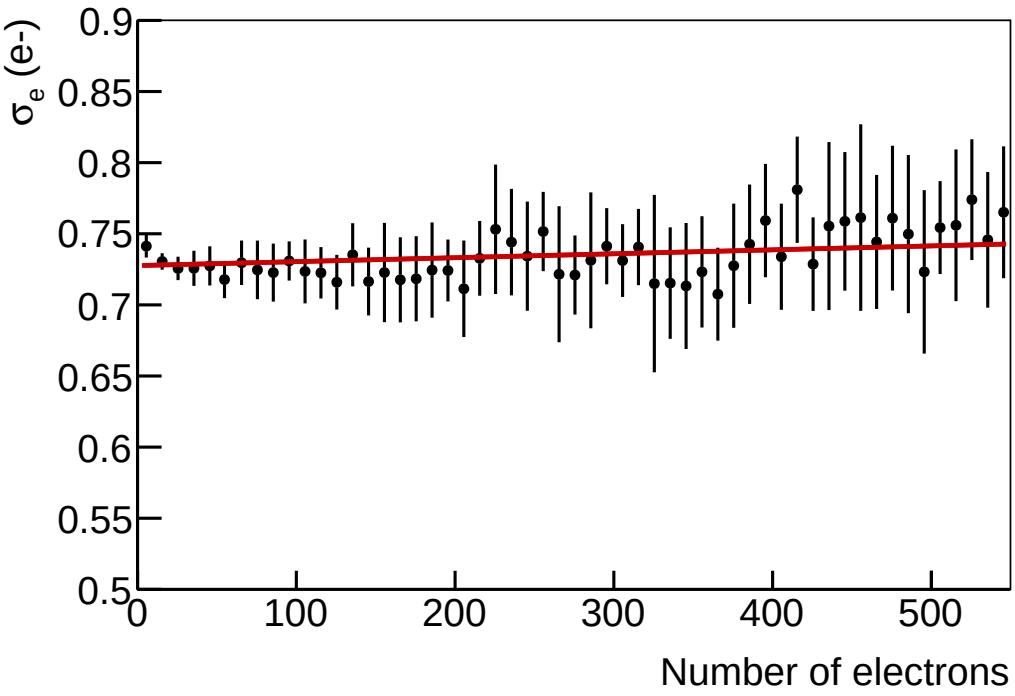

Figure 4.10: Charge resolution for Nskip = 64 as a function of charge up to 550 electrons. The resolution changes by <3% over the entire energy range (red)[54].

detector resolution, or the width of an electron peak, is given by the sigma, σ, parameter. This value decreases as you increase the number of skips in the detector. Figure 4.9 illustrates this effect in a sampled 2000-skip image. We compare the resolution power of our selected data-taking parameters at skip values of 64 and 2000. Notably, we see the large spread present for $N = 64$ vastly reduce from ~ 20 ADU to ~ 5 ADU when total skips are increased to $N = 2000$. While the disparity is large, one might be motivated to ask: *why not always operate the CCD at large skip values*? When operating the detector at such large N, readout times increase drastically. Data images taken for this measurement at 64 skips take roughly 45 seconds to finalize one image, whilst the 2000 skip images took roughly 8 minutes. Thus, we choose to optimize for time and retain the resolution gain of $\sigma_e = 0.73$ electrons from a conventional CCD which is limited to 2 electron resolution.

4.4.2.3 Calibration Constant

Converting between ADU units and meaningful units is a crucial data processing step. While conventional CCDs require dedicated measurements to convert between ADU and electron volts, Skipper CCDs have direct access to the conversion. When N is sufficiently large and single peaks are resolved, the separation between the zeroth and first electron peaks provides the conversion factor of ADU per electron. During processing, we can apply the electron-hole pair creation value corresponding to our operating temperature – $\epsilon_{e-h} = 3.74$ for this measurement – and conduct a meaningful analysis.

It should be noted that the value extracted from the separation of the zeroth and first peak describes only the low-energy contribution to the calibration constant. At higher energies, there is a non-linearity in the calibration factor – implying an inconsistent separation between peaks – that must be accounted for. Figure 4.10 illustrates how the charge resolution changes as you increase in number of electrons. This effect is measured up to 550 ($\sim$ 2.1 keV) electrons and applied in the final processing done by WADERS.

4.4.3 Clustering

After preliminary processing has been completed by WADERS, we can move towards event reconstruction and identify clusters in a data image. In short, a cluster is formed when ionizing radiation is incident onto the CCD active area and it deposits charge greater than the electron-hole pair creation energy. Charge is then collected in nearby pixels and clocked along the CCD towards the readout electronics. Each cluster usually corresponds to a single ionizing event, but can sometimes correspond to multiple events since readout is not instantaneous. To identify and isolate pixels that have collected charge within our measurement's energy range, a set of cluster parameters must be assigned.

First, WADERS relies on the application of the nearest-neighbor algorithm for cluster identification. Key values that must be identified by the user are seed threshold, σ_{seed},

minimum energy threshold, σ_E, and separation distance in pixels between clusters, N_{pix}. The seed threshold is the minimum energy required to categorize a cluster as originating from an energy deposition corresponding to the science measurement. Effectively, a user is defining a deviation away from the detector resolution, σ_{det}, such that $\sigma_{seed} = N_\sigma \sigma_{det}$. The minimum energy threshold is the user-defined energy boundary classifying a pixel as a member of a cluster; it is given by $\sigma_E = N_\sigma \sigma_{det}$. Finally, N_{pix} defines the maximum separation distance required to classify clusters – that may not share a border – as members originating from the same ionization event. For this Compton measurement, the final cluster parameters were: $\sigma_{seed} = 4.6\sigma_{det}$, $\sigma_E = 3.6\sigma_{det}$, and $N_{pix} = 1$.

4.4.4 Data Quality Monitoring

In addition to data processing and event reconstruction, WADERS also has an added feature of generating diagnostic reports and conducting pre-processing event flagging. This feature was pivotal in providing a robust way to seamlessly integrate data-cleaning algorithms, and omit them from the main reconstruction channels. Further details will be provided in the next section.

4.5 Data Quality Monitoring and Cleaning

Throughout data-taking the data was consistently monitored for quality. At the end of each data run, a data report was generated which detailed diagnostic plots for key parameters such as dark current, baseline values, and detector resolution. Each of these reports gave insights into the sustained consistency and quality of the data being taken. As data accumulated, some images began to show evidence of electrical noise. Two common types of poor-quality images occurred during data taking: images with correlated noise and images with a shifting baseline during readout. Much of the discussion from here on will focus on the latter type, as this effect is responsible for a large injection of low-energy events in the energy spectrum

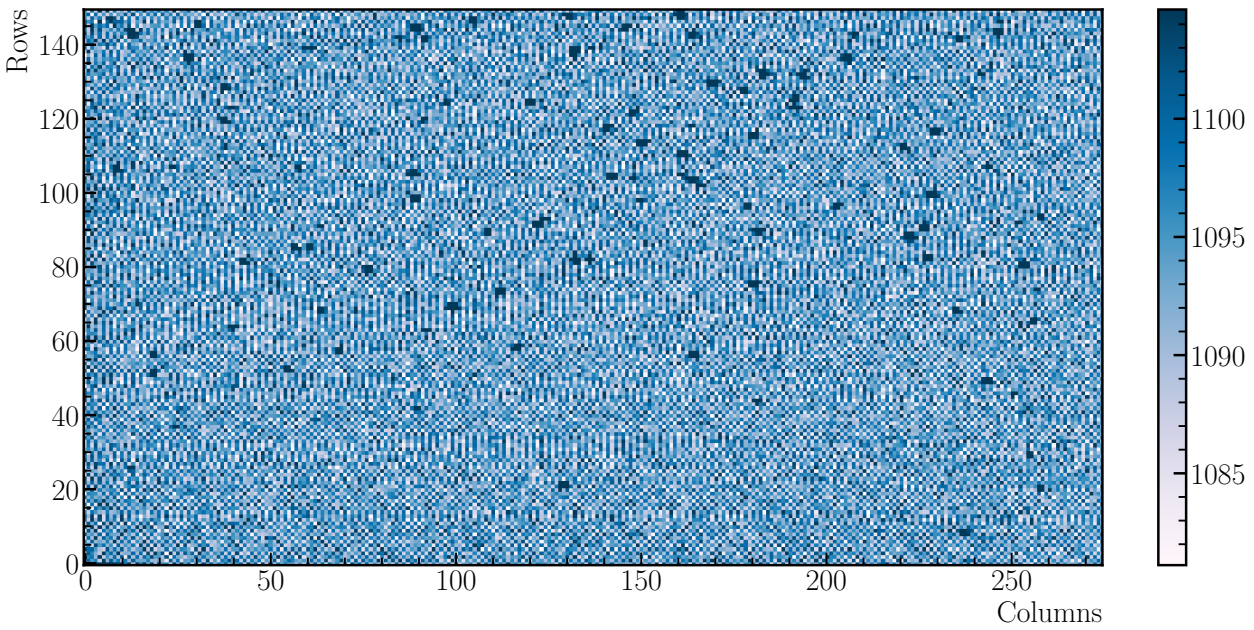

Figure 4.11: Image taken with Am241 source in place. Features corresponding to correlated noise can be seen as bands that traverse the entire image.

as seen in Figure 4.13.

Figures 4.11 & 4.12 provide visual examples of the effects that were affecting data quality. Figure 4.11 shows a common – yet less concerning – set of images exhibiting correlated noise; these images can arise from improper electrical isolation of the detector and readout electronics, or minor vibrations in the environment (e.g. vacuum pump). Figure 4.12 shows what I will refer to as *baseline shift* images, and make up the most concerning and direct cause of large injection for low-energy clusters.

4.5.1 Baseline Shifts

In particular, baseline shifts are a sudden change in the base value provided by the electronics during the read-out process. After a thorough inspection of images with the effect and extensive study, it was found that the nominal *shift* between affected pixels was approximately 12 ADU — or 2 electrons after conversion. While that may not sound like a large deviation, this effect leads to the shifts being misclassified as event clusters by our

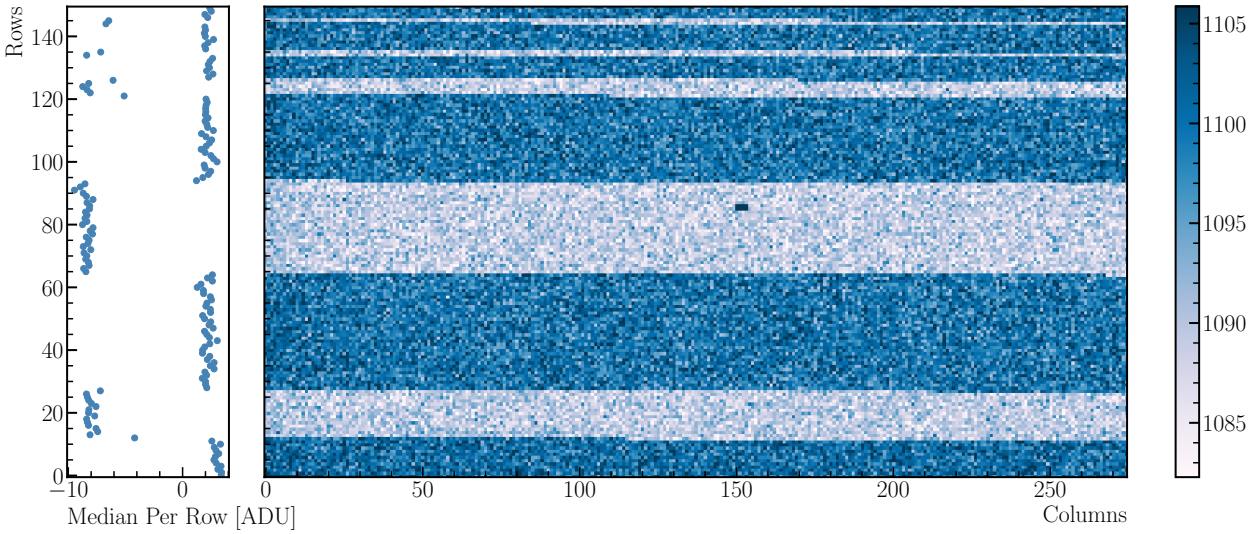

(a) Ambient background image with baseline shift effects.

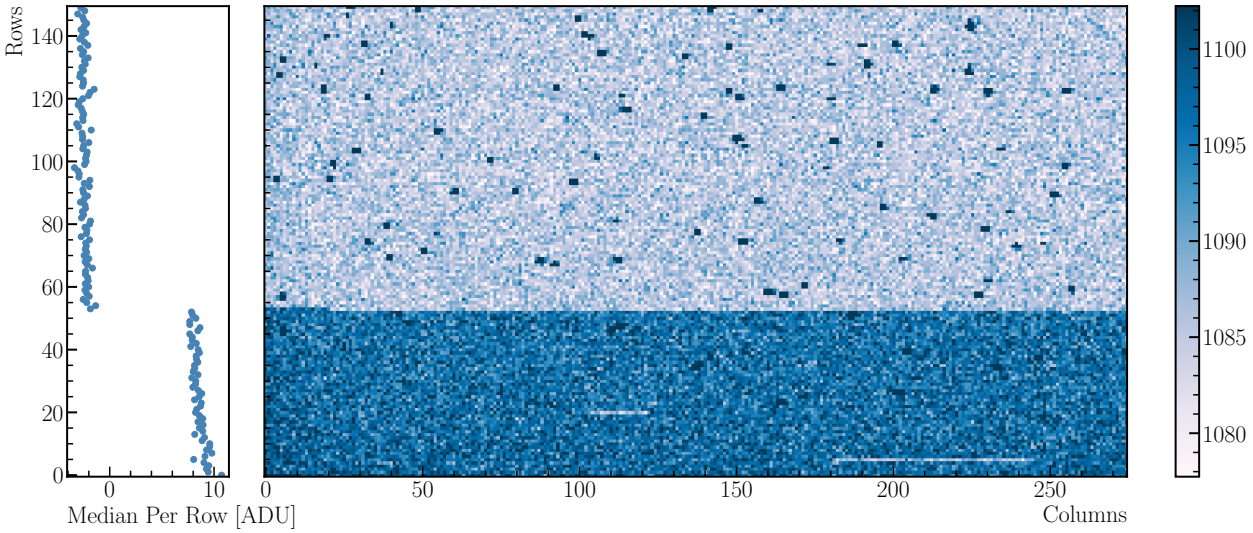

(b) Am241 Source image with baseline shift effects.

Figure 4.12: Images shown exhibit a shifting baseline value during readout. When plotting the median value over all rows, we see a deviation of 12 ADU per both images. All values shown are in Analog Digital Units [ADU].

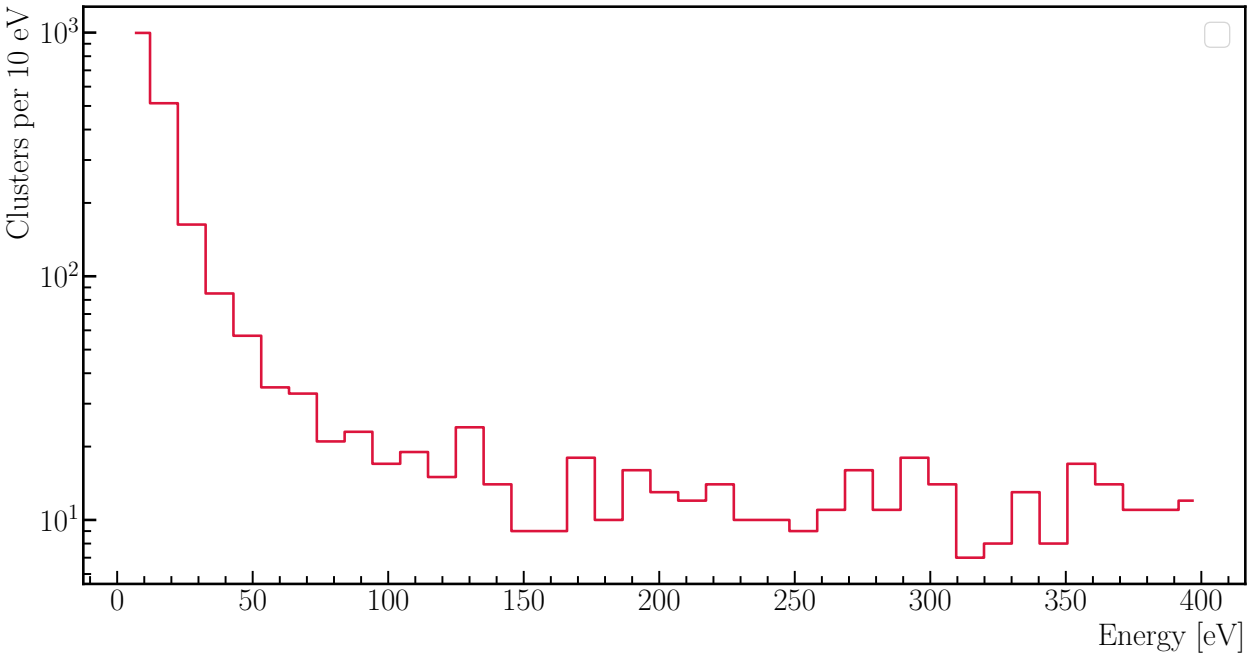

Figure 4.13: Energy spectra from a sample of poor-quality data images. We begin to see an injection of low-energy events below 150 electron volts.

reconstruction algorithm; ultimately, leading to the injection of events below 150 eV as seen in Figure 4.13. Considering the L-shell steps of silicon do not occur until below 150 eV, it is imperative to categorize, flag, and omit any poor-quality images from the final spectral analysis.

4.5.2 Quality Cuts

Fortunately, it was possible to exploit two key features of baseline shift images and develop an algorithm to flag and omit images from reconstruction analysis. First, as seen in the scatter plots in Figure 4.12, there is a significant gap in median ADU value between shifts. Therefore, we can focus on designing an algorithm that searches for a discontinuity between baseline values along rows. Second, for the Compton data campaign, data images took roughly 45 seconds for readout to end, thus, the baseline shifting effect traversed (usually) the entire row and made it possible to isolate the effect on a per-row basis.

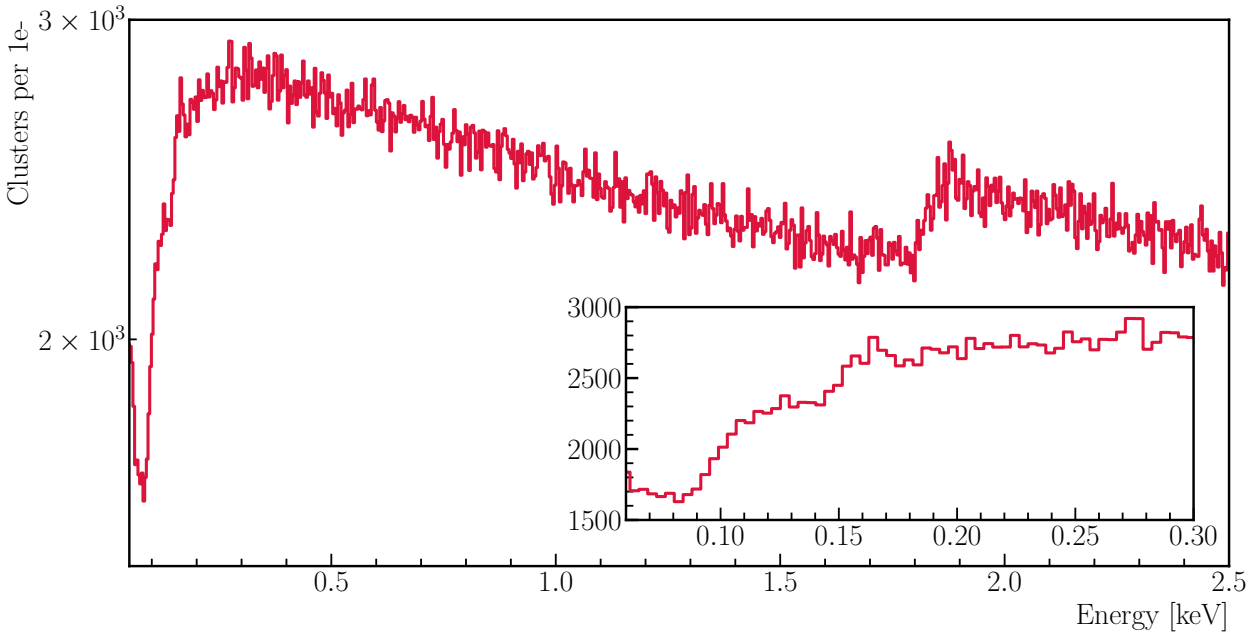

Figure 4.14: Post quality cuts, we see resolved L_1, $L_{2,3}$ steps. Data is a representative sample.

The final cleaning algorithm relied on partitioning the overscan region of the data image – before baseline subtraction – and applying an iterative approach to detect a discontinuity between a partition's median values. When a discontinuity between two partitions is detected, the image is flagged and omitted from the final analysis. Overall, the algorithm effectively flagged and cleared any large injections of low-energy clusters. Runs that had a substantial fraction of poor-quality images after data cleaning were omitted entirely. The remaining good runs had cumulatively less than 1 percent of flagged images; ultimately, resulting in a clean, Compton spectrum with visible L-shell steps as can be seen in Figure 4.14.

4.6 Spectral Analysis

After having collected over 105 exposure-days with the Am-241 source (see Table 4.2) and processed each data set through our cluster reconstruction package (detailed in Section 4.4), we have achieved enough statistical power to report an updated detector threshold with full

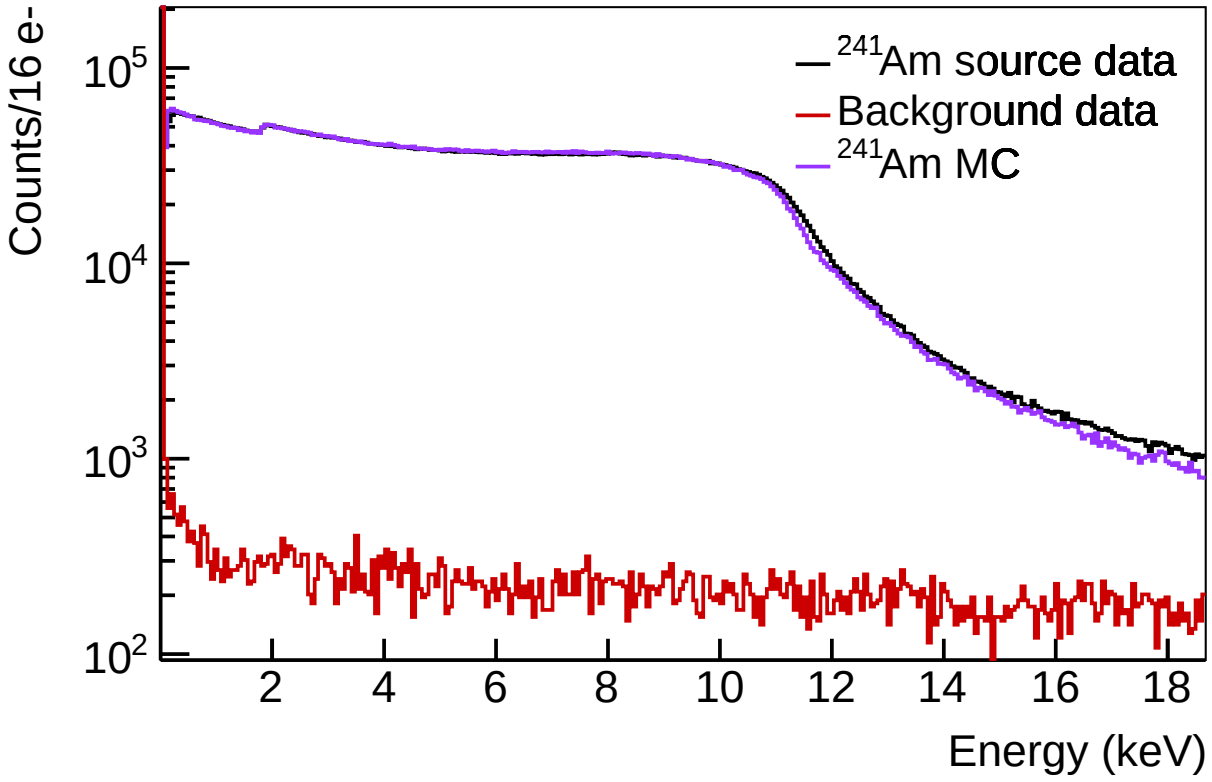

Figure 4.15: Am-241 source data in course binning (16e-) shown with comparison to GEANT4 simulation and ambient background. Data sets are normalized to Am-241 source data set[54].

resolution of the L-shell steps in silicon.

4.6.1 Compton Continuum

After event reconstruction, we recover a Compton profile that matches theoretical predictions from GEANT4. Figure 4.15 shows agreement up to the Compton edge near 10 keV — we note that an increasing disagreement at higher energies is due to limitations in extrapolating the calibration curve with energies >2.1 keV. Furthermore, within the Compton continuum, we see agreement between data and simulation in accurately reproducing the K-shell Compton step at 1.839 keV.

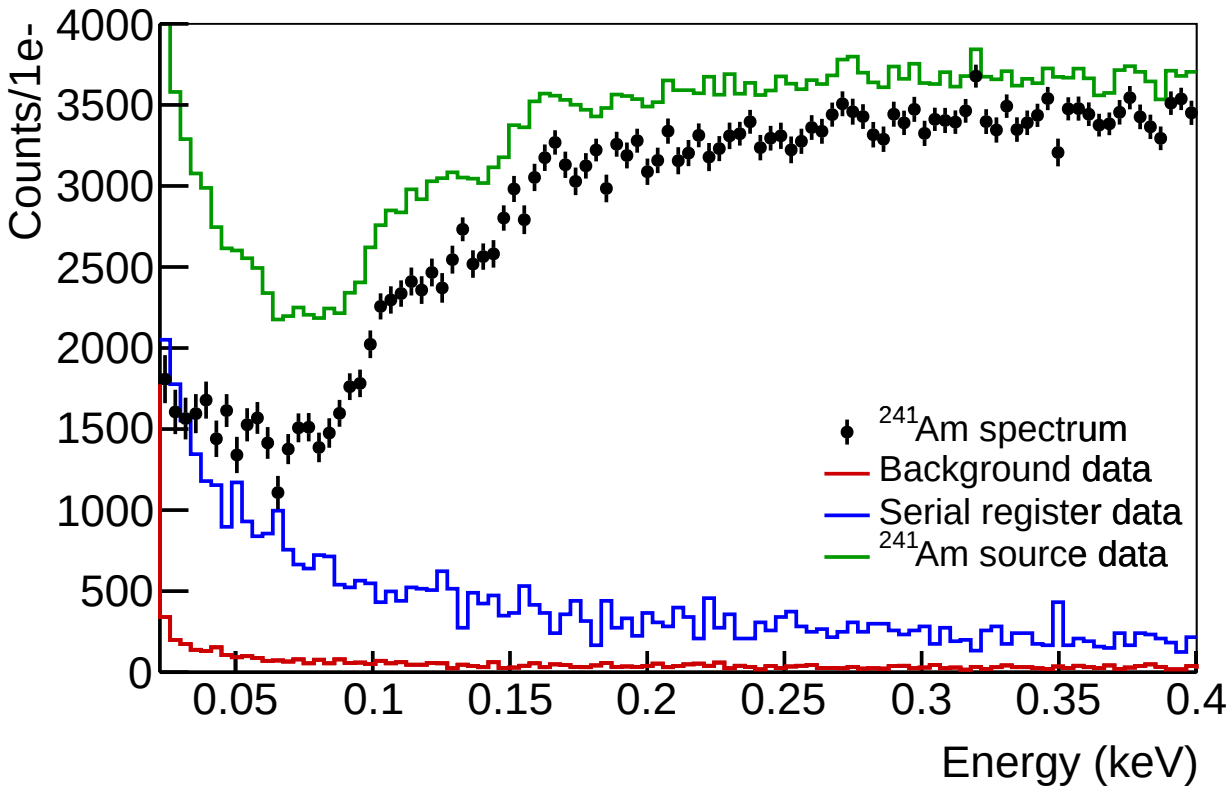

Figure 4.16: Spectral components of contributing to Am-241 source data (green). Serial register data (blue) and ambient background (red) are the main contributors to low-energy excess. Final bin-by-bin subtracted Am-241 spectrum shown (black)[54].

4.6.1.1 Background Subtraction

First, background events must be subtracted to extract a meaningful signal from the source data. In Figure 4.15 we see the ambient background data plotted alongside simulation and source data in coarse 16 e- bins. This arrangement of data shows a flat background – within statistical fluctuations – at energies above 1 keV. The excess of events below 1 keV is due to thermal effects, choice of binning, and serial register events — details can be found in Section 4.3.3.1. Figure 4.16 shows a comprehensive overview of the data components contributing to the low-energy excess < 1 keV at a much finer binning of 1e-. Taking advantage of the full power of Skipper CCDs, we demonstrate the ability to resolve spectral data up to 1 electron resolution. Figure 4.16 demonstrates that ambient background is not the main contributor

to the low-energy excess seen in source data at energies below 100 eV; rather the normalized events contribute up to ∼20 percent of the excess. By comparison, the serial register data contributes the remainder of the low-energy excess found below 100 eV.

Having decomposed the two primary sources of background, we take two methodologies to extract the Am-241 spectrum: the classic bin-by-bin exposure-normalized subtraction between data sets and a new data-driven approach — known colloquially as the *Area Method*. The classic subtraction method is shown in figure 4.16. Where we see silicon's fully-resolved, and distinct L-shell steps.

4.6.1.2 Area Method

The area method is based on a key, intrinsic principle of CCD operation: there is a linear increase in exposure for rows that are further away from the serial register. Therefore, as pixels in the serial register are being read out, pixels in subsequent rows accumulate charge as they are exposed to the Am-241 source — this effect can be seen in Figure 4.17. Moreover, ionizing events that led to the serial register data set remain constant and are implicitly accounted for through the implementation of the data-driven procedure. Figure 4.17 demonstrates the linear increase in counts for clusters with energy < 0.15 keV as a function of row. First, the region shaded in grey is analogous to data taken during background and serial register data runs — events that constitute this region occur at a constant rate and are uniform across the detector. Second, the purple, patterned sliver between grey and light purple regions is a ∼10 percent contribution to charge collection due to a 3-second exposure in the image-taking process. Finally, the area within the light purple region is interpreted as the amount of clusters generated between a designated energy range.

The proper extraction of counts relies on an iterative linear fit of clusters within equally

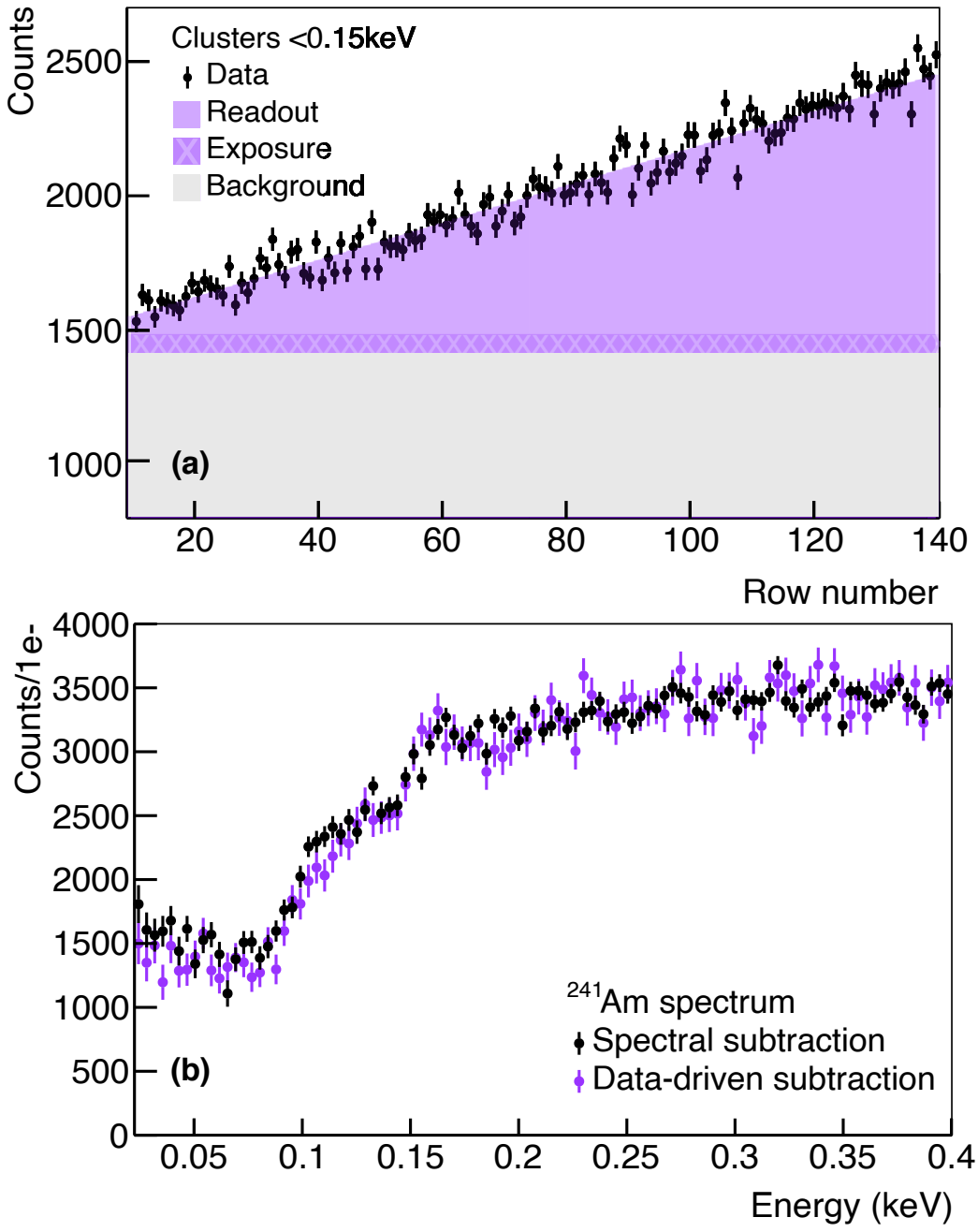

Figure 4.17: (a) Number of reconstructed clusters below 0.15 keV as a function of row in the CCD. The area of the triangle (light purple) is taken as an estimate of the signal, together with the small rectangle right below which accounts for 3s exposure before readout. The larger rectangle (dark purple) represents the subtracted background. (b) Comparison of the spectral subtraction (black) and data-driven (purple) L-shell spectrum[54].

spaced energy bins.

$$A_i = \frac{N_{rows}\,(m_i \cdot N_{rows})}{2} + \frac{N_{rows}\,(m_i \cdot N_{rows})\,t_{exp}}{2t_{readout,i}} \tag{4.5}$$

Equation 4.5 describes the methodology for extracting the spectrum generated on a CCD from a radioactive source. The first corresponds to the bulk amount of events, while the second is a correction term that may be omitted when $t_{readout} >> t_{exp}$. When the area method is applied to the Am-241 data set, we recover a spectrum that is in agreement – without normalization – to the classic spectral subtraction, as can be seen in Figure 4.17.

4.6.2 L-Shell and Energy Threshold

With two independent approaches to extract the Am-241 spectrum, we are confident in the spectral profile achieved down to a threshold of 23 eV. At energies within the bounds of the silicon K-shell, we see agreement between GEANT4 simulations and the extracted spectrum. However, at low energies we notice that there is a softening of the L-shell steps present in the spectral profile. This softening was unexpected and deviated from predictions of the Relative Impulse Approximation (RIA). Figure 4.18 shows predictions from GEANT4 simulations – that employ the RIA model – overestimate the event rate at energies below 0.5 keV up to 20 percent. As our work has ultimately reproduced and verified the measurement by Ramanathan et al in the L-shell region, we are motivated to pursue an alternative theoretical approach to explain the observed features.

To study the cause of the softening L-shell steps, we chose to adapt techniques from X-ray Absorption Spectroscopy (XAS) through their FEFF codes [39, 41, 54, 73]. Rather than basing assumptions on the free-electron approximation, the FEFF codes perform *ab initio* calculations and a full quantum mechanical treatment to compute $S_{nl}\,(q, E)$ found in Equation 4.3. Per the calculation, all transition probabilities are accounted for and summed

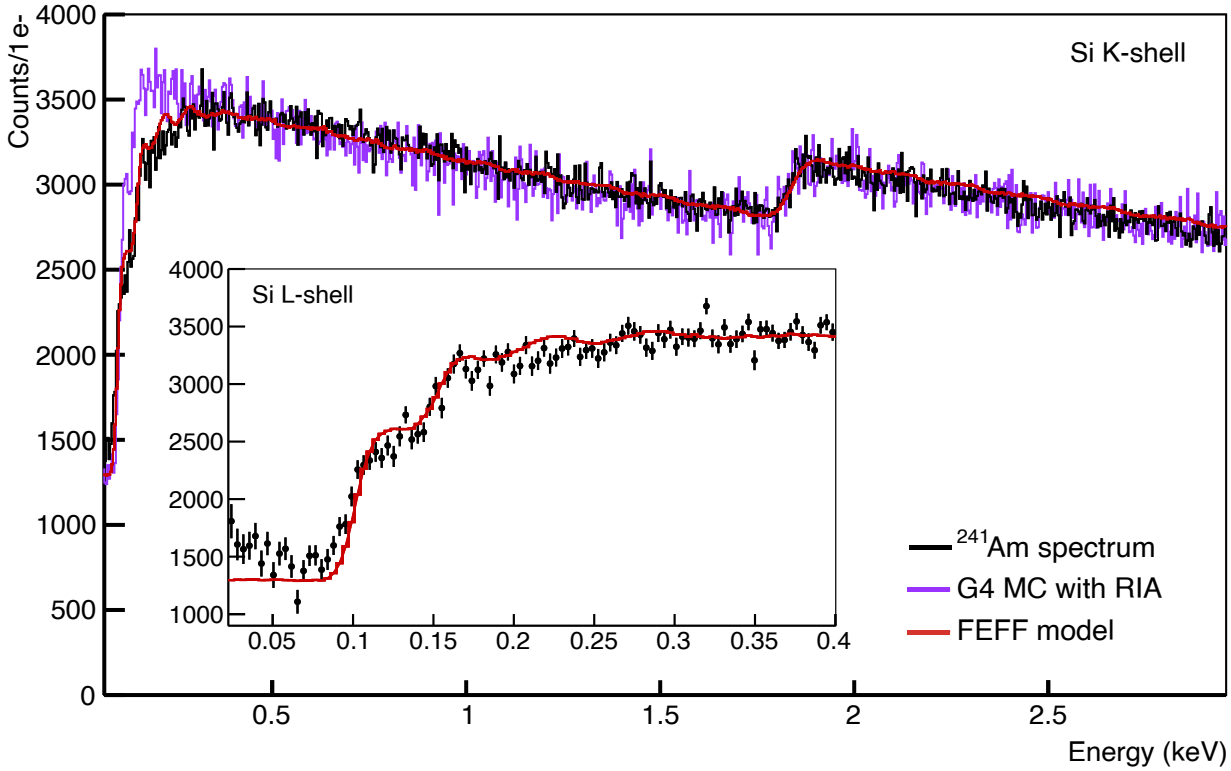

Figure 4.18: The measured 241Am Compton spectrum (black) from the 23eV detection threshold to the K-shell region. The GEANT4 simulated spectrum (purple) which is based on the relativistic Impulse Approximation is also shown. The red line is the prediction from ab initio calculations of the FEFF code, with detector response taken into account. The inset shows data comparison to the FEFF prediction in the L-shell energy range[54].

over; thus, resulting in a more rigorous set of predictions and an accurate spectral model. With the implementation of FEFF, we attain an improved model to explain the observed, softened L-shell steps in silicon to better than a 10 percent agreement between data and model. As seen in the inset of figure 4.18, the FEFF model also predicts a softened set of L-shell steps contrary to the sharp steps seen in the RIA model. Ultimately, with the implementation of the FEFF model, we are confident in our results and present a Compton spectrum with visible steps corresponding to the binding energies of silicon atomic shells.

4.7 Final Remarks

Direct dark matter searches are largely limited by detector resolution and irreducible radiogenic backgrounds. The DAMIC-M experiment will house novel Skipper CCDs – capable of multiple non-destructive charge measurements – in an environment subject to gamma radiation from material impurities in the surrounding environment. With a dedicated Compton scattering measurement, we have characterized the electronic response of our detectors down to a threshold of 23 electron volts — largely due to the reduction of pixel readout noise to $\sigma_{pixel} = 0.73$ electrons. These results demonstrate the efficacy of Skipper CCDs as particle detectors capable of probing an unexplored dark matter space down to a few eV after electronic scattering [8–10, 54].

Furthermore, this measurement validates spectral features seen by previous measurements and extends the spectral profile generated by Compton scattering. For the first time, we have a confirmed measurement of the silicon atomic shells: $L_1, L_{2,3}, K$ and have just bridged into the plateau predicted by theoretical models corresponding to silicon's valence shell. Notably, however, the L-shell region exhibits a softening not predicted by the RIA model but can be recovered – up to 90 percent agreement – through the implementation of FEFF codes found in X-ray Absorption Spectroscopy.

Overall, this measurement highlights the potential capabilities of Skipper CCDs and the

necessity for an updated theoretical model in simulation packages like MCNP or GEANT4 which employ the relative impulse approximation. Since these packages are the standard in estimating background events within detectors, naive use will lead to overestimation of gamma backgrounds as detectors probe lower energies in search of elusive dark matter particles.

CHAPTER 5

IONIZATION YIELD FROM NUCLEAR SCATTERS

5.1 Overview

DAMIC-M Skipper CCDs have two primary channels for ionization event generation: nuclear scatters and electronic scatters. In an electronic scatter, an incident particle's energy deposition is directly proportional to the charge ionized in the detector — limited only to the electron-hole pair creation energy, ϵ_{e-h}. However, in a nuclear scattering event energy is deposited onto the nucleus of the scattering atom, and charge ionization is a secondary process after relaxation. This energy *quenching* process between nuclear recoil deposition energy (eV_{nr}) and ionized charge collected by the detector (eV_{ee}) can be modeled and an ionization yield, or quenching factor, can be measured. Dedicated measurements for the nuclear ionization efficiency (ionization yield) are necessary for experiments whose detection channels involve nuclear scatters – such as dark matter and neutrino experiments – since the energy deposited as the ionized charge will be much less than the recoil energy of the scattering particle; for dark matter experiments in particular, successful detection of a candidate requires an accurate mapping of the particle's momenta.

In addition to nuclear scatters from dark matter particles, our experiment will be subject to a neutron background whose interactions will mimic dark matter scattering events in the silicon bulk of our detector. While a neutron flux is directed towards our experiment from cosmic-ray interactions in the atmosphere, the Col du Fréjus mountain above our laboratory effectively shields our detector from any cosmic-ray neutrons [10]. Neutrons will therefore originate from other sources in the laboratory environment. In general, our detector is most susceptible to neutrons originating from material decays in the surrounding rock (from isotopes such as ^{238}U) and the environment of the detector; (α, n) reactions that occur when an alpha particle has sufficient energy to overcome the Coulomb barrier of an

accepting nucleus and ultimately emits a neutron; and muon-induced neutrons [2, 10, 15, 42]. Neutrons generated from these processes are attenuated with a thick polyethylene shield that encapsulates the detector, further reducing the neutron scatters during dark matter searches. Nonetheless, the detectors must be characterized to differentiate dark matter interactions from other nuclear scatters, and a quenching factor model for silicon must be measured to the full detector energy threshold.

5.2 Ionization From Nuclear Scatters

The primary ionization channel for charge-coupled devices is through electron excitation. However, particles that are neutrally charged do not directly interact with electrons through Coulomb forces, rather ionization must occur through secondary processes.

As an incident particle of energy, E_i, scatters off the nuclei of the target medium, the particle imparts some of its energy, E_r, onto the incident atom's nucleus. The energy transfer is given by,

$$E_r = \frac{4mM}{2\left(m+M\right)^2} E_i \left(1 - cos\phi\right) \tag{5.1}$$

Here, Equation 5.1 is calculated in the center-of-mass frame where the incident particle and target nucleus are modeled as hard spheres. In the equation, the energy transfer, or recoil energy, is given by E_r, the mass of the incident particle is m, the mass of the nuclei is M, the initial energy of the inbound particle is E_i, and the scattering angle is ϕ. From the equation, a maximum recoil energy occurs when a particle backscatters off of its target with an angle $\phi = \pi$. In this case, $\cos\phi = -1$ and the maximum recoil energy is given by, $E_r^{max} = 4mM/(m+M)^2$. This result is useful in estimating the maximum ionization signal that a detector can measure.

After impact, the target atom's nucleus recoils and interacts with other atoms' nuclei in its environment; subsequently depositing some of its energy onto the collided atoms. During

this process, some energy is transferred to the electrons of the recoiling atoms and ionization occurs if the minimum energy transferred corresponds to multiples of the electron-hole pair creation energy of the target material, ϵ_{e-h}; otherwise, the transferred energy is converted into phonon generation. The processes that govern the transfer of energy towards either the motion of the recoiling nuclei[1] or charge ionization have been encapsulated into a set of equations developed by Lindhard in 1963 [48, 67]. In Lindhard's theory, the secondary charge ionization arises from the collision of two ions; one ion which is referred to as the incident ion traveling with a kinetic energy, E, through a homogeneous substance until it scatters with another ion and the ion recoils with a recoil energy, E_r. The recoil energy E_r can be written in the form, $E_r = H + N$, where H represents the fraction of energy given to the electrons in the atom and N represents the fraction of energy given to the motion of the ions. This form is then reduced to a dimensionless quantity through a scaling factor $c_Z = 11.5Z^{-7/3}\text{keV}^{-1}$, where Z is the atomic number of the species. The reduced dimensionless form is given by,

$$\epsilon_r = \bar{\eta} + \bar{\nu} \tag{5.2}$$

where $\epsilon_r = c_Z Er$, $\bar{\eta}$ is the averaged quantity for $\eta = c_Z H$, and $\bar{\nu}$ is the averaged quantity for $\nu = c_Z N$ [48, 67]. To arrive at an empirical solution, Lindhard placed five key approximations. One, ionized electrons do not generate any appreciable atomic recoils. Two, the binding between atoms can be neglected under the assumption that it is generally small compared to the energy of the recoiling ion, thus implying $\epsilon_r \approx \epsilon$. Three, the energy transferred towards the ionization of electrons is small compared to the energy transferred to the recoiling ions. Four, the effects of atomic and electronic collisions can be treated separately. Five, the transfer of energy between subsequent collisions of atoms in the lattice is small compared to the kinetic energy of the recoiling ion (ie. the first recoiling atom scatters off a

1. In the Lindhard model, the model is built in regards to colliding ions moving through a homogeneous medium. The referenced ions inferred to represent a charged particle incident on a positively charged nucleus; or the positively charged nucleus of one bound atom, recoiling with another [48, 67].

nearby atom). With these assumptions, Lindhard arrived a numerical solution of the form,

$$f_n(\epsilon) \approx \frac{\bar{\eta}(\epsilon)}{\epsilon} = \frac{\epsilon - \bar{\nu}(\epsilon)}{\epsilon} \tag{5.3}$$

where,

$$\bar{\nu}(\epsilon) = \frac{\epsilon}{1 + \kappa g(\epsilon)}, \qquad g(\epsilon) = 3\epsilon^{0.15} + 0.7\epsilon^{0.6} + \epsilon \tag{5.4}$$

Equations 5.3 and 5.4 form the basis to modeling the ionization yield from a nuclear scatter in a target medium. In the equations, $f_n(\epsilon)$ corresponds to the quenching factor, or ionization yield, $\bar{\eta}(\epsilon)$ is the fraction of energy given to the electrons, $\bar{\nu}(\epsilon)$ is the fraction of energy given to the motion of the ion, κ relates to the electronic stopping power of the target medium and is given by $\kappa = 0.133Z^{2/3}A^{-1/2}$, and $g(\epsilon)$ is a parametric equation to approximate his solution [48, 67].

The set of equations provided by Lindhard's theory have been validated in germanium and silicon by several measurements throughout the years[51, 67]. In germanium, the model has been validated to recoil energies of $E_r \sim 250$ eV, but in silicon the model has only been validated to an approximate recoil energy of $E_r \sim 3 - 4$ keV [26, 48, 67]. For DAMIC-M, and other silicon-based experiments looking for rare processes, this limitation presents a motivation to experimentally measure the ionization yield for silicon at recoil energies $E_r < 4$ keV. Otherwise, the detector's sensitivity to low-energy deposits will be limited to the uncertainty of the Lindhard model.

5.2.1 Recent Measurements

In recent years, a few measurements have been undertaken to determine the ionization yield in silicon at low-recoil energies. Of particular interest to DAMIC-M, a measurement in 2016 was made using DAMIC generation CCDs; this measurement employed a ^{9}Be(γ, n)^{8}Be photo-nuclear source to generate monochromatic neutrons as the incident particle on the

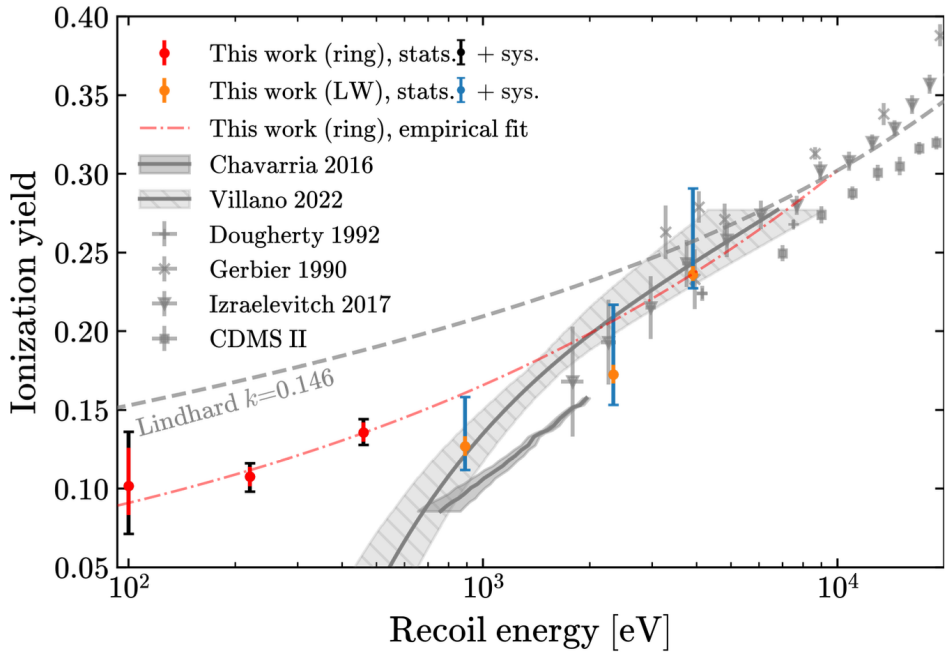

Figure 5.1: Comparison of results from the measurement of SuperCDMS. SuperCDMS presents an ionization yield that deviates from the Lindhard model and the 2016 result from DAMIC [4].

CCD detector. This detector was not capable of conducting multiple non-destructive charge measurements and was limited to its readout noise of ~ 2 electrons per pixel. Nonetheless, the measurement presented a leading measurement of the ionization yield in silicon down to a recoil energy of 680 eV [18]. The results presented a yield that deviated from Lindhard's model, indicating that at low recoil energies the theory may not hold for all target media. Additionally, in 2022 SuperCDMS conducted an additional measurement with their silicon based detector; their detector is capable of detecting both phonons and ionized charge. In their measurement, they measured an ionization yield down to a recoil energy of 100 eV by directing a pulsed proton beam towards a lithium target to incite the $^7\mathrm{Li}(p,n)^7\mathrm{Be}$ reaction. Additionally, through their experimental campaign they provided a measurement of the nuclear Fano factor for the first time at these energies — the nuclear Fano factor will be discussed at a later section. The results from SuperCDMS deviated from both the Lindhard

model and the measurement from DAMIC in 2016. This was unexpected, but indicated that other physical factors, such as temperature, may play a role in charge ionization at low energies. The results from these measurements can be found summarized in Figure 5.1 [4].

Now, with a silicon based CCD capable of achieving a sub-electron readout noise the ionization yield must be measured to extend the results achieved from the 2016 measurement from DAMIC CCDs. As DAMIC-M aims to probe lower dark matter masses, the community must be certain of the calibration results used to either exclude dark matter masses, or present significant excess at low ionization yields from nuclear scatters. As a natural continuation from the 2016 measurement, DAMIC-M will use a photo-neutron source with a silicon Skipper CCD as the detector of choice. The experimental campaign will be undertaken at the University of Chicago and the campaign will be lengthy due to interaction cross-section between the detector material and incident particles. The remainder of this chapter will detail the experimental measurement commissioning and its analyses.

5.3 Experimental Setup

This experiment requires a long data-taking campaign due to the low interaction rate between the active silicon mass and the inbound flux of neutrons. Therefore, the choice of neutron source, experimental hardware, and data acquisition parameters must be optimized to balance neutron signal and data quality.

5.3.1 Source Selection

For this measurement, we want to consider a neutron source that is portable enough to easily alternate between dedicated neutron *On* and neutron *Off* data runs, and active enough to produce sufficient neutron interactions within the active silicon mass. Several physical processes and reactions are capable of producing neutrons such as nuclear fission, alpha-neutron (α, n) reactions, and photo-nuclear (γ, n) reactions. The former two choices have the dis-

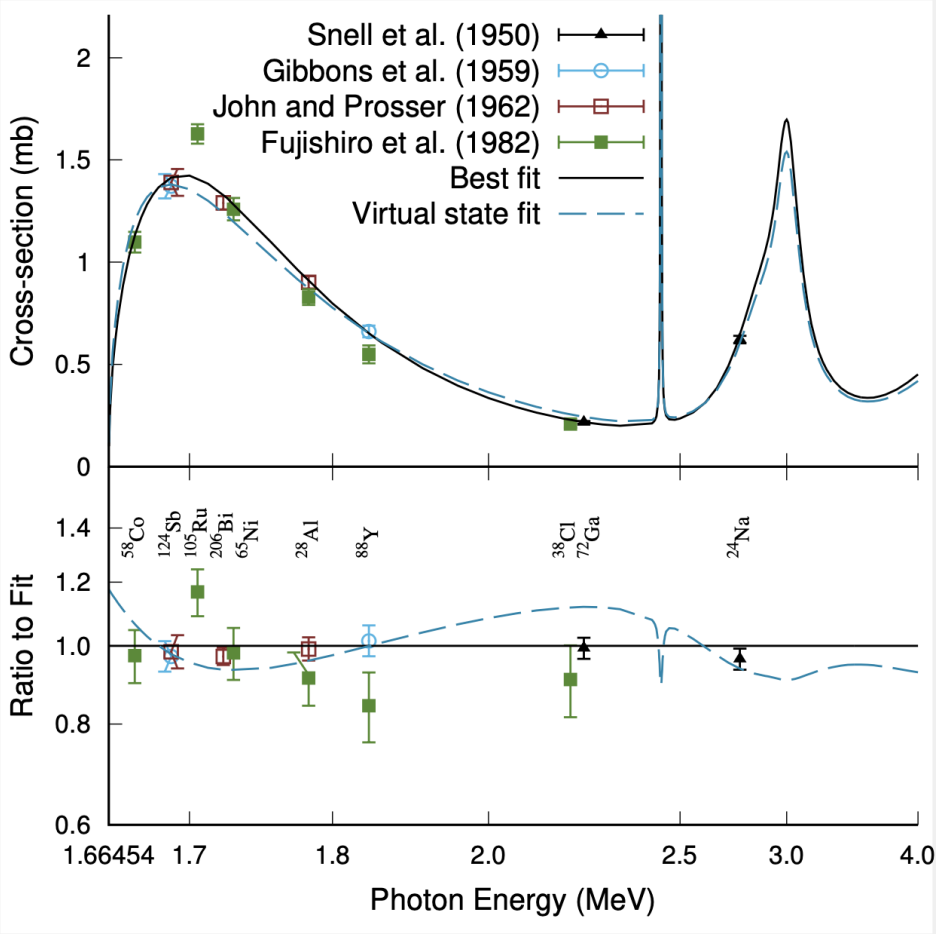

Figure 5.2: Reanalyzed cross sections of the ^{9}Be(γ, n)^{8}Be reaction [64].

advantage of either producing other particles whose interactions will muddle the detector or neutrons whose energy spectrum will be large, and broad enough to require long data campaigns. However, neutrons produced from photo-nuclear reactions are nearly monoenergetic; such sources are colloquially referred to as photoneutron sources [42].

A common photoneutron target material is Beryllium-9. The general reaction is,

$$ {}^{9}_{4}Be + E_{\gamma} \rightarrow {}^{8}_{4}\,Be + {}^{1}_{0}\,n \tag{5.5} $$

where the associated Q-value is, $Q = -1.66$ MeV [42]. The Q-value being negative indicates that in order for the reaction to occur, a gamma, E_{γ}, of at least 1.66 MeV must be captured

by ^{9}Be. After capture, the excited ^{9}Be will emit an ^{8}Be isotope and a neutron with kinetic energy dependent on the following formula,

$$E_n(\theta) \simeq \frac{M\left(E_\gamma + Q\right)}{m+M} + \frac{E_\gamma\sqrt{(2mM)(m+M)\left(E_\gamma + Q\right)}}{(m+M)^2}\cos(\theta) \tag{5.6}$$

where θ represents the angle between the captured gamma and emitted neutron, M is the mass of the recoiling nucleus $\times c^2$, m is the neutron mass $\times c^2$, and E_γ is the incident gamma energy [42]. Here, we can infer that given the square in the denominator, the denominator will dominate and the second term will add little variability to the spread of neutron energies produced from the reaction. A notable constraint for this reaction is the cross-section. Figure 5.2 shows the cross-sections for the ^{9}Be(γ, n)^{8}Be reaction; where only the contribution from the most intense gammas from each radioisotope are plotted [64].

From the figure, we can infer that the gamma energy needed to maximize the neutron yield from the photo-nuclear reaction occurs at either $\sim$ 1.7 MeV or $\sim$ 3.0 MeV. The measured radioisotopes that represent these regions are ^{58}Co, ^{124}Sb, ^{105}Ru, ^{206}Bi, and ^{24}Na. All radioisotopes in this list – except for ^{124}Sb – have half-lives that are too short for any practical use, or the gamma energies that are above the Q-value have a branching ratio that is too low. Therefore, the Antimony-124 isotope is the most practical choice.

The Antimony-124 isotope has a reported half-life of 60.2 days. It decays via beta emission ($\beta-$) into Tellurium-124. The gamma energies emitted that are above the Q-value of the ^{9}Be(γ, n)^{8}Be reaction are the 1.69 MeV gamma and the 2.09 MeV gamma; each of which have a respective branching ratio of 0.4749 and 0.05498 [16]. Each of these gammas can produce neutrons via the photo-nuclear reaction expressed above, and the 1.69 MeV gamma is well-positioned to maximize the neutron yield from a Beryllium target with a reported cross-section of 1.41 mb—neutrons generated through this reaction peak at $\sim$ 23 keV for gamma energies of 1.69 MeV. Figure 5.3 illustrates the simulated neutron yield from

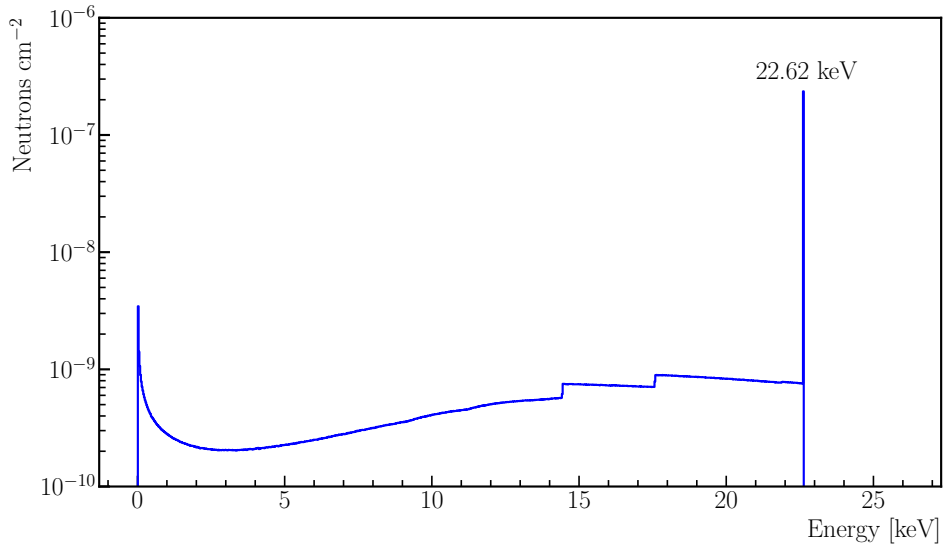

Figure 5.3: MCNPX Simulation of ^{9}Be(γ, n)^{8}Be reaction using 10^{9}, 1.69 MeV gammas and Alan Robinson's reanalyzed cross-section libraries[64]. The neutron energy distribution from 1.69 MeV gamma peaks at 22.62 keV with a decreasing low-energy tail. The observed steps correspond to neutron scatters with Beryllium and Oxygen nuclei. The low-energy rise is due to neutron attenuation from the polyethylene vial that encapsulates the antimony pellets.

the photo-nuclear interaction peaking at 22.62 keV. This simulation was carried out with MCNPX and employs Alan Robinson's updated ^{9}Be(γ, n)^{8}Be reaction cross-section library [64]. Further information is summarized and can be found in Table 5.1.

For this measurement, we employ an Antimony-124 gamma source and produce neutrons via the ^{9}Be(γ, n)^{8}Be photo-nuclear reaction. Further details on the material targets and source irradiation are discussed in the next sections.

Source	Half-Life [days]	Emission Type	Energy [keV]	Photons per 100 disintegration
^{124}Sb	60.208 (11)	Gamma	602.7278 (21)	98.254 (21)
		Gamma	1690.9842 (45)	47.49 (19)
		Gamma	2090.951 (5)	5.498 (24)

Table 5.1: Emission lines from Sb-124 isotope that occur in the energy region of interest, or have a dominant branching ratio. Values taken from reference [16].

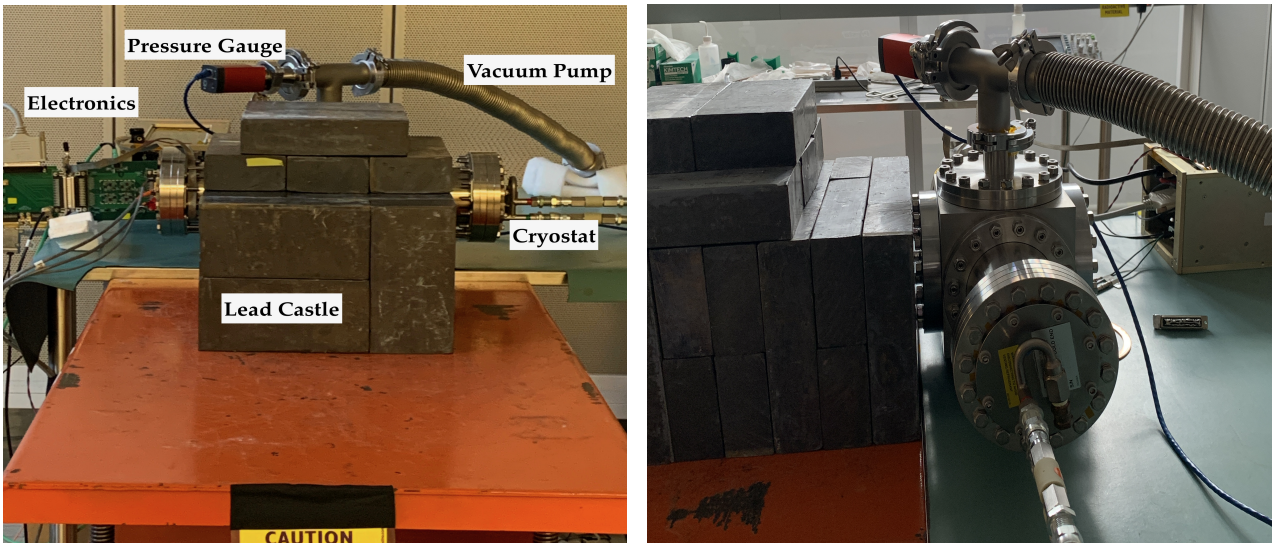

(a) Experimental setup with labeled components. (b) Side view of setup.

Figure 5.4: The experimental setup is shown. The lead castle is seen to be configured in an alternating pattern and pressed onto the stainless-steel chamber. The readout electronics, vacuum pump, and cryostat leads are also shown.

5.3.2 Hardware

This measurement was carried out in an above-ground laboratory at the University of Chicago campus. The experiment retained many of the key components detailed for the Compton scattering measurement (Chapter 4) including the 1K $\times$ 6K Skipper CCD, the stainless-steel vacuum chamber, and the electronic systems.

In addition to the core components, some modifications and additions were made to accommodate the expected activity of the Antimony-124 source and neutron flux. First, the front stainless-steel flange was swapped for a thinned aluminum flange to reduce the material between the detector and the neutron source. Second, a height-adjustable table was used to center the source to the detector. Finally, a lead castle was built to attenuate the intense gamma flux emanating from the antimony source. There is 20 cm of lead between the source and the chamber configured in an alternating pattern to attenuate the 1.69 MeV gamma flux to $I/I_0 = exp(-(\mu/\rho)\lambda) \simeq 1.23E-5$ of the initial source intensity (per the Beer-Lambert law). The attenuation received is sufficient to expect a minimal gamma background

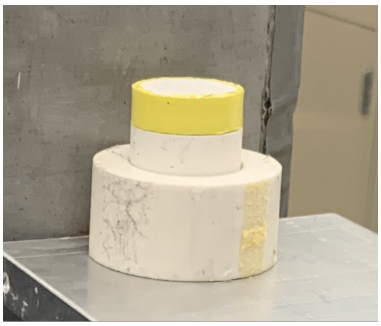

(a) BeO target used to encapsulate Antimony source.

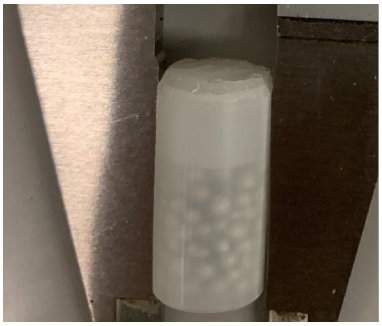

(b) Polyethylene vial with Antimony pellets before irradiation at Oregon State University.

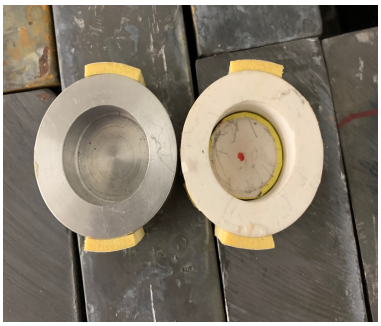

(c) Base of Aluminum and Beryllium targets attached side-by-side.

Figure 5.5: Material targets and Antimony source pellets are shown.

in the detector — this claim will be explored in the following sections. The experimental configuration can be seen in figure 5.4.

For the neutron source we use a Beryllium-Oxide target (BeO) and Antimony pellets encased in a polyethylene vial. For this measurement two, 5 gram Antimony sources were prepped and sent to Oregon State University (OSU) to be irradiated to 5 mCi of activity. Each source was measured to a reported 5.4 mCi on February 28, 2022 and July 7, 2022 respectively by OSU. Data taking with the neutron source began immediately upon retrieval of each source. For neutrons On data runs, the activated source was placed inside the BeO target such that the source was fully encased by the target material. For neutrons Off data runs, an aluminum target was used instead to collect a background data set that would be representative of the attenuated gamma flux incident on the CCD during neutrons ON data collection. Figure 5.5 displays the target materials used for this measurement as well as the Antimony source before irradiation. Of note, the BeO target shown in sub-figure 5.5a is comprised of 3 parts: the base, the hollowed cylindrical center, and a cap; this is also the configuration for the aluminum target used for the neutrons OFF data set. Additionally, sub-figure 5.5c displays two pieces of foam attached to the exterior of the base, these pieces were added to provide a better fit of the targets in the source cell of the lead castle (see

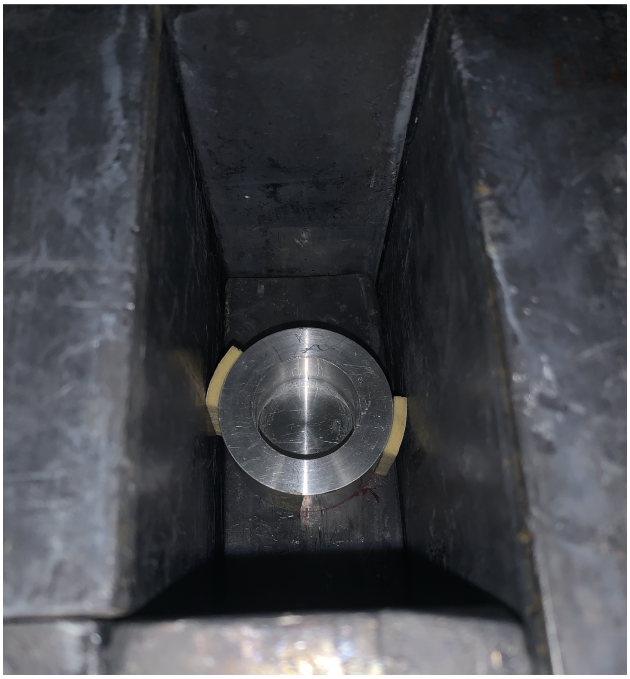

Figure 5.6: Aluminum target inside the source cell of the lead castle. A trace of the base is drawn on the lead to facilitate placement of target materials, and pieces of foam are placed around the exterior of target bases to achieve a snug fit within the cell.

Figure 5.6) and enhance reproducibility between neutrons ON/OFF configurations.

During the data-taking campaign, vacuum was held at 10^{-7} mbar, and the CCD was nominally cooled to 122 K. The CCD was fully depleted and lateral diffusion was diminished by applying a substrate voltage of 95 V. The CCD was controlled and data was collected via a commercial CCD electronic system (Astronomical Research Cameras, Inc). All instruments were remotely controlled and monitored via a dedicated slow-control system.

5.3.3 Data Runs Configuration

This measurement employs a photoneutron source that relies on the intense gamma output from the ^{124}Sb decays. Although, we are primarily interested in the neutron flux generated through the ^{9}Be(γ, n)^{8}Be reaction, an attenuated gamma flux will persist and its contribution towards the reconstructed energy spectrum must be accounted for. Figure 5.7 shows the simulated neutron flux (a) and gamma flux (b) incident on the CCD's active area. From these

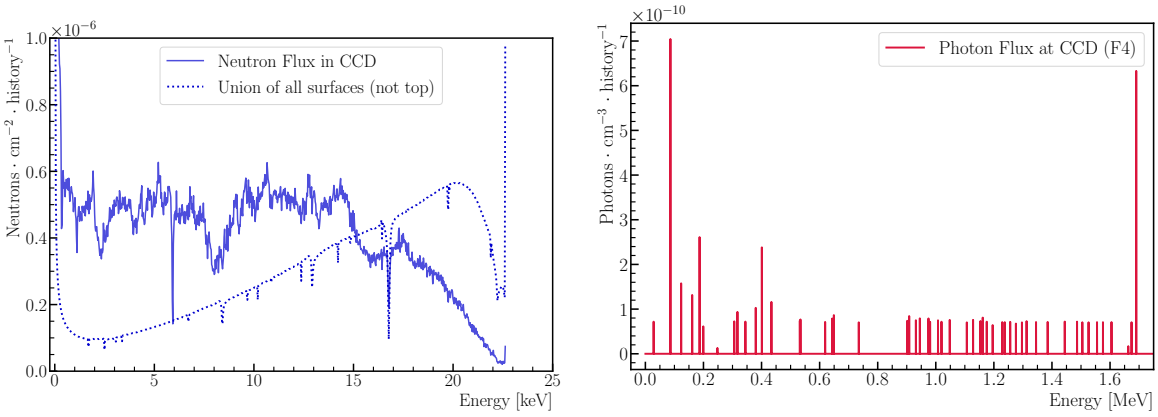

Figure 5.7: MCNP simulated flux through CCD. 10^9 neutrons were simulated; their energies were sampled from the distribution in Figure 5.3. 10^9, 1.69 MeV gammas were sampled. Simulation involved full experimental assembly.

simulations, we can estimate an expected interaction rate between the silicon and inbound radiation from Figure 5.8 — that details the interaction cross-section between neutrons and silicon. From the relevant cross-section, we can infer that given the active mass in our detector, we require a sufficient exposure time to accumulate neutron scattering event clusters per image. Additionally, the gamma flux simulation indicates that gamma interactions in the detector will not introduce a significant signal in the detector, thus the expected signal during the long readout periods will be representative of neutron scattering events.

For this experiment, we consider two independent science runs with two independent sources and data configurations. Each science run was divided into an Antimony-Beryllium (SbBe), or neutrons ON, run; an Antimony-Aluminum (SbAl), or neutrons OFF, run; and an ambient background run (no source present). During preliminary data-taking, neutrons ON and neutrons OFF data runs were cycled in equivalent intervals to mitigate the effects the decay of the source could have on the measurement. Each data run – irrespective of data type – consisted of 12 primary data images, each lasting approximately 25 minutes to read out; 1 full sized, single-skip image to be used as a diagnostic tool; and 1 single 2000-skip image to be used for run calibration as needed — similar to the run configuration presented in the Compton measurement (see Chapter 4.3.3).

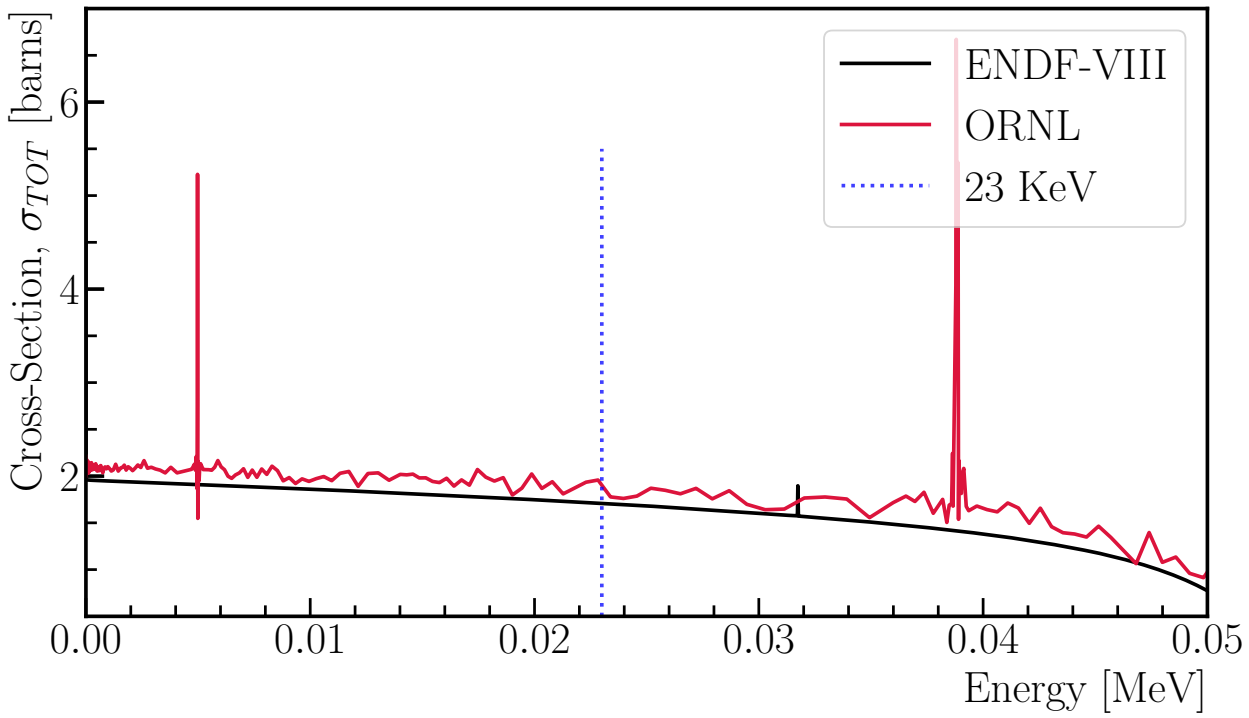

Figure 5.8: Neutron cross-section in silicon comparison between the Oak Ridge National Lab measurement and widely used ENDF-VIII libraries available in Monte-Carlo transport codes [44].

The first science run began on March 14, 2022 with Antimony source 1. As detailed in Table 5.2, the activity of this source was measured at 5.4 mCi on February 28, 2022. Data taking began with the neutrons ON configuration. During the first science run, the primary data sets consisted of images with 400-skips, 950 rows, and 275 columns. A 4×4 pixel binning was applied to the read out, and the calculated readout noise was 0.28 e- in the zero electron peak of the pixel-energy distribution — see Figure 5.9. During the 400-skip, source 1 data taking, approximately 18 days of good-quality neutrons ON data was accumulated, and 17 days of neutrons OFF data. The total 400-skip data campaign lasted through a little over one half-life of the Antimony source; at which point the process to transition to a higher-resolution data set began.

Near the one half-life mark of the first science run, it was decided useful to conduct a second science run with a higher resolution data set (ie. an increased number of skips) for

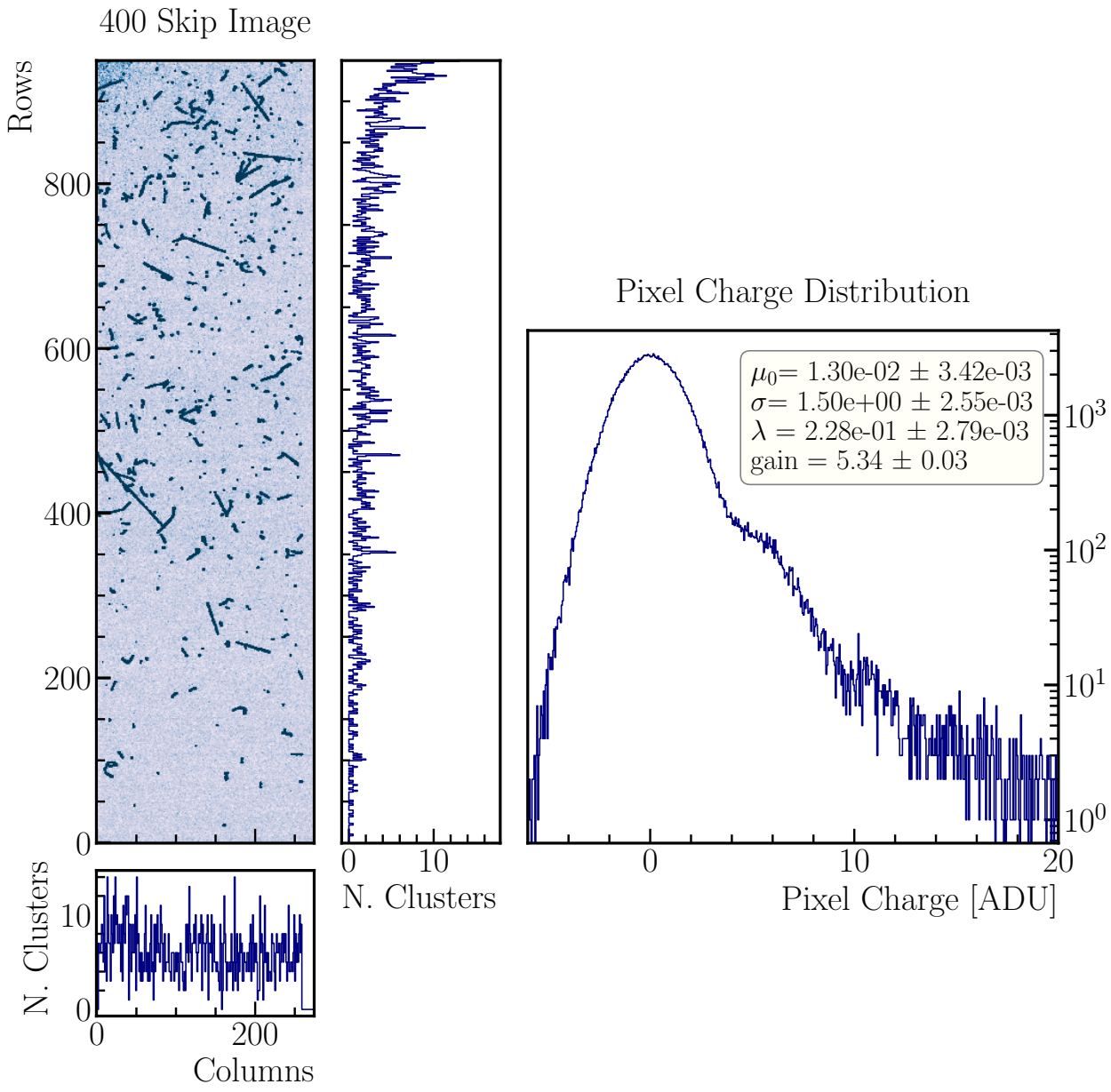

Figure 5.9: Detailed characteristics of selected 400-skip data image. The far left image shows an example image with particle tracks, the accompanying histograms represent the number of clusters along each column/row respectively, and the right figure is the pixel charge distribution of the image.

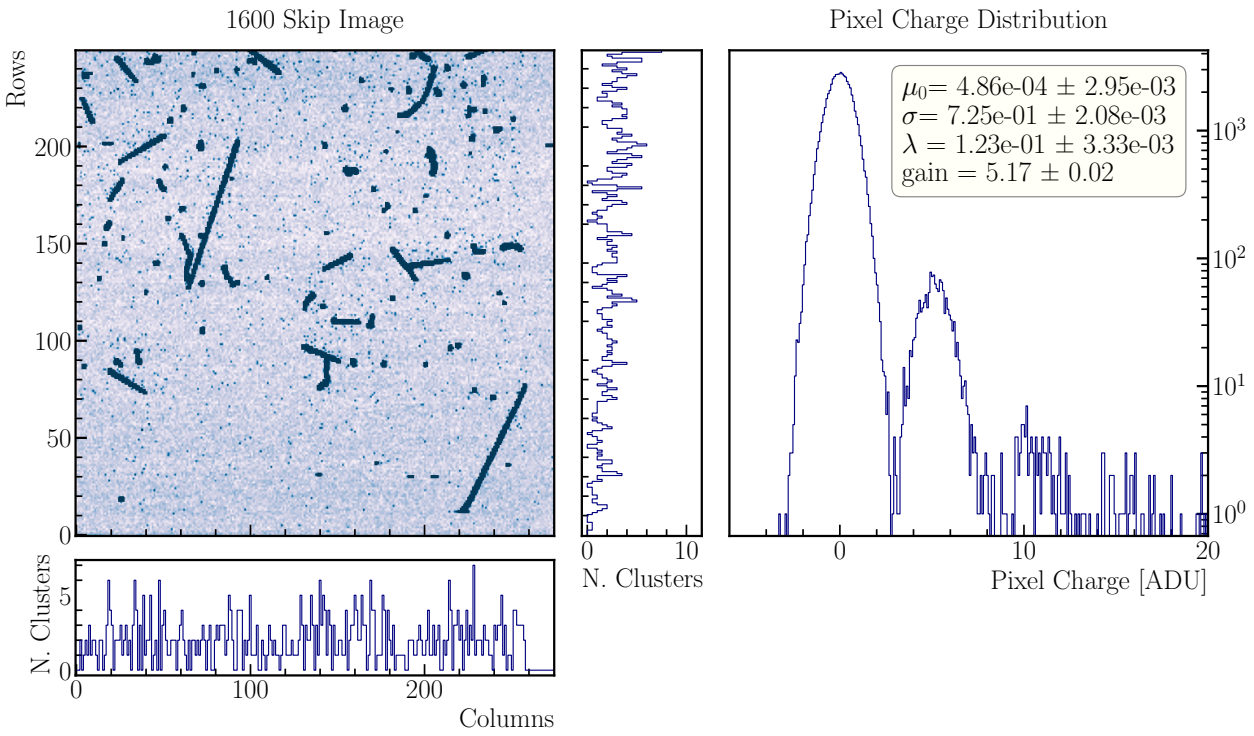

Figure 5.10: Detailed characteristics of selected 1600-skip data image. The far left image shows an example image with particle tracks, the accompanying histograms represent the number of clusters along each column/row respectively, and the right figure is the pixel charge distribution of the image.

two reasons: One, to constrain data taking to a low defect region of the CCD; and two, to probe to a lower detector threshold and hence, provide a more complete ionization efficiency yield measurement.

The primary data set configuration involved 12 1600-skip images, with 250 rows, and 275

Source	Activation Date	Activity (OSU)	Data-Taking Start Date	Activity (γ) (UChicago)	Activity (n) (UChicago)
Sb-1	Feb 28 2022	5.4 ± 0.54 mCi	Mar. 11 2022	4.083 ± 0.185 mCi	9015 ± 52 n/s
Sb-2	July 7 2022	5.4 ± 0.54 mCi	Jul. 14 2022	—	9508 ± 76 n/s

Table 5.2: Activity of the 1.69 MeV line as measured by Oregon State University and an in-house measurement with a NaI detector. The in-house measurement was done with only the first irradiated source. An attempt with the second source was conducted with a BGO detector after several half-lives of decay, but the systematic uncertainties were too large for an accurate measurement. Neutron measurements of the 22.62 keV neutron with a He-3 counter for both sources are also presented.

columns. Each image's pixels were 4 × 4 binned during readout, and a zero electron peak resolution of 0.14 e- was achieved — see Figure 5.10. During the first science run, neutrons ON and neutrons OFF data were taken, but insufficient statistics for a neutron signal were achieved with this configuration given the decay of the source. However, approximately 13 days of good-quality accumulated neutrons OFF data was taken and studied for quality. On July 11, 2022, the second irradiated Antimony source was received and on July 14, 2022, data taking in a neutrons ON configuration began. At the end of the data campaign with neutrons ON and neutrons OFF data, ambient background data sets were taken with 1600-skip images. A comprehensive summary of data statistics can be found in Table 5.3.

5.4 Data Processing

The data for this measurement was processed using WADERs — the standard analysis package for the DAMIC-M collaboration. As described in section 4.4.1, this package can perform key metric analysis on a per-image basis.

5.4.1 Overview

Per each data image, we: compress the raw skipper image; perform a pedestal baseline subtraction; apply a calibration process to convert from ADU to electron units; apply column

Source	Type	Binning [row×col]	Image size [row×col]	NDCMs	Images	Exposure [days]
BeO Target	source 1	4×4	900×275	400	1 074	18.3
Al Target	source 1	4×4	900×275	400	1 048	17.8
BeO Target	source 2	4×4	250×275	1600	2 011	35.7
Al Target	source 1/2	4×4	250×275	1600	1 513	26.9
None	ambient background	4×4	250×275	1600	1 016	23.2

Table 5.3: Summary of the data sets used in the analysis. 1600-Skip data taken with Al target in place is presented in aggregate between source 1 & 2 to represent the total gamma-background statistics.

and row masks to the images; and finally apply a cluster finder algorithm to locate energy depositions in the active image region of the CCD. This corresponds to the standard outline of processing done for the 400-skip and 1600-skip data sets. Figures 5.9 and 5.10 detail some key characteristics of selected data images from the respective data sets. In particular, for Figure 5.9 we note that when plotting cluster position along the column axis, we have an apparent uniform distribution along the columns; except for the first several columns depicting a 'bump' in the distribution. This bump is representative of a major hot column in the CCD that traverses the upper left region of the 400-skip images. The effect of this hot column can be further seen in the plot to the right of the image (that details the cluster positions along the rows). Here, we note that as we increase in row – and naturally, in exposure time – we not only see a linear increase in the number of clusters but rows > 700 exhibit a significant increase in the number of clusters due to this hot column. Therefore, for 400-skip images, we opt to mask rows above 700 before performing a spectral analysis of the data.

A contrasting feature between the 400-skip and 1600-skip data sets is the single electron peaks that become resolved in the 1600-skip data set. While the 400-skip data images can begin to resolve the 1-electron peak, there is insufficient resolution to clearly distinguish the 0-electron peak from the 1-electron peak. Thus, while we can perform a dark current fit estimation from the pixel-charge distribution, we cannot clearly distinguish single-ionization events from noise events. In contrast, with 1600-skip data images, we have a clear separation between electron peaks, and a much improved zero-electron peak resolution of $\sigma_{e-} \simeq 0.14$ e- (as seen in Figure 5.10). With the improved resolution, we can confidently discriminate signal from background events and probe toward the full detector resolution threshold.

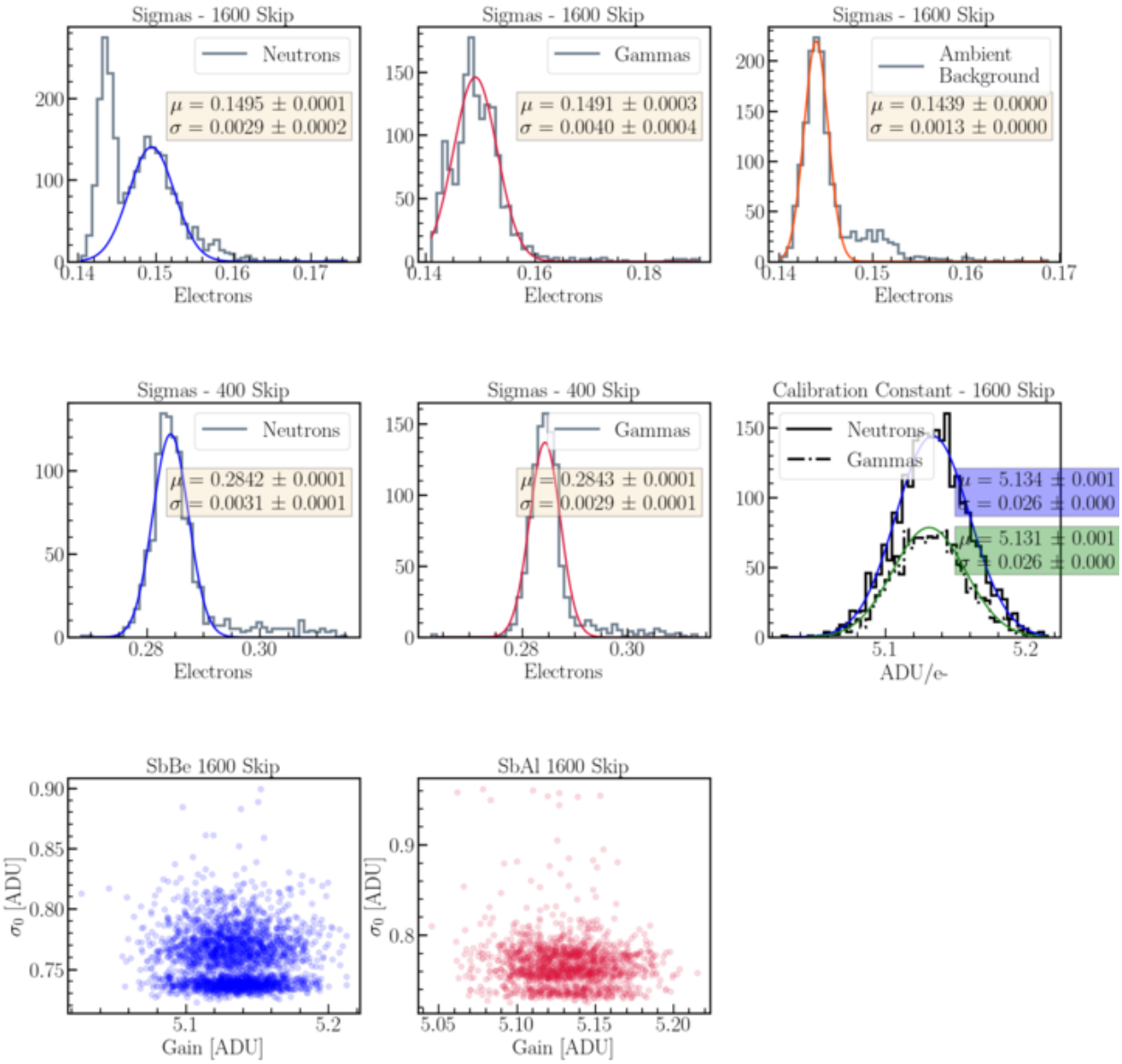

Figure 5.11: A mosaic representation of an image's zero-peak sigma (RMS) and the gain (ADU/e-) for all good images. Fit parameters are used in the cluster-reconstruction of the data images.

5.4.2 Calibration Constant

A key processing parameter is the calibration constant used to convert from ADUs to electron units and ultimately to electron volts. As previously mentioned, this constant is represented as the separation between the electron peaks; for low-energy, single-image measurements, the linear separation from the 0-electron peak and the 1-electron peak is a first-order approximation to the true calibration constant. In the Compton measurement, it was necessary to use the 2000-skip images to measure, to second order, the calibration constant and account for the shifting separation between peaks as you go higher in energies (order of 1 keV). For this measurement, we are interested in energies below 500 eV_{ee} and do not need to worry about second-order effects. Nonetheless, the main data-set is processed using a calibration constant that is fit to second-order from the respective data images. Figure 5.11 shows a mosaic of gains and zero-peak sigma values for images used in the analysis. The fit values are used during the data processing step to either indicate σ_{det} for the clustering parameter or the calibration gain (estimate).

5.4.3 Clustering Parameters

Perhaps the most important processing step for this measurement is choosing the optimal clustering parameters. Choosing an optimal cluster parameter set balances noise rejection and neutron signal acceptance. As previously mentioned, neutrons only deposit a fraction ($\sim 10\%$) of the nuclear recoil energy as ionized charge after scattering off the silicon nuclei. From Figure 5.7 it can be seen that the neutron fluence through the detector will span a range of energies, and therefore deposit a spectrum of ionized charge as signal. When considering these low-energy scatters, we can assume that energy deposits – after charge diffusion – will be point-like and localized to only a few binned pixels. Additionally, the clustering parameters should be chosen to exploit the single-electron resolution power of the selected data configurations — especially the 1600-skip data sets.

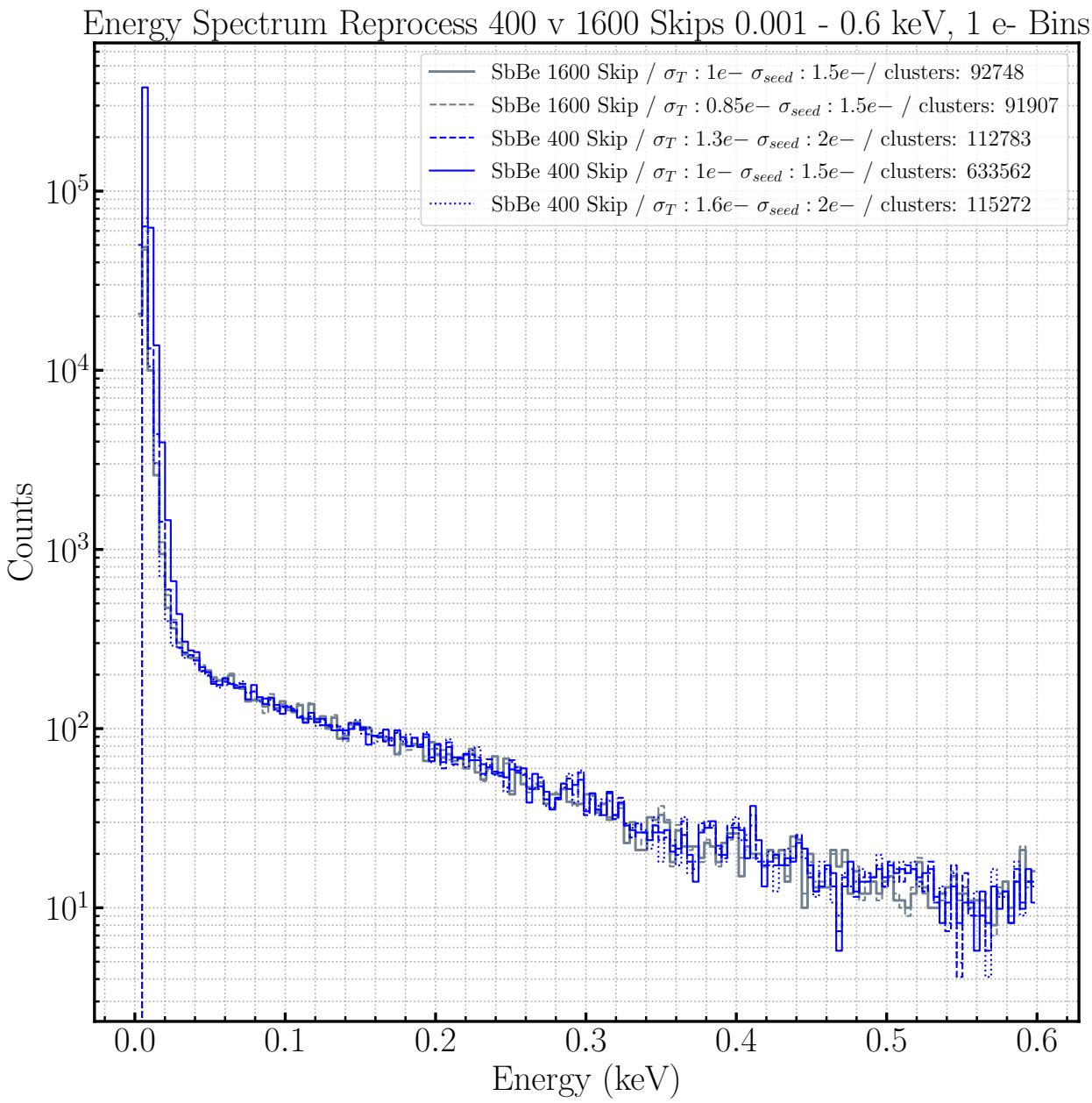

Figure 5.12: Comparison of clustering parameters at high energies for 400-skip and 1600-skip data. For 1600-skip data the decrease in cluster count with the lower σ_E indicates that clusters are merging and increasing in size. For 400-skip data, the drastic reduction in clusters due to changing the seed indicates the rejection of noise clusters.

For this measurement, we studied the effects the minimum energy threshold, σ_E, and the seed threshold, σ_{seed}, would have on the reconstructed energy spectrum for each data configuration. Given the increased resolution with the 400-skip and 1600-skip data sets, we

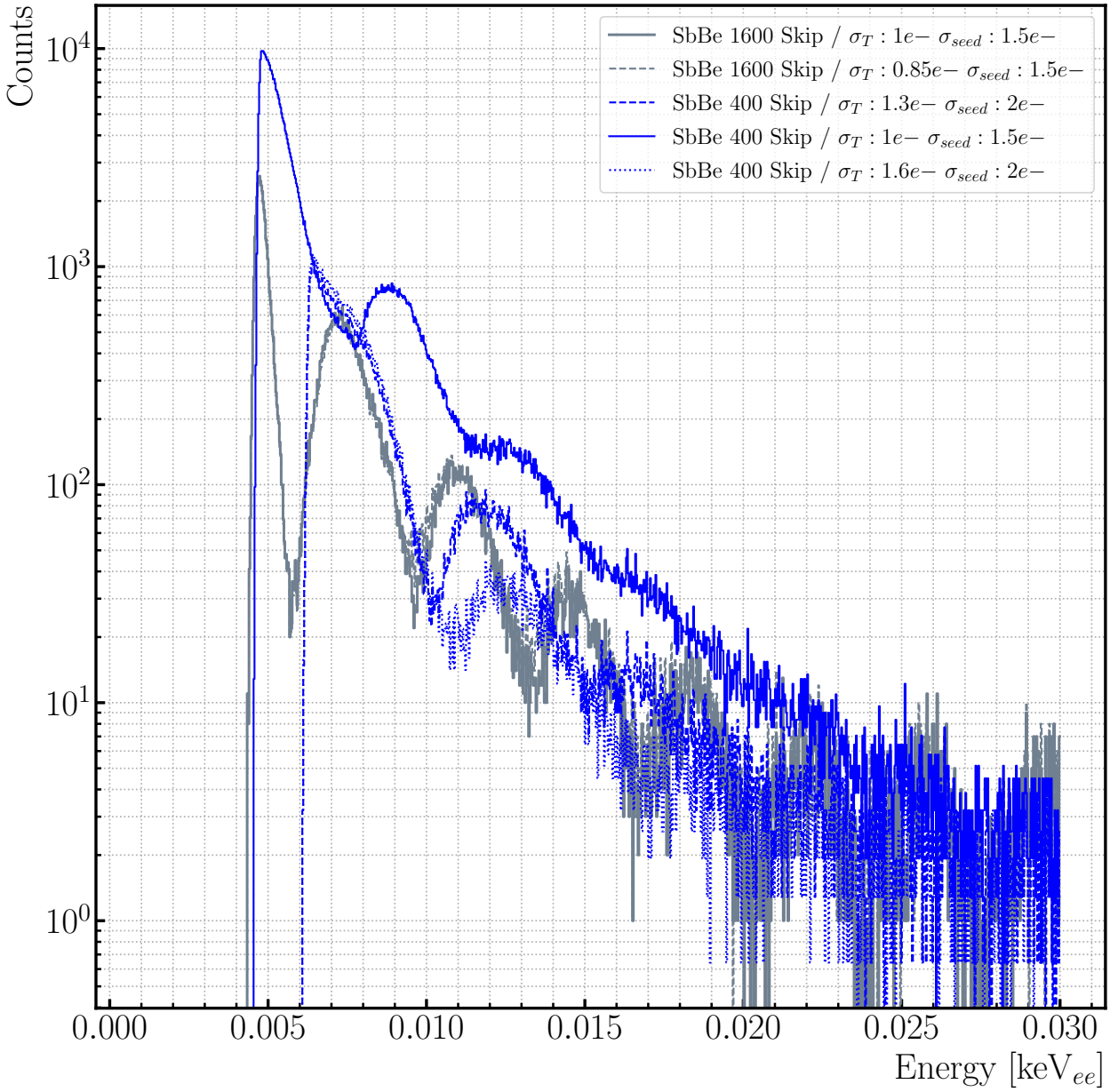

Figure 5.13: Comparison of selected clustering parameters for the 400-skip and 1600-skip data sets. The binning is arbitrarily fine to highlight the pixel cluster peaks.

can expect to push the seed threshold down to single electron peak energies. Figure 5.12 depicts some of the different clustering configurations used for this study. At high energies, the differences are indistinguishable, however at low energies – below ≤ 60 eV$_{ee}$ – there are more noticeable differences. In the 400-skip comparison with fine binning (Figure 5.13), we see the peaks that correspond to the low-energy pixel-cluster regions shift towards the right

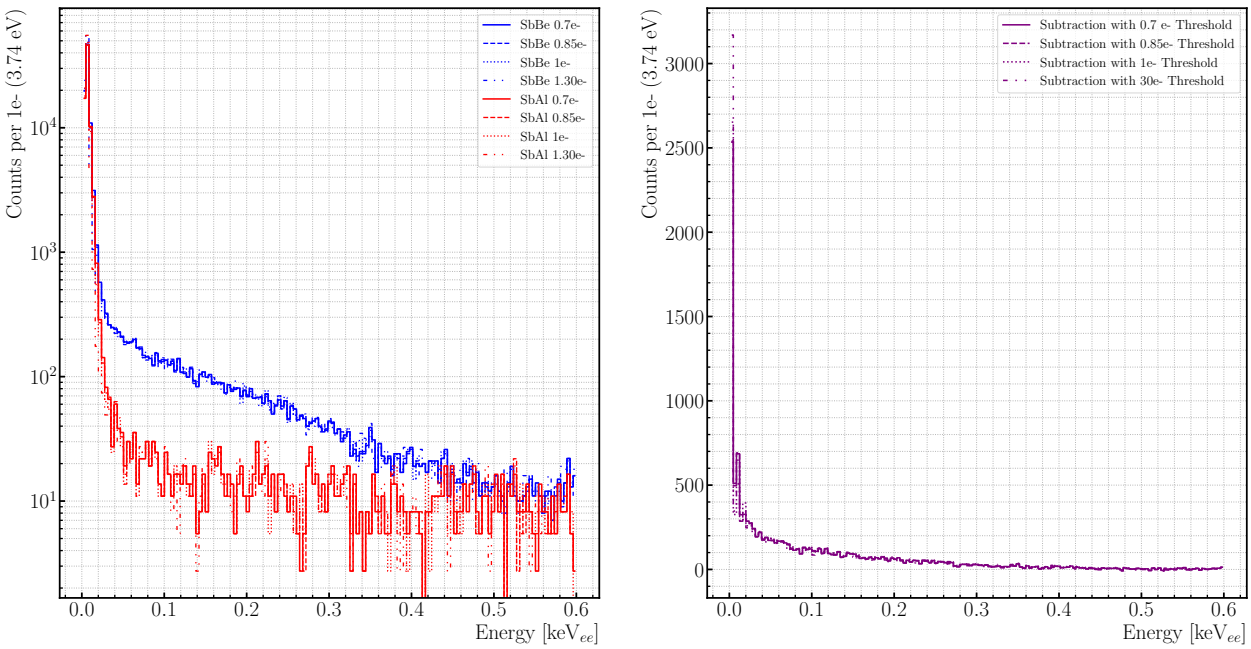

Figure 5.14: Comparison of clustering parameters at high energies for the 1600-skip data.

in relation to the 1600-skip data. This effect is due to σ_E and the resolution limitations with the 400-skip dataset seen in Figure 5.9. Since 400 skips are near the minimum resolution required to resolve the electron peaks and a clear distinction between the 0-electron peak and the 1-electron peak cannot be made, a $\sigma_{seed} = 1.5$ e- and $\sigma_E = 1$ e- cannot be applied to the 400-skip data since there will be a large injection of noise pixels into the cluster reconstruction. Therefore, an increase to a seed threshold of 2 electrons yields a better noise-to-signal ratio. The final cluster parameters chosen for the 400-skip data configuration are a seed threshold of 2 electrons and a minimum energy threshold of 1.3 electrons.

For the 1600-skip data, the electron peaks are much better resolved and we can afford to be more ambitious in our cluster selection criteria. Figure 5.14 details the spectral comparison between various minimum energy threshold values and the corresponding spectral subtraction. For each varied value, the selected seed threshold was 1.5 e-; since the pixel-charge distribution in Figure 5.10 shows a clear separation between individual electron peaks, thus the contribution of the 0-electron peak in the 1-electron peak is negligible. Therefore,

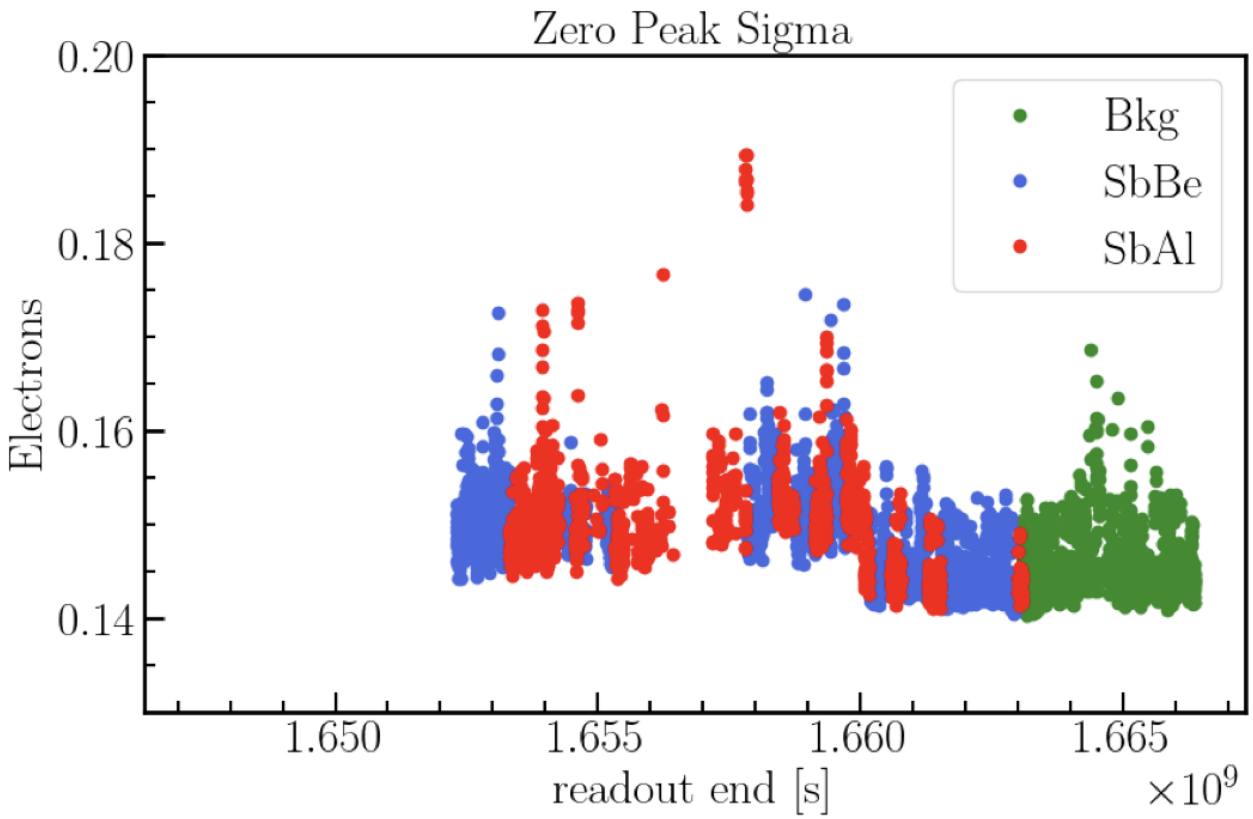

Figure 5.15: Distribution of the zero-peak sigma (RMS) of all data images used in the analysis. Data points that trend upwards are likely due to instabilities in the electronics from external sources.

we can be certain to discriminate against readout noise and include any low-energy scatter neutron deposits in the cluster reconstruction. With a seed threshold of 1.5 e-, we accept clusters with at least 5.61 eV_{ee}. At a minimum energy threshold of $\sigma_E \sim 0.7$ e- we expect a larger acceptance of noise pixels, while at $\sigma_E > 1$ e- we expect a decrease in detector threshold (as inferred from Figure 5.13).Therefore, for the 1600-skip data sets we choose a seed threshold of 1.5 e- and a minimum energy threshold of 1 e- as the main clustering parameters.

In addition to choosing the seed threshold, σ_{seed}, and the minimum energy threshold, σ_E, the selection of the detector resolution sigma, σ_{det}, was also necessary. As mentioned in the previous section, there are statistical fluctuations in the calibration constant, and

henceforth the resolution of the detector — determined from the zero-peak sigma, $\sigma_{det} = \sigma_{e-}$. Therefore, we assume that the reconstructed energy spectrum will be susceptible to the variations in resolution from this effect. The best example of this effect can be seen in the 1600-skip data of Figure 5.13 where the first couple of peaks are not Gaussian as expected, but rather seem distorted. This effect is related to a higher acceptance of noise pixels in the spectrum when reconstructing the images with each image's respective resolution, or $\sigma_{det} = Null$. Furthermore, what appears to be a truncated peak at the lowest energy, is not the first cluster peak, but rather is due to a shift in resolution that occurred during the data-taking campaign with source 2 on August 9, 2022. The shift occurred when the clean room fan was turned off to stop the injection of noise clusters – colloquially referred to as *skyline shifts*, and that will be discussed in the following section – during the readout process. Figure 5.15 illustrates the nominal shift in resolution near the midpoint of the data-taking campaign. Ultimately, the shift required the 1600-skip data to be processed with the two detector resolution sigma values that correspond to the respective resolution data. Figure 5.11 details the results of the detector resolution to be used per each data configuration. From the figure, we see that amongst the data types for a given configuration, the resolution is consistent; the only difference occurring from a shift from 400-skip data to 1600-skip data, or before and after August 9 data sets (as shown in Figure 5.15). The final selections for detector resolution sigmas are: for 400-skip images, $\sigma_{det,400} = 0.284$ e-; for 1600-skip data before August 9, $\sigma_{det,1600} = 0.149$ e-; and for 1600-skip data after August 9, $\sigma^{'}_{det,1600} = 0.143$ e-.

5.4.4 Data Cleaning

Throughout the data campaign, poor-quality images were observed. The observed effects mimicked the baseline shifts seen in the Compton measurement — see section 4.5. However, due to the time required to complete an image readout, many of the observed shifts did not

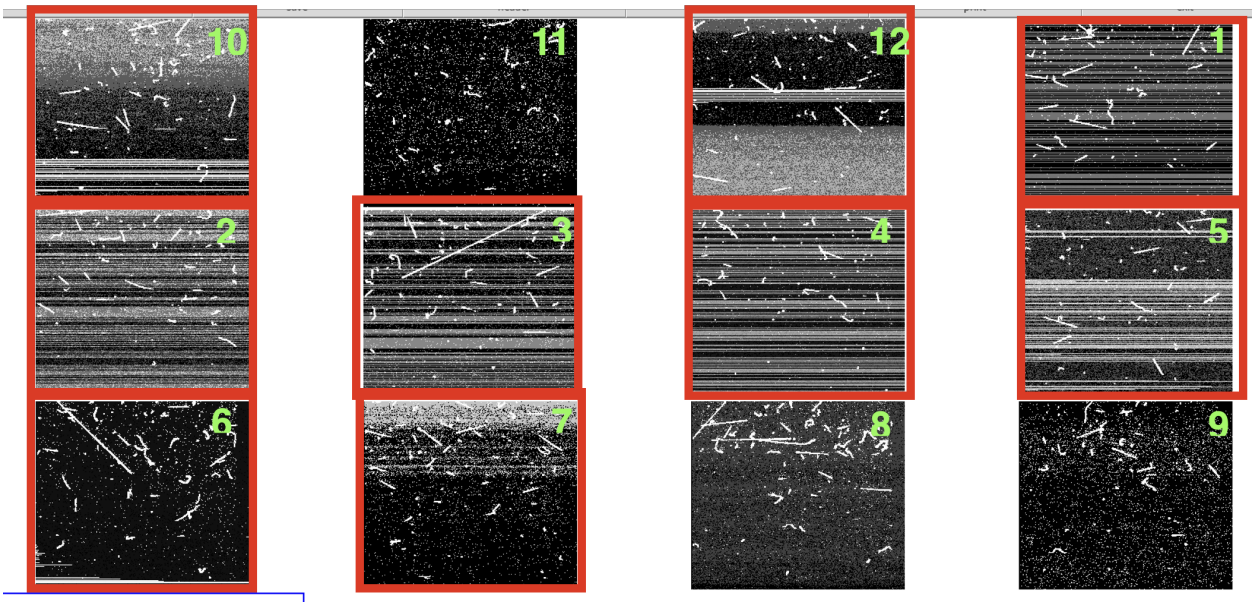

Figure 5.16: Selected 1600-skip data run with skyline shifts present. Images encased in red box are those that are flagged by data cleaning algorithm.

traverse the full row of the image, but rather stopped at arbitrary columns. This resulted in an apparent *skyline shift* that was present in a compressed image (see Figure 5.16). The skyline shifts retained the same $\sim$ 10 ADU shift in baseline, or about 2 e-, as the effects previously seen in the Compton measurement. Consequently, the presence of skyline shifts in an image resulted in each shift being reconstructed as a low-energy cluster; largely due to its consistent 2e- shift and span of an arbitrary length along a row. When these effects occurred next to each other, they would result in larger, 2 e- per pixel energy clusters. Additionally, due to there only being 12 data images per run, each image's contribution to the spectral analysis was heightened. Therefore, it was imperative to effectively tag any image exhibiting any characteristic of a skyline shift and reject it from the analysis. Figure 5.17 demonstrates the low-energy rise due to the skyline shift clusters.

Throughout the data campaign, exhaustive measures were taken to isolate the source of the skyline shifts and eliminate it. It was ultimately discovered that the electric infrastructure of the laboratory building was the main source; the final experimental setup isolated the readout electronics from any external sources of noise. The final change that was made was

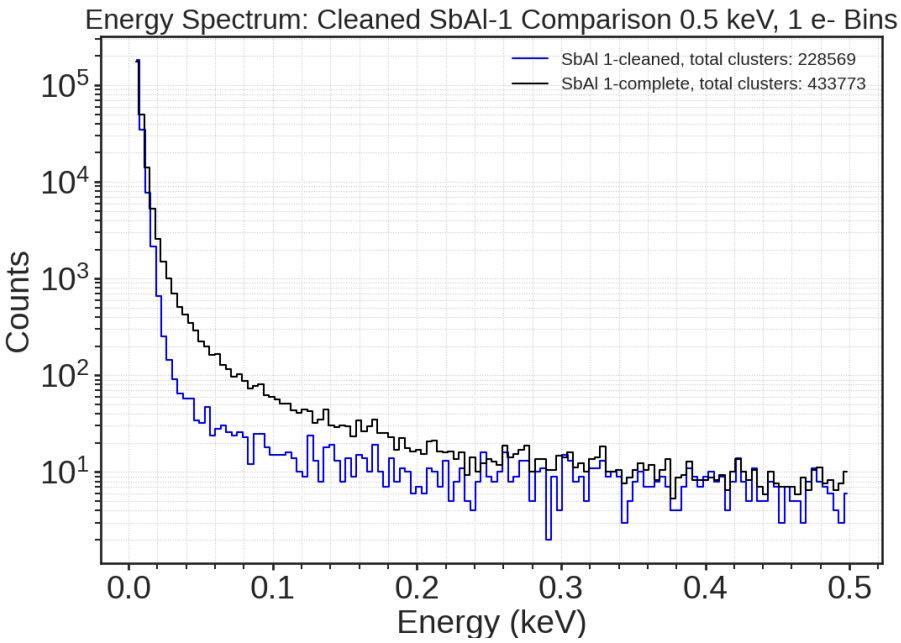

Figure 5.17: Selected energy spectrum showcasing the cluster injection at low energies caused by SS clusters. The spectrum designated as 'complete' corresponds to SS-clusters and signal clusters. An evident low energy rise is seen in the complete spectrum versus the cleaned spectrum.

turning off the clean room fan that caused the shift in the detector resolution during source 2 data-taking.

5.4.4.1 Skyline Shifts

A skyline shift is an effect that injects artificial charge into an image during the readout stage. When a pixel is being read out, the sense node will 'read' how much charge is present in a pixel; the total charge read in a pixel is the baseline value – that corresponds to the electronic signal – plus excess charge. If there is no charge present in a pixel, only the baseline value will be recorded. However, when the read out electronics aren't properly isolated from external noise sources, an upward shift in the baseline value can occur during readout. This shift injects artificial charge to pixels that would otherwise carry zero charge, and consequently injects clusters that muddle the low-energy region of the reconstructed

spectrum.

When the effect traverses the full row in an image – including the overscan region – the effect is subtracted out during the pedestal subtraction phase of the data processing. Under this condition, the shifted baseline has zero effects on the reconstructed energy spectrum since there weren't any artificial clusters generated. However, this condition needs to be met by every row in an image, otherwise the skyline clusters will persist and the image will need to be rejected.

Through inspection of images with skyline shifts, a couple defining features were discovered. First, the shift in baseline is consistently at $\sim$ 10 ADU, or $\sim$ 2 electrons. This is fortunate because it provides a distinctive signature to detect. Second, they start at the beginning of a row (ie. column 1) and extend to an arbitrary column i. Therefore, we can classify them as low-energy horizontal clusters; where instead of the cluster's corresponding pixels having a diminishing gradient of accumulated charge, each pixel in the skyline cluster should carry approximately 2 e- of charge.

The culmination of the two defining features lends itself to the development of an algorithm to detect the presence of skyline shifts in an image. The algorithm was developed, and integrated into the data quality monitoring module of WADERs. The following subsection will discuss the methodology and procedure for skyline shift flagging.

5.4.4.2 Skyline Shift Detection Algorithm

To develop an algorithm capable of detecting a skyline shift on an image, we first start by leveraging the distinguishing features of a skyline shift — the artificial charge is $\sim$2 e- and uniform, and the shift will truncate at some arbitrary column. Therefore, the first step to is to take a pedestal subtracted image and mask any pixel whose value exceeds the baseline signature. This value is generally determined through the inspection of afflicted images, but it must be optimized by testing various mask values; Figure 5.18 a) demonstrates the

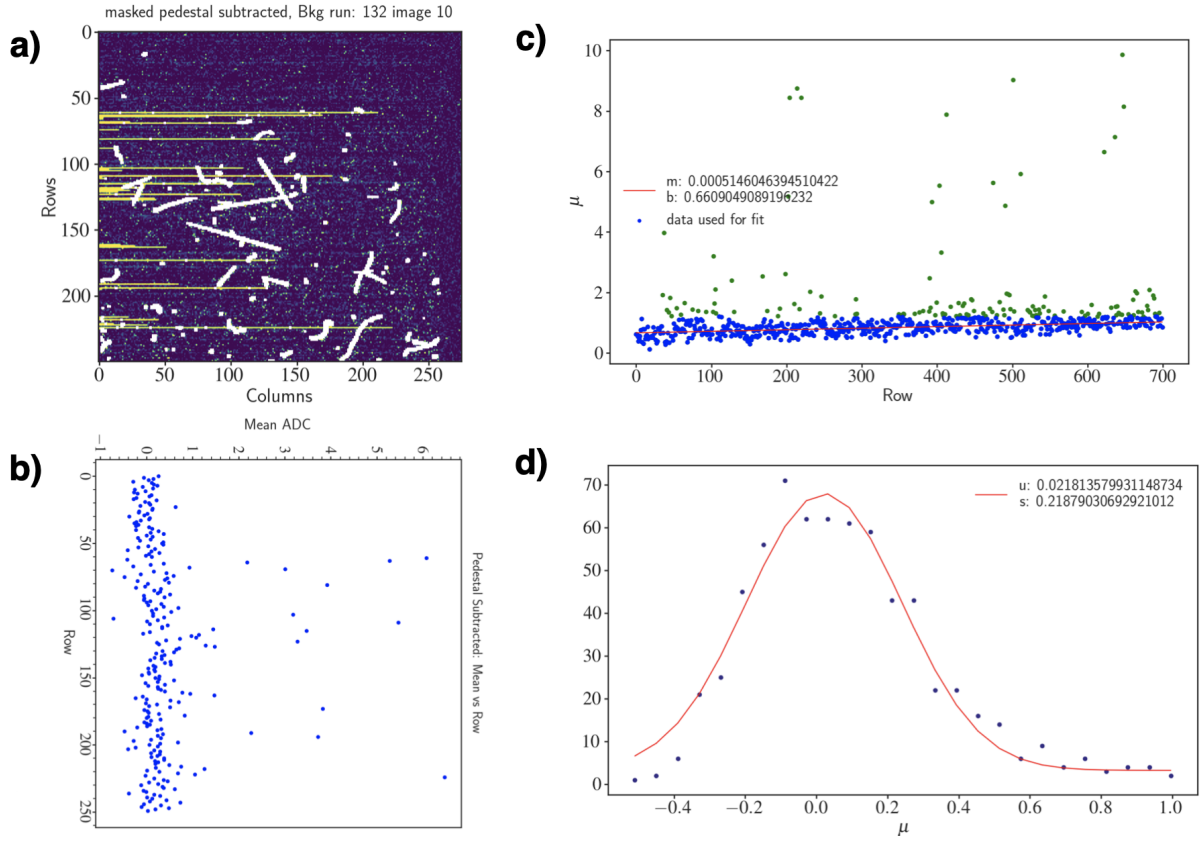

Figure 5.18: a). Example of an image exhibiting skyline shifts. Any pixel with an ADU value above threshold (user specified) is masked and shown in white. b) A scatter plot of the mean ADU value along each row. Rows with a skyline shift have a mean that deviates from the nominal baseline. c) The calculated means are masked (green) and the unmasked (blue) values are used to fit a line. The fit parameters are used to 'correct' for the exposure from the row. d) All unmasked values are histogrammed and fit with a Gaussian distribution.

pixel masking procedure. The next steps are to calculate the mean value of each row, μ_{row}, and then correct for the linear increase in clusters per row. For rows that exhibit skyline shifts, the mean value of that row will be many sigma multiples above the expected mean value of zero for a pedestal subtracted image. Figure 5.18 b) shows the mean value per row of a selected bad image. The final steps to calculate the expected baseline distribution per image are: apply a mask to any μ_{row} with a value above the designated multiple of the mean absolute deviation, N_{MAD} MAD; histogram the unmasked mean values and fit a Gaussian distribution – the mean value should be centered around zero – to extract the nominal spread, σ_0, of the distribution of values; and designate a allowed deviation, N_{max}, from the mean, μ_0. Therefore, any images exhibiting any rows with $\mu_{row} \geq N_{max}\sigma_0$ will be flagged and excluded from the analysis.

The steps outlined above form the general description to detect prominent skyline shifts in an image and Figure 5.18 depicts the general procedure through each step.

5.4.4.3 Skyline Shift Cluster Masking

In addition to the skyline shift flagging algorithm, it was necessary to take additional efforts to eliminate all effects from a skyline shift in an image. While the developed algorithm was effective in flagging most images with skyline shifts, there were some images that exhibited minuscule baseline shifts that were undetectable by the cleaning algorithm. Figure 5.21 provides examples of 1600-skip images that exhibited a skyline shift too small to be detected. However, even though these images were not flagged by the algorithm, the skyline shift signatures remained consistent, thus a more detailed study was carried out.

In order to flag and identify any remaining skyline effects, we must:

i. Determine the mean energy, μ_{SS}, and the energy spread, σ_{SS}, of skyline shift pixels.

ii. Develop an algorithm to isolate skyline shift clusters and determine how many remain.

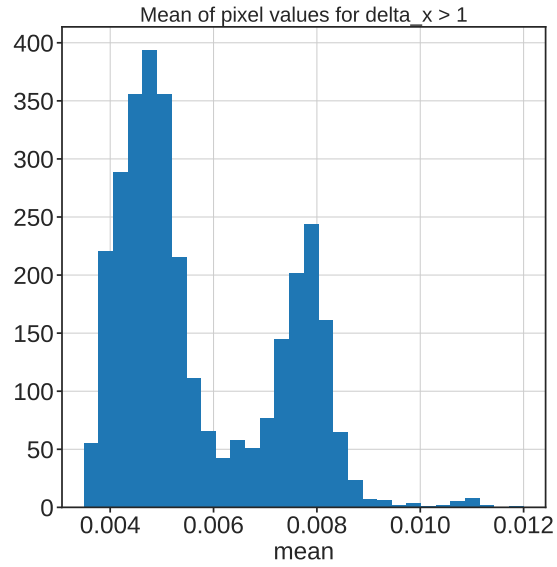

(a) Distribution of mean pixel energies from clusters with x > 1.

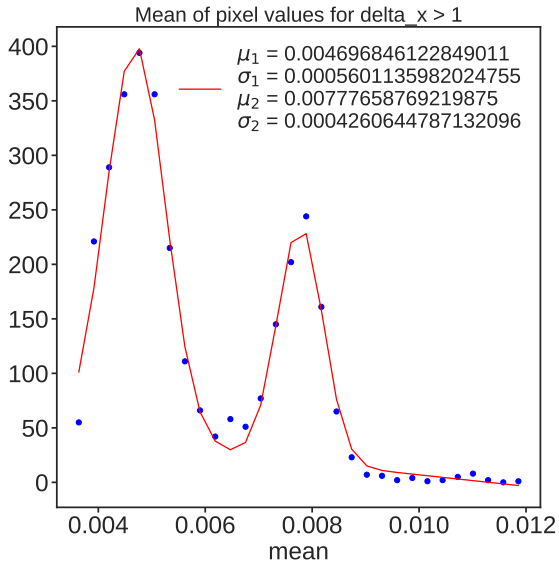

(b) Fit of mean pixel energies.

Figure 5.19: Cluster with at least a width of 2 pixels are queried, and their mean pixel energy is calculated. The distribution outlines two prominent peaks: the lowest-energy peak that corresponds to the clustering parameters threshold energy, and the second peak provides the mean pixel energy from a skyline shift, as well as the spread of available energies.

iii. Develop a method to eliminate any remaining skyline shift clusters from the analysis.

For the first item, we can leverage the fact that a skyline shift cluster develops as a horizontal cluster, in contrast to an expected neutron signal whose generated charge should diffuse normally. Thus, if we query clusters that span several columns (ie. x > 1), calculate the mean pixel energy in a queried cluster, and plot the distribution we should see a signature corresponding to skyline shift events. Figure 5.19 depicts the two prominent peaks that arise from this methodology. The first peak corresponds to the mean energy of a cluster that is composed of one pixel with 1.5 e- of energy and one pixel with 1 e- of energy, or ≈ 4.68 eV$_{ee}$, for 1600-skip data. The second peak corresponds to the distribution of skyline shift cluster pixels. Here, we determine the mean energy of a skyline shift pixel to be, $\mu_{SS} = 7.78$ eV$_{ee}$, and the spread of energies to be, $\sigma_{SS} = 0.43$ eV$_{ee}$; these results are in agreement with the 2

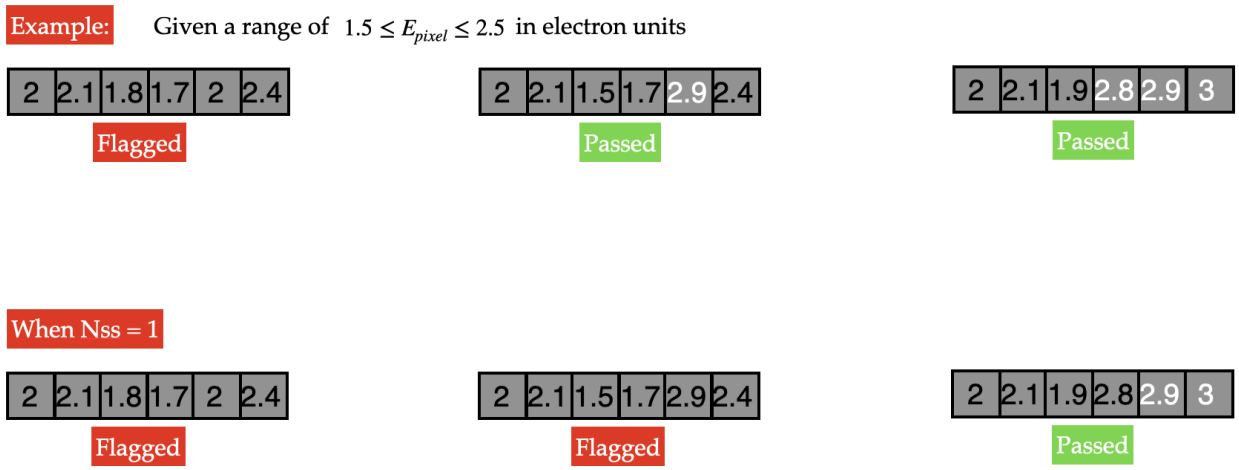

Figure 5.20: An example of clusters that are flagged based on their pixel energies. The top represent a general example, while the bottom has the $N_{SS} = 1$ condition applied — thus, one pixel is allowed to deviate from μ_{SS}.

e- energy estimate for a pixel belonging to a skyline shift cluster.

After determining values for μ_{SS} and σ_{SS} , it was possible to develop an algorithm to detect pixels in a cluster that may be members of a skyline shift cluster. The purpose of this algorithm, is to iterate through all pixels in cluster[2] – within the energy range of interest – and determine whether the pixel energies correspond to a baseline shift. Equation 5.7 provides the base criteria required for a pixel to be considered a member of a skyline shift cluster.

$$\mu_{SS} - (N_\sigma \sigma_{SS}) \leq E_{pixel} \leq \mu_{SS} + (N_\sigma \sigma_{SS}) \tag{5.7}$$

From the equation above, we utilize the previously measured values for μ_{SS} and σ_{SS} to define an acceptable energy range for a skyline shift pixel. Here, N_σ designates the deviations from the mean allowed for a given pixel energy. When scanning a cluster's pixels, it is important for every pixel in the cluster to be consistent with μ_{SS}, otherwise the pixel's charge corresponds to a physical event rather than artificial charge injection. However, the parameter N_{SS}

2. For the algorithm implementation we iterate through all clusters irrespective of topography. This contrasts the previous paragraphs that queried clusters with skyline shift features; the querying was done simply to isolate skyline shift cluster parameters.

was introduced into the algorithm to allow a select amount of pixels to deviate from μ_{SS}. Since skyline shift clusters can be quite large, the chance that a real event, or dark current, occurs in the afflicted active area is non-negligible; thus, some lee-way is introduced to ensure thorough skyline shift cluster tagging. Figure 5.20 provides two pictorial examples of the pixel flagging algorithm. The top example is more generic, and demonstrates that all pixels in a cluster must be within the range indicated by Equation 5.7 to be flagged as a skyline shift cluster, otherwise it will pass as a normal cluster. Furthermore, the figure highlights the necessity for the N_{SS} parameter since in the top example, the middle cluster contains a single pixel that barely escaped the flagging algorithm, but would be otherwise flagged through inspection. Ultimately, through this study, a parameter value of $N_{SS} = 1$ was the optimal configuration to flag skyline shift clusters.

The final step to this study involved analyzing the flagged clusters based on their position in the active region. Figures 5.21 and 5.22 show the pixel positions for every cluster flagged across the respective data set. The frequency maps indicate the skyline shift clusters do originate at the beginning of a row (ie. column 1), and any stray, single pixel cluster is most likely due to dark current. Additionally, from the figures it is evident that the source 1 data sets contain the largest quantity of skyline shift clusters; this is to be expected since any hardware intervention occurred at the tail-end of the source 1 data taking to ensure source 2 data sets were free from noise injections. Furthermore, Figure 5.23 demonstrates that the low-energy injections occurring in the energy spectrum are indeed due to the remaining skyline shift clusters. Therefore, these clusters must be cut from the analysis.

The analysis package WADERs has the function to apply row and column selection cuts during the cluster reconstruction process. This algorithm checks whether the location of pixels in a cluster correspond with a column, or row, designating to be cut; as long as any pixel is in 'contact' with a specified column, or row, the entire cluster will be rejected from the energy spectrum. Therefore, it is possible to apply column selection cuts to remove

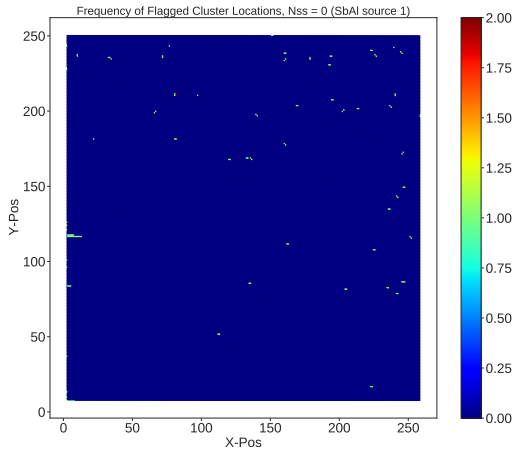

(a) SbAl source 1 flagged cluster pixel positions.

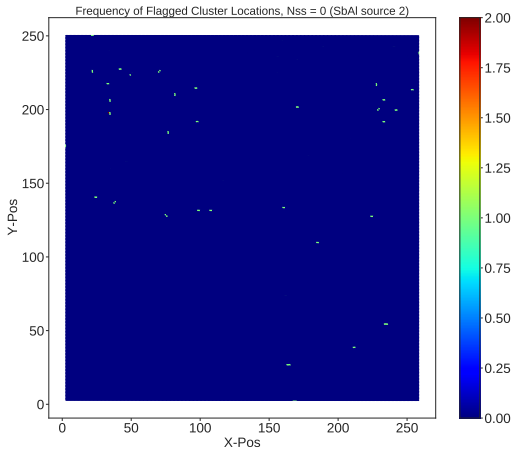

(b) SbAl source 2 flagged cluster pixel positions.

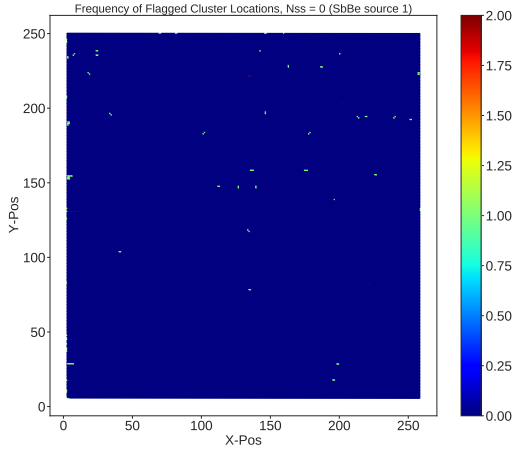

(c) SbBe source 1 flagged cluster pixel positions.

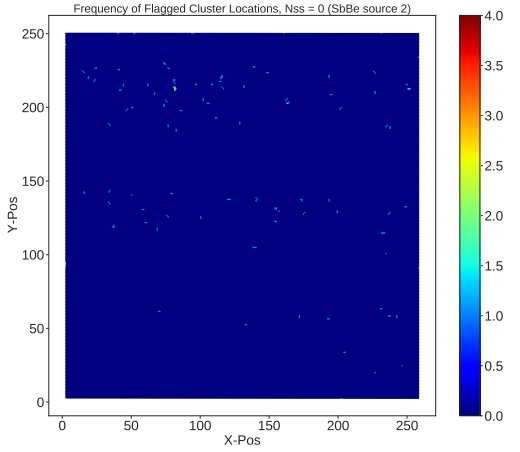

(d) SbBe source 2 flagged cluster pixel positions.

Figure 5.21: Flagged cluster positions per each data type with $N_{SS} = 0$. SbBe corresponds to Neutrons ON, and SbAl corresponds to Neutrons OFF. The frequency maps show the remainder of skyline shift clusters originated at column 0 and spanning a short range towards higher columns. Source 1 data sets have the higher rate of flagged clusters.

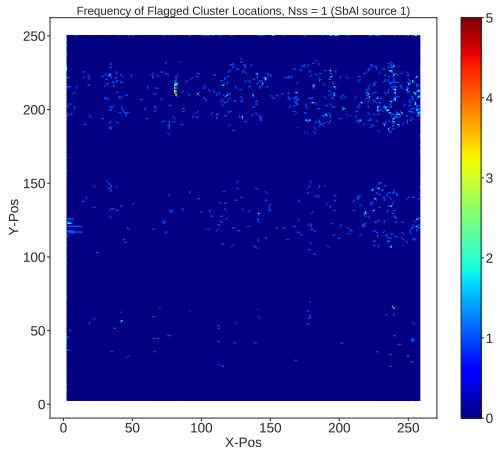

(a) SbAl source 1 flagged cluster pixel positions.

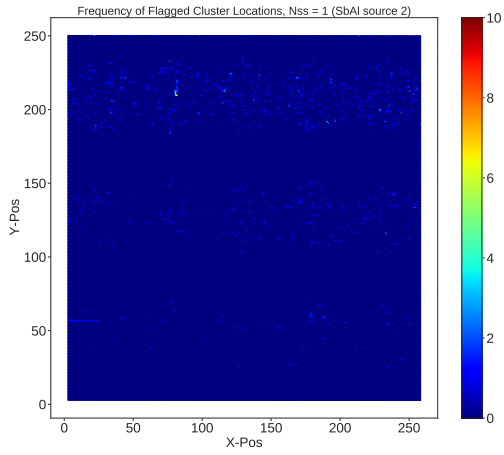

(b) SbAl source 2 flagged cluster pixel positions.

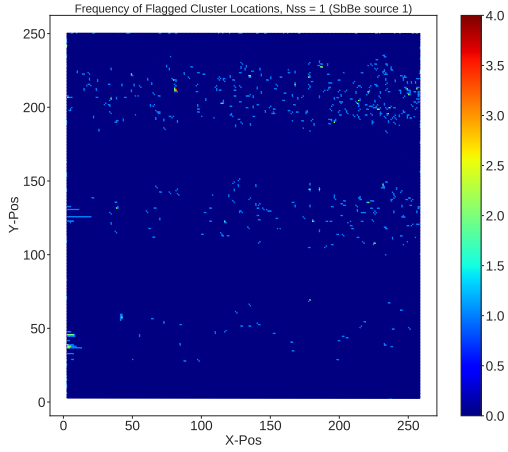

(c) SbBe source 1 flagged cluster pixel positions.

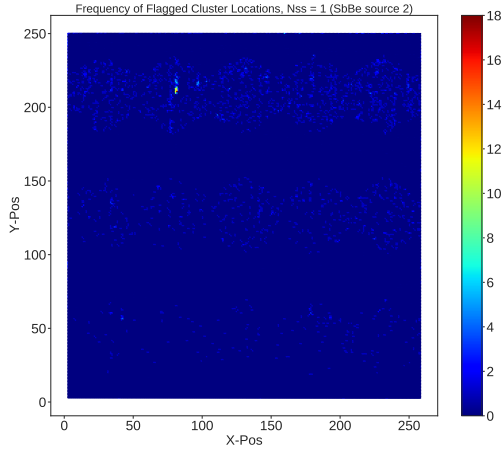

(d) SbBe source 2 flagged cluster pixel positions.

Figure 5.22: Flagged cluster positions per each data type with $N_{SS} = 1$. SbBe corresponds to Neutrons ON, and SbAl corresponds to Neutrons OFF. The frequency maps show the remainder of skyline shift clusters originated at column 0 and spanning a short range towards higher columns. Source 1 data sets have the higher rate of flagged clusters.

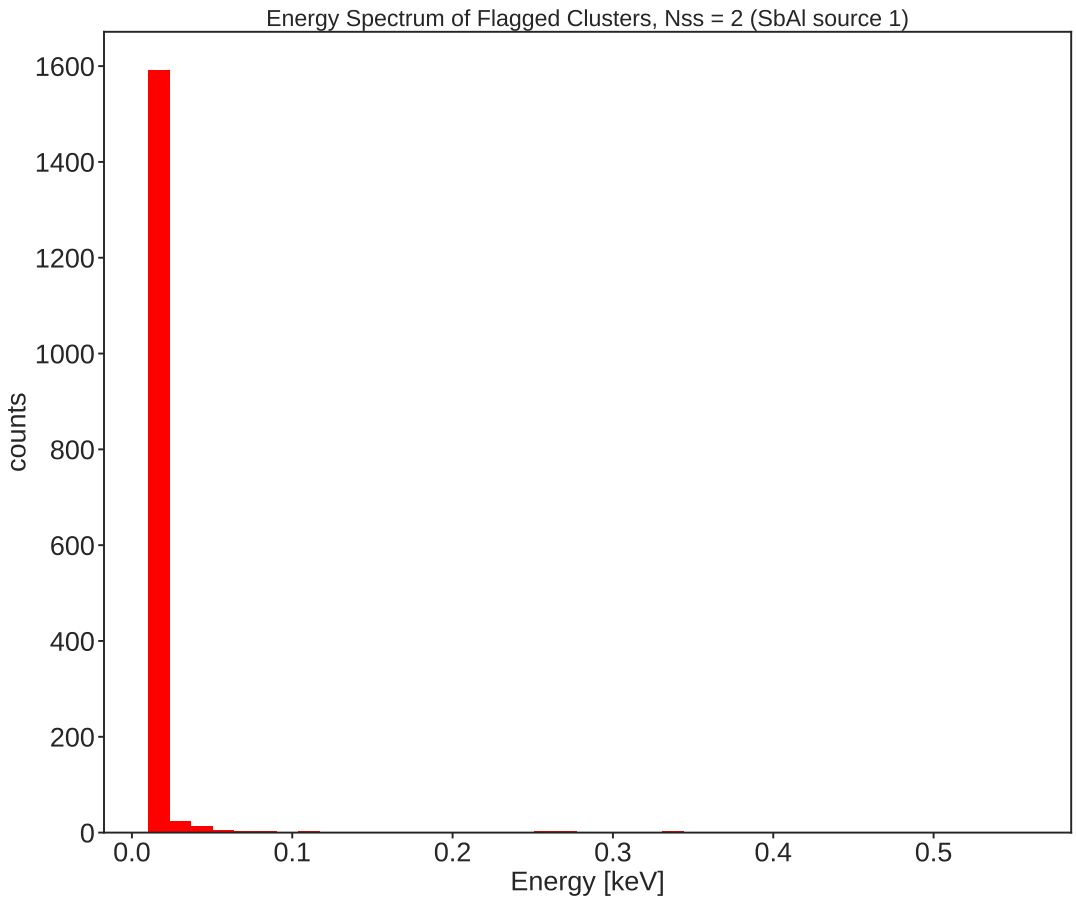

Figure 5.23: For the source 1, neutrons OFF data set, we see a large noise injection at low energies. The distribution of flagged clusters with $N_{SS} = 2$, indicate that the remaining injections will muddle the lowest energy of the reconstructed spectrum.

any remaining clusters from the analysis. Figure 5.24 shows a study with various column cuts applied to the source 1, neutrons OFF data set. Here, any pixel from a cluster that lies on a specified column is rejected from energy spectrum. From the figure it is evident that the largest cluster rejection occurs when columns $x \leq 5$ are selected. This implies that we can optimize skyline shift cluster rejection with minimal loss to the active region. This procedure was repeated for each data configuration, and was consistent amongst them. The final column cuts applied to both 400-skip and 1600-skip data was column≤ 5.

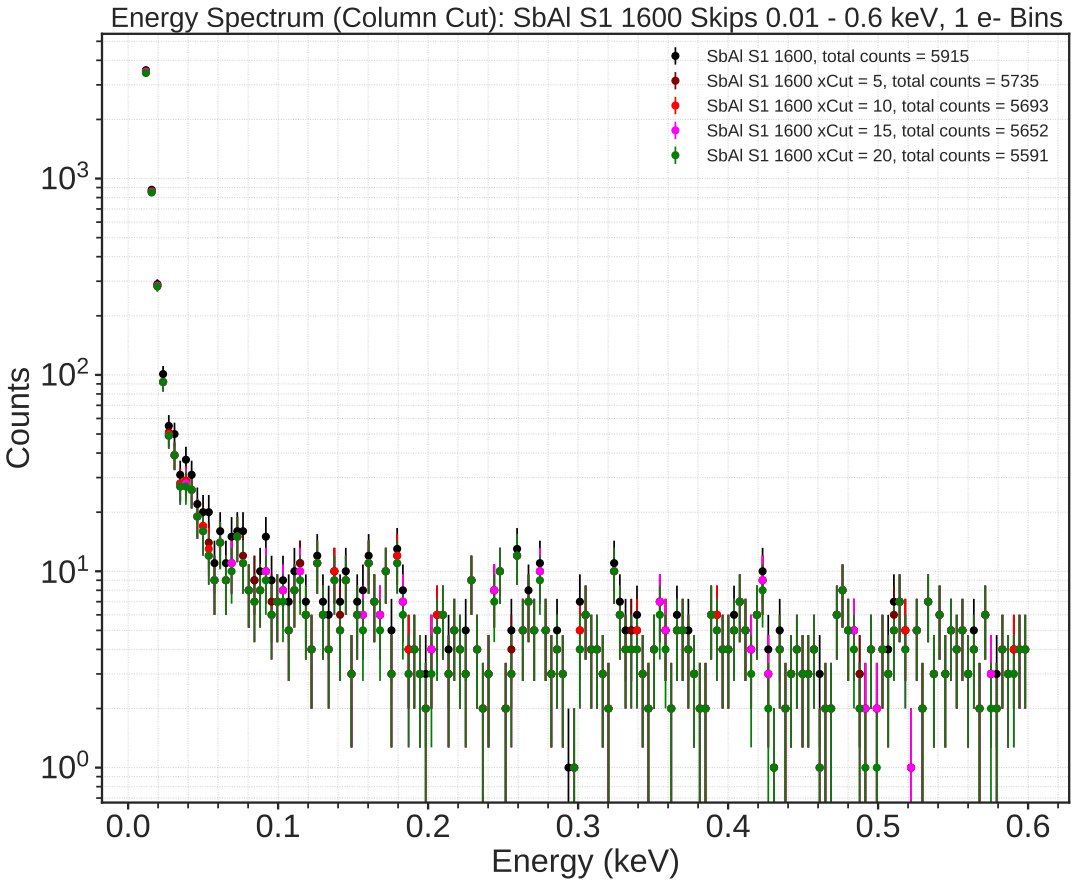

Figure 5.24: Neutrons OFF data with various column cuts applied to reject skyline shift clusters. Any pixel from a cluster that lies on the specified column, or below, is rejected from the energy spectrum.

5.4.4.4 Row Selection Cuts

The final portion of the processing involved located any regions in the active region of the CCD that contained hot rows or columns. As previously mentioned, and can be seen in Figure 5.9, the 400-skip data set had a prominent hot column in the upper left corner that injected an excess of charge to rows above $y \geq 700$; therefore any clusters with pixels in these rows were cut from the analysis. For the 1600-skip data set, Figure 5.25 shows the distribution of clusters – along rows and columns – across all images in the source 2 data

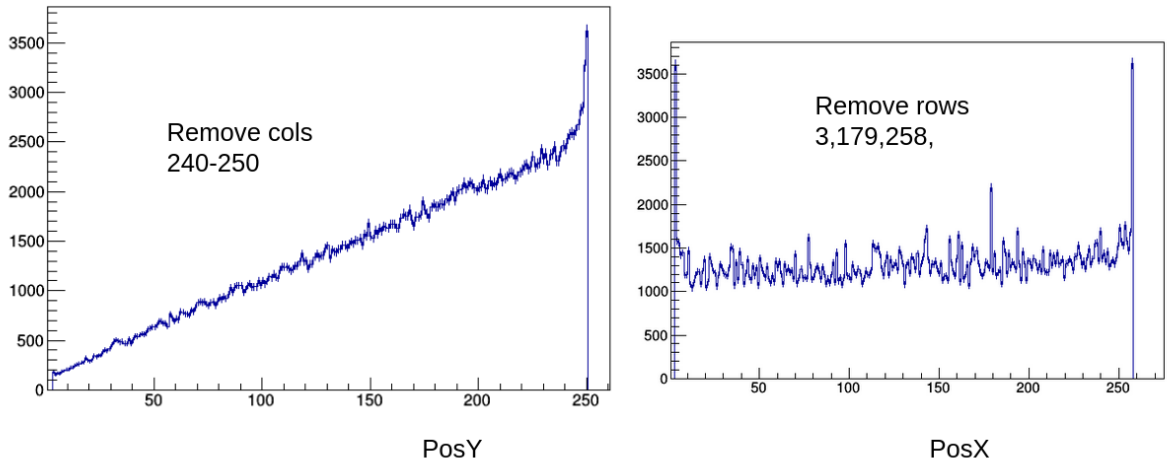

Figure 5.25: Analysis of the cluster positions per row and columns for the 1600-skip data sets.

set. In the row (PosY) distribution, you begin to see a rise inconsistent with the expected linear cluster rate; thus, we removed rows above 240. The inconsistency in this region is likely due to accumulated exposure for these rows; since it takes roughly 20 minutes for the rest of the CCD to be read, the cluster density above row 240 is much higher. Secondly, the column (PosX) distribution indicates the presence of additional hot columns in the active region – notably column 179 and column 258 – therefore clusters with pixels that lied on these columns were also removed from the analysis.

5.4.4.5 Summary

The culmination of all processing steps, studies, and cuts presented in this section were necessary to achieve the best quality data set possible. The following sections will detail the resulting analysis and results with all these processing conditions applied.

5.5 Spectral Analysis

5.5.1 Overview

The results presented in this section, and the following sections, represent the data processed with the parameters and quality cuts described in the previous section. This section will present the reconstructed energy spectrum for both the 400-skip and 1600-skip data sets. Since the basic procedure is the same for both data configurations, figures will be presented in parallel where appropriate. Any differences that occur due to the increased resolution power of the 1600-skip data sets will be discussed at the end of this section.

5.5.2 Average Cluster Rate and Gamma Intensity

Before the neutron signal can be extracted from the accumulated data, the gamma contribution to the data must be assessed. If a significant gamma signal is present in the data, there should be a notable decay in the cluster rate of the neutrons OFF data sets and a Compton profile should be present.

Figure 5.26 shows the average cluster rate per run for source 1, 400-skip data and source 2, 1600-skip data. Each data point represents the average clusters found in the clean images for a given run between 30 and 400 eV_{ee}. In each figure, the data is plotting against the timestamp of the clean image in the respective run; therefore, notable gaps in the figure for a respective data type represent the alternating between neutrons Off and neutrons On configurations. In the figure, the neutrons On data demonstrate a cluster rate decay that corresponds to the decay of the Antimony-124 source. The cluster rate data was fit with an exponential decay model, and the estimated decay constant, λ_0, is found to agree with the measured value, $\lambda_{Sb} = 1.33E-9$, to 97 % with the 400-skip data and 83 % with the 1600-skip data when keeping the background constant at a fixed value to account for the gamma rate. Additionally, the neutrons OFF (gamma-rate) cluster rate data appears to be

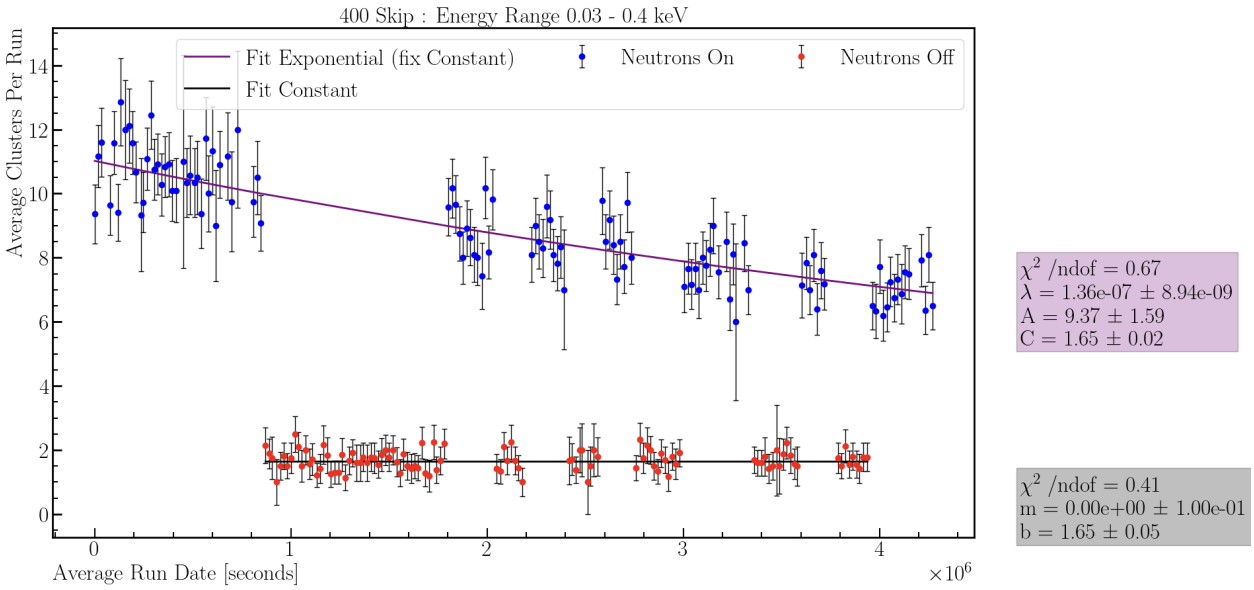

(a) Average cluster rate for the 400-skip data set.

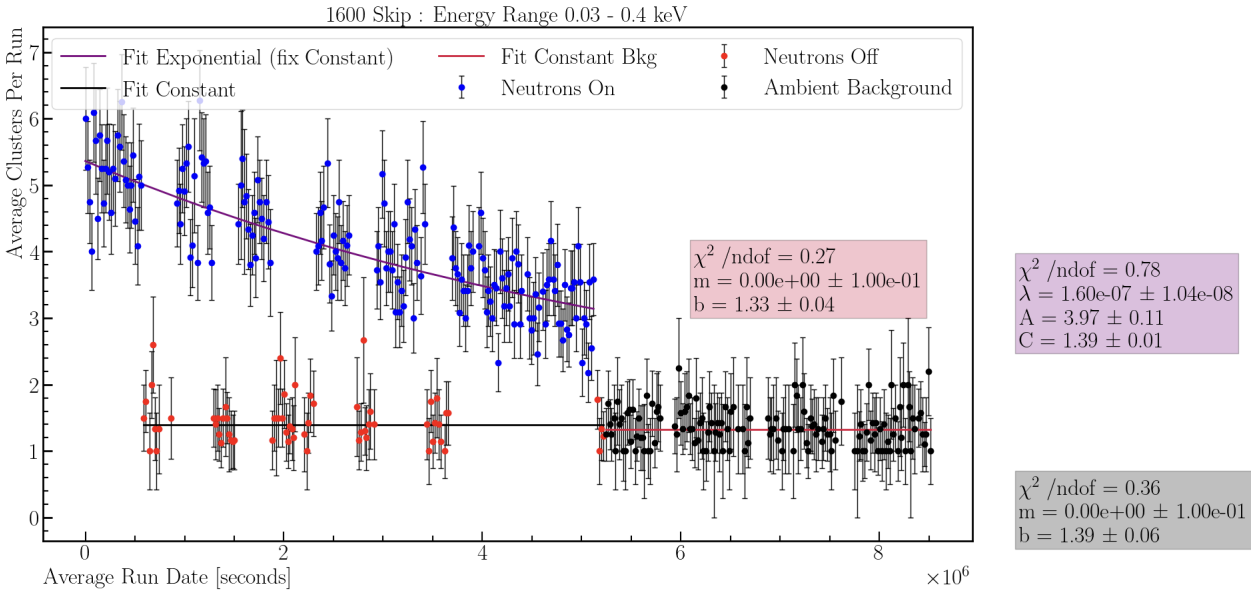

(b) Average cluster rate for the 1600-skip data set.

Figure 5.26: The average cluster rate in a run is calculated and plotted against the timestamp (in seconds) of the last clean image in the respective run. The neutrons ON data demonstrates an appreciable decay that corresponds to the half-life of the Antimony-124 source. The neutrons OFF and ambient background data are in agreement with a uniform average cluster rate.

flat and without a noticeable decay. For both the 400-skip data and the 1600-skip data, the gamma-rate data is fit with a constant value and its result is consistent with zero. For the 1600-skip data, the ambient background cluster rate is also fit with a constant value; the estimated constant is also consistent with zero and in agreement with the gamma-rate value within one sigma. Overall, the cluster rates depicted in 5.26 demonstrate the effectiveness of the lead castle in shielding the detector from the intense gamma-rays emitted from the source and our ability to isolate the neutron signal in the cluster reconstruction.

While the cluster rate for the neutrons OFF data appears to be flat, consistent with zero, and in agreement with the ambient background data. It is worth a check to conduct a spectral subtraction between the neutrons OFF data and the ambient background. Figure 5.27 is the comparison between the two aforementioned data sets, exposure normalized. From the comparison of the two datasets, it is apparent that for most energies the only difference between the two sets are statistical, but for energies $\lesssim$ 20 eV the neutrons OFF data contributes an excess of events. This effect is clearly seen in the residual subplots shown in the figure. The excess events are likely due to the small portion of gammas that were not fully shielded by the lead, and managed to interact in the active silicon. In Figure 5.7, the right plot shows the gamma flux expected in the detector. From this figure we can estimate the gamma related events incident on the detector during the measurement campaign to be quite low — for a simulation of 10^9 1.69 MeV photons, the flux of photons through the CCD are fractional. With such a low predicted flux, we do not expect much signal in the detector. In terms of highly energetic scatters, in the residual spectrum we do not notice any significant features corresponding to gamma events (ie. Compton steps, Compton profile, fluorescence peaks) — rather the spectrum appears flat. These results further strengthen our confidence in the shielding provided by the lead-castle, and we confident that we can conduct a spectral subtraction between the neutrons ON and neutrons OFF data by only considering an accumulated exposure normalization. However, these results also highlight

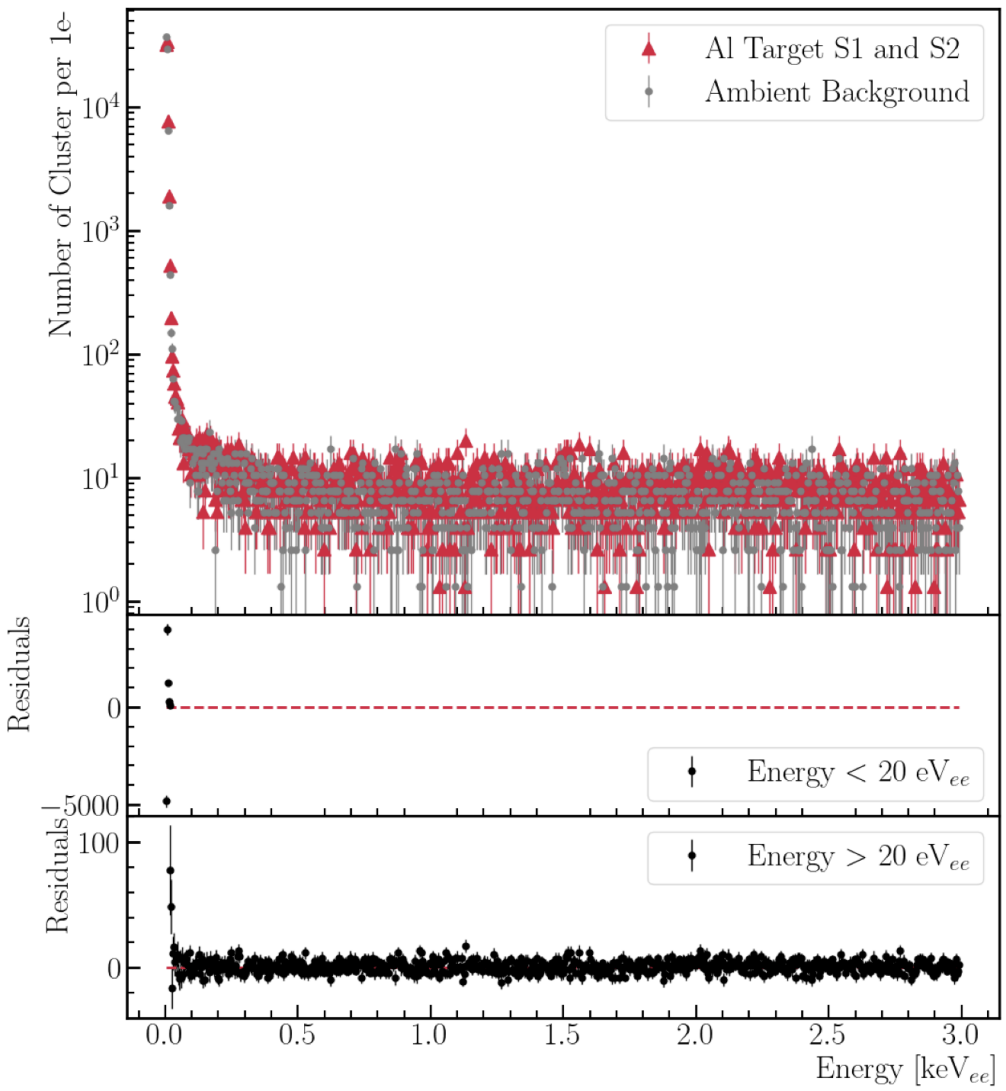

Figure 5.27: Neutrons OFF data compared to the Ambient Background data with 1600-skips. Data sets are exposure normalized. Residual plots at energies below 20 eV, and above 20 eV are shown.

that the ambient background and neutrons OFF data are incompatible at lower energies, thus we cannot combine the ambient background and neutrons OFF data to increase the statistical power of the analysis. Therefore, any spectral analysis in this measurement will consists solely between neutrons ON and neutrons OFF data.

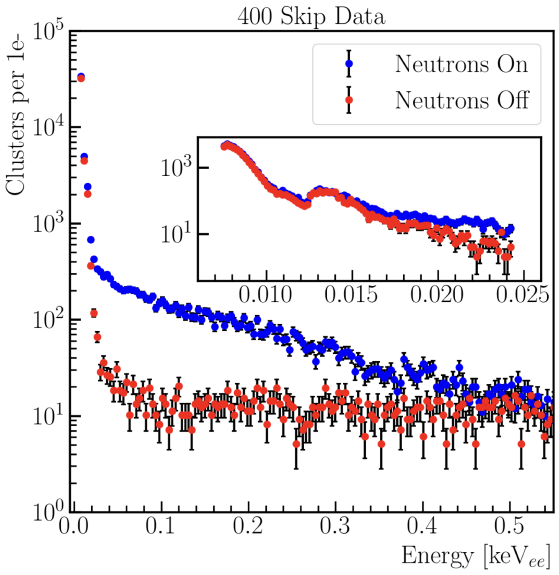

(a) Comparison of 400-skip neutrons ON and neutrons OFF data. Data is exposure normalized.

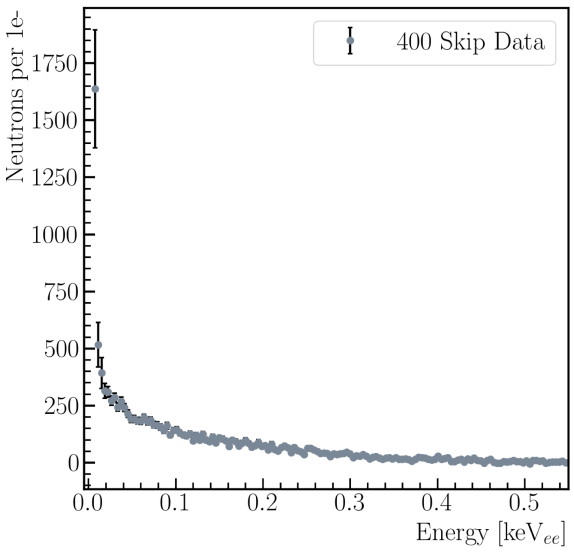

(b) Recovered neutron signal after spectral subtraction.

Figure 5.28: The left figure shows the 400-skip reconstructed energy spectrum per data type. The neutrons OFF data set is exposure-normalized to the neutrons ON data set. Each set is binned to a 3.74 eV bin width, or 1 e-. The right figure shows a direct spectral subtraction between the neutrons ON and neutrons OFF data. The recovered signal is the neutron ionization spectrum.

5.5.3 Standard bin-by-bin Subtraction

For this measurement, we expect a maximum recoil energy of ∼3 keV and can estimate a max ionization signal of ∼ 500 eV$_{ee}$. Therefore, our reconstructed energy spectrum will be shown up to 550 eV$_{ee}$, unless otherwise specified. In addition to performing an independent measurement of the nuclear ionization efficiency in silicon, our goal is to extend the measurement towards lower energies from the 60 eV$_{ee}$ threshold presented by Chavarria et al [18]; thus primary focus will be placed on exploring our measurement's low-energy capabilities.

Figure 5.28 shows the 400-skip reconstructed energy spectrum and the recovered neutron signal. For the energy spectrum, a 3.74 eV, or 1 e-, binning is applied to the main figure ranging from 0 to 550 eV$_{ee}$. The inset in figure (a) represents energies below 25 eV$_{ee}$ down to the detector threshold of 7.48 eV$_{ee}$, or 2 e-; this figure is arbitrarily binned to a much

finer bin-width to assess the energies that we can confidently discriminate between noise and signal. For the 400-skip data, we begin to see a clear excess of events occur near 18 eV_{ee} between the neutrons ON and neutrons OFF data. This region marks the accepted measurement threshold for the 400-skip data. When a direct bin-by-bin subtraction is applied onto the exposure-normalized data sets from subfigure (a), we recover the neutron ionization signal corresponding to the 22.62 keV neutrons emanating from the photoneutron source. Subfigure (b) represents the neutron ionization signal for the 400-skip data; where we see an increasing number of ionization events trending towards lower energies. This feature implies that most ionization events are from low-energy scatters. Furthermore, it's important to note that while the majority of events represented in the neutron signal correspond to the 22.62 keV neutron, there is a small contribution in the spectrum corresponding to the higher energy neutrons, ∼378 keV, originating from the 2.09 MeV gamma. This contribution will be subtracted out from the neutron signal and discussed in a following section.

For the 1600-skip data, we focus on the neutrons originating from the second photoneutron source, but note that while the neutron signal corresponds solely to the second photoneutron source, the neutrons OFF data constitutes both source 1 and source 2 data. Additionally, since there was a shift in the resolution of the detector on August 9, 2022 – as described in section 5.4.3 and shown in Figure 5.15 – the 1600-skip data set needed to be split into before and after August 9, 2022 data sets; therefore the source 1 neutrons OFF data is only represented in the before August 9 data sets since the source 1 data taking ended on July 14, 2022. Figure 5.29 shows the before and after data sets binned to a 1 e- bin-width. The insets in each sub-figure show the low-energy, detector threshold at a fine bin-width to highlight the measurement threshold potential. The clear contrasting feature between the 400-skip and 1600-skip data set is the resolution power observed at a fine bin-width. While the 400-skip data set is able to confidently push the measurement threshold down to ∼18 eV_{ee}, the 1600-skip data is able to fully resolve single electron peaks in the reconstructed

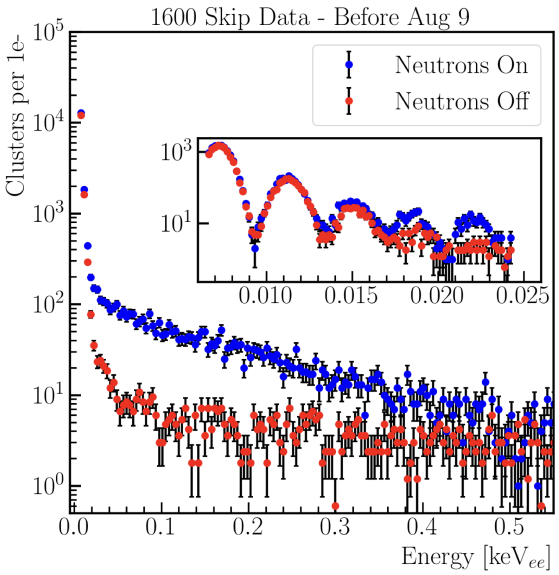

(a) Comparison of 1600-skip neutrons ON and neutrons OFF data before August 9, 2022. Data is exposure normalized.

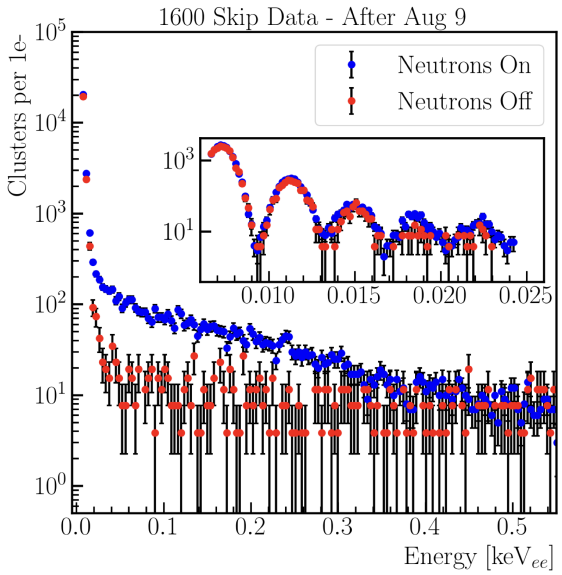

(b) Comparison of 1600-skip neutrons ON and neutrons OFF data after August 9, 2022. Data is exposure normalized.

Figure 5.29: The neutrons ON and neutrons OFF data compared by data-type for the 1600-skip configuration. The *left* figure corresponds to data taken before August 9, 2022, and the *right* figure corresponds to the data taken after. In both figures, the neutrons OFF data is exposure-normalized to the neutrons ON data. Each data set is binned to 1e- for the main figure, the *inset* is binned to an arbitrary-fine bin-width to highlight the single-electron resolution and measurement threshold.

energy spectrum. In the respective inset, the first peak that appears corresponds to a mean energy of ∼7.48 eV$_{ee}$, or 2 e-, and a detector threshold of 5.61 eV$_{ee}$. With the exposure-normalized spectrum, the neutrons ON spectrum appears to be systematically above the neutrons OFF spectrum, implying that the measurement threshold for the 1600-skip data will be the full detector threshold. This claim, and the single electron resolution power of the 1600-skip data will be explored in the following section.

Since the 1600-skip data set had to be split into before and after data sets, the spectral subtraction must also be done in parts. Figure 5.30 shows three sub-figures that detail the results of the analysis. Sub-figure 5.30a is the bin-by-bin subtraction compared between the before and after August 9 data sets without any normalization applied; thus the ob-

served neutron signal corresponds to the raw values of each partition. Sub-figure 5.30b is the neutron-normalized version of the previous figure. For this figure, the total neutrons that were seen by the detector throughout the data set's campaign were calculated. The details of the calculation will be discussed in a following section. After the data sets were neutron-normalized, agreement between the two spectrum's is observed. The third sub-figure represents the direct bin-by-bin summation of the non-normalized values represented in sub-figure 5.30a. Here, we consider the spectrum's contribution in this way because both data sets a solely representative of the second photoneutron source, and are only split due to the resolution shift that happened during data taking. This shift required the two data sets to be reconstructed with their own respective detector resolution as a clustering parameter, but it did not affect the amount of neutrons that were detected during the respective data-taking periods. For the neutron signal represented in sub-figure 5.30c, there is a consistent excess in the neutrons ON data set down to the detector threshold, thus we add confidence that we can push the measurement threshold down to the detector threshold.

5.6 Spectral Fit

5.6.1 Overview

In the previous section, we discussed the 1600-skip data set's ability to resolve single electrons in the reconstructed energy spectrum. When the data is binned to a sub-electron bin-width, the resolved peaks have a Gaussian profile with peaks centered around an integer multiple of the electron-hole pair creation energy, $n\epsilon_{e-h}$. Therefore, we have access to a new analysis channel for the 1600-skip data. The new proposed method for analysis is applying a cumulative Gaussian fit to the data, and retrieving the counts associated with each energy bin. With a cumulative Gaussian fit, we are able to determine the true counts associated with each peak; since an *ith* peak's tail extends towards neighboring energy bins and contributes

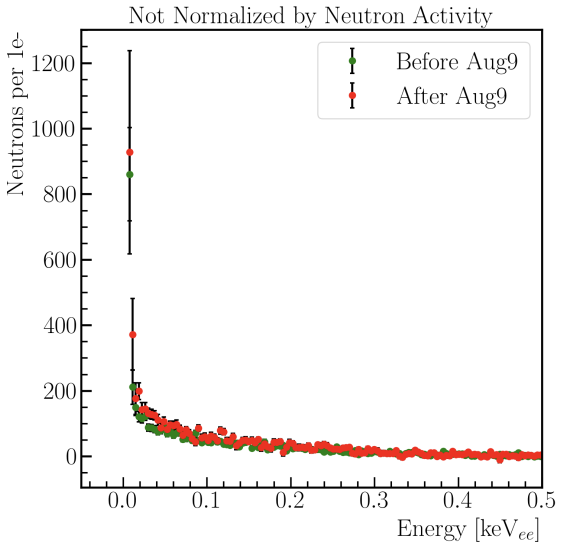

(a) Spectral subtraction comparison between before and after Aug. 9 data sets. No neutron normalization is applied.

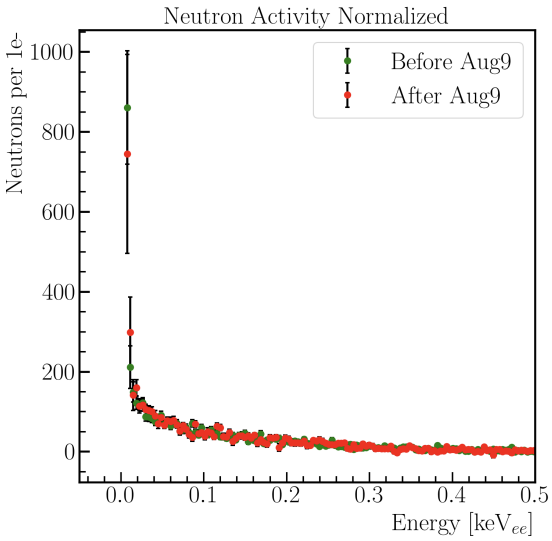

(b) Spectral subtraction comparison between before and after Aug. 9 data sets. Neutron-normalization is applied.

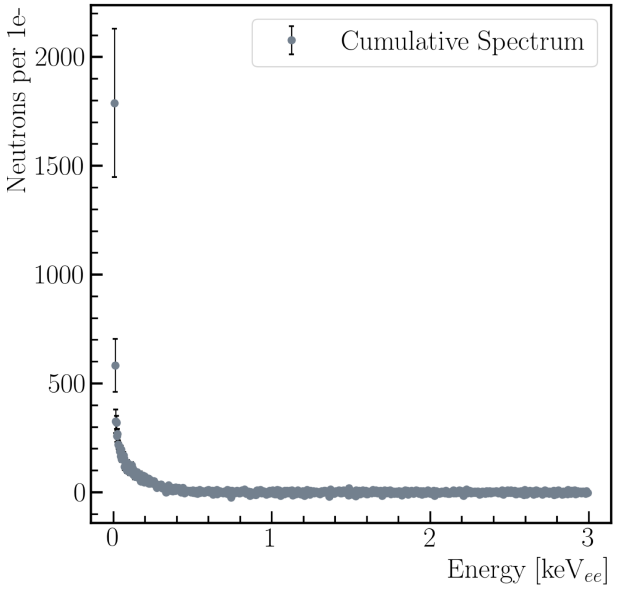

(c) Spectral subtraction of 1600-skip data after summing before and after Aug. 9 data sets.

Figure 5.30: *Top Left*: A comparison of the spectral subtraction between the before and after August 9th data is shown. In this figure, there is no neutron normalization that is applied and the respective counts are the real neutron events in the data. *Top Right*: A comparison of the spectral subtraction between the before and after August 9th data is shown. In this figure, there is a neutron normalization that is applied and the counts are relative to each other. *Bottom*: The figure details the summation of events represented in the *top left* figure. This spectrum is the neutron signal corresponding to the source 2, 1600-skip data.

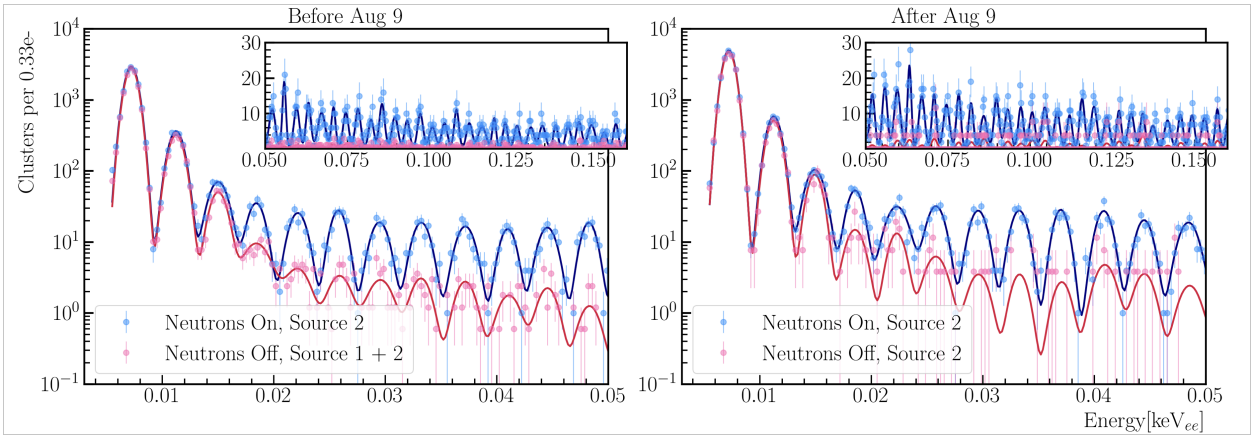

Figure 5.31: This figure shows the Cumulative Gaussian fits on the energy spectrum per each data set for the first 50 peaks. Each data set is binned to 0.33 e-, and single electron resolution is observed for all peaks in neutrons ON data. The neutrons OFF data is able to resolve the first few peaks before counts are greatly diminished. The *left* figure is representative of data taken before August 9th, and neutrons OFF data consists of both source 1 and source 2 data. The *right* figure is only representative of data taken after August 9th.

towards the counts of the neighboring bins.

This section will detail the analysis of the 1600-skip data using a cumulative Gaussian fit, and compare the results against the bin-by-bin subtraction method.

5.6.2 Cumulative Gaussian Fit

In section 5.3.3 we discussed the resolution power of the 1600-skip images to be less that 0.15 e- — as seen in Figure 5.10. Therefore, it is possible to observe the same level of resolution in the energy spectrum of cluster reconstruction. In Figure 5.31 we see the profile of the energy spectrum represented as Gaussian peaks when binned to 0.33 e-, or 1.23 eV$_{ee}$. For the neutrons ON data set, the resolution is sustained well past 150 eV$_{ee}$, but the neutrons OFF data only has clearly defined peaks up to ∼30 eV$_{ee}$. This is to be expected since the neutrons OFF data is meant to represent the background signal during the data campaign, so we do not expect an excess of counts past this energy range.

The left-plot in the figure represents data taken before August 9th, and the corresponding neutrons OFF data contains data from both source 1 and source 2 data sets. The right plot in

the figure represents data taken after August 9th and is limited to source 2 data. For both data partitions, the analysis procedure remained consistent. Given the Gaussian profile of each peak, the spectrum per each data type can be modeled with a sum of Gaussian distributions.

$$y\left(x|\Theta_i\right) = \Sigma z_i e^{-\frac{\left(x-\mu_i\right)^2}{2\sigma_i^2}} \tag{5.8}$$

Here, Equation 5.8 represents the model that is fit to the energy spectrum. Where z_i is the integrated density[3], μ_i is the position of the peak center and the *ith* electron, and σ_i represents the spread of the peak. In this model, we allow the sigma value to be fit per each peak; this decision is made because there is a shift in the sigma as you increase in the number of electrons. Therefore, it is not possible to fit all the peaks with the same sigma value. Since the data was binned and our interest was in the total counts in each peak, an extended binned log-likelihood fit was applied on the data. For the neutrons ON data sets, the peaks are well resolved in the energy range of interest and the fit converges. However, for the neutrons OFF data sets, the statistics are limited and only the first few peaks are well defined and can be fit without fixing any parameters; therefore, for peaks above 25 eV_{ee} the electron peaks are fit by fixing the μ_i and σ_i to the corresponding neutrons ON peak, and only allowing the integrated density as a free parameter. After applying proper guesses, the fits converge and we retrieve the model's free parameters.

From the integrated densities that are retrieved from the fit, we are able to apply a direct subtraction between the neutrons ON and neutrons OFF data. Figure 5.32 presents 3 sub-figures corresponding to this analysis. Sub-figure 5.32a shows the comparison of the fit results corresponding to the before and after data sets. Similar to the figure shown using the bin-by-bin subtraction method, we arrive to the neutron signal for each data set; in this figure, the values are compared without any neutron activity normalization. Each bin's

3. The minimization package used for this analysis is iminuit. Per the iminuit documentation, the integrated density represents the total counts under a distribution. To retrieve the amplitude of the distribution, you must multiply by the data's bin width.

energy position is determined by the μ_i values extracted from the neutrons ON data. Each μ-value corresponds to an electron peak, and therefore is equivalent to a 1 e- bin-width. From Sub-figure 5.32a we can directly sum counts per bin, and arrive to Sub-figure 5.32b. This figure represents the total neutron signal for the source 2 data — as determined from the cumulative Gaussian fit. When compared to the bin-by-bin subtraction, the two spectrum are overlaid and in strong agreement with each other as shown in Sub-figure 5.32c. These results are shown without any neutron activity normalization. Due to the strong agreement, we are confidently able to use the spectral fit as the primary analysis method for the first 50-peaks of the energy spectrum. After the final fit data point, the bin-by-bin subtraction method is respectively stitched onto the spectral fit result in order to construct a complete neutron signal when up to 3 keV_{ee}. This methodology assures that we have precise results at low energy, and that we have enough of a tail to perform a study on the high-energy neutron signal originating from the 378 keV neutron scatters.

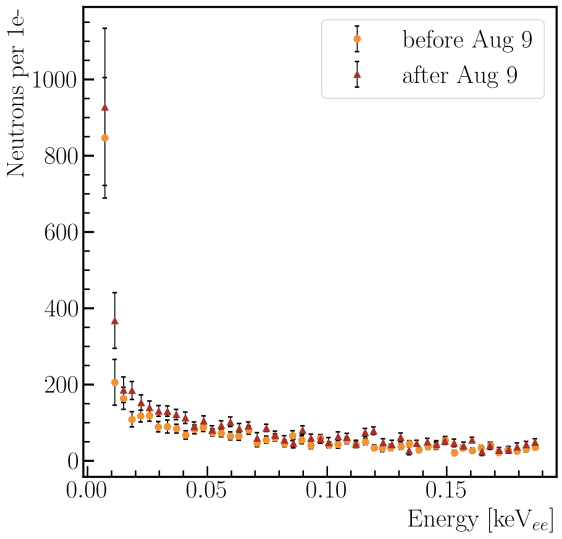

(a) Spectral subtraction comparison between before and after Aug. 9 data sets. No neutron normalization is applied.

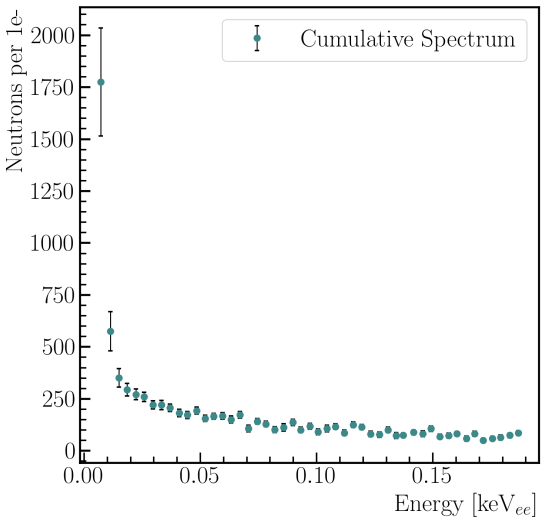

(b) Spectral subtraction of 1600-skip data after summing before and after Aug. 9 data sets.

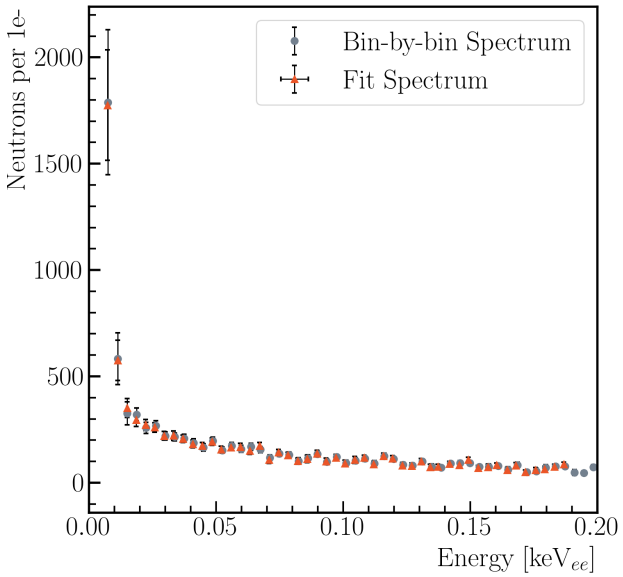

(c) Comparison between fit spectrum and bin-by-bin subtraction.

Figure 5.32: *Top Left*: The figure details the spectral subtraction for the before and after data sets when fitting the first 50 electron peaks with a cumulative distribution. There is no neutron normalization that is applied. Each data point represents the *ith* electron — remembering that the first peak corresponds to 7.48 eV$_{ee}$, or 2 e-. *Top Right*: The figure shows the direct summation of events from the *top left* figure. *Bottom*: The figure details the comparison between the fit subtracted spectrum and the bin-by-bin spectrum without any normalization.

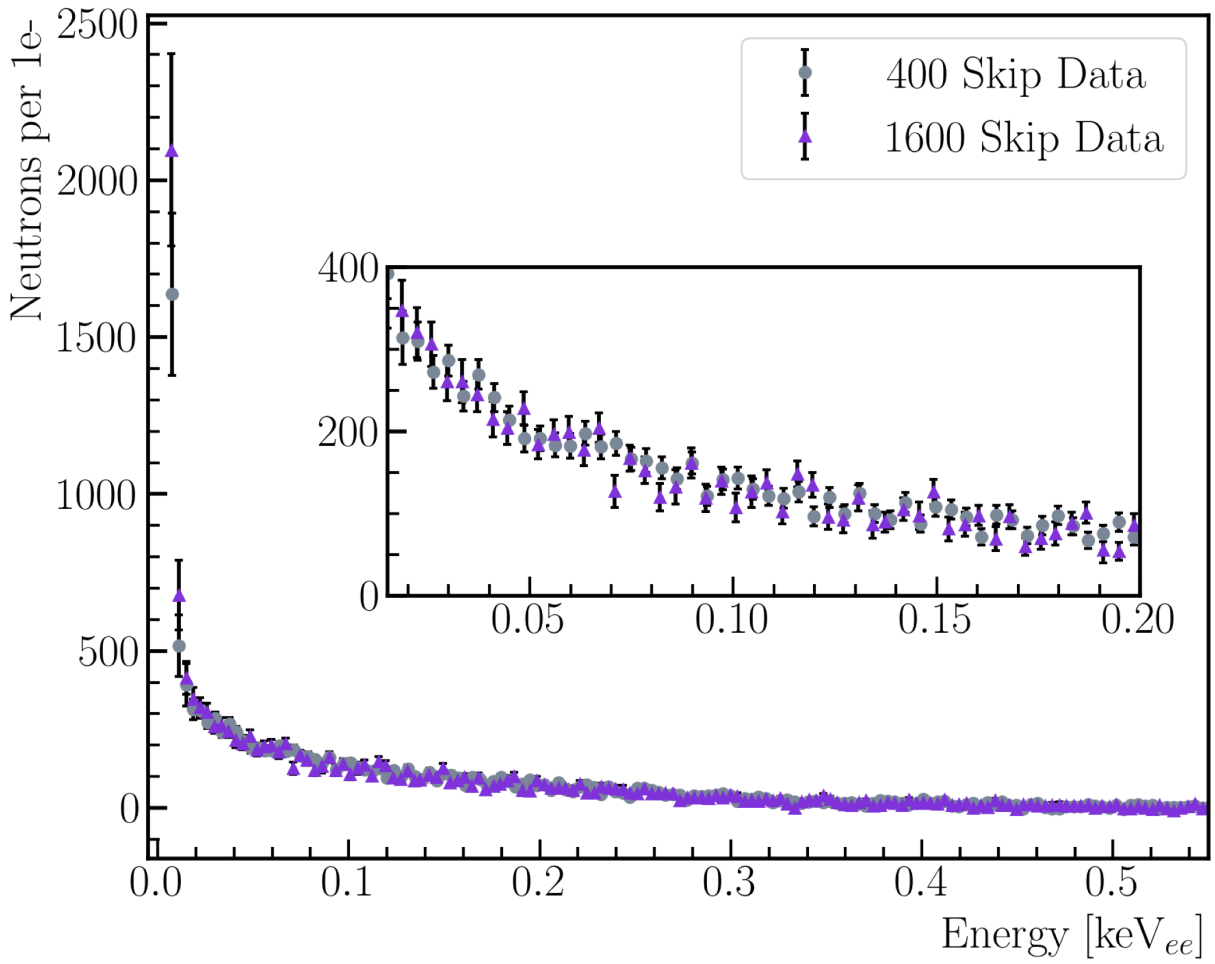

Figure 5.33: This figure compares the neutron signal corresponding to the 400-skip and 1600-skip data sets. The data is normalized to neutron activity and active mass. The inset highlights the excellent agreement between the two data sets within the specified energy range.

5.6.3 400-Skip and 1600-Skip Comparison

Now that the spectral fit and analysis for the 1600-skip data is complete. We can move forward in comparing the neutron signal of the 400-skip and 1600-skip data sets.

Since the experimental setup between both configurations remained consistent throughout the measurement campaign, we do not expect any disagreement between the neutron signal profile. The key differences to expect in each data configuration are limited to the neutron activity, active silicon mass in the detector, and the resolution corresponding to the

data set. The first two points can be corrected by applying a neutron-activity normalization that takes the active mass into account, and the final point merely dictates the measurement threshold of the data configuration.

Figure 5.33 presents the comparison between the 400-skip data and the 1600-skip data. As can be seen in the figure, there is excellent agreement between the two data configurations after normalization. While the first two points agree within an error bar, the respective energy values are outside the measurement threshold of the 400-skip data. However, given the single electron resolution achieved with the 1600-skip data, we are confident that the measurement threshold for the 1600-skip data will span near the full detector threshold. With these results, we present two independent measurements of the neutron signal from our photoneutron sources. We are now ready to move onto the retrieval on the ionization efficiency in silicon.

5.7 Ionization Efficiency

5.7.1 Overview

The main objective of this measurement is to extract the ionization efficiency of silicon from nuclear scatters. As discussed at the beginning of this chapter, when a neutrally charged particle scatters off the nucleus of a silicon atom, only a fraction of the nuclei's recoil energy is converted into ionized charge; the remainder of the imparted energy is dissipated via lattice vibrations in the detector. With Skipper CCDs we can only collect and record the ionized charge generated after the scattering events. To map the ionized charge collected by our detector to a nuclear recoil energy, the neutron flux in the active region of our detector must be known, and the nuclear recoil energy spectrum must be simulated via Monte Carlo methods.

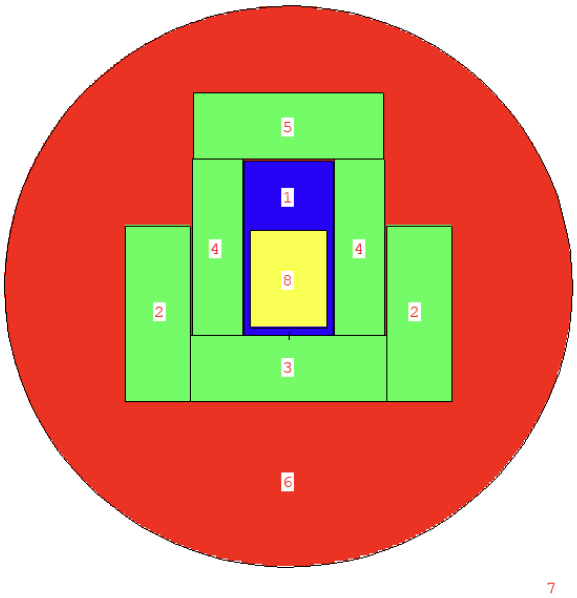

Figure 5.34: MCNPX geometry for ^{9}Be(γ, n)^{8}Be photonuclear reaction. The 3 piece, BeO target (green) encapsulates the polyethylene vial (blue) containing irradiated Antimony pellets. Cell number 8 is the source cell (yellow), and represents the origin of 10^{9} gammas. The boundary encasing the colored regions represents the location of neutron tallies.

5.7.2 Nuclear Recoil Spectrum

With our detector, we only have access to the ionized charge that is generated through a scattering event, and we cannot directly map the nuclear recoil energy (nr) to the electron equivalent energy (ee). However, by employing Monte Carlo transport codes, we can simulate the path a source particle will take to reach our detector and its resulting attenuation after traversing the various materials within its path. In addition, transport codes such as MCNP or GEANT4 rely on the use of nuclear data tables to calculate the likelihood of nuclear scattering or reactions that occur throughout the lifetime of the particle. These processes can either reduce the energy of the inbound neutron, change its direction, or produce secondary radiation that can deposit energy in the detector.

GEANT4 is a standard Monte Carlo transport code used throughout the particle physics community. It is capable of simulating various particle types and radiation environments;

including the creation of any daughter particles for a given particle track. Originally, its use was intended for the modeling of the high-energy reactions that are prevalent at accelerator facilities. Since then, it has been further developed and the toolkit expanded to accommodate a wide range of applications. In contrast, MCNP was developed by Los Alamos National Lab and intended as a tool kit for modeling reactor facilities and nuclear processes. The base MCNP package is only capable of transporting neutrons, electrons, and photons; but it is the most accurate package for simulating low-energy neutron reactions. With the MCNPX and MCNPX-PoliMi extensions, MCNP gains the ability to simulate additional particle types and heavy ions; it is capable of modeling photonuclear reactions; and recording per particle energy depositions and reaction types. The primary Monte Carlo transport code used for this measurement is MCNP and its package extensions when appropriate. However, comparisons with GEANT4 are made when simulating interactions that are readily handled by either simulation package.

To simulate the nuclear recoil energy from neutron scatters in our detector, the first step is to determine the neutron energy spectrum generated from the ^{9}Be(γ, n)^{8}Be photonuclear reaction. Figure 5.3 shows the energy spectrum of neutrons generated via the ^{9}Be(γ, n)^{8}Be reaction. This spectrum was simulated using MCNPX and the updated photonuclear libraries by Alan Robinson for ^{9}Be [64]. This simulation uses a 10^{9} 1.69 MeV gamma source, encapsulated by a polyethylene vial in the Beryllium Oxide target depicted in Figure 5.34. The updated cross-section libraries predict a peak neutron energy of 22.62 keV, with a decreasing tail due to neutron scattering within the source material. The neutron flux originating from the reaction is assumed to be isotropic.

After determining the neutron energy spectrum, it is possible to convert the spectrum into a probability distribution and use it as the source energy definition for subsequent simulations. This methodology ensures that we retain the most accurate representation of

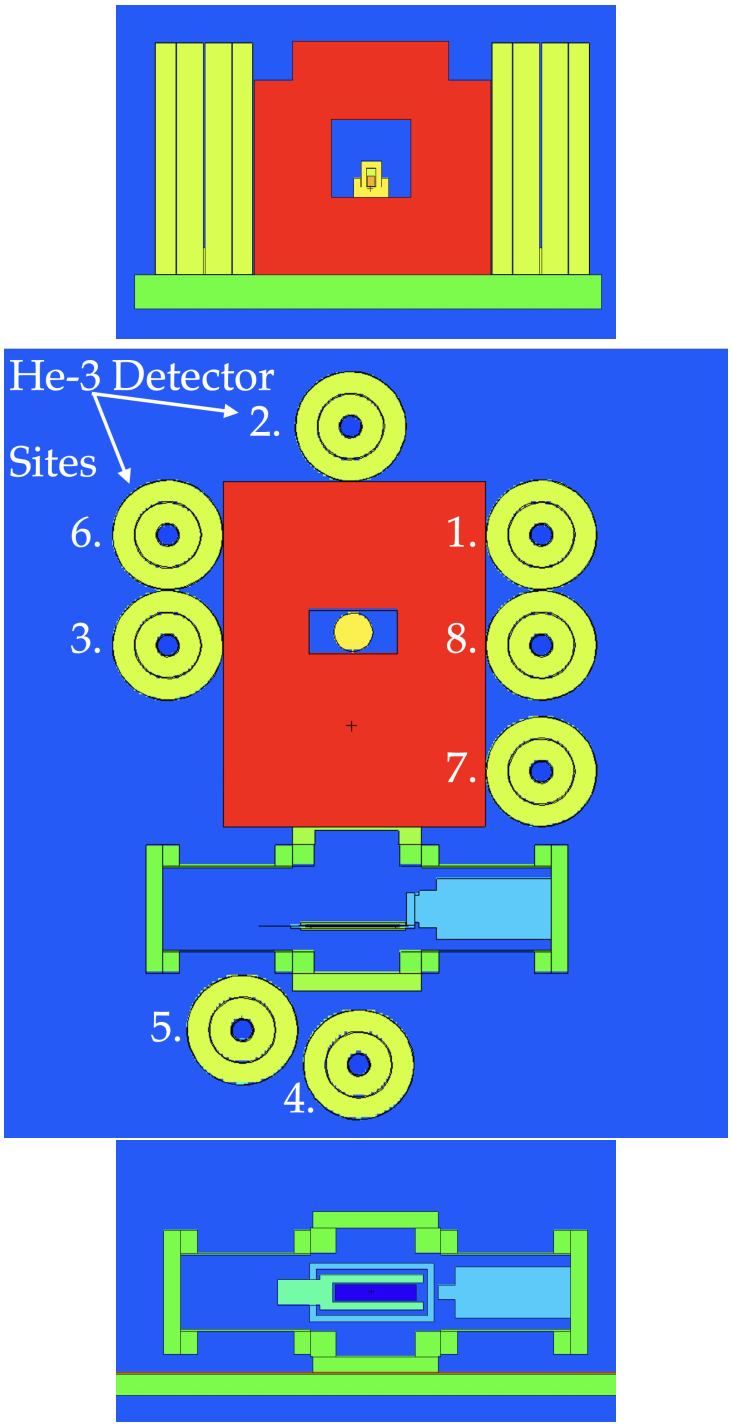

Figure 5.35: *Top*: The source cell and location of BeO target material is shown. *Center*: Top view of experimental setup and geometry. The lead castle (red), chamber components (blue, green), and He-3 detector sites (yellow) are shown. *Bottom*: Chamber and table (green), cryocooler (light blue), and detector (blue) are shown. Yellow cylindrical objects represent locations for the He-3 detector measurements. They are shown for visual purposes only.

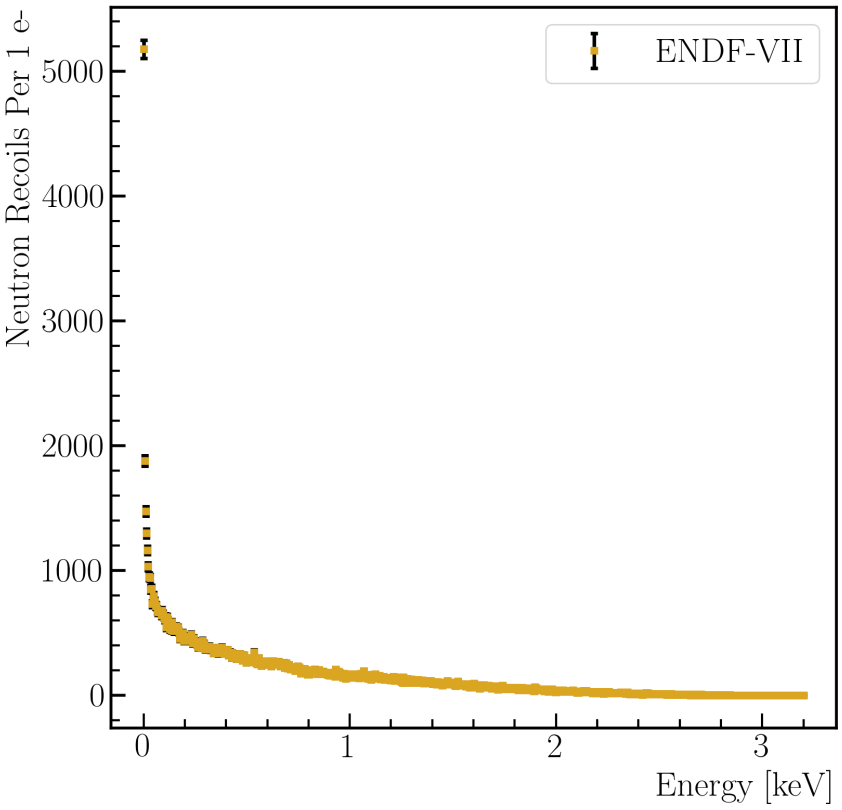

Figure 5.36: The nuclear recoil energy spectrum obtained from the simulation of 10^{10} neutrons in the source cell of our experiment. The ENDF-VII library was chosen as the primary neutron data library for relevant materials.

neutron energies emanating from the source while retaining statistical power[4]. Therefore, the use of this technique requires the removal of the source from the simulation geometry, and instead, the source particles are sampled from a sphere of equal radius in which they were captured. The following will retain the BeO target geometry as a visual reference only.

Now, to simulate the energy deposition in the detector and extract the nuclear recoil energy spectrum the full experimental geometry must be accounted for. Figure 5.35 shows

4. The simulation of the full photonuclear reaction in each simulation requires a maximal input of 10^9 source particles; a fraction of which are then converted into neutrons. This ultimately reduces the statistics of energy depositions in the detector. Alternatively, the choice of generating monochromatic neutrons from the BeO target ignores the potential depositions of the lower energy neutron tail in the detector.

the full MCNPX geometry used for determining the nuclear recoil spectrum, in addition to the location of the He-3 detector measurement sites that will be used to validate the neutron flux around the experiment — this measurement will be discussed later in the Systematic Checks section. The simulation geometry contains the concrete floor from the laboratory, the tables that prop up the lead castle and the chamber, the rubber mat that electrically isolates the chamber from the table, the chamber, the detector and its flex cable, the lead castle, and the source cell. Using MCNPX-PoliMi, 10^{10} neutrons were isotropically sampled from the aforementioned photonuclear probability distribution and propagated through the materials — for this simulation, the primary choice of library for neutron cross-sections was the ENDF-VII library. Any energy depositions in the detector's active volume were recorded, and are summarized in Figure 5.36. The figure extends from 0 to 3 keV; in this energy range, there are far more events with low-energy deposits. The profile of the nuclear recoil spectrum agrees with the profile of the ionization signal recorded by our detector and seen in Figure 5.33.

5.7.2.1 ENDF-VII vs. Oak Ridge National Lab Cross-Section

As previously stated, the primary choice of library for neutron cross-sections is the ENDF-VII library (on applicable isotopes). Figure 5.8 presents a comparison between the ENDF-VIII library – this library is not available for the versions of MCNP used for this experiment – and the Oak Ridge National Lab (ORNL) measured results for the total neutron scattering cross-section[44]. The primary difference between the two libraries is that the Oak Ridge data presents the measured total cross-section for neutrons in silicon, while the ENDF libraries present the evaluated cross-sections. The evaluated cross-section libraries present the best attempt at the extraction of the true cross-section values through the coalescence of experimental data and nuclear models [34]. For this experiment, we are interested in modeling the scattering and ionization of any neutron scatter in our detector; thus our interests lie more

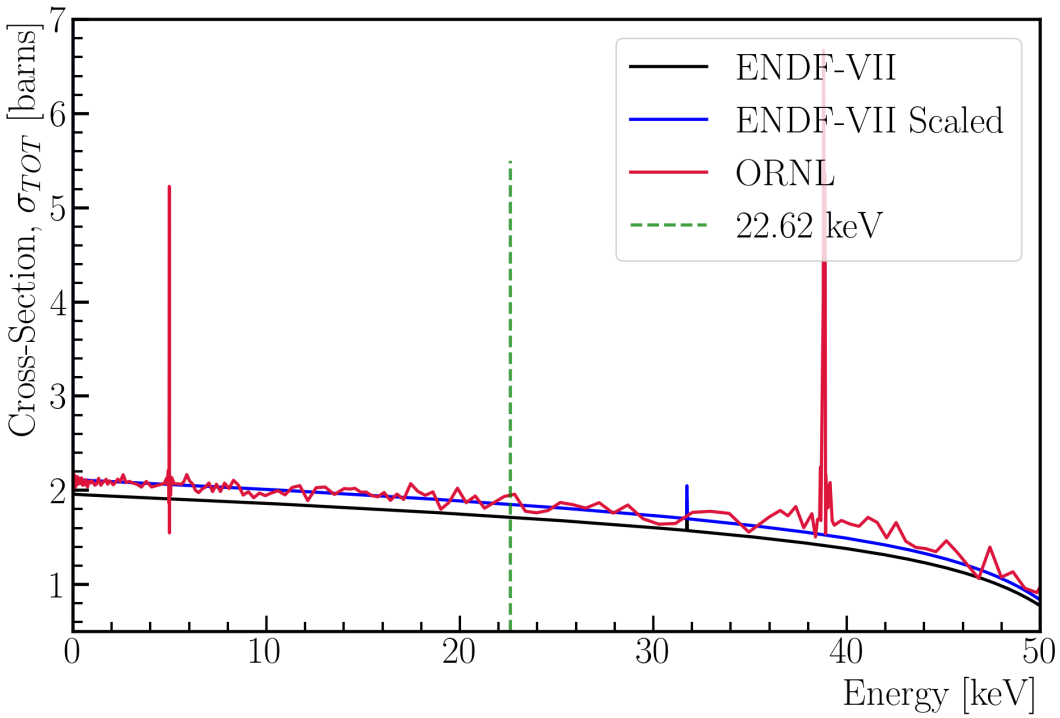

Figure 5.37: Comparison of the total cross-section for neutron scatters in silicon between ENDF-VII, ENDF-VII Scaled, and Oak Ridge National Laboratory. A scale value of 1.08 is used to scale the ENDF-VII library to ORNL data.

closely in the measured data available from Oak Ridge National Laboratory. Since this data set provides us with the measured rate of interaction for neutrons with energies within our region of interest, it is best suited to model the nuclear recoil energy of silicon nuclei after a scattering event. However, MCNP does not explicitly contain the data set as a library option for calculating the scattering cross-section, so a workaround is to scale the available ENDF-VII library to the ORNL data set. Figure 5.37 compares the cross-section from the ENDF-VII library to the measurements from the ORNL data set for neutron scatters in silicon. The inspection of the black and red curves indicates a similar profile. If a scaling of 1.08 is applied to the ENDF-VII library, the ENDF-VII library is in good agreement with the ORNL data set as seen in the figure. Therefore, the nuclear recoil spectrum that is calculated through MCNPX-PoliMi can be scaled by 1.08 as well to represent the results from

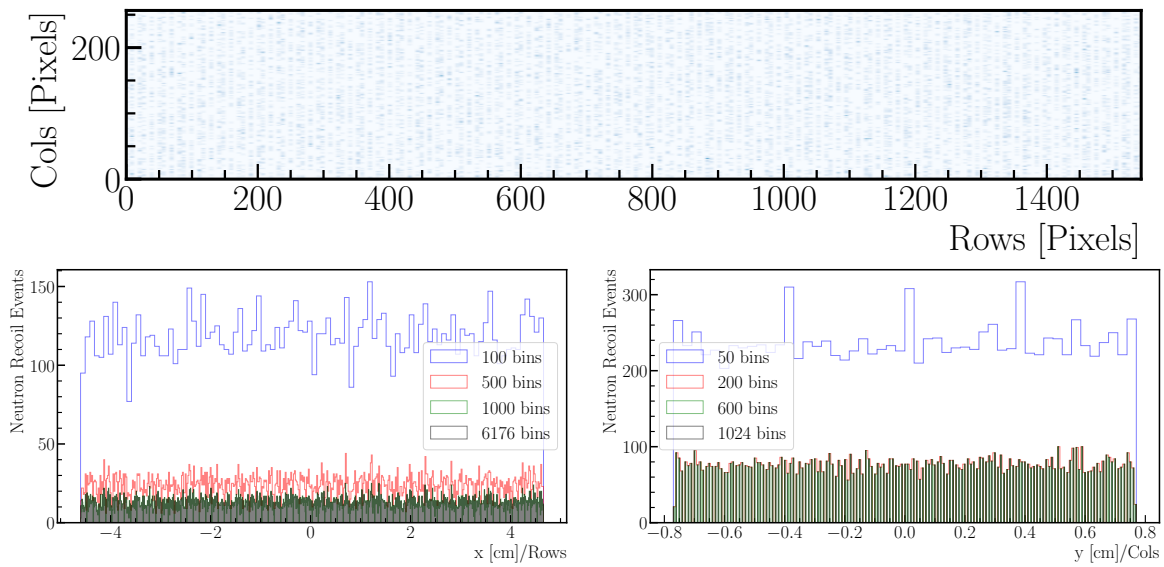

Figure 5.38: *Top*: A hexbin plot showing the distribution of neutron events in the active silicon of the detector. The plot is binned to the pixel size of the detector (6176 × 1024) *Bottom Left*: Distribution of neutrons along the rows of the detector. *Bottom Right*: Distribution of neutrons along the columns of the detector. For the bottom left and right figures, various bin widths are applied to ensure uniformity is not biased.

Oak Ridge National Laboratory. This scaling factor is applied to the final results presented in this chapter.

5.7.2.2 Neutron Distribution In Detector

From the MCNPX-PoliMi output, we can assess how the neutron flux and energy depositions are distributed in the active area of the detector. Figure 5.38 presents 3 figures that show the distribution of neutron depositions in the active area of the detector. In the simulations, the entire active area of the detector was simulated (ie. 6176 × 1024 pixels). This allows us to assess how the inbound neutrons interact in the detector and determine if there are any preferential deposition locations. The top sub-figure shows the distribution of neutrons across the CCD; here, the neutron events are binned to the pixels of the detector. The bottom left and bottom right sub-figures are the corresponding neutron distributions across the rows and columns of the detector, respectfully. Figure 5.38 demonstrates a uniform

neutron distribution across the CCD. This simulation was also conducted with GEANT4, and similar results were observed.

While the overall neutron distribution uniformity across the CCD was determined from the simulations. A final check on the uniformity per the individual image sizes was also done. For the check, we focused on the ratio between the neutron events, N_i, in a sub-area, A_i. If the ratio of events in the sub-area to total events is approximately equal to the ratio of the sub-area to the total area such that,

$$\frac{N_i}{N} \simeq \frac{A_i}{A} \tag{5.9}$$

then the distribution of neutrons within the corresponding image size is said to be uniform. This check was conducted and confirmed to be true for both the 400-skip and 1600-skip configurations. With these checks, we confirm that we do not require any geometric corrections to the calculation of the neutron flux through the CCD per data image.

5.7.3 Calculation of Neutron Flux Throughout Data Taking

Now that we have gathered both the nuclear recoil energy spectrum and the nuclear ionization signal (Figures 5.36 and 5.33 respectively), we must normalize the two distributions to their respective neutron signals. For the nuclear recoil energy spectrum, the calculation is trivial and involves jotting down the simulation parameters. For this simulation, 10^9 neutrons were generated across the whole active silicon mass of 9 cm $\times$ 1.5 cm, or 6176 $\times$ 1024 pixels. However, the data images taken have effective active regions smaller than the simulated geometry, and the neutron flux is variable across each data campaign. Therefore, care must be taken during the neutron normalization calculation.

For this calculation, we are interested in knowing how many neutrons are emitted by

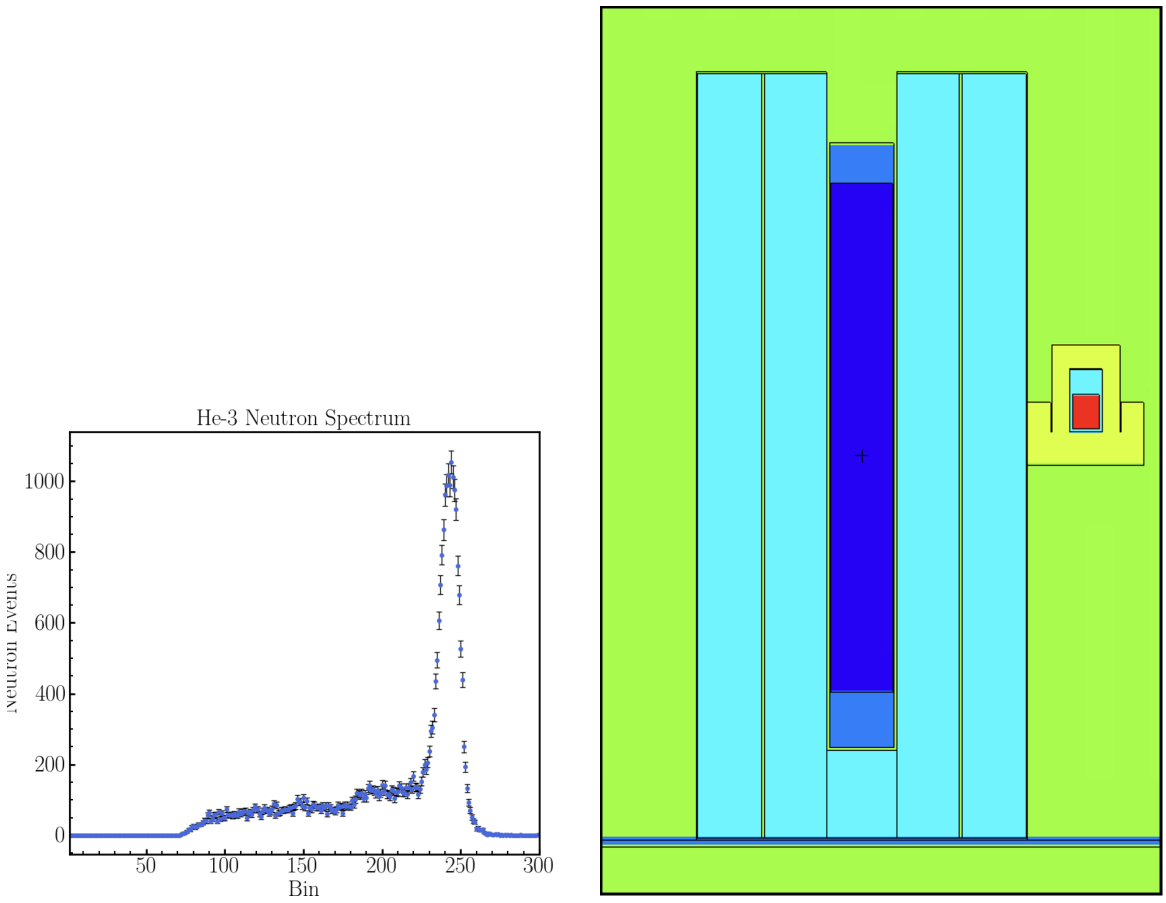

Figure 5.39: *Left*: Data collected from the He-3 Proportional Counter. The signal includes the full energy peak and wall effects. *Right*: MCNP geometry of He-3 Proportional Counter (light-blue, blue, powder-blue) with Beryllium target (yellow, red, light-blue) positioned at a height, against the wall of the detector.

the source during the exposure and readout stage of the detector[5]. Therefore, the first step for the calculation is to measure and determine the neutron activity from the source at the start of the data-taking campaign per each source. This can be accomplished via a dedicated measurement with a Helium-3 proportional counter, or He-3 counter for short. He-3 counters

5. We are interested in counting the neutrons emitted during the data taking, rather than counting the neutrons that scatter off the detector because we cannot directly count neutron scatters in the detector since we only have access to the ionized charge generated after a scattering event. Thus, the counting of neutrons emitted is the best way to relate the neutron activity in the simulations to the experiment.

are sensitive to thermal neutrons, and detection is based on the following reaction,

$$He^3 + n^1(thermal) \rightarrow H^1 + H^3 + Q \tag{5.10}$$

where Q = 764 keV [42]. For our specific detector configuration, the He-3 counter is housed within a thick polyethylene shell and thin cadmium wall to thermalize the inbound neutrons produced via the photonuclear reaction. Once the thermalized neutrons have entered the He-3 counter, the He^3(n, p)H^3 reaction occurs, and a signal proportional to the incident neutrons is produced. The cross-section for the reaction with thermal neutrons is 5330 barns, making the interaction rate large enough that we can expect the signal produced from the reaction to be reflective of the neutron activity from our source [72]. However, we must note that the signal produced only counts the neutrons that undergo the He^3(n, p)H^3 reaction. To extract the source's nominal activity, the experimental setup's efficiency must be simulated. Figure 5.39 shows an example of the neutron signal acquired from our characterization measurement, and the corresponding MCNP simulation geometry. This simulation is meant to extract the geometric efficiency associated with the He^3(n, p)H^3 reaction. Since the total neutron output during the simulation runtime is preset by the user, we can simulate the He^3(n, p)H^3 reaction and determine how many neutrons underwent the reaction based on the experimental geometry. This efficiency value can then be applied to the measured neutron count to extract the neutron rate.

$$N_{yield}(t) = N_{meas}\left[\epsilon_{sim}\right]^{-1}\left[e^{-\frac{ln(2)\cdot t_{days}}{T_{1/2}}}\right]^{-1}\left[t_{meas}\right]^{-1} \tag{5.11}$$

Equation 5.11 details the parameters needed to determine the initial neutron activity, N_{yield}, at the start of the data campaigns. Here, ϵ_{sim} represents the simulation efficiency, N_{meas} represents the total neutrons detected by the He-3 counter, t_{meas} represents the total measurement run-time, and the decay term accounts for the time elapsed from the measurement

date to the start of the data campaign, where $T_{1/2}$ is the half-life for ^{124}Sb. Once the initial neutron yield per source has been calculated, we can begin to calculate the neutrons during an image readout.

An additional method of calculation the initial neutron rate is to instead use the gamma activity of the irradiated source. For source 1, we set up a measurement of the gamma-activity by use of a NaI detector. This measurement, relied on counting the events present in the full-energy deposition peak and calibrating those counts in respect to the geometric efficiency of the experimental setup (similar to the He-3 counter measurement). The geometric efficiency was simulated with MCNP. With knowledge of the geometric efficiency, the 1.69 MeV gamma branching ratio, and the measurement results, we were able to determine the full activity of the source to be 4.08 $\pm$ 0.19 mCi. This result is summarized in Table 5.2. Once the gamma activity is known, the neutron rate is determined by leveraging the results from the photo-nuclear reaction simulation. Since this simulation includes the most recent cross-section for photoneutron production, we can use a simple relation to attain the the expected measured rate.

$$\frac{N_{sim}}{\gamma_{sim}} = \frac{N_{meas}}{\gamma_{meas}} \tag{5.12}$$

Where N corresponds to the neutrons emitted for the simulation of measurement respectively, γ_{sim} corresponds to how many source gammas were generated in the simulation, and γ_{meas} corresponds to how many gammas were measured by the NaI detector. This relationship provides direct access to extract the expected neutron rate from the measured gamma activity. It should be noted that there was only an on-site measurement of the first irradiated antimony source. For the second source, we scaled the result of the first source by the results provided from Oregon State; this scaling factor was determined to be 1.083. This values are also summarized in Table 5.2.

With the initial neutron activity corresponding to each source, the neutron activity can be calculated for each data image based on its readout-start time stamp. For both the

400-skip data set and the 1600-skip data set, there was a consistent swapping between the neutrons ON and neutrons OFF data types. To count the neutrons that contributed to the respective signals, each data image must be individually accounted for. Thus, the time stamp indicating the image's readout-start is key. Per each image, the neutron activity is calculated through the application of the following equation,

$$N_i = N_0 e^{-\frac{\ln(2)(t_0 - t_{start} - t_{exp})}{T_{1/2}}} \tag{5.13}$$

Where N_i is the neutrons associated with a data image, N_0 is the neutron activity at the start of the data-taking campaign, t_0 is the date associated with N_0, t_{start} is the readout-start time, and t_{exp} is the exposure time[6].

After the neutron activity per image, N_i, is calculated. The next step is to create a matrix detailing the accumulated exposure of each pixel. Due to the delay in readout a subsequent pixel encounters, each pixel is continuously exposed and subject to potential charge generation from neutron scatters. The accumulated exposure of the *ith* pixel[7] is determined by the following relation,

$$t_i = \begin{cases} t_{exp} & i = 1 \\ t_{i-1} + \frac{t_{readout}}{t_{row} t_{col}} & i \geq 2 \end{cases} \tag{5.14}$$

where i is the pixel index starting at 1, t_i is the accumulated exposure of each pixel, $t_{readout}$ is the total readout time, t_{row} is the time to read out one row, and t_{col} is the time to read out 1 column. This method accounts for the neutron flux received by all pixels in the CCD during the exposure stage, and the accumulated exposure experienced by each pixel as it

6. The first stage of data taking always involves a 3-second exposure, where the CCD pixels are held in stasis and allowed to accumulate charge. At the end of the exposure stage, the first pixel enters the readout stage, and the image readout begins.

7. While a matrix is generally referenced in terms of ij indices, my reference to the pixel elements is restricted to an ith index since I am referencing the order that a pixel is read out. Generally, this involves moving an entire row (j) onto the serial register and reading the first pixel in the corresponding column (i).

awaits readout. The first entry in the matrix will always have a value of 3 seconds, and the final entry will have a value $\left(t_{readout} - \frac{t_{readout}}{t_{row}t_{col}}\right)$ that reflects the time required for that final pixel to be read out. After creating this accumulated exposure matrix, the next step in the calculation is to convert the accumulated exposure matrix into a decay matrix. To convert the matrix, we simply apply the decay factor across each element of the matrix and integrate it.

$$\int_0^{t_i} N_0 e^{-\lambda t} dt = N_0 \left[\frac{1}{\lambda} - \frac{e^{-\lambda t_i}}{\lambda}\right] \tag{5.15}$$

In the above equation, N_0 is the neutron activity associated with the data image, λ is the decay constant for the ^{124}Sb isotope, t_i is the accumulated exposure of the ith pixel, and the integral is evaluated from 0 – the exposure matrix is relative to the neutron activity of a given image – to t_i. The resultant decay matrix defines how many neutrons each pixel *saw* emitted before it was read out.

Now, we can apply the same pixel-masking to the corresponding elements of the decay matrix as was applied to the images during the cluster reconstruction process. As an example, Figure 5.40 represents the image mask applied to the 1600-skip data images during the cluster reconstruction process. The blue regions correspond to the columns and rows that were found to be hot regions of the CCD, the box cuts that are implemented to mask hot pixels, or the overscan region between columns 260 to 275. These selected regions must also be removed from the neutron calculation since any neutron events originating in these regions are not considered in the neutron signal. After the application of the image mask onto the decay matrix, we sum all the neutrons that are seen by each of the unmasked pixels together to acquire the effective total neutrons seen, N_{seen}. This value is then converted to a neutrons $\cdot$ grams value by the following relation,

$$neutrons \cdot grams = N_{seen} \cdot \rho_{Si} \cdot x_{pixel} \cdot y_{pixel} \cdot z_{pixel} \cdot 16 \tag{5.16}$$

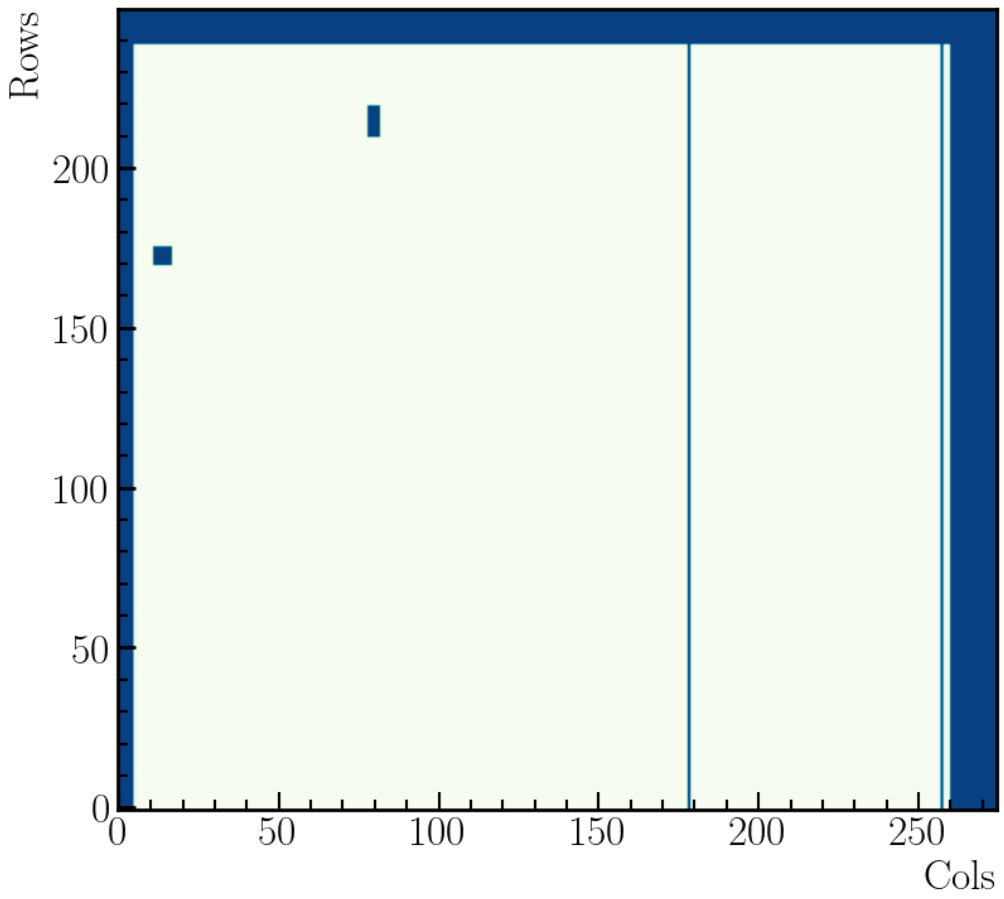

Figure 5.40: The image mask that is applied to the 1600-skip data images. The blue regions represent the pixels that are excluded during the cluster reconstruction, and any cluster that has an associated pixel in the region is also excluded. Additionally, columns 260-275 represent the overscan region of the image.

where the final value represents the neutron exposure for the total active silicon mass in an image. Here, N_{seen} is the total neutrons seen by the unmasked pixels in the CCD, ρ_{Si} is the density of silicon, x_{pixel} is the width of a pixel, y_{pixel} is the length of a pixel, z_{pixel} is the depth of a pixel or the CCD thickness, and the factor of 16 accounts for the 4×4 binning that is applied during the readout of an image.

After calculating the neutron exposure for all images in a data set, the value can be used to normalize the neutron signals acquired from the 400-skip and 1600-skip data sets (as seen in Figures 5.30b and 5.33), or be used to normalize between the neutron data and the nuclear recoil energy spectrum acquired from the Monte Carlo simulations.

5.7.4 Data Preparation

Now, having determined the normalization value between the simulations and the neutron data, we are almost ready to calculate the corresponding ionization yield in silicon. However, a few corrections to the data must first be accounted for.

5.7.4.1 Cluster Reconstruction and Characterization Efficiency

When a neutron scatters off of a silicon nuclei and deposits enough energy in the detector, ionized charge drifts and diffuses towards the pixel where the total charge is collected and stored until readout. The pixels that collect the charge, constitute the cluster corresponding to the scattering event. However, there is no guarantee that another environmental particle may scatter in a nearby region and generate charge that masks the presence of the low-energy neutron scatter. The likelihood of these types of events occupying a space in an image increases as a function of row. This is to be expected, since pixels in later rows are exposed for longer periods, compared to pixels in rows closer to the readout amplifier. Thus, motivating the need to simulate the cluster reconstruction efficiency in an image.

The cluster reconstruction efficiency, in general, describes the ability of our cluster reconstruction algorithm to isolate clusters that solely correspond to a neutron scattering event. To determine this energy-dependent efficiency factor, we can conduct a simulation that samples neutron cluster energies from the measured neutron signal and diffuses the respective charge in the detector according to operating conditions to generate a pixel cluster in an image. In these studies, we use neutrons OFF data images, to include any cluster contributions that an incident gamma could have in the detector during the readout stage. Figure 5.41 shows the reconstruction efficiency for the main processing configuration of the 1600-skip data set. In this figure, we notice that clusters $\lesssim$ 1.2 keV_{ee} are consistently reconstructed at $\sim$89 percent efficiency until the lowest energies of $\sim$5 electrons (18.7 eV). At these lowest energies, there is an instability in the efficiency for reconstructing low-energy clusters. This

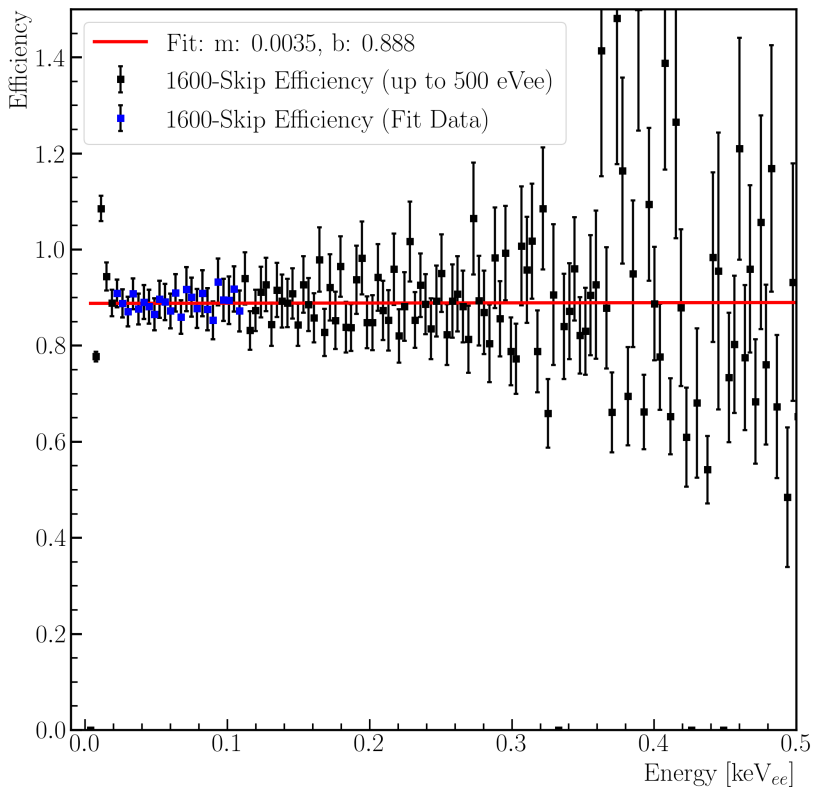

Figure 5.41: The cluster reconstruction efficiency calculation. Neutron energies are sampled from the measured neutron signal, to ultimately generate charge clusters in a neutrons OFF image.

is not a surprise. At the 2, 3, and 4 electron cluster energies, a cluster is likely to be a single pixel cluster, and if the scattering event occurred in a region that is read out later during the readout stage, it has a much greater likelihood of being 'absorbed' by a particle cluster that has a much higher energy deposition. Additionally, these low-energy clusters are more susceptible to the choice of clustering threshold, and intrinsic detector noise has a greater chance of affecting the reconstruction of these low-energy events. Taking a focused look at the 2 e- and 3 e- cluster efficiency, we notice two peculiarities: the 2 e- cluster has a substantial drop in reconstruction efficiency ($\sim$78 percent) and the 3 e- clusters are being over-constructed. These two effects are coupled. Given that the 1600-skip data is being

processed with a 1 e- cluster threshold and 1.5 e- cluster seed, there is a higher chance for a potential 2 e- cluster to be affected by dark current. This means that a 2 e- neutron event can become reconstructed as a 3 e- cluster event when it absorbs a nearby noise-generated charge carrier —hence the overestimation. Ultimately, this result implies the unreliability of the 2 e- cluster and shifts our measurement threshold to a 3 e- threshold (11.22 eV) since the overestimation of the 3 e- can be corrected. Now, for energies greater than $\gtrsim$ 1.2 keV$_{ee}$ we notice a large dispersion in efficiency. This effect is due to the lower neutron counts that occur at these energies. Since we are sampling from the neutron data, high energies will be sampled less frequently when compared to the lower energies of the spectrum. However, at such high energies, the choice of detector threshold no longer plays a significant role in the cluster's reconstruction, rather the main contribution to the reconstruction efficiency is the population of other particle tracks in the image. As previously mentioned, the image is more densely populated by particle tracks in the later rows, the neutron cluster reconstruction efficiency will decrease in this region. Since all cluster energies are equally susceptible to this effect, we can fit a line starting from the 5 e- point, and estimate the efficiency at all energies above 5 e- (18.7 eV) to be the intercept of the line, b, and the error to the fit is assigned as the efficiency error. The result of this fit is seen in Figure 5.41. Ultimately, determining the cluster reconstruction efficiency in our measurement is critical since this factor is a necessary correction to the neutron events in a given energy bin. As we will discuss at the end of this chapter, the counts in an energy bin will directly map to a nuclear recoil energy; this is exactly the value that we want to determine.

Another necessary and adjacent check to the cluster reconstruction efficiency is the cluster characterization efficiency. This simulation determines how accurately the cluster reconstruction algorithm can determine the energy corresponding to a neutron ionization event. Figure 5.42 shows the cluster characterization efficiency for the main set of reconstruction parameters of the 1600-Skip data images. In this figure, we notice a strong agreement between the

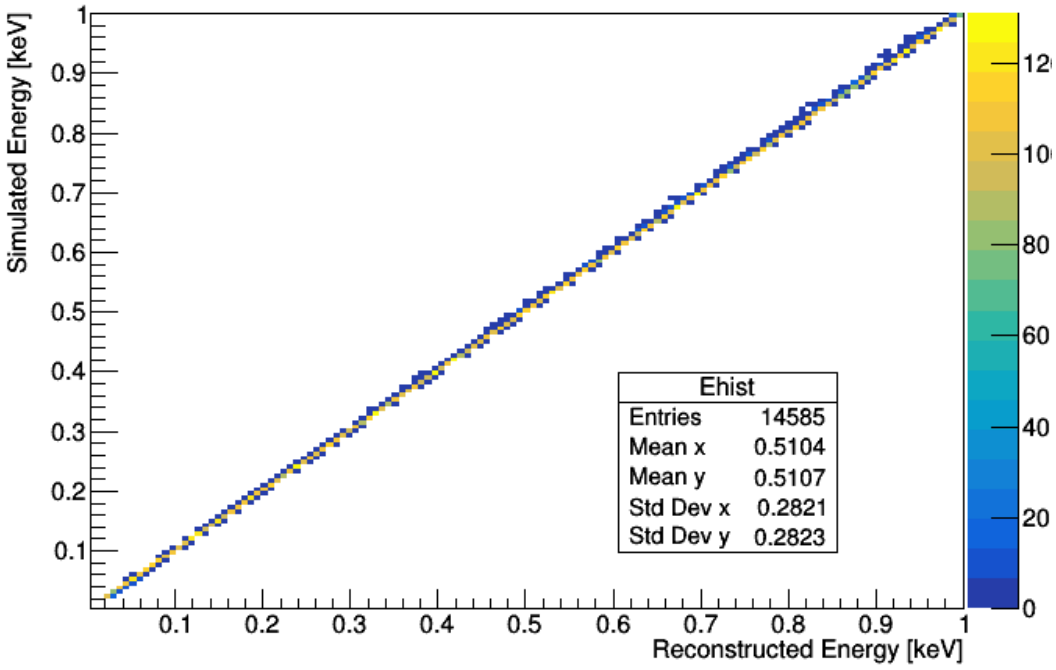

Figure 5.42: This figure demonstrates the accuracy in the cluster reconstruction algorithm in determining the neutron ionization energy in a cluster given a set of reconstruction parameters. Here, we notice a consistent agreement between the simulated energy and the reconstructed energy.

simulated energy and the reconstructed energy. This indicates that the clusters are being reconstructed to an excellent degree of accuracy, and thus, they are appropriately binned in their respective reconstructed energy spectrum histograms.

5.7.4.2 High-Energy Neutron Contribution

The next correction that needs to be applied to the neutron signal, is the reduction of the contribution in the neutron signal that corresponds to the 378 keV neutron scatters. Based on MCNPX simulations, we expect an initial neutron emission rate of $N_{378keV} \sim 200$ neutrons per second at the start of the data-taking campaign per each source. With this neutron rate, we do not expect the higher energy neutrons to contribute significantly to the neutron signal. However, it is still necessary to correct the spectrum, and subtract the neutrons contribution from the spectrum. Figure 5.43 presents the projection of events for the 400-

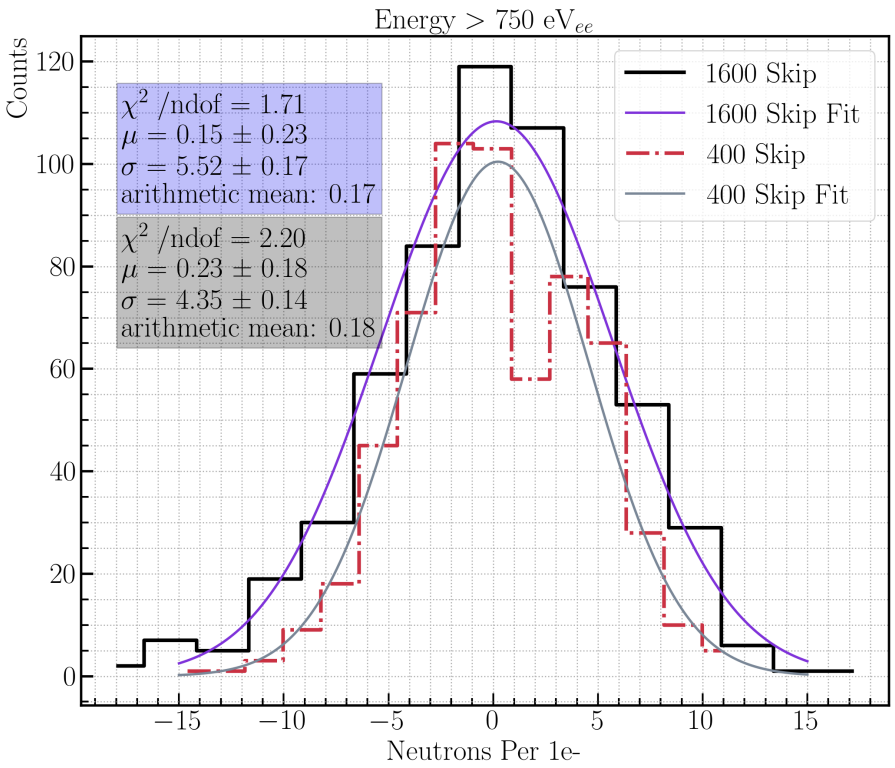

Figure 5.43: This figure presents the projection of events for the 400-Skip and 1600-Skip data sets above 750 eV$_{ee}$ along the y-axis. The fit of the histogram of these events highlights whether the distribution is centered around zero, or a slightly larger value. This offset from zero corresponds to the contribution of the 378 keV neutrons.

Skip and 1600-Skip data sets for energies between 750 eV$_{ee}$, to 3 keV$_{ee}$ along the y-axis. If there were not any 378 keV neutron scatters in the detector, the distribution of these events should be centered around zero since 750 eV$_{ee}$ is above the maximum ionization energy from the 22.62 keV neutron scatters. However, as can be seen in the figure, the distribution is centered slightly above zero for both the 400-Skip and 1600-Skip data sets. This offset indicates that there is a slight contribution to the neutron signal from the 378 keV neutrons that needs to be accounted for. The most straightforward correction for this contribution is to systematically subtract the mean corresponding to this energy region. While a fit to the distribution is possible with some patience, the arithmetic mean is a more robust measure to the neutron offset since it is less reliant on the statistics that make up the distribution.

Thus, for the purpose of a robust estimation of the 378 keV neutron contribution to the neutron signal, the arithmetic mean is calculated for energies between 1 keV_{ee}, to 1.6 keV_{ee} and systematically subtracted from the neutron signal.

5.7.5 Ionization Yield

Now, with the measurement data and simulation data all in order, we are able to finally move onto the determination of the ionization yield. To start, we consider the maximum energy deposition that is imparted in the detector by a scattering neutron, $E_{nr,max}$. This energy deposition will always generate the maximum ionization energy in the detector, $E_{ee,max}$, when considering that the ionization efficiency in silicon (or any material) should be modeled as a function of nuclear recoil energy, $E_{ee} = f(E_{nr})$. Thus, creating a functional coordinate pair, $(E_{nr,max}, E_{ee,max})$. From this functional condition, it follows that all nuclear recoil energies have a corresponding ionization energy, and they form a respective coordinate pair, $(E_{nr,i}, E_{ee,i})$. Once all of the neutrons ON images are processed, and all of the ionization events are characterized and binned into a histogram to form an energy spectrum, the normalized counts associated with an energy bin form the basis to map a nuclear recoil ionization energy with its respective nuclear recoil energy.

If we return to the example of the maximum energy deposition from a neutron scatter in the silicon medium, we know that in our detector we only saw $N_{ee,max}$ ionization events that are associated with $E_{nr,max}$. Any counts in bin energies greater than $E_{ee,max}$ correspond to statistical fluctuations from background events. Therefore, when the simulated nuclear recoil energy spectrum is normalized and binned in accordance to the neutron signal, the respective energy bins where $N_{ee,max}$ equals $N_{nr,max}$ form the coordinate pair $(E_{nr,max}, E_{ee,max})$. Now, due to the limited statistics in the experimental data and simulation it is not possible to apply this methodology to the remainder of the signal, since the statistical fluctuations in the energy-bin counts can cause the values to hover near each other and prevent a 1-to-1

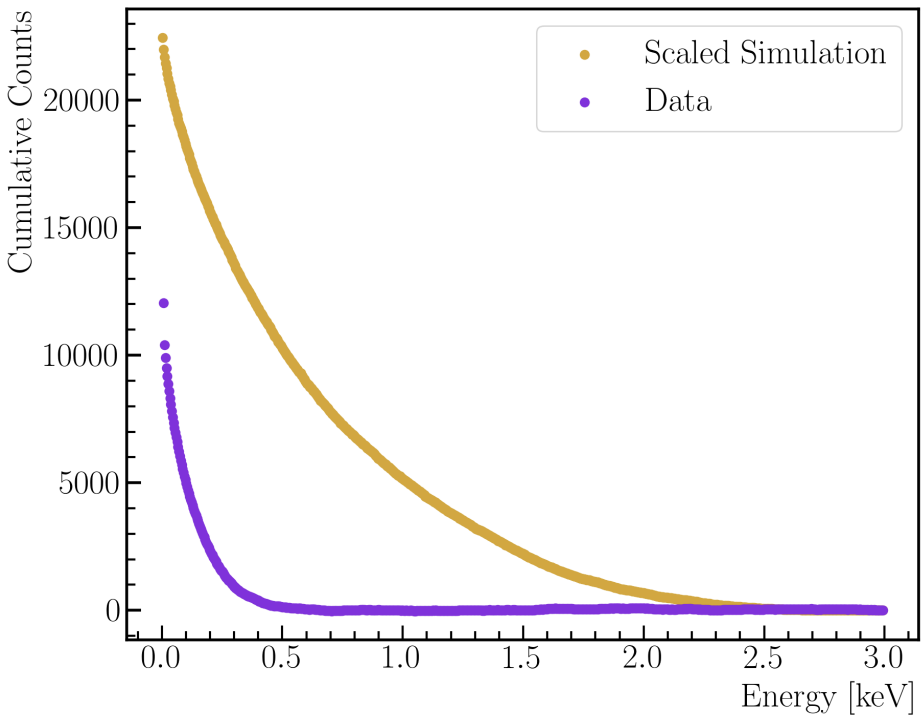

Figure 5.44: This figure demonstrates the reverse cumulative histograms that need to be built to apply the integral method. The simulation data is normalized to the neutron signal recovered from the measurement, and it is scaled to account for the difference between the ENDF-VII library and the measurement data from Oak Ridge National Lab.

mapping to the nuclear recoil spectrum. However, a simple fix is to take the integral of events starting at a designated upper bound, down to the detector threshold, and form a cumulative histogram. With this procedure each bin retains its original count, N_{ee}, and acquires the accumulated events associated with the next highest energy bin, $N'_{ee} = N_{ee} + \Sigma N_{ee+i \cdot 3.74}$. This way, the second term acts as a 'step' that 'props' up the events in an energy bin, and allows for the proper matching of counts between the nuclear recoil ionization energy spectrum and the nuclear recoil energy spectrum. This method is termed the integral method, and has been adapted for this analysis from Chavarria et al [18]. Figure 5.44 depicts an example of the cumulative histograms associated with the normalized nuclear recoil ionization spectrum and the nuclear recoil energy spectrum. From this figure, we note that since the histogram is monotonically decreasing towards higher energies, the nuclear

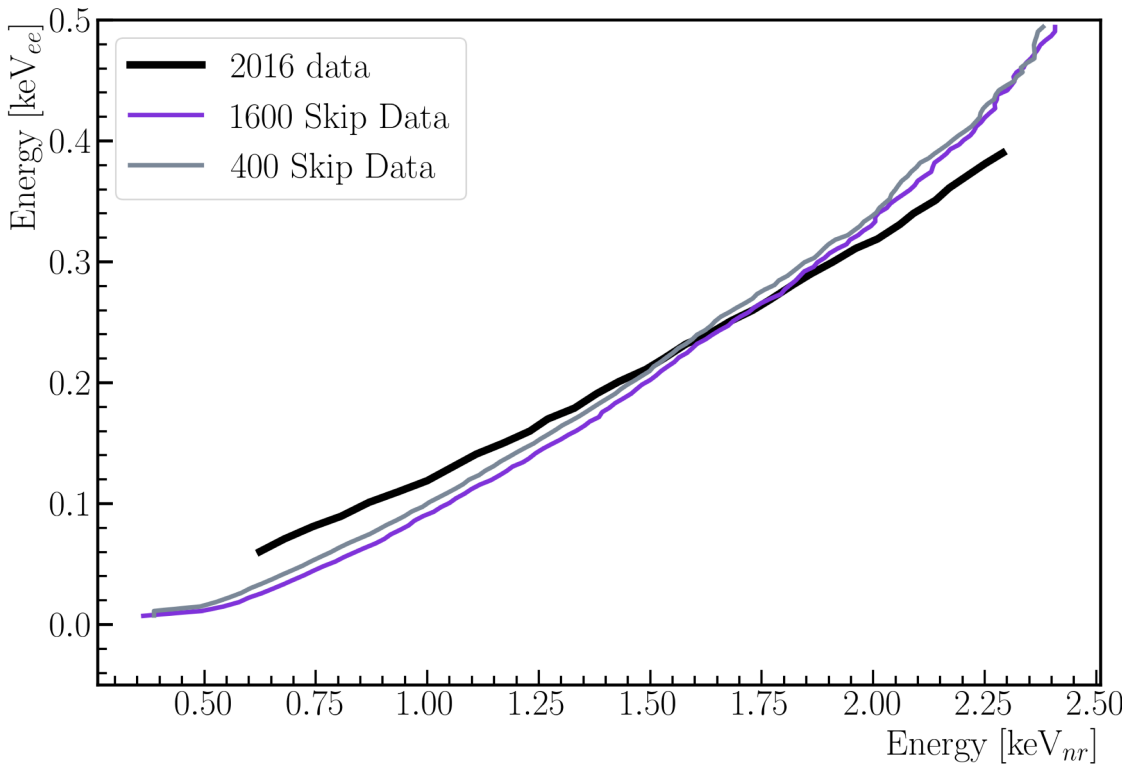

Figure 5.45: The ionization yield for the 400-skip data and 1600-skip data sets. Here, the nuclear Fano factor is assumed to be set to zero.

recoil energy can be fit with an interpolating spline. The resulting parametrization of the simulation data and an application of a root finding algorithm, facilitates the calculation of the ionization yield. The resulting ionization yield for the 400-skip data and the 1600-skip data can be seen in Figure 5.45.

From this figure, we can see that the resulting ionization yields for the two data sets are in agreement with each other. The agreement provides confidence in our methodology since the only differences in the two data sets (after neutron normalization) should be the resolution in the detector and the measurement threshold. However, this is not the end of the story with the recovery of the ionization yield, since the integral method assumes a nuclear Fano factor of zero, and we must account for the variance in charge ionization after a nuclear scatter.

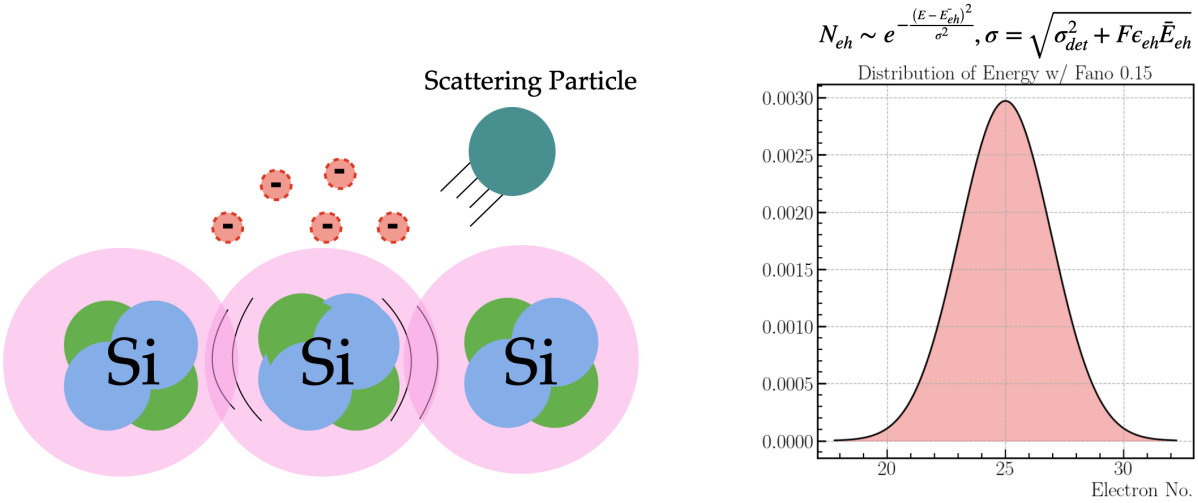

Figure 5.46: *Left*: Cartoon depicting charge ionization from a nuclear scatter. *Right*: Figure demonstrating the variance for a high-energy nuclear recoil ionization event. Here, we assume a Gaussian model for charge ionization, where σ is dependent on the resolution of the detector and the nuclear Fano factor. 25 electrons corresponds to ∼93.5 eV and is within the energy region of interest for this measurement.

5.8 The Nuclear Fano Factor

5.8.1 Overview

Until now, we have assumed that the charge ionization resulting from a nuclear scatter was deterministic. This means that given a set of initial conditions and known material properties (such as the quenching factor), one could calculate exactly how much charge will be ionized after a nuclear scatter. However, this is not the case. At the particle level, the processes that govern charge ionization are inherently quantum in nature, and hence statistical. Therefore, there will be variability in the total charge generated for a given nuclear recoil energy, E_{nr}. The dispersion in the charge-generation process is modeled by a nuclear Fano factor.

$$F = \frac{\sigma_e^2}{\bar{n}_e} \tag{5.17}$$

Equation 5.17 is the generic representation of the Fano factor, where F is the Fano factor, σ_e is the standard deviation of charge generated, and $\bar{n}_e$ is the mean number of charge generated from a nuclear scatter with associated recoil energy, E_{nr}. The variability in charge ionization due to this statistical process indicates that the aforementioned integral method may not be correctly mapping nuclear recoil ionization events to their respective nuclear recoil energies if there is a chance that the variance in charge generation could span multiple bins. Therefore, the effects that this charge *smearing* may have on the ionization yield must be explored and accounted for.

5.8.2 The Nuclear Fano Factor in Silicon

For a given nuclear scatter, the recoiling nucleus will either transfer some of its energy toward heat, or phonon generation, or charge ionization. The fraction of energy, Q, that is transferred to charge ionization, $Q = E_{ee}/E_{nr}$, is known as the ionization yield. The problem that we are attempting to address is that the ionized charge energy, E_{ee}, generated from a nuclear recoil is variable and dependent on the nuclear Fano factor in silicon. Furthermore, measurements at recoil energies $\gg 3$ keV have shown the nuclear Fano factor to be energy dependent [51]. We can express the nuclear Fano factor as,

$$F_{nr} = \bar{n}_e \xi^2 = \frac{E_{nr} Q}{\epsilon_{e-h}} \xi^2 \tag{5.18}$$

where F_{nr} is the intrinsic nuclear Fano factor, $\bar{n}_e$ is the average charge generated by a nuclear scatter, ξ^2 is the intrinsic fractional ionization width (where $\xi = \sigma/\bar{n}_e$, E_{nr} is the nuclear recoil energy), Q is the ionization yield, and ϵ_{e-h} is the electron-hole pair creation energy [51]. Here, we can directly see that the nuclear Fano factor tends to increase as E_{nr} increases; and consequently, the variance of charge generation is also affected. Therefore, it is evident that a charge ionization model needs to be implemented to account for the variance in charge

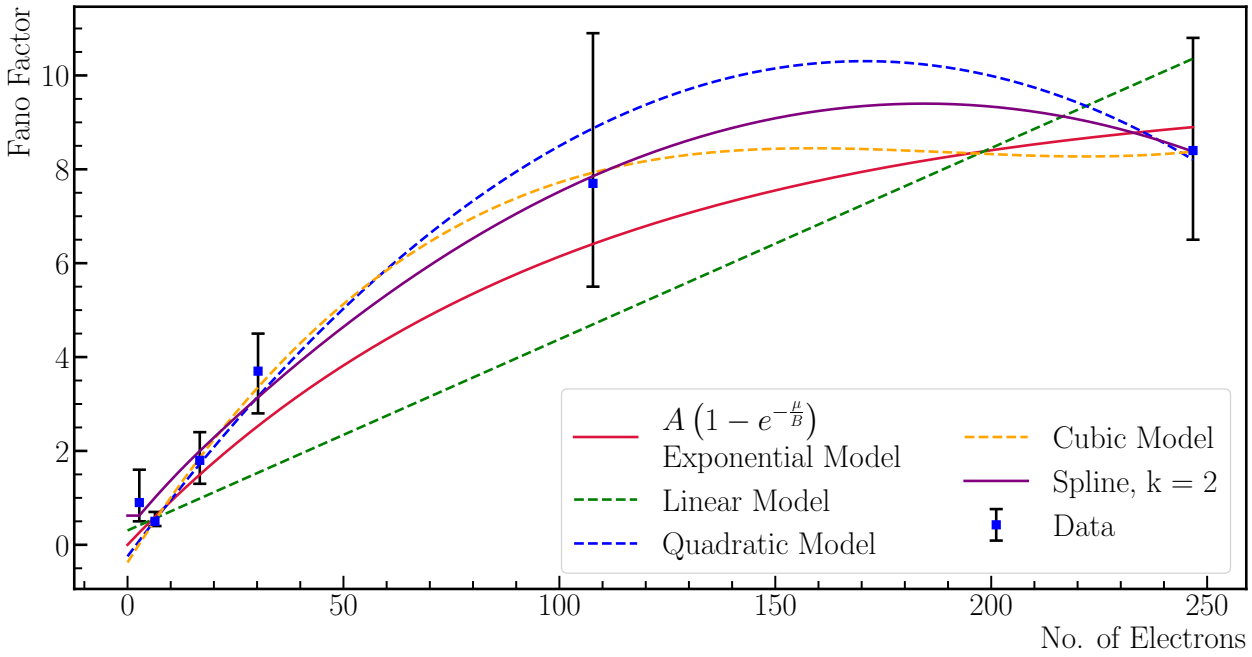

Figure 5.47: Measured Fano factor values by SuperCDMS for recoil energies of 0.10, 0.22, 0.46, 0.89, 2.33, 3.91 keV$_{nr}$ respectively [4]. The energy axis is represented in the number of electrons as a visual aid for the Poisson charge ionization model. This axis does not directly represent the nuclear recoil energy, but rather, it has been converted to mean ionized charge based on the measured ionization yield. Best fit models are also presented in this figure. Solid lines are the primary models of interest.

generation at different nuclear recoil energies.

For this measurement, the charge ionization model needs to be reflective of the range of energies that correspond to our measurement. At a peaked 22.62 keV neutron energy, from MCNPX-PoliMi we expect a maximum recoil energy of $\sim$ 2.9 keV. The measurements that were presented by M. Matheny, reflect recoil energies above 3 keV, and thus, are not best suited for use in this measurement [51]. However, recent results from SuperCDMS presented a first measurement of the nuclear Fano factor in silicon down to 100 eV nuclear recoil energy [51]. Figure 5.47 presents the results from the SuperCDMS measurement in terms of mean ionized charge. Here, we see six data points with asymmetric systematic errors and best-fit models to the data. The data was fit with a modified least-squares regression function that accounts for the asymmetric errors, using the iMinuit python package. Of the several models

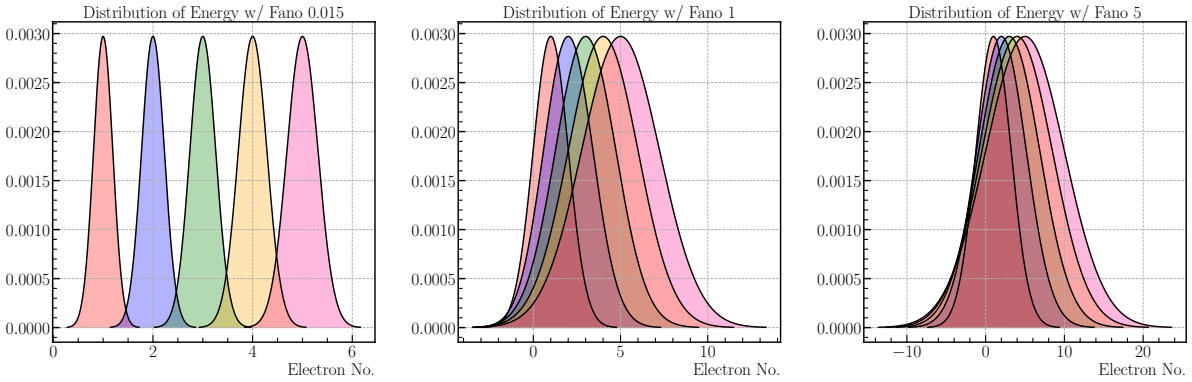

Figure 5.48: The figures depict the variance in ionized charge centered around 1, 2, 3, 4, and 5 electrons. The distribution includes two variance contributions: one from the Fano factor and the second from the detector resolution.

that are presented, the exponential model and the quadratic spline present the best match to the data. Since current ionization models have failed to predict the yield represented in low-energy ranges, the spline model is the best choice for describing the trend presented by the data. This data well-encompasses the energy range in the measurement that we are sensitive to and thus will be used to develop a charge ionization model and modify the integral method.

5.8.3 A Charge Ionization Model

To properly model how charge from a nuclear ionization event may have been distributed along the recovered neutron signal, a charge ionization model needs to be developed. As a first pass, a Gaussian distribution appears suitable, since at high energies enough charge is generated such that the mean number of charge is normally distributed — as dictated by the central limit theorem. However, when the model is applied at low recoil energies, the Gaussian model predicts negative amounts of charge; this is nonphysical. This effect is exacerbated at larger Fano factors as is seen in Figure 5.48. The figures demonstrate the

effect that a variance in the form of σ_T from Equation 5.19 has on the predicted ionization.

$$\sigma_T = \sigma_{Fano} + \sigma_{detector} \tag{5.19}$$

In this equation, σ_T represents the total variance in charge ionization, σ_{Fano} represents the variance corresponding to the Fano factor, and $\sigma_{detector}$ represents the resolution of the detector. When charge ionization is modeled with a Gaussian distribution in this way there are two glaring issues. One, at large Fano factors we predict negative charge. And two, at Fano factors $\gtrsim 1$ an energy deposition equivalent to the electron-hole pair creation energy has a chance to generate multiple electron-hole pairs in the detector. Neither of these predictions is sensible, and we require a better model for charge ionization.

Considering that the Fano factor from Equation 5.17 is defined under a counting process and can be thought of as a measure of the dispersion in said process, it is sensible to pursue a discrete probability distribution that will model charge ionization created for a given nuclear recoil energy. From the SuperCDMS data seen in Figure 5.47, at low energies the Fano factor trends towards a value of one. When the Fano factor is one, then $\sigma^2 \approx \bar{n_e}$ and the behavior of charge ionization is similar to a Poisson process. So, we can develop a model based on the Poisson distribution that will accommodate the Fano factor and the SuperCDMS data.

Consider a Poisson distribution, $Pois(\bar{n}_e)$, where the mean number of ionized charge, $\bar{n}_e$, is equal to its variance, σ_e^2. If this same distribution is scaled by a factor, α, along the independent axis, then it follows that the variance and mean number of ionized charge should scale accordingly.

$$\begin{aligned} \bar{n}'_e &= \alpha \bar{n}_e \\ \sigma'^2_e &= \alpha^2 \sigma_e^2 \end{aligned} \tag{5.20}$$

Here, we note that the mean and variance of the distribution are simply scaled by the same factor to first or second order, respectively. When applying this methodology to the Fano

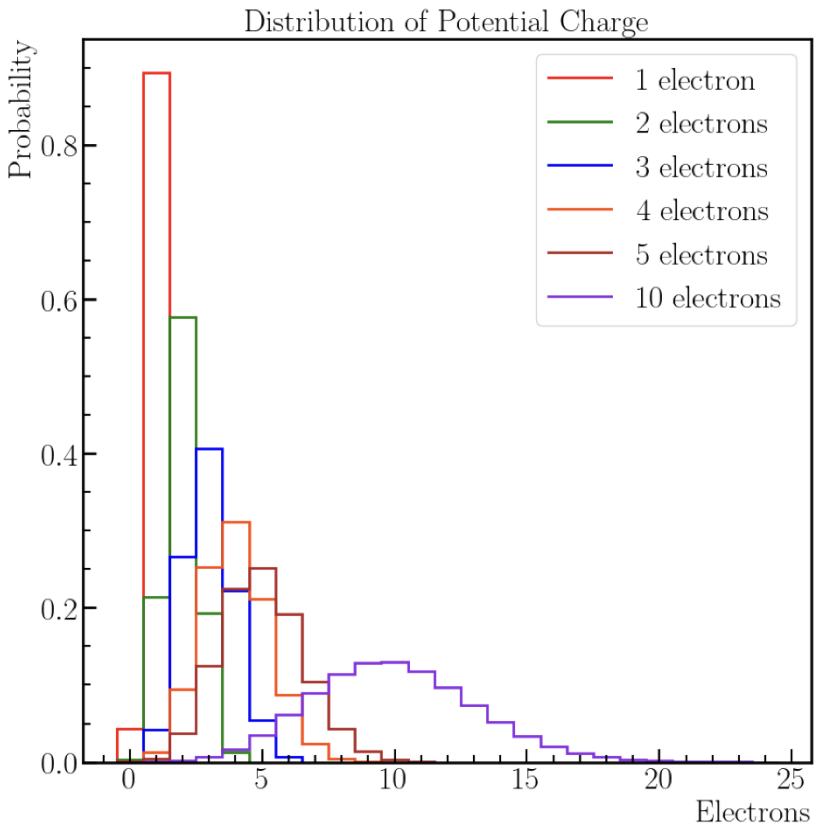

Figure 5.49: Sampling distributions for generating ionized charge in the detector. Each distribution is determined by the Fano factor results from SuperCDMS and corresponds to a unique nuclear recoil energy. The independent axis represents ionized charge.

factor, we arrive at the following relation.

$$F_{nr} = \frac{\sigma_e^2}{\bar{n}_e} \rightarrow F'_{nr} = \frac{\sigma_e'^2}{\bar{n}'_e} = \alpha \frac{\sigma_e^2}{\bar{n}_e} = \alpha F_{nr} \tag{5.21}$$

Where we note that the Fano factor is simply scaled by the same factor, α; and since the Fano factor for the non-scaled distribution is defined to be one for a Poisson process, we arrive at a solution where $F'_{nr} = \alpha$. This result allows us to parameterize the SuperCDMS Fano factor data as a function of mean ionized charge, $\bar{n}_e$; where the scaling factor α will now be defined as the corresponding Fano factor for a given $\bar{n}_e$. This factor can then be used to construct a Poisson distribution for any recoil energy, but it will be constructed in terms of the mean ionized charge parameter, $\bar{n}_e$. Therefore, by construction, to build a Poisson

distribution that is representative of the measurement Fano factor data, we need only to determine $\alpha(\bar{n}_e)$ and define the Poisson constant lambda as $\lambda = \bar{n}_e = \bar{n}'_e/\alpha(\bar{n}_e)$. From here, it is straightforward to calculate the variance in the distribution as well. From a technical perspective, we can now use the parameter λ to define a Poisson distribution and integrate it from the lower bin edge value to the upper bin edge value[8]. This integral will correspond to the probability of generating a respective amount of ionized charge in the detector. The results of this model can be seen in Figure 5.49 with $\bar{n}_e$ values ranging from 1 to 10. As can be seen in the figure, we are no longer predicting negative charge, and each value of $\bar{n}_e$ is bound within a reasonable amount as would be expected; at larger values, the distribution trends towards a normal distribution as expected from the Central Limit Theorem.

For the future sections of this chapter, the Poisson charge ionization model will be the main model utilized unless otherwise specified.

5.8.4 The Iteration Method

Now, that we have a charge ionization model, we can develop an algorithm to explore the effects that the Fano factor can have in the calculation of the ionization yield. To do so, we employ the iteration method detailed by Chavarria in Reference [18]. This method relies on the previous calculation of the ionization yield. For a quenching factor, Q_i, where $Q_i = E_{ee,i}/E_{nr,i}$, an ionization signal can be simulated by sampling recoil energies, E'_{nr}, and 'quenching' them, $E'_{nr} \rightarrow E'_{ee} = Q_i \cdot E'_{nr}$. This ionization signal is then smeared with the ionization model and detector resolution to attain a new, smeared, ionization signal, $E'_{ee,s}$; the smeared ionization signal can then be converted to a recoil energy by reversing the quenching process we started with, $E'_{ee,s} \rightarrow E'_{nr,s} = E'_{ee,s}/Q_i$. The newly *smeared* nuclear recoil spectrum can be used with the original neutron signal acquired from the measurement data, and a new ionization yield is calculated. This iteration process will continue until the

8. To integrate the Poisson distribution, the standard distribution was converted from $\frac{\lambda^k}{k!}e^{-\lambda}$ to $\frac{\lambda^k}{\Gamma(k+1)}e^{-\lambda}$

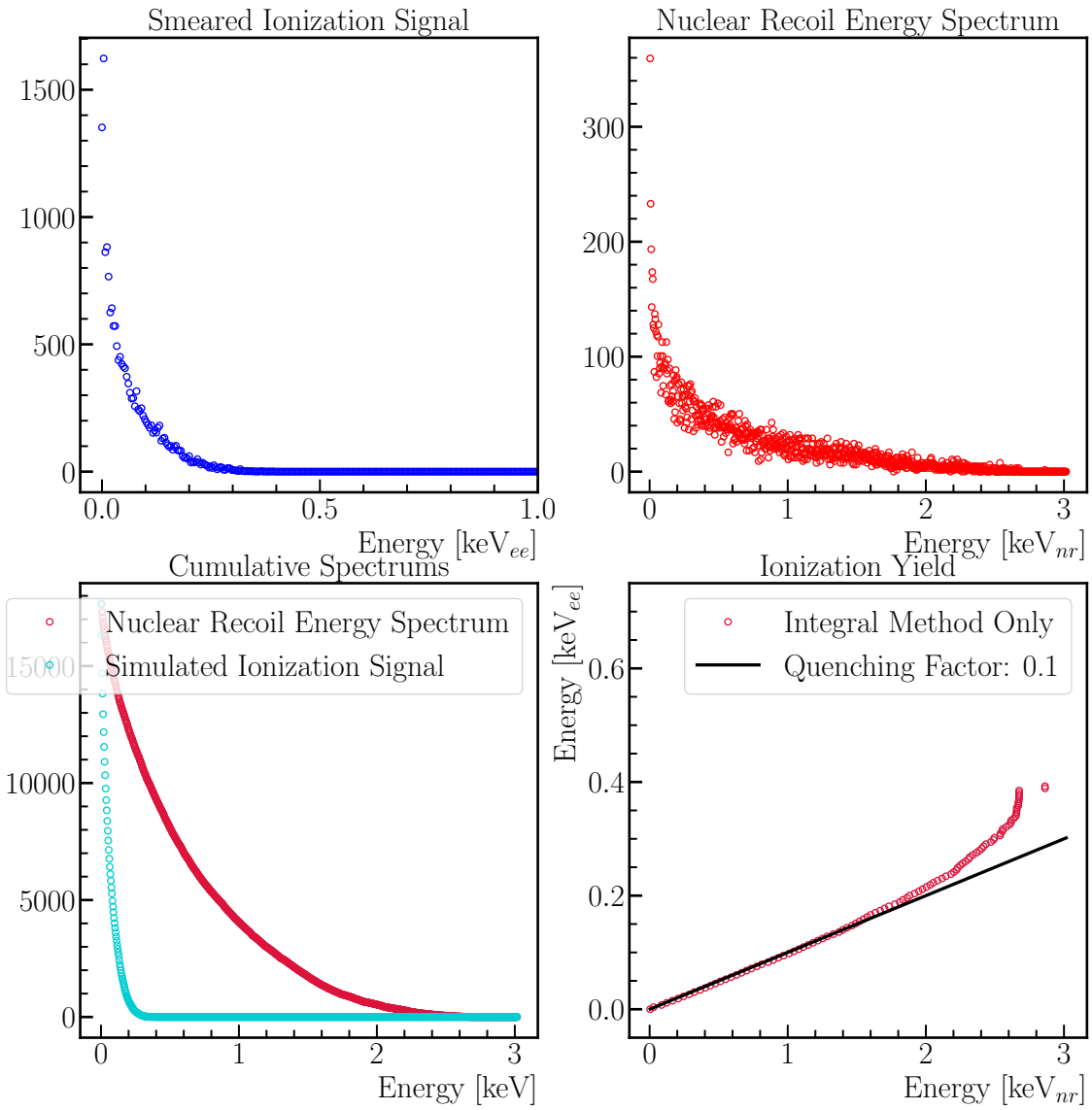

Figure 5.50: A selected example for the Toy Monte Carlo was used to validate the iteration method. *Top Left*: An example of a simulated ionization signal using a constant quenching factor of $Q = 0.10$ and the nuclear recoil energy spectrum. *Top Right*: The nuclear recoil energy spectrum. This spectrum remains unchanged and is used to generate the ionization signal and ionization yield after smearing with the charge ionization model. *Bottom Left*: The reverse cumulative spectrums. *Bottom Right*: The ionization yield is calculated with the integral method. The red data points correspond to the simulated ionization yield, and the black line represents the applied quenching factor, or true ionization yield.

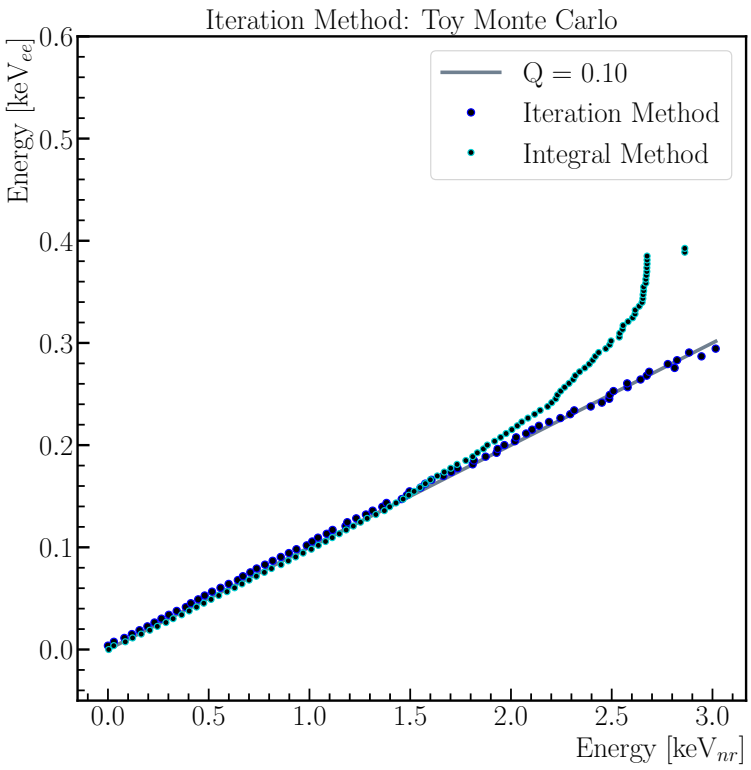

Figure 5.51: This figure demonstrates that the iteration method was able to successfully recover the true ionization efficiency when applied to a simulated ionization signal. The light blue data points correspond to the integral method without the iteration procedure, and the darker blue data points correspond to the iteration procedure. The black line is the true ionization yield in this simulation.

quenching factor converges. The resultant ionization yield from this iteration process will present a systematic for the calculation of the ionization efficiency.

To validate the iteration method, a series of toy Monte Carlo simulations were deployed. In each simulation, a smeared ionization signal was generated with a constant quenching factor. The ionization signal was then used to calculate an ionization yield using the integral method and the nuclear recoil energy spectrum; after which, the iteration procedure is applied. If the iteration method can revert the smeared ionization signal to a constant quenching factor, then the iteration method algorithm is validated. Figure 5.50 demonstrates selected plots for a selected toy Monte Carlo simulation. In the top left figure, you can see the simulated ionization signal that is acquired after applying a constant quenching factor

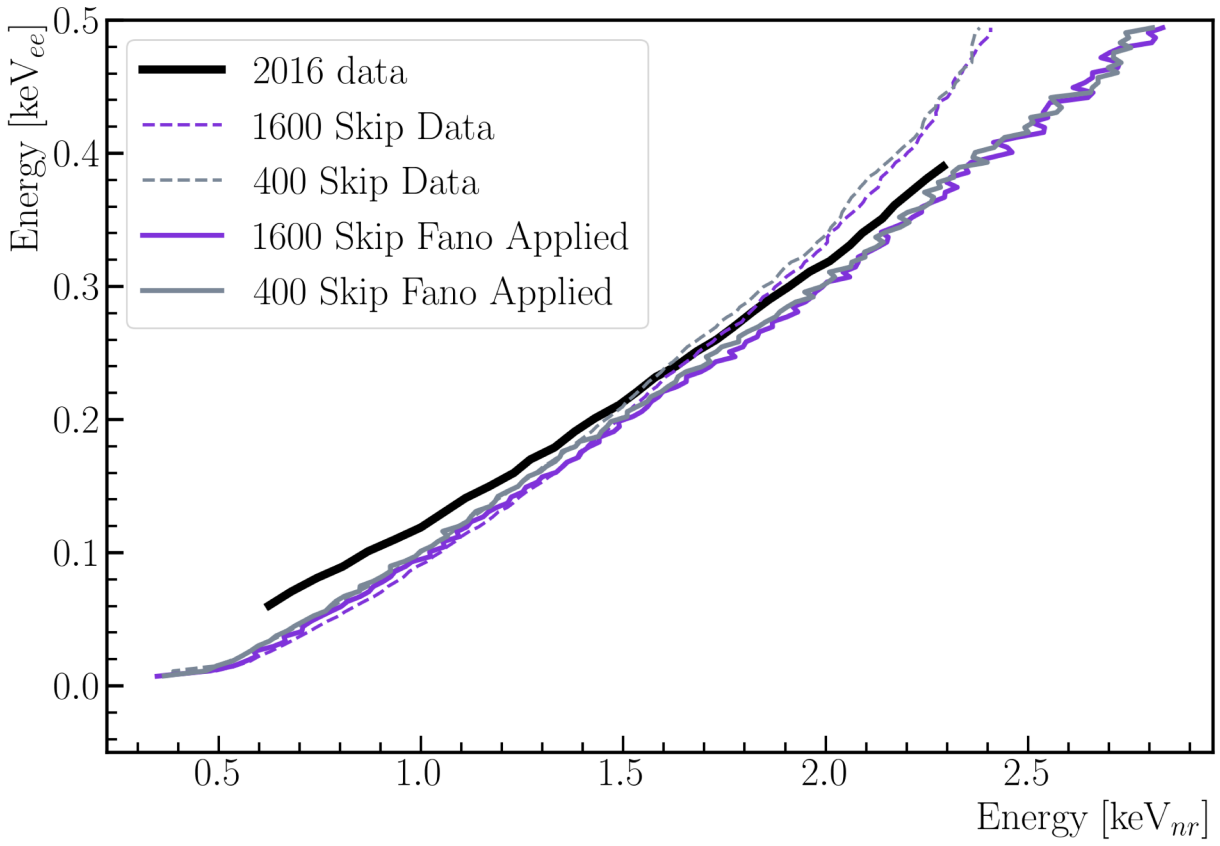

Figure 5.52: This figure shows the results of applying the iteration procedure with the SuperCDMS data onto our 400-skip and 1600-skip measurement data. The solid lines represent the result with the iteration procedure applied, while the dashed lines are the results with only the integral method.

and the charge ionization model. The resultant ionization yield is seen in the bottom right plot and is seen to deviate from the true ionization yield that corresponds to the applied quenching factor. In Figure 5.51 we see that after the application of the iteration procedure onto the simulated ionization signal, we can recover the original ionization efficiency; thus, validating the developed iteration method for calculation of the ionization yield. This method was further validated with varying quenching factors and the use of the ionization yield that corresponds to the integral method. In all systematic variations, the iteration method algorithm performed as expected.

Now, that we have a way to explore the effects that the nuclear Fano factor has on the

ionization yield, we can apply it to our data to arrive at a result. Figure 5.52 presents the results of the iteration method when applied to the 400-skip and 1600-skip data respectively. The solid lines in the figure represent the result from the iteration method and demonstrate that both measurements continue to agree with one another. Furthermore, we note that the largest effect the Fano factor has on the spectrum is on the high-energy end, while the lower-energy portion of the spectrum remains relatively unchanged. At the high-energy region of the ionization yield, the variance in the charge ionization becomes large due to the large Fano factor values and higher recoil energies; while at the lower energies, the Fano factor is one, and we do not expect much charge ionization variance — see Figure 5.49.

Ultimately, the minimal variation in the ionization yield after the application of the iteration method is promising since this is the region of interest. With the addition of the iteration method, we report a measurement of the ionization yield in silicon down to 3 electrons with a Skipper CCD. The final section of this chapter will present a brief summary of the analysis steps, and discuss the systematic checks leading to the final result.

5.9 Systematic Checks

5.9.1 Baseline Configuration

Before moving forward to the systematic checks, it is important to summarize some of the key results of the analysis and present the baseline configuration set. First, I have consistently shown the agreement between the 400-skip and 1600-skip data sets throughout the analysis procedure, and given the increase in sensitivity that the 1600-skip data set presents, this thesis will focus on the results from the 1600-skip data. The processing parameters of the 1600-skip data for the main, baseline calculation of the yield are: a fixed sigma value (determined for both the before and after data sets), a 1 e- clustering threshold, a 1.5 e- clustering seed, and a stitch between the fit results and the bin-by-bin method for spectral

subtraction (where the first 50 points are extracted from the fit). Second, it was mentioned that there is a clustering efficiency associated with the data set. This efficiency calculates the ability of our clustering algorithm to detect all clusters that correspond to the inbound flux of neutrons. From studying the results of the reconstruction efficiency, we determine our measurement threshold to be 3 e- (11.22 eV) for the 1600-skip data set. The reconstruction efficiency shown in Figure 5.41 is applied in the baseline calculation. Third, during neutron data taking there is a potential neutron-induced background (ie. γ-rays from neutron capture) that can contribute to the neutron signal; this background is in addition to the higher-energy neutrons produced from the 2.09 MeV γ-rays of ^{124}Sb [18]. This background is estimated by taking the arithmetic mean of events within 1 - 1.6 keV$_{ee}$, and then systematically subtracted from the measured neutron signal. Fourth, when applying the integral method, a cutoff energy must be specified for the measured charge ionization signal. For a neutron energy of $\sim$23 keV, we do not expect charge ionization past $\sim$500 eV$_{ee}$. Thus, any exceeding signal is assumed to be dominated by background fluctuations. For the baseline calculation, the integral of events is formed for energies $<$ 1 keV$_{ee}$. And fifth, the contributing errors associated with the data: statistical errors in the neutron signal, the reconstruction efficiency, and the neutron background estimation are all propagated in quadrature. Once the cumulative histogram is generated, the central value of the cumulative histogram is shifted by its statistical uncertainty, and a corresponding recoil energy is calculated to account for a lower and upper bound on the central recoil energy. This concludes the baseline consideration for the measured neutron signal. Next, we will discuss the baseline configurations of the yield calculations for the simulation and normalization factors.

As a summary, the determination of the ionization yield requires a combination of the measured charge ionization and a simulated nuclear recoil spectrum. A normalized, cumulative histogram (integral of events starting from high energies to low energies) of the two data sets is required to match the recorded charge ionization to a nuclear recoil energy. First, the

nuclear recoil energy spectrum must be scaled by 1.08 so the ENDF-VII library most closely matches the silicon cross-section measurements from Oak Ridge National Lab. Second, the normalization factor needs to be determined from the measured activity of the source. The measured activity of ^{124}Sb for source 1 was 4.08 $\pm$ 0.19 mCi on the start of data taking. For source 2, there was not an on-site dedicated measurement of the activity, however, given the measurements of the activity provided by Oregon State, we are able to scale the source 1 activity for source 2. With the activity in hand, the expected neutron rate is determined by applying the neutron production results from the photo-nuclear simulation. This simulation employs Robinson's reanalyzed cross-section for the ^{9}Be(γ, n)^{8}Be reaction; the cross-section is 1.41 $\pm$ 0.04 mb [64]. The neutron rate calculated from these values is then used to determine the normalization between the measured neutron signal and the simulated nuclear recoil spectrum.

These values and criteria define the baseline parameters for the final yield. In the following subsection we will discuss systematic checks, and compare their deviation from the baseline calculation.

5.9.2 Systematic Checks

To start, there are systematic uncertainties associated with the quantities used to calculate the normalization factor. In particular, there is a 2.8% uncertainty associated with the ^{9}Be(γ, n)^{8}Be reaction; there is a 4.7% uncertainty in the measurement of the gamma activity for the antimony source; and there is a 3% uncertainty associated with the neutron-silicon cross-section from Oak Ridge National Lab [44]. Additionally, there was a designated set of neutron measurements taken to validate the neutron flux around the experimental site. Figure 5.35 demonstrates all the associated sites where the neutron flux was measured. The results of these measurements are summarized in Table 5.4. From these measurements, we determine that the measurements for source 2 are consistent among each other at $\lesssim$10% uncertainty,

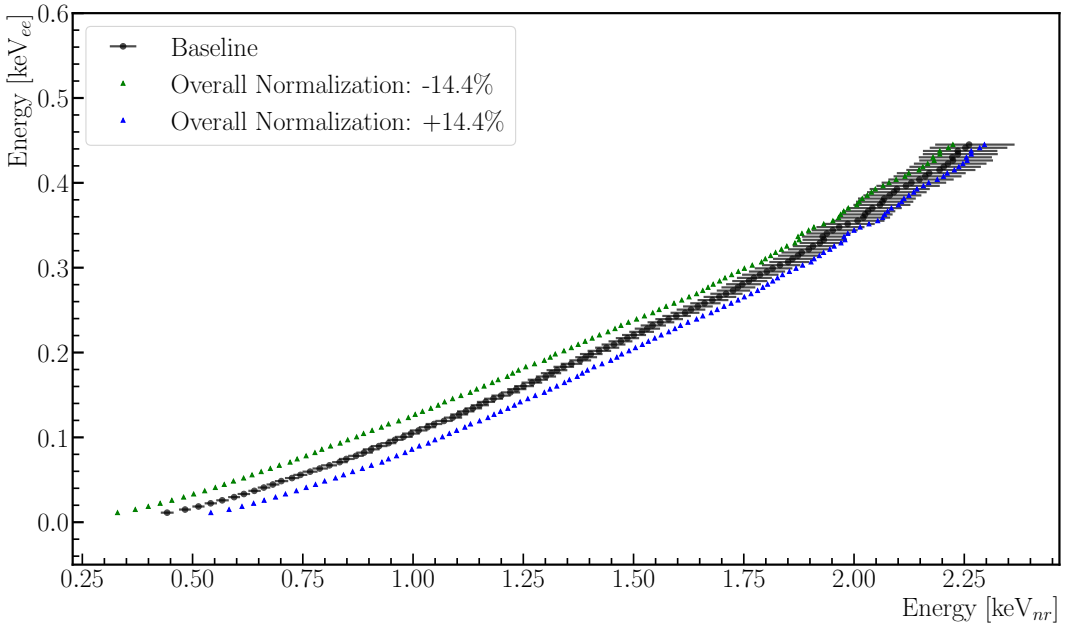

Figure 5.53: The ionization yield was calculated with a scaling of ± 14.4% to determine the systematic uncertainty on the yield.

and demonstrate a ∼13.5% agreement to the expected neutron rate. This 13.5% uncertainty will be considered in quadrature for an overall systematic check to the normalization factor. The overall systematic check to the normalization factor will involve the 13% uncertainty from the neutron flux measurements, the 2.8% uncertainty from the ^{9}Be(γ, n)^{8}Be reaction, the 4.7% uncertainty from the gamma activity measurement, and the 3% uncertainty from the ORNL measurement; after propagating these values in quadrature we arrive to an overall systematic uncertainty of 14.4% on the normalization factor. Figure 5.53 shows the ionization yield calculated with the application of the systematic uncertainty.

Additionally, a series of systematic checks were carried out to test the robustness of the ionization yield calculation. These checks included the selection of the cutoff energy in the measured neutron signal during application of the integral method; the estimation of the neutron induced background; the reconstruction efficiency; the decision of calculating the yield from the gamma activity or the neutron measurement with a He-3 counter; or the processing parameters for 1600-skip data. The results of these studies can be seen in Figures

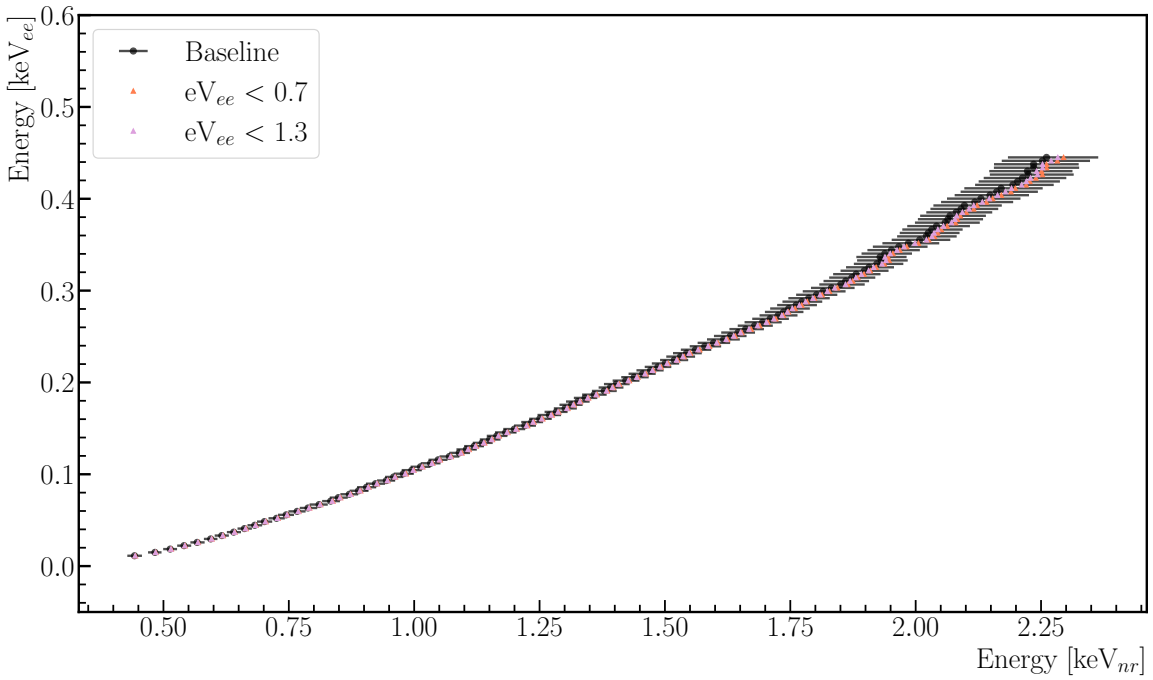

(a) Systematic check on the cutoff energy for the neutron signal.

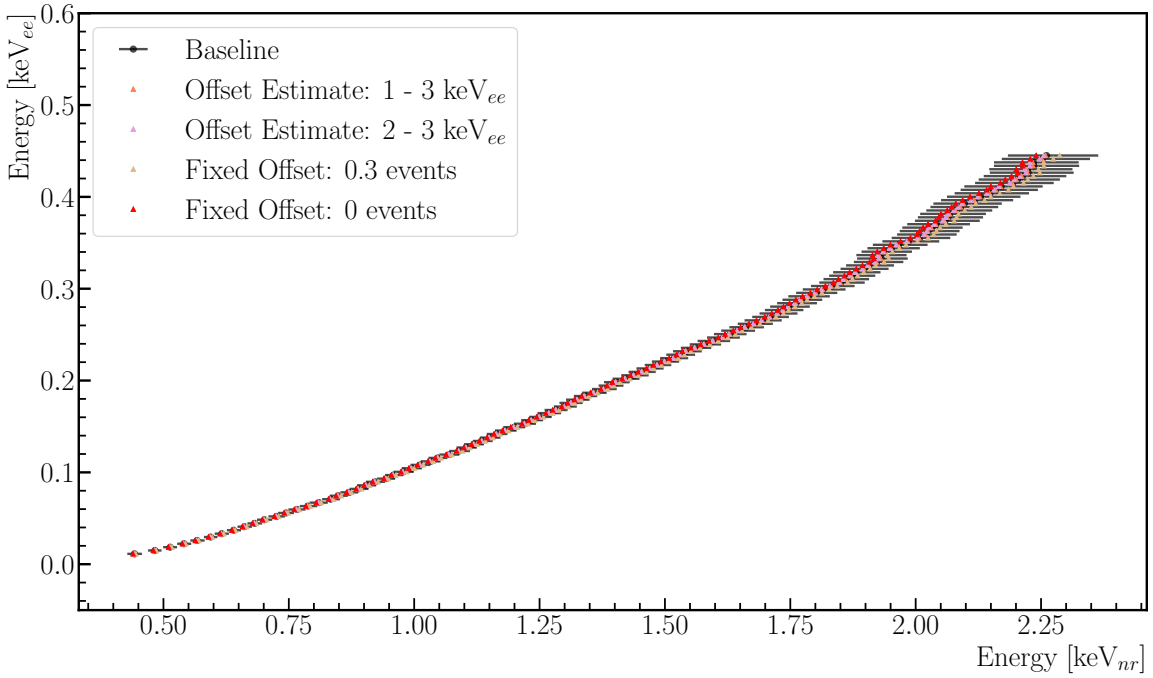

(b) Systematic check on the neutron induced background estimation.

Figure 5.54: *Top*: Comparison of the calculation of the ionization yield with a cutoff energy of 0.7 keV$_{ee}$, 1 keV$_{ee}$ (baseline), and 1.3 keV$_{ee}$. *Bottom*: Comparison of the calculation of the ionization yield with neutron induced background estimates determined from the arithmetic mean within 1 - 3 keV$_{ee}$, 1 - 1.6 keV$_{ee}$ (baseline), 2 - 3 keV$_{ee}$, and a fixed value of 0 and 0.3.

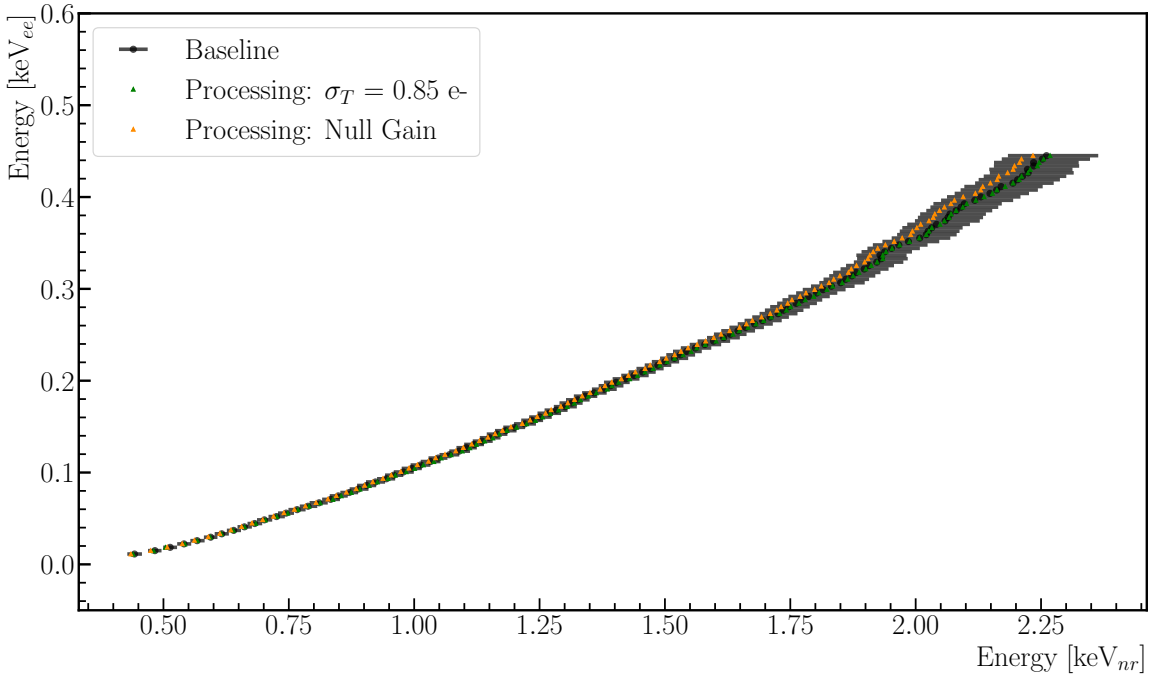

(a) Systematic check on the processing selections.

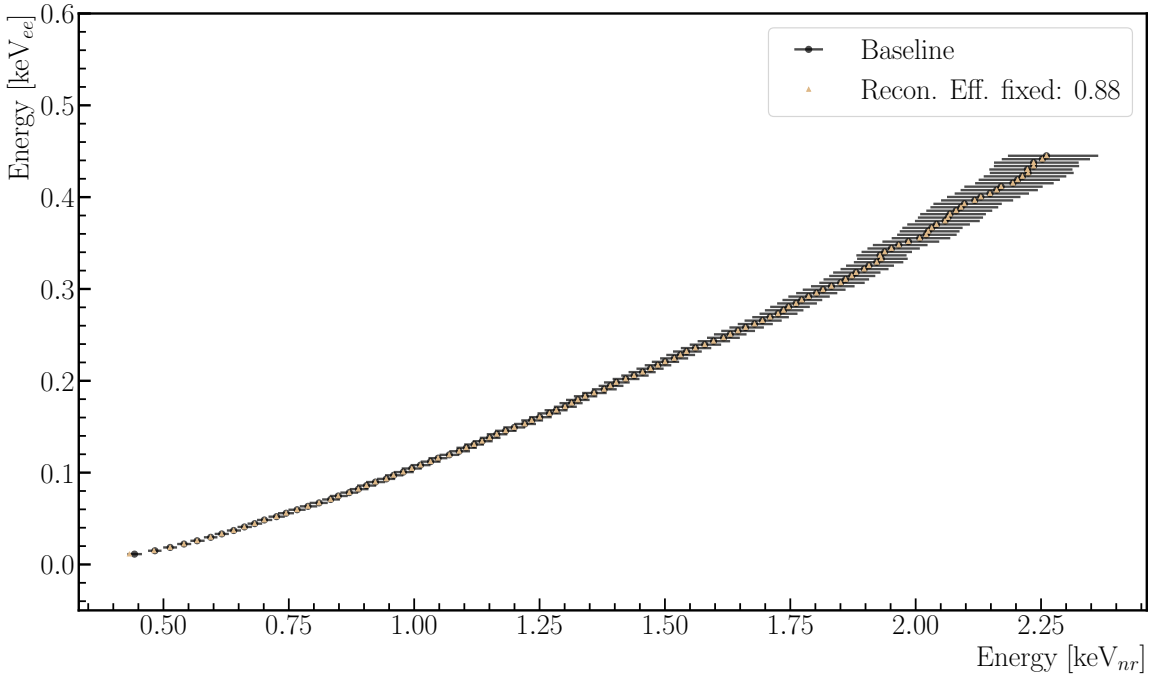

(b) Systematic check on the reconstruction efficiency.

Figure 5.55: *Top*: Comparison of the calculation of the ionization yield with varied processing parameters for the 1600-Skip data. *Bottom*: Comparison of the calculation of the ionization yield with the nominal reconstruction efficiency and a constant efficiency.

5.54 & 5.55. The systematic checks on the selection of the cutoff energy demonstrate $< 1\%$ difference in the calculation of the ionization yield as compared to the baseline yield. The neutron offset checks result in $< 1\%$ difference compared to the baseline yield; of interest the calculation of the yield without a neutron induced background estimate results in a 0.7% difference in the yield when compared to the baseline. While not shown in the figures, calculating the normalization factor with the neutron measurement showed a 1.8% difference when compared to using the gamma activity (baseline); however, the uncertainty on the normalization is dominated by the previously reported 14.4% systematic uncertainty. The choice of of threshold on the 1600-skip data resulted in <1% difference when comparing the 0.85 e- threshold to the 1 e- threshold (baseline). The choice of image calibration method resulted in an average ∼1% difference when compared to using the calibration constant fit to second-order versus the self-calibration of each image. The check on the reconstruction efficiency resulted in a <1% difference when comparing the baseline efficiency to a fixed value of 0.88.

Now that we have determined the systematic uncertainty associated with our measurement with the 1600-skip data, we can arrive at a final result for our measurement. Furthermore, the results from the systematic checks strengthen the decision in calculation parame-

	Detector Efficiency	Source 1 Meas/**Yield** [n/s]	Measured Date	Source 1 Expected Rate	Source 2 Meas/Yield [n/s]	Measured Date	Source 2 Expected Rate
Site 1	2.370E-3	11.62/**4903.0**	4/25/2022	5558.5	10.68/**4506.3**	9/9/2022	4932.2
Site 2	2.539E-3	11.47/**4517.5**	4/25/2022	5558.5	10.60/**4174.9**	9/9/2022	4932.2
Site 3	4.065E-3	18.23/**4484.6**	4/25/2022	5558.5	16.51/**4061.5**	9/12/2022	4764.7
Site 4	2.311E-4	1.13/**4889.7**	4/26/2022	5494.8	1.04/**4500.2**	9/11/2022	4819.9
Site 5	2.779E-4	1.43/**5145.7**	4/22/2022	5753.8	—	—	—
Site 6	2.461E-3	11.73/**4766.4**	4/25/2022	5558.5	10.90/**4429.1**	9/10/2022	4875.7
Site 7	1.832E-3	8.43/**4601.5**	4/25/2022	5558.5	7.53/**4110.3**	9/10/2022	4875.7
Site 8	3.913E-3	17.77/**4541.3**	4/25/2022	5558.5	16.66/**4257.6**	9/10/2022	4875.7

Table 5.4: This table presents the results from the neutron flux measurements taken during data operation. The site locations are shown in Figure 5.35. The detector efficiency is determined with dedicated MCNP simulations. The measured rate is determined by the detector itself, while the yield is determined from by applying the detector efficiency to the measured results. The expected rates are determined from the neutron characterization measurements listed in Table 5.2 by propagating to the measurement date.

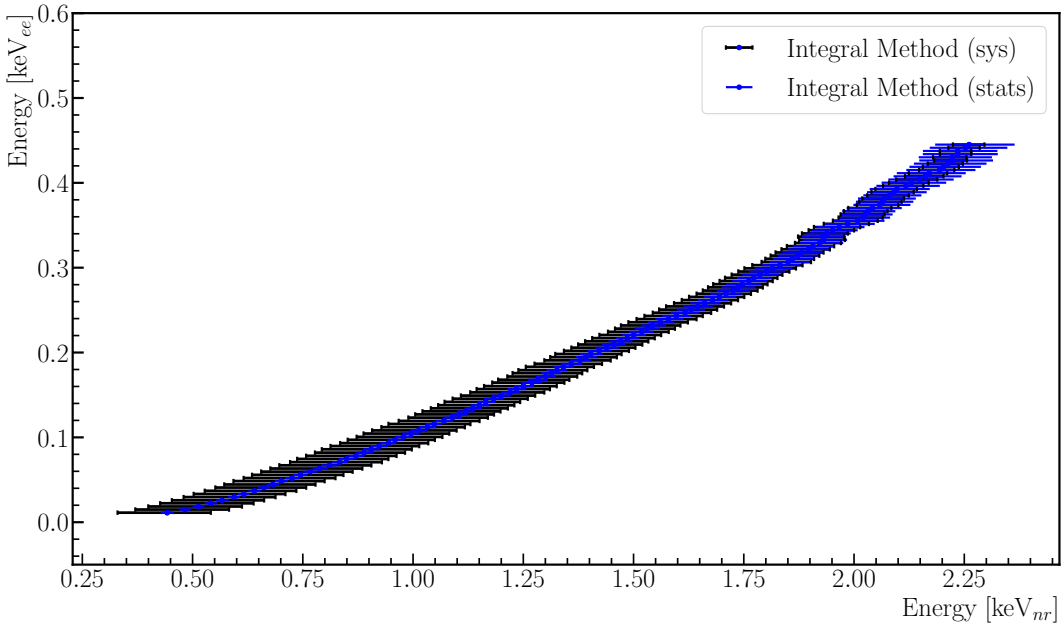

Figure 5.56: The ionization yield with statistical and systematic uncertainties overlaid. The blue error bars correspond to the statistical errors in the data, while the black error bars correspond to the systematic uncertainty.

ters.

5.10 Results

Figure 5.56 presents the results of the systematic uncertainty on the yield when calculated with the integral method. Since the integral method does not account for the variance in charge ionization that occurs due to the Fano factor, this result is funneled through the iterative procedure described in Section 5.8.4. The final result is shown in Figure 5.57 presented alongside recent measurements from SuperCDMS and DAMIC [4, 18]. A summary of these results can be found in Table 5.5. This thesis reports a measurement of the ionization yield to a 3 e- (11.2 eV) charge ionization threshold. At 3 e- we are sensitive to nuclear recoils of 427 keV$_{nr}$ in silicon. This result extends the previous measurement of the ionization yield with silicon CCDs from 60 eV$_{ee}$ to 11.2 eV$_{ee}$ [18]. As seen in the figure, at 60 eV$_{ee}$ of ionization, this result is consistent with the 2016 result. Moreover, when the SuperCDMS

results are represented in E_{ee} vs E_{nr} the results of this thesis are in fair correspondence with SuperCDMS. With this measurement, we demonstrate the improved sensitivity of Skipper CCDs when compared to conventional CCDs; having extended the recoil energy sensitivity from 680 keV_{nr} to 427 keV_{nr} we are able to probe lighter dark matter masses with more confidence.

Eee	**Enr**	**stats -**	**stats +**	**sys -**	**sys +**	**totalErr -**	**totalErr +**
[keVee]	[keVnr]	(-)	(+)	(-)	(+)	(-)	(+)
0.0113	0.427	0.0143	0.0148	0.1125	0.0991	0.1134	0.1002
0.0149	0.4685	0.0137	0.0132	0.1129	0.0997	0.1138	0.1006
0.0185	0.4915	0.014	0.0137	0.1139	0.0986	0.1147	0.0996
0.0223	0.5189	0.0136	0.0144	0.1145	0.0974	0.1153	0.0985
0.0258	0.5322	0.0135	0.0149	0.1142	0.0951	0.115	0.0962
0.0296	0.5589	0.0136	0.0134	0.1146	0.0939	0.1154	0.0948
0.0332	0.5715	0.0142	0.0141	0.1139	0.0943	0.1148	0.0954
0.037	0.6108	0.0136	0.0146	0.1126	0.0953	0.1134	0.0964
0.0409	0.6224	0.0138	0.0149	0.1099	0.0961	0.1108	0.0973
0.0445	0.6446	0.0144	0.0149	0.1102	0.0968	0.1111	0.0979
0.0484	0.6626	0.0147	0.0156	0.1086	0.0982	0.1096	0.0994
0.052	0.688	0.016	0.0166	0.1097	0.0986	0.1109	0.1
0.0558	0.7078	0.0163	0.0156	0.1099	0.0974	0.1111	0.0987
0.0596	0.7388	0.0173	0.0169	0.111	0.0964	0.1123	0.0979
0.0633	0.7552	0.0164	0.0185	0.1119	0.0968	0.1131	0.0985
0.067	0.7765	0.019	0.0173	0.1137	0.095	0.1153	0.0966
0.0708	0.7973	0.0171	0.0185	0.1124	0.0959	0.1137	0.0977
0.0746	0.8395	0.0171	0.0188	0.1116	0.0954	0.1129	0.0972

E_{ee}	**E_{nr}**	**Stats.**	**Stats.**	**Sys.**	**Sys.**	**Total**	**Total**
[keV$_{ee}$]	[keV$_{nr}$]	(-)	(+)	(-)	(+)	(-)	(+)
0.0782	0.8346	0.0179	0.0176	0.1131	0.092	0.1145	0.0936
0.082	0.8511	0.0175	0.02	0.1114	0.093	0.1127	0.0951
0.0859	0.8724	0.0189	0.0192	0.1119	0.0922	0.1134	0.0942
0.0897	0.886	0.0189	0.0192	0.11	0.0912	0.1116	0.0932
0.0932	0.9173	0.0186	0.0176	0.1099	0.09	0.1115	0.0917
0.0971	0.9322	0.0171	0.0192	0.1073	0.0905	0.1086	0.0925
0.1006	0.9548	0.0191	0.0208	0.1064	0.0882	0.1081	0.0906
0.1045	0.9634	0.0202	0.0199	0.1076	0.0869	0.1095	0.0891
0.1082	0.9835	0.0198	0.0199	0.1055	0.0862	0.1074	0.0884
0.112	1.0051	0.0197	0.0199	0.1046	0.0847	0.1064	0.087
0.1157	1.0299	0.0193	0.0186	0.1036	0.0824	0.1054	0.0844
0.1194	1.0464	0.0196	0.0199	0.1027	0.0807	0.1045	0.0831
0.1233	1.0853	0.0197	0.0216	0.1005	0.08	0.1024	0.0829
0.127	1.0762	0.0198	0.0209	0.0992	0.0796	0.1012	0.0823
0.1306	1.1189	0.02	0.0196	0.0983	0.0787	0.1003	0.0811
0.1342	1.1327	0.0188	0.021	0.0953	0.0795	0.0971	0.0822
0.1379	1.1241	0.0197	0.0216	0.0936	0.0793	0.0956	0.0822
0.1418	1.1467	0.02	0.0212	0.0933	0.0781	0.0954	0.081
0.1456	1.1758	0.0213	0.0218	0.0927	0.0778	0.0951	0.0808
0.1492	1.1835	0.0221	0.0215	0.0912	0.0773	0.0938	0.0803

Table 5.5: Summary of the measured ionization (E_{ee}) and the calculated nuclear recoil energy (E_{nr}) are presented up to 0.150 keV$_{ee}$ of charge ionization. The statistical (Stats.) and systematic (Sys.) uncertainties are also shown. 'Total' corresponds to the statistical and systematic uncertainties added in quadrature.

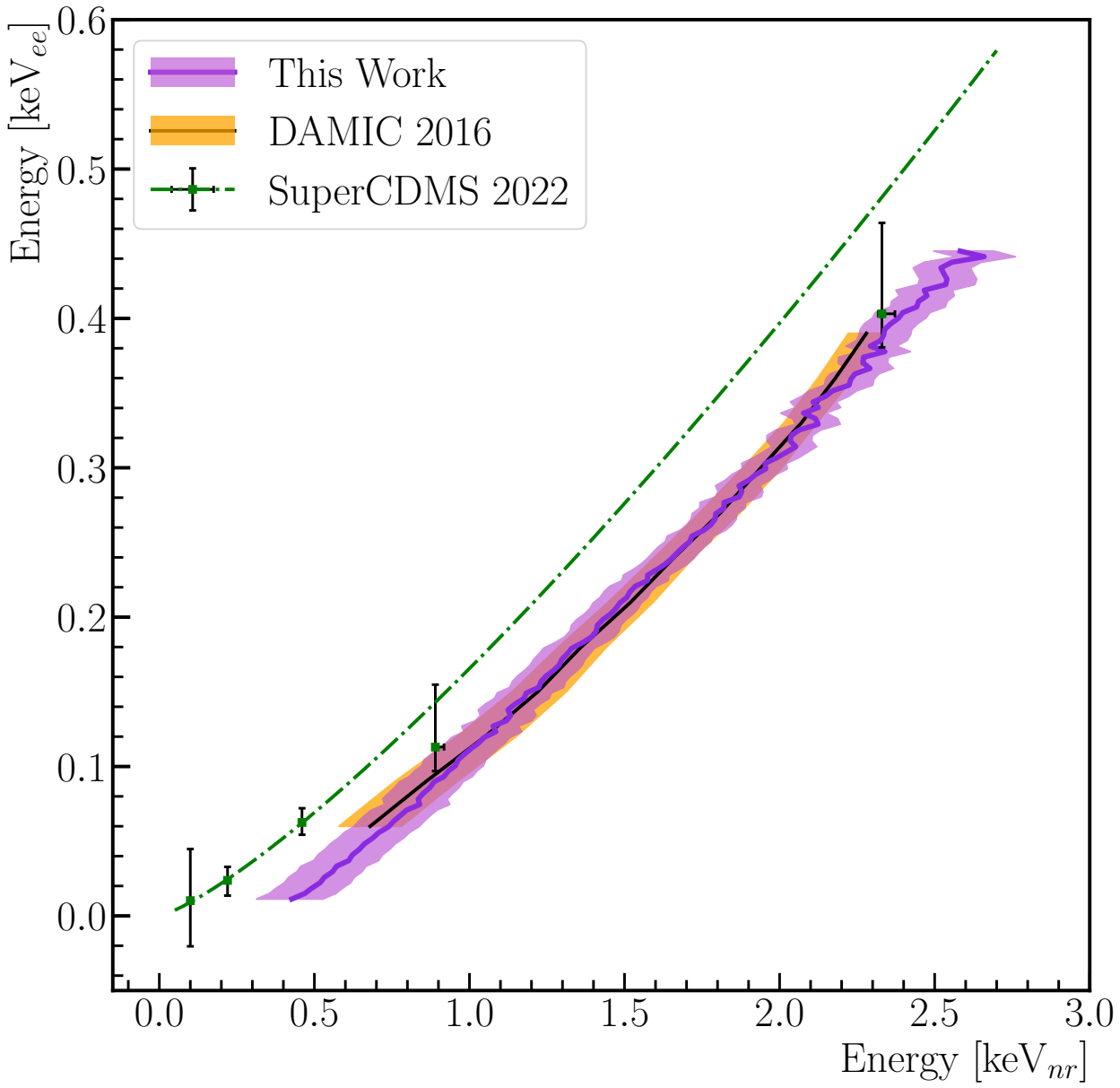

Figure 5.57: The ionization yield after taking the Fano factor reported by SuperCDMS into consideration. In purple, this result is show where the error band incorporates the contribution from the statistical and systematic uncertainty. The orange yield corresponds to the results from DAMIC 2016. The data points correspond to SuperCDMS results in 2022.

5.11 Final Remarks

Direct dark matter experiments that search for nuclear scattering events from an incident particle are reliant on the ionization efficiency in their detector. DAMIC-M employs silicon Skipper CCDs that reduce the readout noise of a pixel by repeating multiple non-destructive charge measurements. For every NDCM, the readout noise of the pixel is reduced by a factor of $1/\sqrt{N}$. This feature of the detector increases the sensitivity for rare event searches by providing measurement data with sub-electron resolution. A previous measurement of the ionization efficiency in silicon was carried out with conventional CCDs. These CCDs were limited in their sensitivity due to the limitation in readout noise ($\sim$2 e-). Nonetheless, these measurement carried out by A. Chavarria on behalf of the DAMIC collaboration, reported a measurement down to a 60 eV_{ee} charge ionization threshold [18]. This measurement extends the ionization efficiency down to 11.2 eV_{ee} and demonstrates the efficacy of Skipper CCDs as ultra-sensitive particle detectors — capable of resolving single electrons in the reconstructed energy spectrum. Ultimately these results, DAMIC-M will be able to probe lower dark matter masses that scatter off of silicon nuclei.

CHAPTER 6

CONCLUSION

To date, the dark matter community has been unable to confirm the detection of the elusive particle. As more of the dark matter mass parameter space is excluded, experiments have undergone rigorous research and development efforts to increase the sensitivity of their detectors. This thesis reported my contributions as a member of the DAMIC-M collaboration. With the employment of Skipper CCDs, DAMIC-M is uniquely positioned to explore dark matter interactions with silicon nuclei and atomic-shell electrons. Moreover, the experiment is sensitive to interactions down to 1.1 eV (corresponding with silicon's band-gap).

This thesis began by presenting my R&D contributions to the DAMIC-M experiment. Having successfully commissioned multiple test chambers for testing of Skipper CCDs, as well as commissioned a chamber to undergo two key calibration measurements for the collaboration. Furthermore, my work contributed to the successful development of the UChicago slow-control and monitoring system; a system that has been adopted by all test systems at the University of Chicago, as well as the LSM where the prototype Low-Background Chamber is installed and where the DAMIC-M experiment will be commissioned next year.

The measurement of the Compton scattering on atomic-shell electrons demonstrated the efficacy of the Skipper technology in greatly reducing the readout noise in the detector. From the measurement, we achieved a 23 eV measurement threshold with only 64 NDCMs. This measurement provided us with knowledge of the spectral features incited by small-angle scatters from radiogenic gammas. Furthermore, we reported the resolved L_1, $L_{2,3}$ steps and valence shell electrons in the spectral profile. This work ultimately led to the successful measurement constraints of dark matter electron scattering.

The measurement of the ionization efficiency in silicon further validated the efficacy of Skipper technology. By increasing the NDCMs to 1600, we achieved single electron resolution in the reconstructed energy spectrum. The increased resolution from $\sim$2 e- (with

conventional CCDs) to ∼0.14 e- (with Skipper CCDs) provided the sensitivity necessary to report a measurement threshold of 11 ev_{ee} and 427 eV_{nr}. This measurement remained consistent with results from DAMIC in 2016 and will allow the DAMIC-M experiment to probe to much lower WIMP masses in future dark matter searches.

Ultimately, this work proves to be crucial to the validation of Skipper technology, and calibrating the detectors for the electronic and nuclear response from incident particles. Ultimately allowing for better discrimination between radiogenic background depositions and dark matter interactions. With this work, the collaboration (as well as the community) will be more sensitive to dark matter candidates, and will be well positioned to answer the question 'what is dark matter?'.

Figure 6.1: A particle track in a Silicon CCD.

BIBLIOGRAPHY

[1] G. Adhikari *et al.*, "An induced annual modulation signature in COSINE-100 data by DAMA/LIBRA's analysis method," en, *Sci Rep*, vol. 13, no. 1, p. 4676, Mar. 2023, ISSN: 2045-2322. DOI: 10.1038/s41598-023-31688-4.

[2] A. Aguilar-Arevalo *et al.*, "Characterization of the background spectrum in DAMIC at SNOLAB," en, *Phys. Rev. D*, vol. 105, no. 6, p. 062 003, Mar. 2022, arXiv:2110.13133 [hep-ex], ISSN: 2470-0010, 2470-0029. DOI: 10.1103/PhysRevD.105.062003.

[3] A. Aguilar-Arevalo *et al.*, "Confirmation of the spectral excess in DAMIC at SNOLAB with skipper CCDs," en, *Phys. Rev. D*, vol. 109, no. 6, p. 062 007, Mar. 2024, arXiv:2306.01717 [astro-ph], ISSN: 2470-0010, 2470-0029. DOI: 10.1103/PhysRevD.109.062007.

[4] M. Albakry *et al.*, "First Measurement of the Nuclear-Recoil Ionization Yield in Silicon at 100 eV," en, *Phys. Rev. Lett.*, vol. 131, no. 9, p. 091 801, Aug. 2023, ISSN: 0031-9007, 1079-7114. DOI: 10.1103/PhysRevLett.131.091801.

[5] G. F. Amelio, M. F. Tompsett, and G. E. Smith, "Experimental verification of the charge coupled device concept," *The Bell System Technical Journal*, vol. 49, no. 4, pp. 593–600, 1970. DOI: 10.1002/j.1538-7305.1970.tb01791.x.

[6] C. Amole *et al.*, "Dark Matter Search Results from the PICO - 60 C 3 F 8 Bubble Chamber," en, *Phys. Rev. Lett.*, vol. 118, no. 25, p. 251 301, Jun. 2017, ISSN: 0031-9007, 1079-7114. DOI: 10.1103/PhysRevLett.118.251301.

[7] I. Arnquist *et al.*, *The DAMIC-M Experiment: Status and First Results*, en, arXiv:2210.12070 [hep-ex], Nov. 2022.

[8] I. Arnquist *et al.*, "First Constraints from DAMIC-M on Sub-GeV Dark-Matter Particles Interacting with Electrons," en, *Phys. Rev. Lett.*, vol. 130, no. 17, p. 171 003, Apr. 2023, ISSN: 0031-9007, 1079-7114. DOI: 10.1103/PhysRevLett.130.171003.

[9] I. Arnquist *et al.*, "Search for Daily Modulation of MeV Dark Matter Signals with DAMIC-M," en, *Phys. Rev. Lett.*, vol. 132, no. 10, p. 101 006, Mar. 2024, ISSN: 0031-9007, 1079-7114. DOI: 10.1103/PhysRevLett.132.101006.

[10] I. Arnquist *et al.*, *The DAMIC-M Low Background Chamber*, en, arXiv:2407.17872 [physics], Sep. 2024.

[11] R. Bernabei *et al.*, "Final model independent result of DAMA/LIBRA–phase1," en, *Eur. Phys. J. C*, vol. 73, no. 12, p. 2648, Nov. 2013, ISSN: 1434-6052. DOI: 10.1140/epjc/s10052-013-2648-7.

[12] G. Bertone and D. Hooper, "History of dark matter," en, *Rev. Mod. Phys.*, vol. 90, no. 4, p. 045 002, Oct. 2018, ISSN: 0034-6861, 1539-0756. DOI: 10.1103/RevModPhys.90.045002.

[13] G. Bertone, D. Hooper, and J. Silk, "Particle dark matter: Evidence, candidates and constraints," en, *Physics Reports*, vol. 405, no. 5-6, pp. 279–390, Jan. 2005, ISSN: 03701573. DOI: 10.1016/j.physrep.2004.08.031.

[14] J. Boldeman, B. Allen, A. de L. Musgrove, and R. Macklin, "The neutron capture cross section of natural silicon," *Nuclear Physics A*, vol. 252, no. 1, pp. 62–76, 1975, ISSN: 0375-9474. DOI: https://doi.org/10.1016/0375-9474(75)90601-6.

[15] R. Bunker, "A Low-Threshold Analysis of Data from the Cryogenic Dark Matter Search Experiment," en, Tech. Rep. FERMILAB-THESIS–2011-64, 1128108, Dec. 2011, FERMILAB–THESIS–2011–64, 1128108. DOI: 10.2172/1128108.

[16] M.-M. Bé and Bureau international des poids et mesures, Eds., *Table of radionuclides. Vol. 5: A=22 to 244* (Monographie BIPM 5), eng. Sèvres: BIPM, 2010, vol. 5, ISBN: 978-92-822-2234-8.

[17] N. Castello-Mor and D.-M. Collaboration, *DAMIC-M Experiment: Thick, Silicon CCDs to search for Light Dark Matter*, arXiv:2001.01476, Jan. 2020.

[18] A. E. Chavarria *et al.*, "Measurement of the ionization produced by sub-keV silicon nuclear recoils in a CCD dark matter detector," *Physical Review D*, vol. 94, no. 8, pp. 1–7, 2016, arXiv: 1608.00957, ISSN: 24700029. DOI: 10.1103/PhysRevD.94.082007.

[19] A. Chavarria *et al.*, *DAMIC at SNOLAB*, en, arXiv:1407.0347 [physics], Jun. 2014.

[20] X. Collaboration *et al.*, *The XENONnT Dark Matter Experiment*, arXiv:2402.10446, Feb. 2024.

[21] J. I. Collar, "Applications of an Y88/Be photoneutron calibration source to dark matter and neutrino experiments," *Physical Review Letters*, vol. 110, no. 21, pp. 1–4, 2013, arXiv: 1303.2686, ISSN: 00319007. DOI: 10.1103/PhysRevLett.110.211101.

[22] J. I. Collar, A. R. L. Kavner, and C. M. Lewis, "Germanium response to sub-keV nuclear recoils: A multipronged experimental characterization," *Physical Review D*, vol. 103, no. 12, p. 122 003, 2021, Publisher: American Physical Society, ISSN: 24700029. DOI: 10.1103/PhysRevD.103.122003.

[23] A. H. Compton, "A quantum theory of the scattering of x-rays by light elements," *Phys. Rev.*, vol. 21, pp. 483–502, 5 1923. DOI: 10.1103/PhysRev.21.483.

[24] DAMIC Collaboration *et al.*, "Search for low-mass WIMPs in a 0.6 kg day exposure of the DAMIC experiment at SNOLAB," *Phys. Rev. D*, vol. 94, no. 8, p. 082 006, Oct. 2016, Publisher: American Physical Society. DOI: 10.1103/PhysRevD.94.082006.

[25] DAMIC Collaboration *et al.*, "Results on Low-Mass Weakly Interacting Massive Particles from an 11 kg d Target Exposure of DAMIC at SNOLAB," *Phys. Rev. Lett.*, vol. 125, no. 24, p. 241 803, Dec. 2020, Publisher: American Physical Society. DOI: 10.1103/PhysRevLett.125.241803.

[26] B. L. Dougherty, "Measurements of ionization produced in silicon crystals by low-energy silicon atoms," *Phys. Rev. A*, vol. 45, pp. 2104–2107, 3 1992. DOI: 10.1103/PhysRevA.45.2104.

[27] R. Essig *et al.*, "Direct detection of sub-GeV dark matter with semiconductor targets," en, *J. High Energ. Phys.*, vol. 2016, no. 5, p. 46, May 2016, ISSN: 1029-8479. DOI: 10.1007/JHEP05(2016)046.

[28] W. L. Freedman and B. F. Madore, "The Hubble Constant," en, *Annu. Rev. Astron. Astrophys.*, vol. 48, no. 1, pp. 673–710, Aug. 2010, ISSN: 0066-4146, 1545-4282. DOI: 10.1146/annurev-astro-082708-101829.

[29] K. Freese, M. Lisanti, and C. Savage, "Annual Modulation of Dark Matter: A Review," en, *Rev. Mod. Phys.*, vol. 85, no. 4, pp. 1561–1581, Nov. 2013, arXiv:1209.3339 [astro-ph], ISSN: 0034-6861, 1539-0756. DOI: 10.1103/RevModPhys.85.1561.

[30] M Fujishiro, T Tabata, K Okamoto, and T Tsujimoto, "Cross section of the reaction 9 Be(γ, n) near threshold," *Canadian Journal of Physics*, vol. 60, no. 11, pp. 1672–1677, 1982, ISSN: 0008-4204. DOI: 10.1139/p82-224.

[31] G. Giroux, "Search for Dark Matter with the PICO-500 Experiment," en, *J. Phys.: Conf. Ser.*, vol. 2156, no. 1, p. 012 068, Dec. 2021, ISSN: 1742-6588, 1742-6596. DOI: 10.1088/1742-6596/2156/1/012068.

[32] K Hämäläinen and S Manninen, "Resonant and non-resonant inelastic x-ray scattering," *Journal of Physics: Condensed Matter*, vol. 13, no. 34, pp. 7539–7555, 2001. DOI: 10.1088/0953-8984/13/34/306.

[33] H. Hirayama, "Lecture Note on Photon Interactions and Cross Sections," en,

[34] *History of the endf project*, https://www.nndc.bnl.gov/endf/history.html.

[35] D. Hooper, *Particle cosmology and astrophysics*, eng. Princeton Oxford: Princeton University Press, 2024, ISBN: 978-0-691-23504-2.

[36] E. Hubble, "A relation between distance and radial velocity among extra-galactic nebulae," en, *Proc. Natl. Acad. Sci. U.S.A.*, vol. 15, no. 3, pp. 168–173, Mar. 1929, ISSN: 0027-8424, 1091-6490. DOI: 10.1073/pnas.15.3.168.

[37] J. R. Janesick, *Scientific charge-coupled devices*, en. Bellingham, Wash: SPIE Press, 2001, ISBN: 978-0-8194-3698-6.

[38] J. R. Janesick *et al.*, "New advancements in charge-coupled device technology: Sub-electron noise and 4096 x 4096 pixel CCDs," en, M. M. Blouke, Ed., Santa Clara, CA, Jul. 1990, pp. 223–237. DOI: 10.1117/12.19452.

[39] J. J. Kas *et al.*, "Advanced calculations of X-ray spectroscopies with *FEFF10* and Corvus," *Journal of Synchrotron Radiation*, vol. 28, no. 6, pp. 1801–1810, 2021. DOI: 10.1107/S1600577521008614.

[40] O. Klein and Y. Nishina, "Über die streuung von strahlung durch freie elektronen nach der neuen relativistischen quantendynamik von dirac.," *Z. Physik*, vol. 52, 853–868, 1929.

[41] E. Klevak *et al.*, "Finite-temperature calculations of the compton profile of be, li, and si," *Phys. Rev. B*, vol. 94, p. 214 201, 21 2016. DOI: 10.1103/PhysRevB.94.214201.

[42] G. F. Knoll, *Radiation detection and measurement*, en, 4th ed. Hoboken, N.J: John Wiley, 2010, OCLC: ocn612350364, ISBN: 978-0-470-13148-0.

[43] V. A. Kudryavtsev, L. Pandola, and V. Tomasello, "Neutron- and muon-induced background in underground physics experiments," en, *Eur. Phys. J. A*, vol. 36, no. 2, pp. 171–180, May 2008, ISSN: 1434-6001, 1434-601X. DOI: 10.1140/epja/i2007-10539-6.

[44] D. C. Larson, C. H. Johnson, J. A. Harvey, and N. W. Hill, "Measurement of the neutron total cross section of silicon from 5 ev to 730 kev," Nov. 1976. DOI: 10.2172/7342186.

[45] S. K. Lee, M. Lisanti, A. H. Peter, and B. R. Safdi, "Effect of Gravitational Focusing on Annual Modulation in Dark-Matter Direct-Detection Experiments," en, *Phys. Rev. Lett.*, vol. 112, no. 1, p. 011 301, Jan. 2014, ISSN: 0031-9007, 1079-7114. DOI: 10.1103/PhysRevLett.112.011301.

[46] J. Lewin and P. Smith, "Review of mathematics, numerical factors, and corrections for dark matter experiments based on elastic nuclear recoil," *Astroparticle Physics*, vol. 6, no. 1, pp. 87–112, 1996, ISSN: 0927-6505. DOI: https://doi.org/10.1016/S0927-6505(96)00047-3.

[47] T. Lin, *TASI lectures on dark matter models and direct detection*, en, arXiv:1904.07915 [hep-ph], Apr. 2019.

[48] J Lindhard, V Nielsen, M Scharff, and P. V. Thomsen, "Integral equations governing radiation effects. (notes on atomic collisions, iii)," *Kgl. Danske Videnskab., Selskab. Mat. Fys. Medd.*, vol. 33, no. 10, Jan. 1963.

[49] M. Markevitch *et al.*, "Direct Constraints on the Dark Matter Self-Interaction Cross Section from the Merging Galaxy Cluster 1E 0657-56," en, *ApJ*, vol. 606, no. 2, pp. 819–824, May 2004, ISSN: 0004-637X, 1538-4357. DOI: 10.1086/383178.

[50] M. Markevitch, *Chandra observation of the most interesting cluster in the Universe*, arXiv:astro-ph/0511345, Nov. 2005.

[51] M. Matheny, A. Roberts, A. Srinivasan, and A. N. Villano, "Intrinsic Fano factor of nuclear recoils for dark matter searches," en, *Phys. Rev. D*, vol. 106, no. 12, p. 123 009, Dec. 2022, arXiv:2206.13639 [physics], ISSN: 2470-0010, 2470-0029. DOI: 10.1103/PhysRevD.106.123009.

[52] D. Mei and A. Hime, "Muon-induced background study for underground laboratories," *Phys. Rev. D*, vol. 73, p. 053 004, 2006. DOI: 10.1103/PhysRevD.73.053004. arXiv: astro-ph/0512125.

[53] J. Nikkel, *astro-slow-control*, version 1.0, Aug. 2019.

[54] D. Norcini *et al.*, "Precision measurement of compton scattering in silicon with a skipper ccd for dark matter detection," *Phys. Rev. D*, vol. 106, p. 092 001, 9 2022. DOI: 10.1103/PhysRevD.106.092001.

[55] D. Norcini, *Chicago Slow Control*, version 2.0, Mar. 2020.

[56] P. J. E. Peebles, "Phenomenology of the Invisible Universe," *AIP Conference Proceedings*, vol. 1241, no. 1, pp. 175–182, Jun. 2010, ISSN: 0094-243X. DOI: 10.1063/1.3462631. eprint: https://pubs.aip.org/aip/acp/article-pdf/1241/1/175/11908220/175_1_online.pdf.

[57] P. J. E. Peebles, "Dark matter," en, *Proc. Natl. Acad. Sci. U.S.A.*, vol. 112, no. 40, pp. 12 246–12 248, Oct. 2015, ISSN: 0027-8424, 1091-6490. DOI: 10.1073/pnas.1308786111.

[58] Planck Collaboration *et al.*, "*Planck* 2018 results: VI. Cosmological parameters," en, *A&A*, vol. 641, A6, Sep. 2020, ISSN: 0004-6361, 1432-0746. DOI: 10.1051/0004-6361/201833910.

[59] R. Pratt *et al.*, "Limitations on the validity of impulse approximation in compton scattering," *Nuclear Instruments and Methods in Physics Research Section B: Beam Interactions with Materials and Atoms*, vol. 261, no. 1, pp. 175–179, 2007, The Application of Accelerators in Research and Industry, ISSN: 0168-583X. DOI: https://doi.org/10.1016/j.nimb.2007.03.085.

[60] K. Ramanathan, "Particles Taking Selfies: Investigation into Light Dark Matter Using Silicon Charge Coupled Devises," Publication Title: University of Chicago Volume: 21 Issue: 1 ISBN: 9789896540821, Ph.D. dissertation, 2020.

[61] K. Ramanathan and N. Kurinsky, "Ionization yield in silicon for ev-scale electron-recoil processes," *Physical Review D*, vol. 102, no. 6, 2020, ISSN: 2470-0029. DOI: 10.1103/physrevd.102.063026.

[62] K. Ramanathan *et al.*, "Measurement of low energy ionization signals from compton scattering in a charge-coupled device dark matter detector," *Phys. Rev. D*, vol. 96, p. 042 002, 4 2017. DOI: 10.1103/PhysRevD.96.042002.

[63] R. Ribberfors and K. F. Berggren, "Incoherent-x-ray-scattering functions and cross sections $(\frac{d\sigma}{d\Omega'})_{\text{incoh}}$ by means of a pocket calculator," *Phys. Rev. A*, vol. 26, pp. 3325–3333, 6 1982. DOI: 10.1103/PhysRevA.26.3325.

[64] A. E. Robinson, "Reanalysis of radioisotope measurements of the Be 9 (γ , n) Be 8 cross section," en, *Phys. Rev. C*, vol. 94, no. 2, p. 024 613, Aug. 2016, ISSN: 2469-9985, 2469-9993. DOI: 10.1103/PhysRevC.94.024613.

[65] V. C. Rubin, N. Thonnard, and W. K. Ford Jr., "Rotational properties of 21 SC galaxies with a large range of luminosities and radii, from NGC 4605 /R = 4kpc/ to UGC 2885 /R = 122 kpc/," en, *ApJ*, vol. 238, p. 471, Jun. 1980, ISSN: 0004-637X, 1538-4357. DOI: 10.1086/158003.

[66] V. C. Rubin and W. K. Ford Jr., "Rotation of the Andromeda Nebula from a Spectroscopic Survey of Emission Regions," en, *ApJ*, vol. 159, p. 379, Feb. 1970, ISSN: 0004-637X, 1538-4357. DOI: 10.1086/150317.

[67] Y. Sarkis, A. Aguilar-Arevalo, and J. C. D'Olivo, "Study of the ionization efficiency for nuclear recoils in pure crystals," en, *Phys. Rev. D*, vol. 101, no. 10, p. 102 001, May 2020, ISSN: 2470-0010, 2470-0029. DOI: 10.1103/PhysRevD.101.102001.

[68] C. Savage, K. Freese, and P. Gondolo, "Annual modulation of dark matter in the presence of streams," en, *Phys. Rev. D*, vol. 74, no. 4, p. 043 531, Aug. 2006, ISSN: 1550-7998, 1550-2368. DOI: 10.1103/PhysRevD.74.043531.

[69] B. J. Scholz *et al.*, "Measurement of the low-energy quenching factor in germanium using an y 88 /Be photoneutron source," *Physical Review D*, vol. 94, no. 12, pp. 1–7, 2016, ISSN: 24700029. DOI: 10.1103/PhysRevD.94.122003.

[70] M. Settimo, *The DAMIC experiment at SNOLAB*, en, arXiv:1805.10001 [astro-ph], May 2018.

[71] P. Sorensen, "Atomic limits in the search for galactic dark matter," en, *Phys. Rev. D*, vol. 91, no. 8, p. 083 509, Apr. 2015, ISSN: 1550-7998, 1550-2368. DOI: 10.1103/PhysRevD.91.083509.

[72] *Tgm-neutron-detectors*, https://web.mit.edu/8.13/www/JLExperiments/38/tgm-neutron-detectors.pdf.

[73] *The FEFF Project*, https://feff.phys.washington.edu/feffproject-portal.html, Accessed: 2022-05-24.

[74] J. Tiffenberg *et al.*, "Single-Electron and Single-Photon Sensitivity with a Silicon Skipper CCD," en, *Phys. Rev. Lett.*, vol. 119, no. 13, p. 131 802, Sep. 2017, ISSN: 0031-9007, 1079-7114. DOI: 10.1103/PhysRevLett.119.131802.

[75] A. N. Villano *et al.*, "First observation of isolated nuclear recoils following neutron capture for dark matter calibration," *Phys. Rev. D*, vol. 105, p. 083 014, 8 2022. DOI: 10.1103/PhysRevD.105.083014.

[76] R. H. Wechsler and J. L. Tinker, "The Connection Between Galaxies and Their Dark Matter Halos," en, *Annu. Rev. Astron. Astrophys.*, vol. 56, no. 1, pp. 435–487, Sep. 2018, ISSN: 0066-4146, 1545-4282. DOI: 10.1146/annurev-astro-081817-051756.

[77] J. Ziegler, J. Biersack, and U. Littmark, *The Stopping and Range of Ions in Solids* (Stopping and ranges of ions in matter). Pergamon, 1985, ISBN: 978-0-08-021603-4.

[78] F. Zwicky, "Die Rotverschiebung von extragalaktischen Nebeln," *Helv. Phys. Acta*, vol. 6, pp. 110–127, 1933. DOI: 10.1007/s10714-008-0707-4.